Methods and Results for Calibration and Track Separation of a GEM based TPC using an UV-Laser

Dissertation zur Erlangung des Doktorgrades des
Department Physik der Universität Hamburg

vorgelegt von
Markus Ball
aus Malsch

Hamburg
Mai 2008

Gutachter der Dissertation	: Prof. Dr. R.-D. Heuer Prof. Dr. K. Desch
Gutachter der Disputation	: Prof. Dr. R.-D. Heuer Prof. Dr. C. Hagner
Datum der Disputation	: 16.10.2008
Vorsitzender des Prüfungsausschusses	: Dr. T. Kipp
Vorsitzender des Promotionsausschusses	: Prof. Dr. J. Bartels
Leiter des Department Physik:	: Prof. Dr. R. Klanner
Dekan der MIN-Fakultät:	: Prof. Dr. A. Frühwald

Abstract

In the last 30 years high energy physics could write an impressive story of success. Since the introduction of the Standard Model (SM), it has met every experimental test. However the final confirmation has to prove the mechanism of electroweak symmetry breaking, which could not be confirmed yet. The most favored theory, which includes the introduction of a Higgs field, could not be verified experimentally. Furthermore there is clear evidence, that the SM is only a low energy description of nature and its principles, as the SM describes only 4 % of the known matter in the universe.
There are two different approaches in accelerator driven high energy physics to clarify the open questions. The Large Hadron Collider (LHC) have a good opportunity to measure some of the missing pieces with its high center of mass energy. The International Linear Collider (ILC) will then measure their parameters with high precision. To guarantee this high precision the detectors have to be able to identify every single particle and determine its properties with high accuracy.
These high requirements to the single detectors as well as the interconnectivity between all detectors are summarised by the concept of particle flow (PFLOW). This means that all particles must be separable, which includes in particular the main tracking device. A possible candidate for the central tracking device is a Time Projection Chamber (TPC). In this work a TPC with Gas Electron Multipliers (GEM) as gas amplification system was used. The GEMs replace the conventional wire amplification system of the TPC.
In this PhD work a method to determine the drift velocity of a TPC was developed and tested using an ultraviolet laser. To ensure a high accuracy of the method all relevant gas parameters were measured with a slow control system. Furthermore the laser was used to investigate the separation capability of nearby tracks. Therefore an existing TPC prototype, which was developed to operate in a 5 T magnet facility, was substantially modified. This work can thus present a comprehensive study and results for the separation capability of nearby tracks, which was done in the ILC TPC community.

Kurzfassung

In den letzten 30 Jahren konnte die Hochenergiephysik eine beeindruckende Erfolgsgeschichte schreiben. Seit der Einführung des Standard Modells (SM) konnte dieses jeder experimentellen Überprüfung standhalten. Denoch steht die vollständige Bestätigung noch aus, da der Mechanismus der elektroschwachen Symmetriebrechung bisher noch nicht experimentell geklärt werden konnte. Die favorisierte Theorie, welche die Einführung eines Higgsfeldes vorsieht, konnte bislang nicht experimentell bestätigt werden. Zudem gibt es klare Hinweise, dass das SM nur eine niederenergetische Beschreibung der Natur und der ihr zugrundeliegende Prinzipien darstellt, da das SM nur ca. 4 % der im Universum bekannten Materie beschreibt.
In der Beschleuniger-Hochenergiephysik gibt es zwei unterschiedliche Ansätze diese offenen Fragen zu beantworten. Der Large Hadron Collider (LHC) hat mit seiner hohen Schwerpunktsenergie gute Chancen einen grossen Teil der fehlenden Bausteine experimentell bestätigen zu können. Der Internationale Linear Collider (ILC) wird ihre dann ihre Eigenschaf mit hoher Präzission bestimmen können. Um diese hohe Präzission zu gewährleisten, müssen die Detektoren in der Lage sein jedes einzelne Teilchen zu identifizieren und seine Eigenschaften mit dem jeweils geeignetesten Detektor mit hoher Genauigkeit zu bestimmen.
Diese hohe Ansprüche an einerseits jeden einzelnen Detektor, sowie auch an die Interkonnektivität aller Detektoren, wird unter dem Begriff Particle Flow (PFLOW) zusammengefasst. Dies bedeutet, dass jedes Teilchen vom anderen separierbar sein muss, was insbesondere für die zentrale Spurkammer gilt. Als eine mögliche Option ist hierfür eine Zeit-Projektionskammer vorgesehen (TPC). In dieser Arbeit wurde eine TPC mit Gas Electron Multiplier (GEM) als Gasverstürkungssystem verwendet. Die GEMs ersetzen hierbei die konventionelle Gasverstärkung mit Drähten.
In der vorliegenden Doktorarbeit wurde eine Methode entwickelt und getestet, die mit Hilfe eines Lasers die Driftgeschwindigkeit einer TPC zu bestimmt. Um eine hohe Genauigkeit dieser Methode zu gewährleisten wurden alle relevanten Gas-Parameter mit Hilfe eines Monitorsystems bestimmt. Desweiteren wurde der UV-laser mit Hilfe eines einfachen optischen Aufbaus zur Bestimmung der Separationskapazität benachbarter Spuren verwendet. Hierfür wurde ein bereits bestehender TPC Prototyp, welcher für Messugen in einem 5 T Magneten entwickelt wurde, umfassend modifiziert. Diese Arbeit kann daher eine umfassende Studie und Ergebnisse zur Quantifizierung zur Separationskapazität benachbarter Spuren innerhalb der ILC TPC Gemeinschaft präsentieren.

Contents

Chapter 1

Introduction

1.1 The Standard Model and its limits

The aim of elementary particle physics is to explain and describe the experimentally observed fundamental constituents of matter and the interactions among them. Our current knowledge of elementary particle physics is summarised in the Standard Model (SM) [1]. According to this model all matter consists of 3 quark generations and 3 lepton generations, given in Table 1.1. The bosonic particles, that are the mediators of the interactions are given in Table 1.2.

Although the Standard Model was very successful over the last decades in particle physics, it still leaves many questions unanswered, such as:

- What is the origin and mechanism of mass production?
- The known constituent of the SM cover only 4 % of the matter of the universe. Where and what are the missing 96 % of the matter?
- Is there a unification of our understanding for the four fundamental forces of nature respective is there a theory or model realised in nature, that unifies the known forces to one fundamental principle?

There are two different strategies to go beyond the Standard Model. One approach is to study rare and tiny processes as for example realised in the broad field of neutrino physics [2]. Experiments like Superkamiokande [3], K2K [4], SNO [5] and KamLAND [6] have established neutrino oscillation. This indicates, that neutrinos have a tiny, but finite mass. In the SM only massless neutrinos are predictedzu bestimmenzu bestimmenzu bestimmenzu bestimmenzu bestimmenzu bestimmenzu bestimmen. If the neutrinos have a mass, they can not travel with speed of light, which means it is possible to

Quarks			
$Q_e = +\frac{2}{3}$		$Q_e = -\frac{1}{3}$	
u	1.5 ... 4 MeV	d	4 ... 8 MeV
c	1.15 ... 1.35 GeV	s	80 ... 130 MeV
t	178.0 ± 4.3 GeV	b	4.1 ... 4.4 GeV
Leptons			
$Q_e = 0$		$Q_e = -1$	
ν_e	< 3 eV	e^-	511 keV
ν_μ	< 19 keV	μ^-	106 MeV
ν_τ	< 18.2 keV	τ^-	1.78 GeV

Table 1.1: *Fermionic particles of the Standard Model. The Leptons and quarks are given with their current mass assumptions or limits.*

interaction	exchange boson	spin	mass	range
strong	8 gluons (g)	1	0	10^{-15}
electromagnetic	γ	1	0	∞
weak	$W^\pm$	1	80.4 GeV	10^{-18}
	Z^0	1	91.2 GeV	10^{-18}
gravity	graviton	2	0	∞
	Higgs	0	?	∞

Table 1.2: *Bosonic particles of the Standard Model. The properties are given in terms of their spin, mass and interaction range. Gravity is not described by the SM.*

find a system, where the neutrino is right-handed. As it have been observed only left-handed neutrinos and right-handed antineutrinos and the the finite mass of the neutrinos implies that the SM is incomplete or at least a lot more profound. One exciting questions among many in this field is to discriminate the true nature of the neutrino. Is it a Majorana or Dirac particle? In case of the Majorana nature of the neutrino, this would mean, that neutrino and antineutrino are identical particles. The neutrinoless double-beta decay is the only known practical approach to discriminate a Majorana from a Dirac neutrino. A Majorana neutrino could be a first indication for the existence of Supersymmetry.
The complememtary approach is to go to high energies and high event rates. The two accelerators, that represents this approach are the Large Hadron Collider (LHC) and the International Linear Collider (ILC). The

LHC is a proton proton collider with a center of mass energy of up to 14 TeV and a peak luminosity of about $10^{34}\frac{1}{cm^2s^2}$ [7]. The ILC is an electron positron collider with an energy up to 500 GeV (1 TeV in the second stage of expansion) and a peak luminosity of about $2 \cdot 10^{34}\frac{1}{cm^2s^2}$ [8]. Due to its tremendous center of mass energy the LHC has a great discovery potential for physics beyond the Standard Model. The ILC has advantages in precision measuremnts due to its clean experimental environment, the possibility of polarized beams and the known collision energy at the interaction point. Evaluation of the interplay between LHC and ILC has been done to study the combined physics potential of both machines [9].

The most compelling and most simple solution to explain the particle masses in the Standard Model is the Higgs mechanism [12]. It describes the particle masses as an effect of the interaction of the particles with a non-vanishing constant vacuum expectation value. The Higgs mechanism predicts the existence of a spinless particle, the Higgs Boson. It is the only particle which has not been experimentally detected yet. In the context of the Standard Model, all properties of the Higgs Boson except its mass are predicted. Using precision data [13] and direct Higgs boson searches [14], its mass m_h can be constrained to 114.4 GeV $< m_h <$ 251 GeV. To prove the existence and verify the properties of the Higgs particle is therefore a test on the validity of the Standard Model in general and one major task for the combined LHC/ILC efforts.

One of the favored theories of physics beyond the Standard Model is Supersymmetry (SUSY). The concept of Supersymmetry was developed 30 years ago [15, 16]. It extends the concept of space-time to superspace, which introduces an additional degree of freedom, that distinguishes if a particle is fermionic or bosonic. It connects every fermionic particle with a bosonic superpartner and vice versa to a multiplett. The particles have the same quantum numbers except the spin, that differs by $\frac{1}{2}$. SUSY can not be an exact symmetry as no superparticle have been discovered yet. Therefore one speaks from a broken symmetry. The center of mass energy range, that will be available at the LHC and the ILC should prove if SUSY is realized in nature or not. If SUSY is realized in nature, it might introduce a new conservation parameter called R-parity conservation. Due to the R-parity conservation the lightest SUSY particle becomes stable and is therefor a good candidate to explain the missing matter in the universe. Another evidence for the existance of Supersymmetric Models is the unification of the coupling constants of electroweak and strong force at the Planck scale. This also leads to an important prediction for the electroweak mixing angle $sin^2\theta_W$. This

angle describes the relative strength of U_1 to SU_2 coupling. If extrapolating this value from the Planck scale one gets

$$sin\theta_W = 0.2355 \pm 0.0017. \tag{1.1}$$

The experimentally observed value is given by

$$sin\theta_W = 0.2310 \pm 0.0002. \tag{1.2}$$

The agreement between the theoretical prediction and experimentally observed value justifies Supersymmetry as a favored theory of physics beyond the Standard Model

1.2 The International Linear Collider

1.2.1 The Accelerator

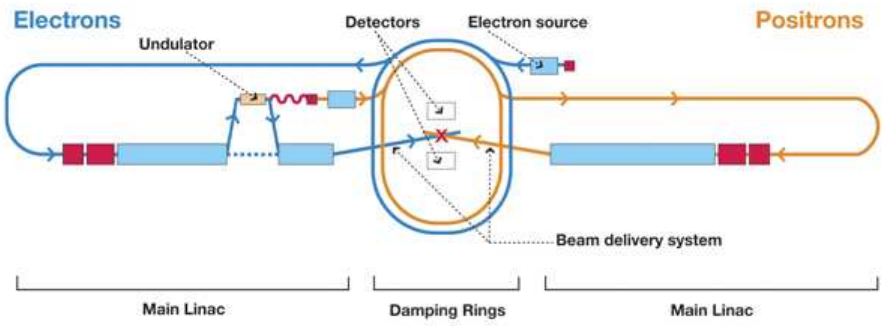

Figure 1.1: *The ILC design as proposed in the ILC Reference Design Report [8].*

The International Linear Collider (ILC) is a 200-500 GeV center-of-mass high luminosity linear electron positron collider based on 1.3 GHz superconducting radio-frequency (SCRF) accelerating cavities. A great breakthrough towards the realization of ILC was the technology decision, which was taken by the International Technology Recommendation Panel (ITRP) in August2004 [11]. At the 2nd ILC Workshop in August 2005, held at Snowmass, Colorado, USA, the efforts to a global concept for the ILC was expressed in the formation of the ILC Global Design Effort (GDE). The GDE

Parameter hline Center of mass energy range	Unit GeV	 200-500
Peak luminosity	$\frac{1}{cm^2 s^1}$	$2{\times}10^{34}$
Average beam current in pulse	mA	9.0
Pulse Rate	Hz	5.0
Pulse length (beam)	ms	$\approx$1
Number of bunches per pulse		1000-5400
Charge per bunch	nC	1.6 - 3.2
Accelerator gradient	MV/m	31.5
RF pulse length	ms	1.6
Beam power (per beam)	MW	10.8
Typical beam size at IP ($h \times v$)	nm	640 $\times$ 5.7
Total AC power consumption	MW	230

Table 1.3: *Basic design parameters for the ILC (for center of mass energy of 500 GeV)*

reflects the global nature of the collaboration, with accelerator experts from all three regions (America, Asia and Europe).
The ILC design has been developed to achieve the following physics performance goals [10]:

- A continous center-of-mass energy range between 200 and 500 GeV.
- A peak luminosity of $\approx\ 2{\cdot}10^{34}\frac{1}{cm^2 s^1}$. This should provide an integrated luminosity of 500 fb^{-1} in the first four years of operation.
- An electron polarization of > 80 % at the Interaction Point (IP).
- An energy stability and precision of ≤ 0.1 %.
- An option for ≈ 60 % positron polarization.
- An option for $e^-\ e^-$ and $\gamma\ \gamma$ collisions.

In Figure 1.6 the schematic layout of the ILC is shown. The machine should be upgradable to a center of mass energy of 1 TeV in a future phase of operation. This guarantees a rich and varied physics program as described in the previous sction. The basic design parameters for the ILC are given in Table 1.3

With the completition of the RDR, the GDE will begin an engineering design study, coupled with a prioritezed R&D program. The goal is to produce an Engineering Design Report (EDR) by 2010, presenting an matured technology, design and construction plan for the ILC, followed by the start of construction in 2012. With a construction phase of seven years the ILC operation could begin in 2019.

1.2.2 Physics Motivation

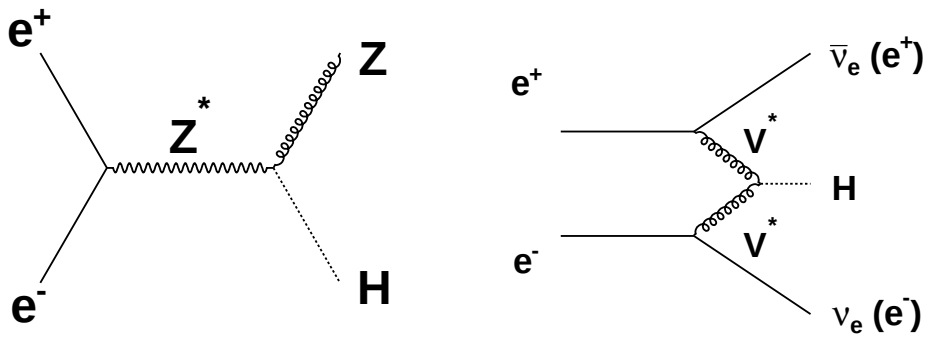

(a) Higgs-strahlung process (b) WW fusion process

Figure 1.2: *Diagrams for the dominant Higgs production mechanisms at the ILC.*

As pointed out the Higgs particle is the last particle of the Standard Model, that misses experimental observation. In e^+e^- collisions the main production mechanism for the SM Higgs particle are the Higgs-strahlung process and WW fusion processes (see Figure 1.2). The cross section for Higgs-strahlung scales as $1/s$ and therefore dominates at low energies, while the one of the WW fusion mechanism rises like $\log(s/M_H^2)$ and becomes more important at high energies. At $\sqrt{s} \approx 500$ GeV, the two processes have approximately the the same cross section (50 fb) for the interesting Higgs mass range 115 GeV $\leq M_H leq$ 200 GeV favored by high precision data. For the integrated luminosity $\mathcal{L} \approx 500$ fb^{-1}, which is expected in about one or two years after the commissioning phase, 30000 to 40000 events can be collected. This sample is more than enough to observe the Higgs particle at the ILC and study its properties such as the Higgs boson mass, spin, parity quantum numbers, couplings to fermions, massive and masseless gauge bosons as well as its trilinear self-couplings with high accuracies. The measurements would allow to probe in all its facets the electroweak

symmetry breaking mechanism in the SM and probe small manifestations of new physics. An example how such a event would look like in the ILC detector is given in Figure 1.3

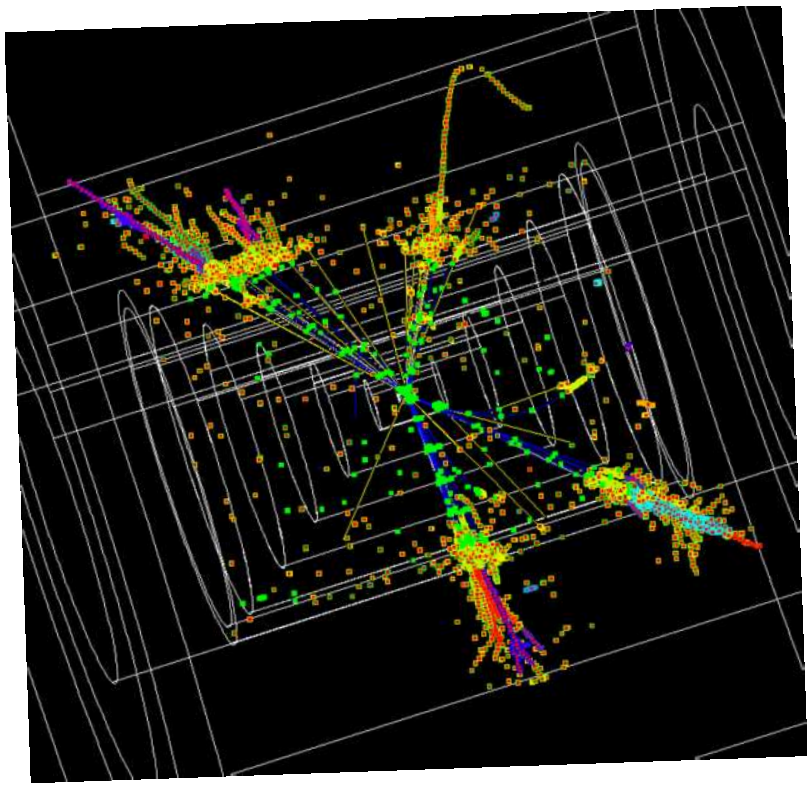

Figure 1.3: *Example of a Higgs event in the ILC detector by Norman Graf [19].*

As examples the determination of the Higgs spin and decay branching ratios are illustrated in Figure 1.4. The determination of the spin quantum number of the SM Higgs boson can be performed in the Higgs-strahlung process. In Figure 1.4(a) the measurement of the rise of the cross section near the production threshold, $\sigma(e^+e^- \rightarrow HZ)$ rules out the 0, 1 or 2 hypothesis for the spin of the Higgs. A threshold scan with a luminosity of 20 fb^{-1} at three different center of mass energies is sufficient to distinguish the various behaviors.
The measurement of the branching ratio of the Higgs boson is of high importance. For Higgs masses below $M_H \leq 140$ GeV, a large variety of branching ratios can be measured at the ILC, since the $b\bar{b}, c\bar{c}$ and gg final

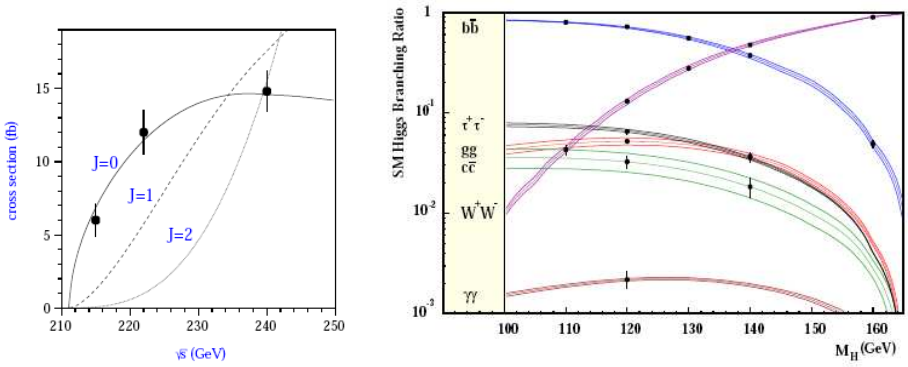

(a) (b)

Figure 1.4: *Figure (a) shows the $e^+e^- \rightarrow ZH$ cross section energy dependence near threshold for $M_H = 120$ GeV for spin $0^+, 1^-$ and 2^+ [18]. Figure (b) shows the branching ratio for the SM Higgs boson with the expected sensitivity at ILC. A luminosity of 500 fb^{-1} at a center of mass energy of 350 GeV are assumed [17].*

states have significant rates and can be very efficiently disentangled by means of micro-vertex detectors. The $b\bar{b}, c\bar{c}$ and $\tau^+\tau^-$ fractions allow to measure the the relative couplings of the Higgs boson to these fermions and to check the prediction of the Higgs mechanism that they are indeed proportional to the fermion masses.

Also physics beyond the Standard Model is an important question for the ILC. As pointed out SUSY is one of the most favored candidates of physics beyond the SM. Although maybe not all SUSY processes can be produced, at least the light supersymmetric particles should be accesable at the ILC. In Figure 1.5(a) this is illustrated in one possible SUSY scenario, which have been used as a benchmark for the ILC, the SPS1a [20]. Due to an inflation of SUSY models, that are currently available it is not sufficient to simply produce the new particles but also verify its most fundamental predictions in a model independent way. One example for a SUSY process, that might be measured at the ILC is the process $\sigma(e^+e^- \rightarrow \tilde{l}^+\tilde{l}^-)$. In the continuum the slepton masses can be obtained from the endpoint energies of leptons coming from slepton decays. In the case of two body decays, $\tilde{l}^\pm \rightarrow l^\pm\chi_i^0$ and $\tilde{\nu}_l \rightarrow l^\pm\chi_i^\mp$, the lepton energy spectrum is flat with the minimum and the maximum energies providing an accurate determination of the masses of the primary sleptons and the secondary neutralino/chargino. A simulation

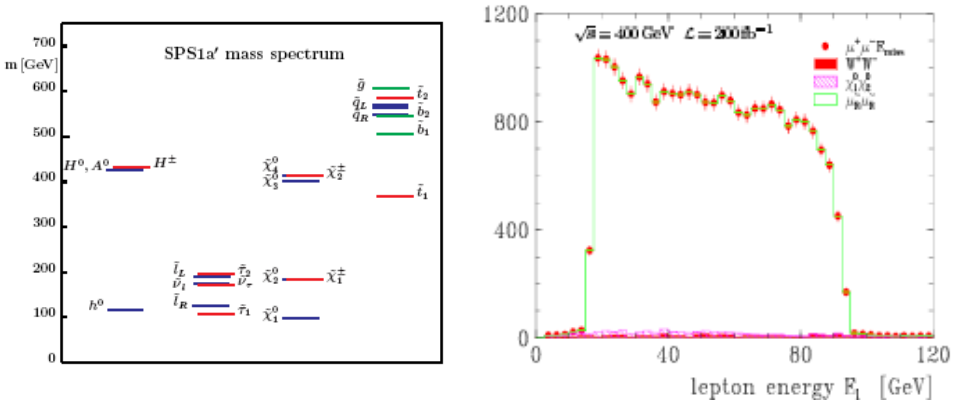

(a) (b)

Figure 1.5: *In picture (a) the spectrum of SUSY and Higgs particle masses in the benchmark scenario SPS1a are show. Picture (b) shows a simulation of the μ energy spectra of $\tilde{\mu}_R^+\tilde{\mu}_R^-$ production at $\sqrt{s}$ = 400 GeV and $\mathcal{L}$ 200 fb^{-1}*

.

of the μ energy spectra of $\tilde{\mu}_R^+\tilde{\mu}_R^-$ production, including beamstrahlung, initial state radiation, selection criteria and detector resolution, is shown in Figure 1.5(b) for SPS1a [21]. With a moderate luminosity of 200 fb^{-1} at $\sqrt{s} = 400$ GeV, one obtains $m_{\tilde{\mu}_R} = 143 \pm 0.10$ GeV and $m_{\tilde{\chi}_1^0} = 96 \pm 0.10$ GeV. Similar results are obtained in the case of selectron production in $\sigma(e^+e^- \rightarrow \tilde{e}_R^+\tilde{e}_R^-)$.

1.2.3 The Large Detector Concept (LDC)

This work is done in the scope of the Large Detector Concept (LDC) [22], which is one proposal for a detector at the ILC. A sketch of the detector layout is given in Figure 1.6 [1]. The aim of the detector design is to reconstruct every particle of an event independent if its charged or neutral. This pushes the detector design in a direction where the separation of the particles is more important than the precise measurement of its parameters. The tracking in such a detector concept has to detect the charged particles with high efficiency. The tracking system of the LDC consists of a vertex detector, intermediate and forward tracker and a large TPC, that is considered as a central tracking device. The main requirement of the tracking system for LDC are:

[1]The LDC has now formed together with the Giant Large Detector (GLD) the International Large Detector concept.

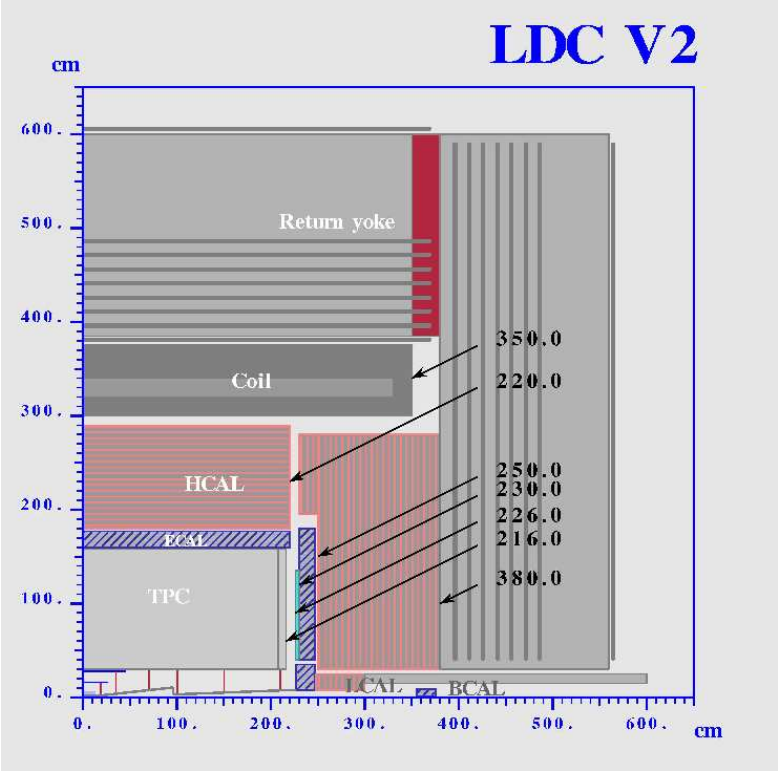

Figure 1.6: *Schematic drawing of the LDC detector showing one quarter of the proposed design [8].*

- Excellent momentum resolution over a large solid angle: $\Delta(1/p) = 5 \times 10^{-5}\ (GeV/c)^{-1}$
- Very good bottom and charm tagging capabilities to separate between final states containing b and c hadrons
- Good momentum resolution in the forward direction, to measure charges of high momentum particles down to lowest angles with small confusion.
- Very good pattern recognition capability over the full solid angle.
- Minimal material to interfere as little as possible with the measurement of electrons and photons in the calorimeter.

The complete tracking system is integrated in a 4T solenoidal magnetic field, aligned with the z-axis. The TPC fulfills especially the last two criteria

of tracking requirements. The complete tracking requirements of the TPC alone are given in table 1.4.

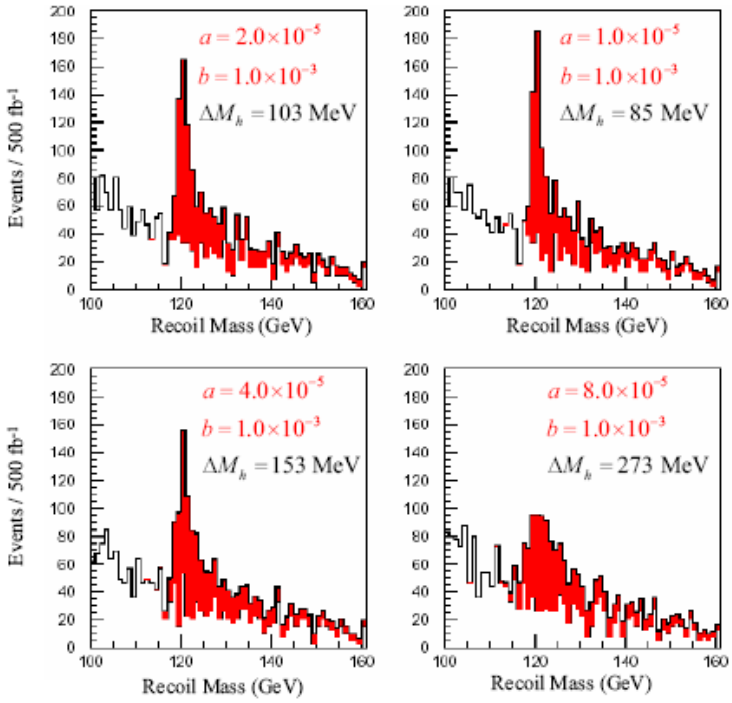

Figure 1.7: *Higgs recoil mass spectra for several values of parameters characterizing the tracker momentum resolution, which is parameterized as* $\delta p_t/p_t^2 = a \oplus b/(p_t sin\theta)$ *[23].*

To demonstrate the importance of an excellent tracking momentum resolution, the precision of the mass measurements in dependency on the momentum resolution of the tracker has been investigated [23, 24, 25]. Figure 1.7 shows the recoil mass distribution for the determination of the Higgs mass for four different values of tracker momentum resolution, characterized by the parameters a and b, assuming the Higgs mass to 120 GeV, $\sqrt{s}$ = 350 GeV, and the integrated luminosity is 500 fb^{-1}. Here the momentum resolution is written $\delta p_t/p_t^2 = a \oplus b/(p_t sin\theta)$. The accuracy for the determination of M_H improves from a = 8×10^{-5} and a value for ΔM_H = 273 MeV to 85 MeV if a is reduced to 1×10^{-5}.

The subject of this work was to study the two track resolution of a TPC. In the progression of this work the TPC design was changed tremendously in regard of the pad size. As the pad size has an enormous effect especially on the two track resolution in rϕ the validity of the results has to be seen in regard of the pad layout of the previous TPC pad design [42]. The pad size of the previous TPC design was $2 \times 6mm^2$. To investigate the two track resolution with high statistic a laser setup was planed, built and evaluated in regard of a operation in high magnetic fields. A TPC prototype was modified the insertion of a laser beam into the drift volume, so that its performance could be studied under reproducible conditions. (see section 5.2.4 and chapter 5). Afterward a data taking with the TPC and the laser setup took place in a superconducting magnet test facility (see section 4.8). A fast and simple Monte Carlo simulation (see section 6.5) was programmed, which allowed a comparison of data and simulation files to understand and test the validity of the measurement results. The results of the track separation capabilities are presented in chapter 9.
A study developed in the general process of laser studies was carried out to cross-check the calibration capability of a laser in regard of the determination of the drift velocity. This study is presented in chapter 7 and is an outlook to the capability of lasers as a calibration tool.

Size	Inner radius 30 cm, outer radius 158 cm, length 4.32 m
Momentum Resolution	$\delta(1/p_t) \approx 10^{-4}$ GeV/c
Solid angle coverage	$cos(\theta) \leq 0.98$
TPC material budget	$0.03X_0$ to outer fieldcage in r $0.30X_0$ for readout endcap in z
Number of pads	$> 10^6$ per endcap
Pad size / number of padrows	$1 \times 6mm^2$ for 200 pad rows
Single point resolution in rϕ	≈ 100 μm
Single point resolution in rz	≈ 2 mm
Two track resolution in rϕ	< 2 mm
Two track resolution in rz	< 5 mm
dE/dx resolution	≈ 5 %
Performance robustness	Full precision / efficiency in backgrounds with 10 % total occupancy

Table 1.4: *List of performance requirements for the TPC in the LDC concept [22]*

Chapter 2

Basic Principles of Time Projection Chambers (TPC)

This chapter should provide the basic understanding of operation principles and physics processes in a Time Projection Chamber. The TPC is one well known and approved realisation of a gaseous detector in High Energy Physics. The first construction and successful operation of a TPC was used in the PEP-4 experiment at the Stanford electron positron storage ring [26]. Also two experiments at the last big electron positron collider LEP, based their tracking on TPCs adapted to larger dimensions but otherwise similiar to the original design [27], [28]. The time projection concept has also found applications in other detectors like the STAR TPC at RHIC [29] in Brookhaven or the ALICE TPC at the LHC [30]. Both TPCs are operating in heavy ion collisions, which shows that the TPC concept is not limited to electron positron collider experiments. The TPC concept is now also considered for neutrino experiments as the Tokai to Kamiokande experiment, which studies neutrino oscillation. In the near detector TPCs are a major part in the whole detector concept [31]. This demonstrates the TPC is a modern detector, which can and will be used for many applications in High Energy Physics.

2.1 Operation Principles

The *Time Projection Chamber*, as introduced in 1974 by D. Nygren [32], has become one of the most popular tracking device allowing three dimensional track reconstruction and particle identification within one detector. In first order it is a gas filled capacitor with a parallel homogenous electric field. The homogenity of the electric field is provided by a field cage, that consists

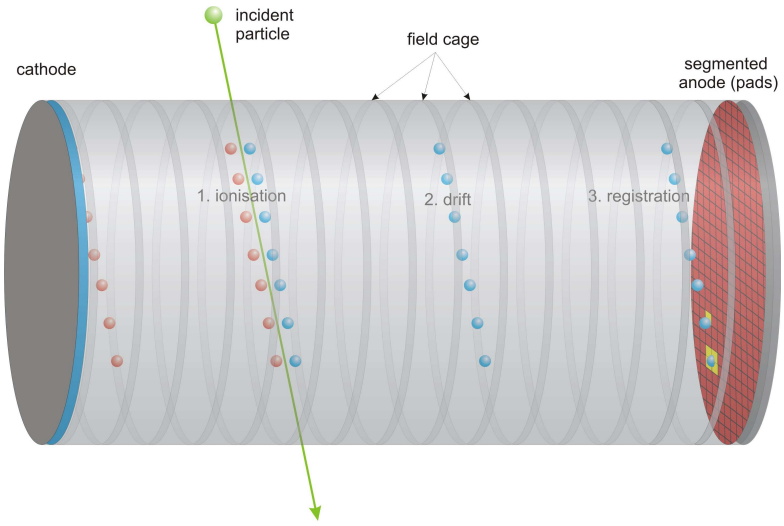

Figure 2.1: *Operation principles of a TPC*

of equidistant ring electrodes, placed along the TPC. The ring electrodes are powered with constant potential differences between a cathode and anode plane. An ionizing particle that traverses the gas volume produces electron-ion pairs. These electron-ion pairs may be viewed as a *track image*. Exposed to the uniform electric field, these electrons and ions drift along the electric field lines in opposite directions towards the anode and cathode. The ions drift very slow due to their higher mass compared to the electrons to the cathode plane and do not contribute to the signal. The electrons drift in the opposite direction and are multiplied in front of the anode by an amplification system.
The anode plane itself is segmented in a row- and columnwise two dimensional structure. A single segmentation is called a pad [33]. By exploiting the information from the deposition of charge on the pads, a two dimensional projection of the track image can be determined. A complete three-dimensional track image can be derived from the knowledge of the drift velocity in presence of a homogenous electric field and the measured time between production of the electron and the detection on the anode plate. This procedure to calculate the z position by the measured time is responsible for the name of *the Time Projection Chamber*. The procedure allows a three dimensional reconstruction of a track image for particle trajectories. For the measurement of particle momenta and the charge of the traversing particle a magnetic field is applied. Typically it is oriented parallel or antiparallel to the electric field.

Symbol	Definition	Units or Value
α	Fine structure constant	1/137.03599911
c	speed of light	3.0 10^8 m/s
$m_e c^2$	Electron mass $\cdot c^2$	0.510998918 MeV
r_e	Classical electron Radius $\frac{e^2}{4\pi\epsilon_0 m_e c^2}$	2.817940325 fm
N_A	Avogadro's number	6.0221415 x $10^{23} mol^{-1}$
ze	Charge of incident particle	
Z	Atomic number of absorber	
A	Atomic mass of absorber	
K	$4\pi N_A r_e^2 m_e c^2$	0.307075 MeV$g^{-1}cm^2$

Table 2.1: Summary of variables used in this section

The direction of the curve is determined by the charge of the particle, the strength of the curvature is determined by the momentum of the particle. With a precise knowledge of the magnetic field, the charge of the particle and the measured radius the momentum of the particle can be derived with equation 2.1. The more accurate the radius respectively the curvature can be measured, the more accurate the momentum can be determined.

$$\frac{mv^2}{R} = q \cdot v \cdot B \Rightarrow \frac{p}{R} = q \cdot B \Rightarrow p = q \cdot B \cdot R \tag{2.1}$$

Besides tracking capabilities a TPC also offers the possibility of particle identification. Due to the high homogeneity of the gas volume, the energy loss per unit length $\frac{dE}{dx}$ in the gas can be measured precisely. If the TPC is operated in proportional gas amplification mode, the signal collected on the anode is proportional to the number of electron-ion pairs from the ionization process and thus proportional to $\frac{dE}{dx}$. With a combination of the energy loss measured along the particle trajectory and the momenta determined via the magnetic field allows efficient particle identification. A detailed description for the ionisation processes in a TPC and particle identification due to the specific energy loss is given in the following sections.

2.2 Primary Ionization in the TPC

Primary electrons are extracted from the gas molecules by electromagnetic interaction with the traversing fast charged particles. The ionization process is quantitavely understood by a single virtual photon exchange [35].

Gas	Z	ρ $[\frac{g}{cm^3}]$	I_0 [eV]	W_I [eV]	dE/dx $[\frac{MeVcm^2}{g}]$	dE/dx $[\frac{keV}{cm}]$	n_{prim} $[cm^{-1}]$	n_{tot} $[cm^{-1}]$
H_2	2	8.38 10^{-5}	15.4	37	4.03	0.34	5.2	9.2
He	2	1.66 10^{-4}	24.6	41	1.94	0.32	4.8	7.8
N_2	14	1.17 10^{-3}	15.5	35	1.68	1.96	(10)	56
O_2	16	1.33 10^{-3}	12.2	31	1.69	2.26	22	73
Ne	10	8.39 10^{-3}	21.6	36	1.68	1.41	12	39
Ar	18	1.66 10^{-3}	15.6	26	1.47	2.44	24.3	94
Xe	54	5.49 10^{-3}	12.1	22	1.23	6.76	44	307
CO_2	22	1.86 10^{-3}	13.7	33	1.62	3.01	36.5	91
CH_4	10	6.70 10^{-4}	13.1	28	2.21	1.48	26.5	53
C_4H_{10}	34	2.42 10^{-3}	10.8	23	1.86	4.50	89.6	195

Table 2.2: Important parameters for frequently used chamber gases. The number in paranthesis are determined by interpolation

For many gases the energy of the extracted electrons is larger than the ionization energy of the gas molecules, such that in subsequent inelastic collisions secondary electrons are set free. The primary electron is spatially correlated with the secondary electrons, i.e., the ionization electrons are produced in clusters. These secondary electrons are so called δ-electrons. This correlation is important for the statistical precision of center of gravity measurements of ionization clouds, as done in a TPC.

The total number of electrons realeased per unit length is given by:

$$\frac{N_{e^-}}{l} = \frac{dE}{dx} \cdot \Sigma \frac{c_i}{W_{Ii}} \tag{2.2}$$

Here W_I is the material dependent average energy needed to produce an electron-ion pair. W_I is not equivalent with the the ionisation potential I_0, that is slightly lower. The ionisation energy I_0 represents the minimal energy, that is needed to produce eletron-ion pairs. W_I represents the average energy, that is needed to produce electron-ion pairs, that do not recombine. A gas mixture has different W_{Ii}-factors, that have specific weights c_i due to the contribution of the gases to the mixture. In table 2.2 the important parameters for frequently used chamber gases is shown.

2.3 Particle Identification

The mean rate of energy loss (or stopping power) is described by the Bethe-Bloch equation:

$$-\frac{dE}{dx} = Kz^2\frac{Z}{A}\frac{1}{\beta^2}[\frac{1}{2}ln\frac{2m_ec^2\beta^2\gamma^2T_{max}}{I^2} - \beta^2 - \frac{\delta}{2}] \tag{2.3}$$

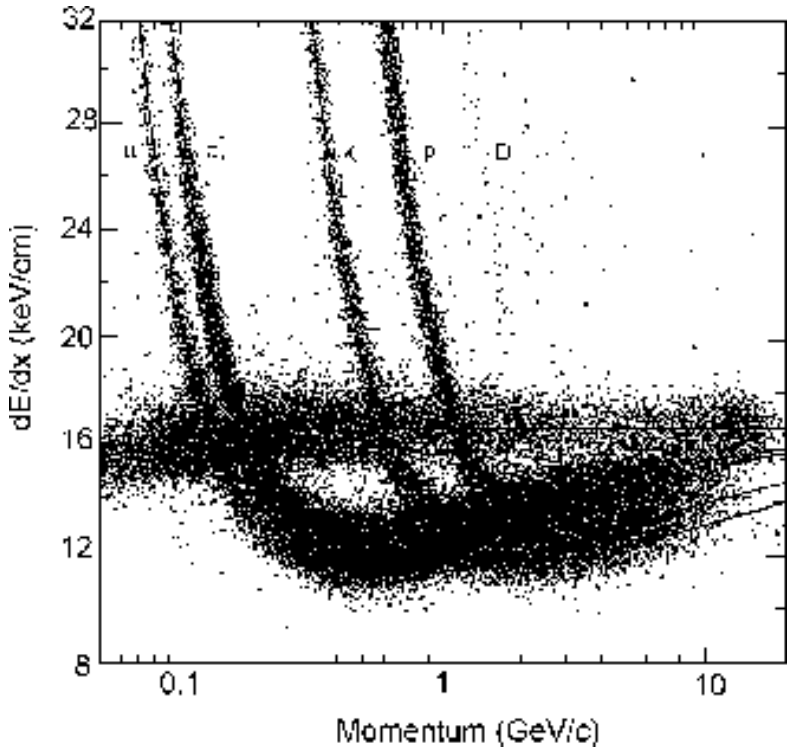

Figure 2.2: *Measured ionization energy loss of electrons, muons, pions, kaons, protons and deuterons in the PEP4/9-TPC [34]*

Here T_{max} is the maximum kinetic energy which can be imparted to a free electron in a single collision. The parameters of the Bethe-Bloch equation are defined in table 2.1. Using the relation $\beta = \frac{p}{mc}$ it can be seen, that the mean energy loss is dependent on the mass of the particle. This can clearly be seen in Figure2.2. Measuring the momentum p and the specific energy loss dE/dx of the charged allows to derive the energy of the charged particle. Therefore a particle identification of the charged particles can be done with the TPC only.

The Bethe-Bloch equation can be modified [36], so that is described as function of the particle velocity ad the charge number Q:

$$\frac{dE}{dx} = \xi \cdot \frac{1}{\beta^2} \cdot Q^2[K + ln(Q^2) + ln(\gamma^2) - \beta^2 - \delta(\beta\gamma)] \tag{2.4}$$

where ξ denotes the electron density of the gas and $\delta(\beta\gamma)$ the density function. As described in [37], it is shown, that the energy loss

- follows a characteristic decrease with $\frac{1}{\beta^2}$,
- reaches a minimum around $\beta\gamma = 3$ to 4,
- and continues with a logarithmic rise ("relativistic rise region"),
- until it saturates ("Fermi plateau", $\propto ln(\gamma^2) - \delta(\beta\gamma)$).

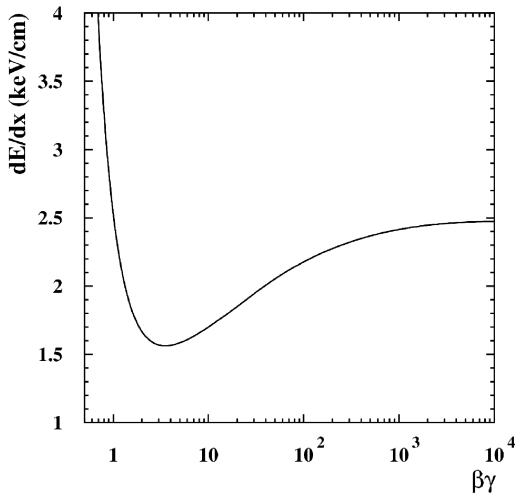

Figure 2.3: *characteristic shape of the $\frac{dE}{dx}$ function*

The density function takes into account the polarization effect in the gas. The characteristic shape of this function is shown in Figure 2.3. In the region of high momentum where the relativistic rise can be seen the separation is in the 10 % regime. Therefore $\frac{dE}{dx}$ measurements with a resolution of a few % are needed to disentangle the different particle species.

A simple and robust method to calculate the specific energy loss is the method of truncated mean. In this widely used method a certain percentage

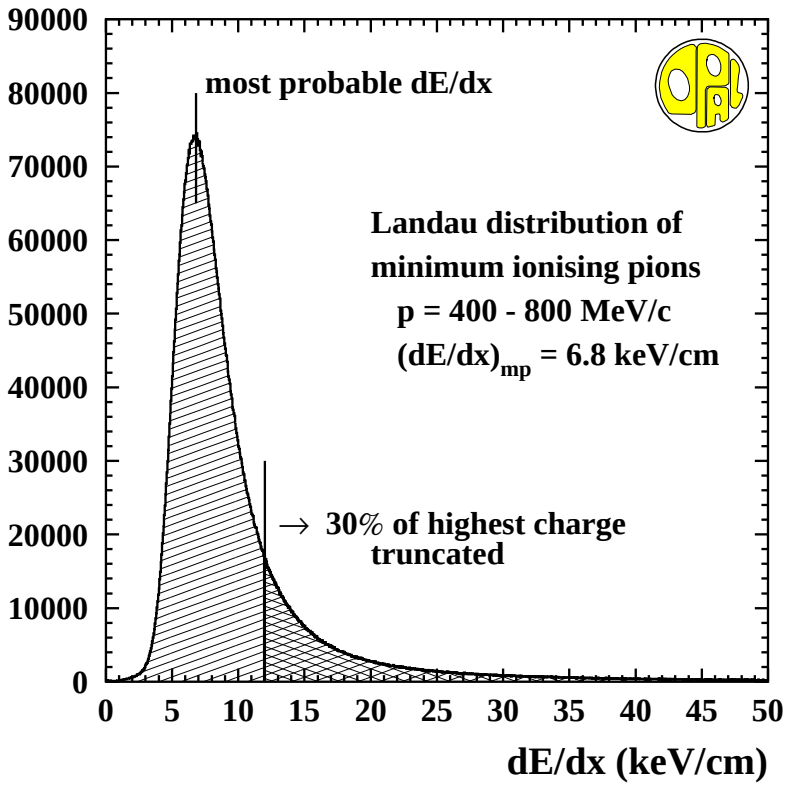

Figure 2.4: *Landau distribution for minimum ionising pions. At OPAL the method of truncated mean is used to determine the average energy loss. In this case 30 % of highest energy and 8 % of the lowest energy loss samples were rejected and not taken into account [38].*

of the lowest and highest measured dE/dx values are rejected from the calculation of the mean energy loss. In fig 2.4 one can see how this method was applied at the OPAL-detector, which was one of the four experiments at the electron positron collider LEP. The reason for the rejection of lowest values is the reduction of the influence of electronic noise or background fluctuation. The reason for the rejection of highest values is mainly the reduction of delta electrons produced in hard collisions.
The dE/dx resolution is mainly dependent on three quantities:

- number of effective samples N
- effective sampling length length (thickness ×pressure)

- gas mixture

The importance of the particle identification is not the dE/dx-resolution itself, but the dE/dx-separation power. It raises the question: How good can two different particle species be identified as separated in charge? In [39] the separartion power between two particle species A and B is defined as:

$$separation\ power = \frac{separation}{resolution} = \frac{\frac{dE}{dx}(A) - \frac{dE}{dx}(B)}{\sigma(\frac{dE}{dx})_{A,B}} \tag{2.5}$$

Here $\sigma(\frac{dE}{dx})_{A,B}$ is the average dE/dx resolution for the two particle species. For a given gas mixture a better dE/dx resolution and separation power can be achieved by increasing the pressure. For the commonly used chamber gases the optimal separation power was found at three to four bar. In the design of a TPC only one parameter of two possible parameter can be optimal. It would be possible to improve the dE/dx resolution significantly, if a high pressure is applied. An increase in pressure would require a pressure vessel, which can stand this higher pressure. This however would increase the active material in front of the calorimeters. The advantage of a improved energy resolution in the TPC would be bought by spoiling the performance of the calorimeters and decrease the total energy resolution. Therefore a operation of TPC at high pressure is not considered as a possible option at the ILC.

2.4 Behaviour of Charges in Gases

After a charged particle has produced a primary ionisation the signal has to be transported and amplified in front of the read-out electronic. The following chapters will describe the physical processes to achieve and understand the quality of a track image.

2.4.1 Drift

The instantaneous velocity $\vec{v}$ of an elctron with charge e and mass m in a gas embedded in an electric $\vec{E}$ and the magnetic $\vec{B}$ field can be expressed by the Langevin equation [40]

$$m\frac{d\vec{v}}{dt} = e\vec{E} + e\vec{v} \times \vec{B} - K\vec{v} \tag{2.6}$$

Here m denotes the mass of the charged particle, e the electric charge and K a quantity, which describes the viscosity of the gas. The term $-K\vec{v}$ represents a time dependent stochastic noise due to scattering with the gas

molecules. The ratio $\tau = \frac{m}{K}$ has the dimension of a time and is the average time between two collisions of the charged particle with the gas molecules. The solution of the Langevin equation for $t \gg \tau$ is:

$$\vec{v} = \frac{e}{m}\tau|\vec{E}|\frac{1}{1+\omega^2\tau^2}(\hat{E} + \omega\tau(\hat{E}\times\hat{B}) + \omega^2\tau^2(\hat{E}\hat{B})\hat{B}), \tag{2.7}$$

where $\hat{E}$ and $\hat{B}$ denote the unit vectors of the electric and magnetic field and $\omega = \frac{e}{m}B$ is the cyclotron frequency. Equation 2.7 describes a steady state for which the derivative is $\frac{dv}{dt} = 0$.
Three important cases are distinguishable:

a) If $|B| = 0$ it follows $\omega = 0$ and the equation is reduced to

$$\vec{v} = \frac{e}{m}\tau\vec{E} = \mu\vec{E}. \tag{2.8}$$

The mobility μ depends for electrons on the strength of the electric field due to quantum mechanical effects between the electron and the atomic electrons, while for ions it is constant over a wide range of E.

b) When $\vec{E}$ and $\vec{B}$ are in parallel, eq. 2.8 is also valid, as can be seen from eq. 2.7.

c) Another very important case is, when there is a significant angle between $\vec{E}$ and $\vec{B}$. In this case the second term in eq. 2.7 becomes dominating and $\vec{v}$ depends also on the magnetic field. An important parameter, on which also the spatial resolution depends, is the *Lorentz angle* α_L. α_L is defined as the angle between $\vec{v}$ and $\vec{E}$. In the extreme case, that $\vec{E}$ and $\vec{B}$ are perpendicular, $|\vec{v}|$ is given by:

$$|\vec{v}| = \frac{e\tau}{m\sqrt{1+\omega^2\tau^2}}|\vec{E}|. \tag{2.9}$$

Here it can be seen that in any case the drift velocity depends on the mass of the charged particle, which leads to a higher drift velocity for electrons than for ions.

2.4.2 Diffusion

Charged particles which are released in a cloud will diffuse isotropically away from their place of production because of their thermal energy. The density distribution of the charged particle after a time t can be described by a Gaussian distribution:

$$n = (\frac{1}{4\pi D})^3 e^{-\frac{r^2}{4Dt}} \tag{2.10}$$

where r is the radial distance to the creation point and $\acute{D}$ is the diffusion coefficient. The width σ of the distribution is given by:

$$\sigma = \sqrt{2\acute{D}t}. \tag{2.11}$$

The diffusion coefficient $\acute{D}$ depends on the chosen gas mixture, temperature T and pressure p by the following formula:

$$\acute{D} = \frac{2}{3\sqrt{\pi}p\sigma_{total}}\sqrt{\frac{(kT)^3}{m_{ch}}} \tag{2.12}$$

The total cross section σ_{total} depends also on the chosen gas and the type of the charged particle. For eq. 2.12 the assumption was made, that the free charges are conserved, this due to recombination of electrons and ions in the presence of electro negative molecules.

Influence of an electric field

Within an electric field the following definition of the diffusion coefficient is more convenient, whereby the width σ of the distribution can be calculated depending on the drift length L:

$$\sigma_D = D\sqrt{L} \tag{2.13}$$

The quantity D is related to $\acute{D}$ by:

$$D = \sqrt{\frac{2\acute{D}}{v_{drift}}} \tag{2.14}$$

In the following D denotes the difussion coefficient. One would naively expect, that the diffusion of an electron cloud within an electric field is the same along the electric field lines (longitudinal) as for perpendicular to it (transverse), but in 1967 it was shown that the longitudinal diffusion D_l changes significantly in an electric field. The reason for this behaviour is, that the leading and the trailing edge of the cloud have different energies. As the collision rate depends on the energy, this leads to a change of the diffusion in the longitudinal direction.

Influence of a magnetic field

Within a magnetic field the transverse diffusion is strongly supressed, while the longitudinal diffusion is unchanged. This can be easily exlained by the

Lorentz force, which influences the particles with a transverse velocity component and forces these on a helical trajectory between two collisions. The diffusion coefficient $D_t(B)$ is given by:

$$D_t(B) = \frac{D_t(0)}{1 + \omega^2\tau^2} \tag{2.15}$$

$D_t(0)$ is the diffusion coefficient in the absence of a magetic field.

2.4.3 Gas Amplification

In electric fields exceeding a value of approximately 10^4 V/cm, electrons can receive enough energy between two collisions, to excite and ionize further atoms, which leads to a gas avalanche multiplication. One distinguishes three characteristic regions of gas amplification: proportional region, limited proportional region and discharge region.

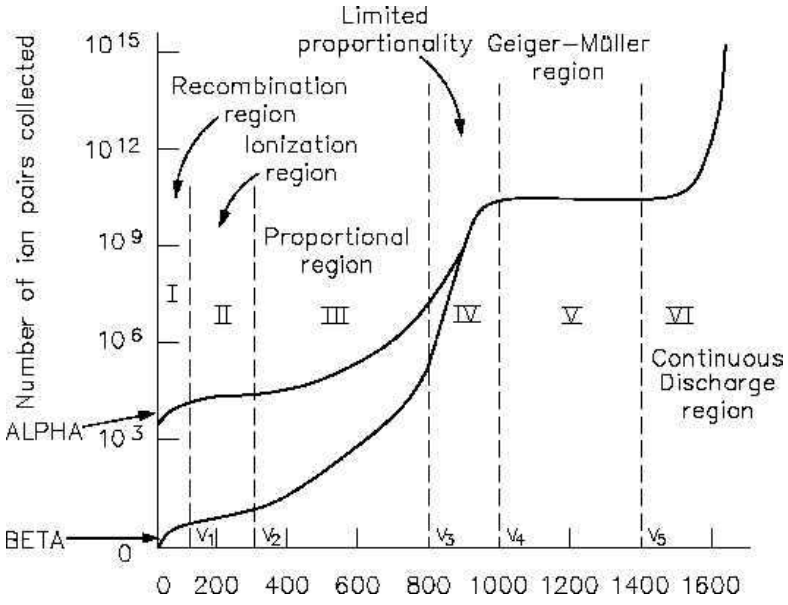

Figure 2.5: *Progression of the gain factor in dependency of the applied electrical field.*

The regions are shown in Figure 2.5. The proportional region covers a certain range of electric field strength, in which the number of newly liberated electrons is proportional to the amount of initially existing electrons (e.g. in

the electric field close to the wire of the proportional counter). During the motion of n electrons along a path dr, dn new electron-ion pairs are produced:

$$dn = \alpha \cdot n \cdot dr \tag{2.16}$$

where α is the first Townsend coeficient, which represents the inverse of the mean free path for ionization and depends on the gas mixture, temperature, pressure and the local strength of the electric field. After proceeding from τ_1 to τ_2 the number electrons increase from n_1 to n_2 according to

$$n_2 = n_1 \cdot G \tag{2.17}$$

where G is the gas gain, which can be calculated by:

$$G = e^{\int_{r_1}^{r_2} \alpha(r)dr} \tag{2.18}$$

The integral describes the dependence of the Townsend coefficient on the locally varying strength of the electric field.

In the region of limited proportionality (see Figure 2.5), the ions produced in in the gas avalanche can become large enough to significantly deform and reduce locally the effective electric field strength, and ultimately lead to saturate multiplication.

The upper limit for charge multiplication is given by the beginning of ultraviolet photon emissionprocess, inducing avalanche spread over the whole gas volume and a discharge or spark breakdown is the consequence. The Raether condition elaborated in detail in reference [57] gives a phenomenological limit for charge multiplication: the maximum avalanche size must not exceed 10^7 to 10^8 electron-ion pairs. The exact number is strongly related to actual charge density and electric field strength. Since the energy distribution of the electrons is statistically distributed, operations at 10^6 can already become critical.

2.4.4 Influences on the gas condition

Of importance is not only the chamber gas itself, but also the thermodynamic state of the gas mixture. Ionisation, diffusion, drift and gas amplification are all depending on the density of the gas. Therefore temperature, pressure and a precise knowledge of the gas composition is crucial for a description of the system. A good aproximation for the thermodynamic state

is the ideal gas equation

$$\rho = \frac{m}{V} = \frac{p}{R_i T} = \frac{p m_m}{RT} \tag{2.19}$$

with R, R_i the universal respective individual gas constant. The influence of the gas conditions will be investigated more detailed in the Chapter about 7.

2.5 Short Review of Chamber Gases for the ILC

Optimization of gas mixtures is obviously a crucial point for the optimization of the performance of a gaseous detector. A detailed study can be found in [41]. The gas mixture has to serve two different issues. First it should have good signal production and transportation capabilities. Second it should provide a sufficient gain in the gas amplification region. As the principle of gas amplification has already been explained in section 2.4.3, this section will concentrate on signal production and transportation capabilities of different gases. A gas mixture generally consists of a *Counting Gas*, which dominates and sustains the charge multiplication process, and a *Quencher Gases*, that dissipates part of the energy to protect the detector from discharges. The gas mixture itself needs the following requirements to be taken into account:

- The total number of released electrons per unit of length should be large in order to allow a good dE/dx resolution.
- The drift velocity should be large to empty the drift region as quickly as possible.
- The drift velocity versus elecric field ratio should provide a maximum of drift velocity with a minimal electric field E_{max}. The drift velocity should be stable in case of fluctuations or distortions at E_{max}, so that one can operate the detector at a plateau of the electic field dependence of the drift velocity.
- The longitudinal diffusion coefficient, D_L, should be small in order not to loose resolution in the direction parallel to the electric field
- The attachment coefficient of the gas in an electric field E_{max} should be small, in order to avoid losses of drifting electrons.
- Multiple scattering should be small enough so that the momentum resolution of the TPC is good even for low momentum particles.

Gas	$X_0[m]$	$N_t[\frac{1}{cm}]$	$\sigma_n[barn]$
He	5299	8	1.34
Ne	345	43	2.628
Ar	110	94	0.683
CO_2	183	91	14.015
CH_4	646	53	333.631
C_2H_6	340	111	503.222
iC_4H_{10}	169	195	842.404

Table 2.3: Radiation length X_0, Number of released electrons per cm N_t and neutron interaction cross-section σ_n of different detector gases

- There should be as little as possible influence of potential pollutants such as water and oxygen
- The gas should have as few H atoms as possible, because of their large interaction cross-section with a potentially high neutron background
- The gas should not be aggressive to prevent ageing of the detector.

A set of three gas properties are summarised in table 2.3. The first three gases are *counting* and the rest *quencher gases*. Argon is a *counting gas* with the highest atomic number, the highest primary ionisation N_t and lowest radiation length X_0. From purely statistical point of view the dE/dx resolution, which is depending on N_t, resp$\frac{1}{\sqrt{N_t}}$, is worsened by 40 %, if one replaces Argon by Neon. Argon is therefore a well suitable *counting gas* for the ILC TPC.
The choice of a *quencher gas* offers a multi dimensional parameter space, which is not easy to optimize.

- An important parameter that has to be considered is the neutron interaction cross-section. As a significantly large neutron background due to beamstrahlung processes can be expected in the TPC at the ILC, CO_2 is the best candidate for reducing this backround. All other *quencher gases* has a large number of H atoms, which are known to have a high interaction cross section for neutrons.
- Drift velocity as a function of electric field should be optimal in view of reasonable E_{max}. As previously said a high drift velocity is needed to readout the TPC as quickly as possible. In Figure 2.6 a mixture of 90 % Argon + 10 % of various *quencher gases* are shown. Here CO_2 turns

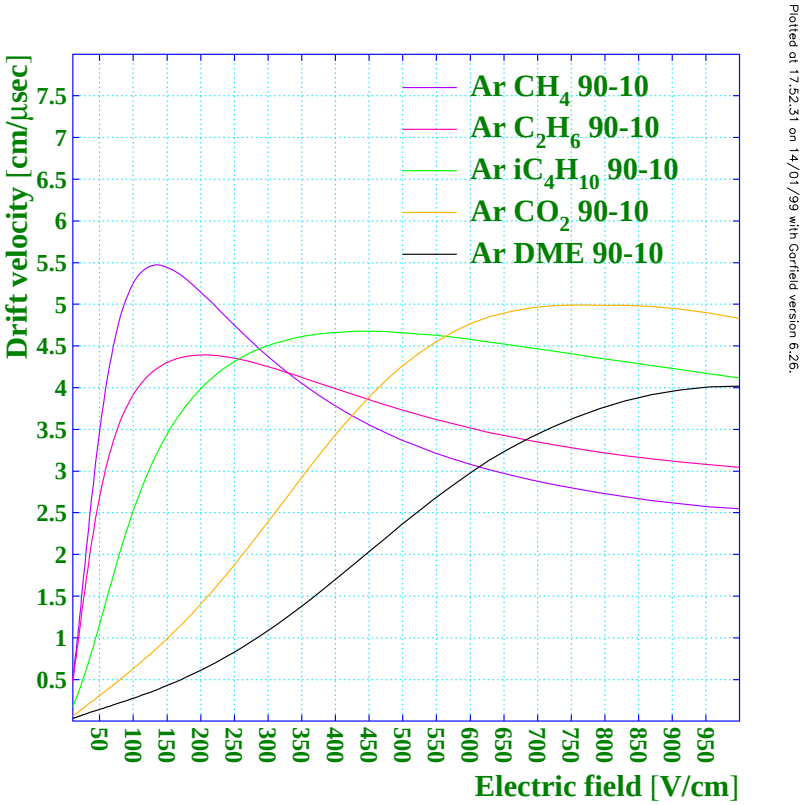

Figure 2.6: *Drift velocity as a function of electric field for 90 % Argon + 10 % quencher gas mixtures. B = 3 T*

out not to be the best choice, because the maximal drift velocity can be reached at an electric field value of 800 V/cm. Although it reaches a plateau, a maximal field E_{max} of about 200 kV assuming a 2.5 m long detector, would not be appropriate. CH_4 requires a smaller field, 135 V/cm, but does not have a flat plateau. It's therefore more sensitive to electric field distortions. C_2H_6 has a acceptable small electric field and flat plateau. iC_4H_{10} has even a flatter plateau, but requires a rather large electric field of about 450 V/cm.

- With respect to the longitudinal diffusion, CO_2 is twice better than CH_4, which means that the spatial resolution in the direction parallel to the drift field is much better with CO_2 than with CH_4. For transverse diffusion, the behaviour is quite the opposite: less diffusion for CH_4 than for CO_2. C_2H_6 and iC_4H_{10} have intermediate diffusion properties.

- Concerning the sensitivity of the performances of the gas mixture to water contamination, CO_2 is the best candidate with 0.4 % change in v_{drift} for a 500 ppm contaminatin of water. CH_4 is the worst candidate with a change of 7.7 %. C_2H_6 and iC_4H_{10} have an intermediate sensitivity to water contamination.

- A point to consider is the attachment coefficient due to oxygen contamination. The attachment coefficient of the gas mixtures considered with 10 ppm oxygen are all about the same, between 0.0014/cm for CO_2 and 0.0024/cm for iC_4H_{10}. The loss of primary ionization after a drift length of 2.5 m in such gas mixtures is between 30 % and 45 %.

The data of this work has been measured with a gas mixture suggested in the Technical Design Report of TESLA [42], that consists of Argon/CH_4/CO_2 in the ratio 93/5/2. Nevertheless more detailed gas studies are planned in the ongoing process of detector optimization torwards the LDC

2.6 Spatial and momentum resolution

The accuracy of the reconstructed track image is determined by the single point spatial resolution σ of a TPC, which to first order is determined by the contributing number of effectively detectable electrons $\hat{N}$ from the ionization process and their spread due to diffusion when arriving at the anode after a drift distance d. The number $\hat{N}$ is given by the ionization per sample length minus losses of electrons before gas amplification. Additional contributions originate from pad geometry, their orientation with respect to the track, and other influences such as electronic noise, cross talk amongst other are summarized in σ_{sys}. If the pad pitch is adapted with respect to the transverse charge spread, i.e. if more than one pad is hit per row, the single point resolution of a pad row improves over the standard deviation of a rectangular uniform distribution $\sigma_{r.u.d.} = \frac{p}{\sqrt{12}}$, with p correspoding to the pad pitch. It can be expressed by:

$$\sigma^2_{r\phi} = \frac{D^2_T \cdot d}{\hat{N} \cdot cos^2\phi} + \frac{L^2 \cdot tan^2\phi}{12 \cdot \hat{N}} + \sigma^2_{sys,T} \tag{2.20}$$

Typical transverse spatial resolutions achievable with a TPC range from 100 to 200 μm.

Transverse momenta p_T of particles are determined by measurement of their trajectory curvature due to the magnetic field. The transverse momentum resolution is given by:

$$\frac{\sigma_{p_T}}{p_T} = \frac{8p_T}{0.3B(R_O - R_I)^2}\ \sigma_s, \tag{2.21}$$

where R_O andR_I are the outer and inner radii of the TPC, p_T is the transverse momentum in GeV/c, and σ_s is the sagitta error and is given by

$$\sigma_s^2 = \sigma_{s,r\phi}^2 + \sigma_{s,ms}^2. \tag{2.22}$$

Here, $\sigma_{s,r\phi}^2$ is given by the Gluckstern formula [43]:

$$\sigma_{s,r\phi}^2 = \frac{\sigma_{r\phi}}{8}\sqrt{\frac{720}{N+4}} \tag{2.23}$$

with N being the number of measured points, and $\sigma_{r\phi}$ the single point resolution given by eq. 2.20.
$\sigma_{s,ms}$ is due to multiple scattering and is given by:

$$\sigma_{s,ms} = \frac{1}{4\sqrt{3}}(R_O - R_I)\frac{14.1}{p_T 10^3 \beta}Z(1 + \frac{1}{9}log\frac{(R_O - R_I)}{X_0})\sqrt{\frac{(R_O - R_I)}{X_0}} \tag{2.24}$$

This shows that the contribution of $\sigma_{s,ms}$ is not depending on p_T in equation 2.21. At energies above 10 GeV/c the momentum resolution is determined by the Gluckstern formula and the contribution from multiple scattering becomes negligble.

The momentum resolution from only the TPC required in the Large Detector Concept is [42]:

$$\delta(\frac{1}{p_T}) = \frac{\sigma_{p_T}}{p_T^2} < 2 \times 10^{-4}(GeV^{-1}) \tag{2.25}$$

2.7 Gas Ionization by Laser

The light of a laser beam that traverses a volume of gas, under favourable conditions, is capable of ionizing the gas so that the laser beam imitates a straight particle track. For this to occur, there must be some ionizable molecules in the gas, and the energy density must be sufficiently high. The ionization is also dependent on the energy level of every single photon, which

means on the wavelength of the laser light. The technique of laser track production has some obvious advantages. With a laser setup it is possible to produce identical tracks in the same place with high statistics [44]. Therefore one can almost get rid of statistical variations, coming from laser itself. Since its first application in 1979 by Anderhub, Devereux and Seiler [45] this technique has been widely used.

2.7.1 The Two Photon Ionization

As shown in Table 2.2 typical chamber gases have rather high ionisation energies compared to photon energies of standard UV lasers. For example a N_2-UV Laser has 3.68 eV photon energy, a Nd-Yag-UV Laser 4.68 eV. Both are originally infrared Laser, using non linear crystals to shift the frequency to ultra violett light. The UV-laser as track production is described in section 5.1. The ionization rate for a multi n-photon process is dependent on the cross section σ of the photon absorbtion level. The probability of a three or four photon process, which means that a photon excites an already excited state, is exremly low, as the probabilty decreases with σ^n. An alternative is to search for substances with high cross-section for two photon ionisation. Their ionisation potential has to be below 9.4 eV in case of a Nd-Yag and 7.4 in case of N_2 laser. Such substances do indeed exist. Composite molecules have a large number of vibro-rotational states which at higher vibrational quantum numbers may overlap and form a quasi continuum. A table of this substances can be found in table 2.4 taken from [46]. In the same paper Hilke showed, that if the lifetime of a real laser level is large compared to the length of the laser pulse, the production of primary electrons n_e is not longer dependend on this parameter. Primary ionisation is given by:

$$n_e = \frac{\sigma^2 n_0 n_\gamma^2}{2s} \tag{2.26}$$

with cross-section for photo absorption σ, the molecule density of the additive n_0, the number of photons per shot n_γ and the size of the beam spot s. As described in equation 2.26 the laser energy ordinary shows a quadratic dependence to energy because of the simple relation $n_\gamma = \frac{E}{h\nu}$. Eq.2.26 can be tranformed to:

$$n_e = \frac{\sigma^2 n_0 (\frac{E}{h\nu})^2}{2s} \tag{2.27}$$

In case of a small concentration of additives plus high laser intensities all molecules along a track reaches the first photon absorption level which leads to a saturation. The ionization probability is then only depending on the photon absorption probability of the second level. This releases the electrons

to the continuum. In that case the dependency becomes linear.

Another production mechanism is the ionization of intrinsic impurities of the chamber gases. The small amount of impurities, that can be beyond the level of detection of ordinary devices, are assumed to produce a virtual photon absorption level with a very short lifetime of $\tau \approx 10^{-16}$ seconds. A second photon that is absorbed within this lifetime is then also able to ionize the molecule. The formula for the production of primary electrons is almost the same as in case of a real photon absorption level with the modification, that because of the small lifetime the timelength of the laser has to be taken into account.

$$n_e = \frac{\sigma^2 n_0 n_\gamma^2 \tau}{sT} \tag{2.28}$$

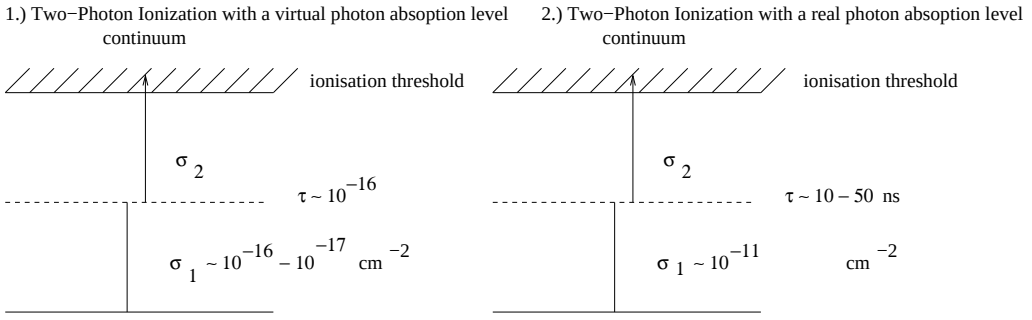

Figure 2.7: *Production Mechanism of Two-Photon Ionization. Main diffrence consists in lifetime and the cross-section of the photon absorption levels.*

with τ the lifetime of the photon absorption level and T the laser pulse duration. In Figure 2.7 the two production mechanism are illustrated.
To summarize the processes:

- virtual photon absorption process ($\tau \ll T$) : $n_e \propto \frac{E^2}{T}$
- real photon absorption process ($\tau \gg T$) *no saturation*: $n_e \propto E^2$
- real photon absorption process ($\tau \gg T$) *saturation*: $n_e \propto E$

2.7.2 Dependence of Laser Ionization on Wavelength

The ionization yield depends very much on the wavelength. Using a tunable dye laser, Ledingham et al. [47] have found an increase of four orders of

Additive	Ionisation Potential	Vapor pressure	Melting point boiling point	Ionisation
	[eV]	[Torr] at 20^o	$[^o]$	$[e^-/\text{cm}]$
Benzene C_6H_6	9.24	77	55/80	5×10^3
Toluene C_7H_8	8.82	22	-95/110	5×10^4
Cumene C_9H_{12}	8.69	3.8	-96/152	11×10^4
n-Butylbenzene $C_{10}H_{14}$	8.69	1	-88/183	5×10^4
m-Xylene C_8H_{10}	8.56	6	-48/139	$\leq4\times10^4$
TMA $(CH_3)_3N$	8.5	6	-117/2.9	60-130
1,3,5 Mesithylene C_9H_{12}	8.4	1.5	-45/165	1.8×10^4
Phenole C_6H_5OH	8.3	3.8	41 -96/152	≥ 250 11×10^4
Naphthalene $C_{10}H_8$	8.12		81/	560
TEA $(CH_3CH_2)_3N$	7.5	50	-114/893	200
DMA $C_6H_5N(CH_3)_2$	7.14	0.25	2.5/194	10^4
TMPD	6.18	2.3×10^{-3}	51/260	6×10^4

Table 2.4: Properties of some additives with low ionisation potential. The ionisation is normed to a laser pulse with an energy of 1 μJ, a size of 1 mm^2, and a partial pressure of 10^{-3} Torr. All additives were investigated with a Nd-Yag laser with a wavelength of 266 nm.

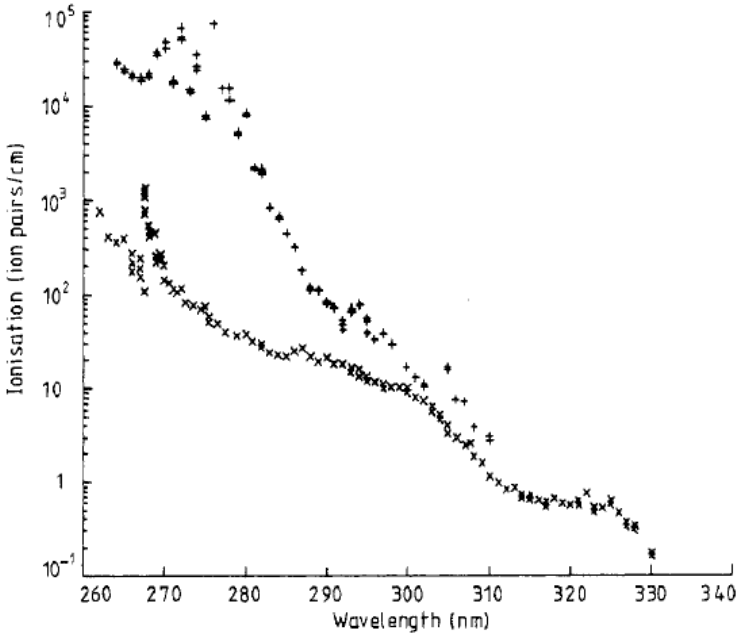

Figure 2.8: *Ionization induced in untreated counter gas $ArCH_4$ in the ration 90:10 by a $1 \times 1mm^2$ pulsed laser beam of $\mu J(\times)$, compared with the same gas seeded with a small amount of phenol* $(+)$ *[47]*

magnitude, when going from $\lambda = 330nm$ to $\lambda = 260nm$. In Figure 2.8 a gas mixture of $ArCH_4$ in the ratio of 90:10 is compared with and without a small amount of phenol. The fine structure that have become visible around 270 nm, was further examined with a higher resolution technique.

Comparing the resolution pattern with the known single-photon UV absorption level of phenol a clear consistency is demonstrated (see Figure 2.9). The possibility to detect characteristic structures in the spectrum of laser induced resonant two-photon ionization (R2PI) makes this method a sensitive tool for the identification of molecules.

2.8 Laser-Beam Optics

In eq. 2.27 and 2.28 it was shown, that the ionization strongly depends of the energy and the size of the laser beam. To achieve a constant ionization per unit track length this energy density has to stay constant. On the other hand an narrow deposition of ionization is needed especially in a gaseous detector as the width of the charged cloud should not be determined by the width

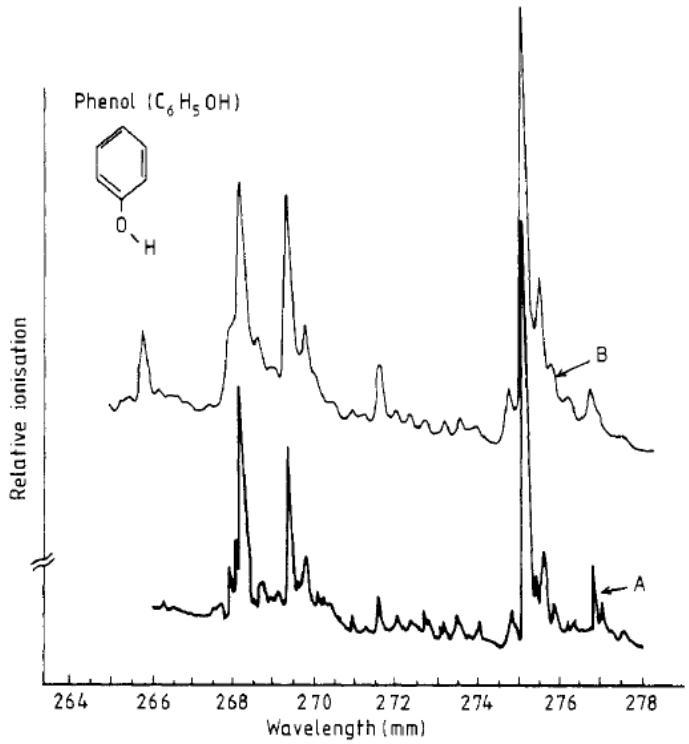

Figure 2.9: *A comparison of a laser-induced spectrum of counter gases doped with a trace of phenol and the single-photon UV absorption spectrum of phenol shows identical wavelength dependence [47]*

of the laser itself, but only by diffusion. To get a narrow ionization, which should also stay constant over a range of meters, a laser beam optics is needed. A boundary condition which is crucial for determination of the appropriate laser optics is Liouville's theorem. It says, that the phasespace volume is a constant of diameter and divergence, *phasespace volume = diameter × divergence*. This means for a laser system, that it is limited by diffraction. To diminish the phase space volume is only possible by using an aperture. This however diminshs also the energy, respectively the total amount of photons. Furthermore the aperture introduces diffraction, which is bad in terms of a homogenous ionization process.
There is also a theoretical limit of the size in phase space of a photon beam. Heisenberg's uncertainty principle of quantum mechanics states that, in each of the two transverse dimensions separately the limits are given by:

$$\Delta x \Delta p_x > \frac{h}{4\pi} \tag{2.29}$$

with

$$\Delta\alpha = \frac{\Delta p_x}{p} = \frac{\Delta\lambda}{h} \ll 1; \tag{2.30}$$

we get

$$\Delta x \Delta\alpha > \frac{\lambda}{4\pi} \tag{2.31}$$

Equation 2.31 tells, that the limit of the size in phase space is the wavelength itself.

2.8.1 Gaussian beam propagation

The definition of a gaussian beam can be expressed as a laser beam where the electric field profile in a plane perpendicular to the beam axis can be described with a Gaussian function, possibly with an added parabolic phase profile. This case is valid if the laser operates mainly in the fundamental mode, the TEM_{00}. An overview of the different modes, that could occur in a laser is given in section 2.8.2. In the following considerations are made with the approximation of the TEM_{00}.
The importance of Gaussian beams results from a number of special properties:

- Gaussian beams have a Gaussian intensity profile at any location along the beam axis. Only the beam radius can vary. This has a special importance concerning the charge production in a gaseous detector. As the intensity of the laser will determine the ionization pattern in the gas a good reproducebility is only given in case of gaussian intensity profile.

- A Gaussian beam stays Gaussian also after passing simple kinds of optical elements (e.g. lenses without aberrations).

The propagation of a Gaussian beam is described by the homogenous Helmholtz Equation, that is propagating in z-direction:

$$\nabla_t^2 \Psi(\vec{r},\omega) - 2ik\frac{\partial}{\partial z}\Psi(\vec{r},\omega) + \frac{\partial^2}{\partial z^2}\Psi(\vec{r},\omega) = 0 \tag{2.32}$$

The *paraxial approximation* is defined by the condition:

$$2ik\frac{\partial}{\partial z}\Psi(\vec{r},\omega) \gg \frac{\partial^2}{\partial z^2}\Psi(\vec{r},\omega) \tag{2.33}$$

This means that the longitudinal variation in the modulation function $\Psi(\vec{r},\omega)$ changes very little in the wavelength associated with the beam. In this

approximation one can neglect the third term, which leads to the paraxial Helmholtz Equation given by:

$$\nabla_t^2 \Psi(\vec{r},\omega) - 2ik\frac{\partial}{\partial z}\Psi(\vec{r},\omega) = 0 \tag{2.34}$$

The solution of this paraxial Helmholtz Equation is given by:

$$\Psi(\vec{r},\omega) = A_0 \frac{w_0}{w_z} exp[\frac{-r^2}{w^2(z)}] exp[-i(kz - \arctan(\frac{z}{z_R}) + \frac{kr^2}{2R(z)})] \tag{2.35}$$

with the peak amplitude A_0 and the minimal waist of the beam w_0 at the beam waist, the wavenumber $k = \frac{2\pi}{\lambda}$, the Rayleigh length z_R and the radius of curvature R(z) of the wavefronts. For obtaining the oscillating (real) electric field, one multiplies this phasor with $exp(\frac{i2\pi ct}{\lambda})$ and takes the real part.
The beam radius varies along the propagation direction according to:

$$w(z) = w_0 \sqrt{1 + (\frac{z}{z_R})^2} \tag{2.36}$$

with the Rayleigh length:

$$z_R = \frac{\pi w_0^2}{\lambda} \tag{2.37}$$

which determines the length over which the beam can propagate without significantly diverging. If the beam has propagated the length of z_R the waist of the laser has increased by the factor of $\sqrt{2}w_0$.
The beam divergence θ resp. w_0 can be determined by:

$$\theta = \frac{\lambda}{\pi w_0} \Rightarrow \; w_0 = \frac{\lambda}{\pi \theta} \tag{2.38}$$

With the eq. 2.36, 2.37, 2.38 the waist of a laser beam can be calculated. In Figure 2.10 the laser waist for three different divergences is plotted starting always with the minimal waist w_0 at point 0 with ± 50 cm. The three divergences are $\theta \approx 0.5$, 1.0 and 2.0 mrad and lead to three different minimal waists of $w_0 \approx 167$, 85 and 42 μm.

This also leads to three different primary ionizations. At the minimal waist w_0 following Equation 2.28 one get $n_e \approx 277$, 1109 and 4437 $\frac{e^-}{cm}$. The expected ionization along ± 50 cm is shown in Figure 2.11.

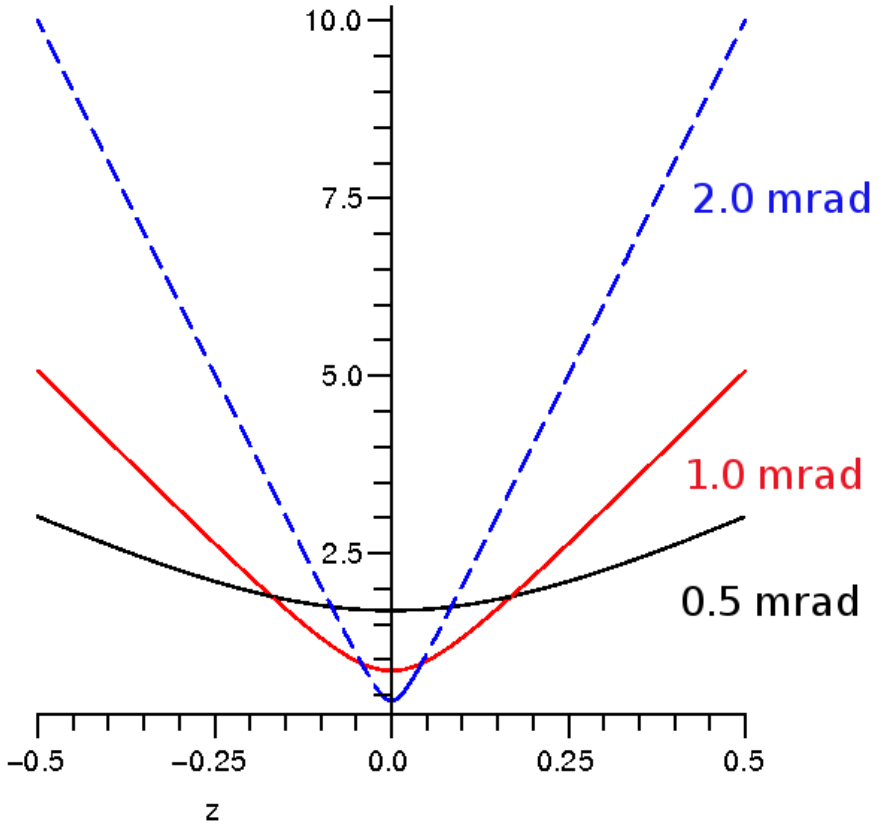

Figure 2.10: *Three laser waists with different values of θ = 0.5, 1.0 and 2.0 mrad. The z-Range is given by $\pm$ 50 cm.*

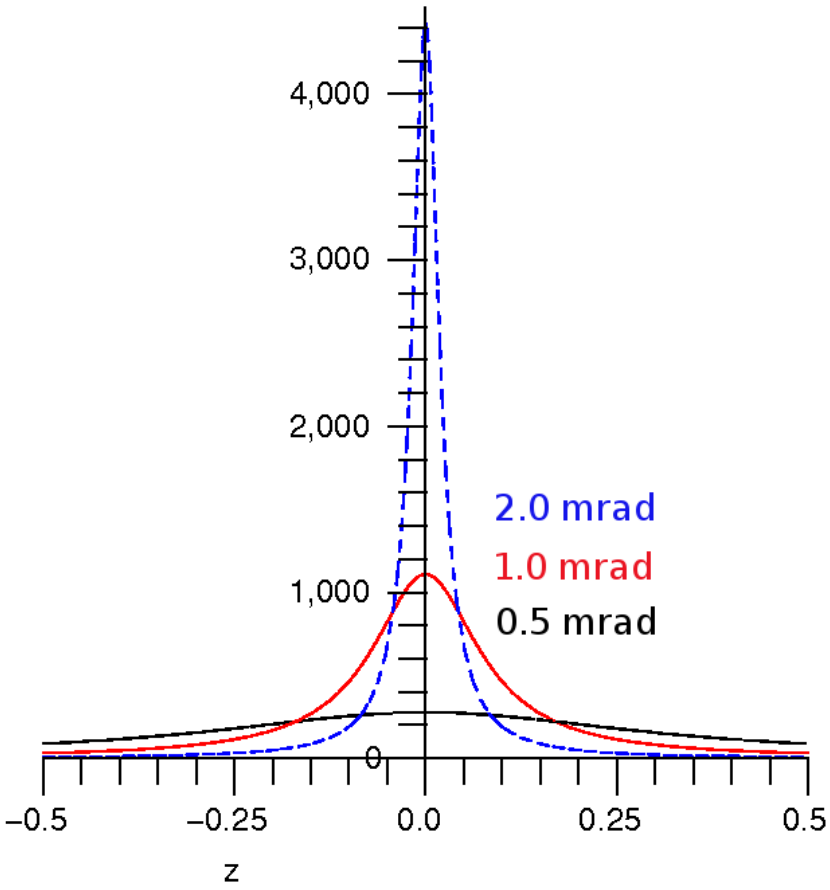

Figure 2.11: *Three different primary ionizations according to the laser waists of Figure 2.10. The laser waist is changing by a factor of two, the primary ionization is affected by a factor four. The same three values for θ = 0.5, 1.0 and 2.0 mrad are plotted.*

2.8.2 Laser Modes

The modes of a cavity with the lowest order in the transverse direction (called TEM_{00} or fundamental transverse modes) are Gaussian modes, if the cavity is stable, all optical media in the cavity are homogeneous, and all surfaces between media are either flat or have a parabolic shape. Therefore, lasers emitting only on the fundamental transverse mode often emit beams with close to Gaussian shape. Deviations from the mentioned conditions, e.g. by thermal lensing in a gain medium, can cause non-Gaussian beam shapes and/or the simultaneous excitation of different transverse modes. Modes of higher transverse order can be described e.g. by Hermite-Gaussian or Laguerre-Gaussian functions.

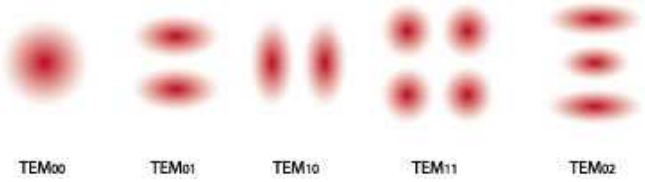

Figure 2.12: *Low-order Hermite-gaussian resonator modes taken from [48]*

In Figure 2.12 some of the lower-order modes are shown. In any case, the deviation from a Gaussian beam shape can be quantified with the M^2 factor (see [48]). A Gaussian beam has the highest possible beam quality, which is related to the lowest possible beam parameter product, and corresponds to $M^2 = 1$.

Chapter 3

The Gas Electron Multiplier (GEM)

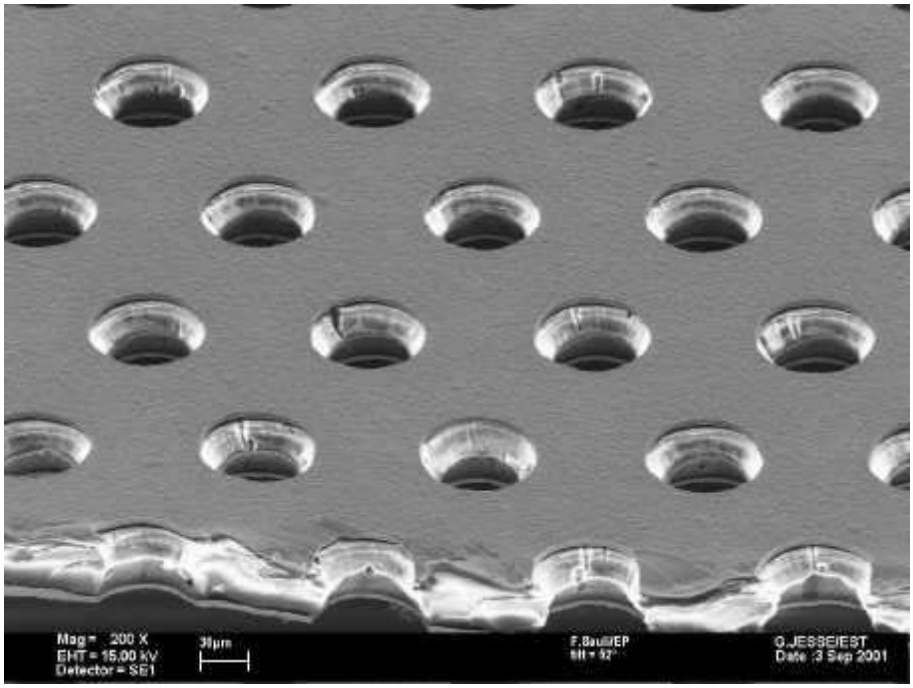

Figure 3.1: *Electron microscope photographs and schematic views of a GEM-foil with standard geometry: pitch = 140 µm, hole diameter = 70 µm [49]*

The *Gas Electron Multiplier* (GEM), as introduced in 1997 by F. Sauli [50], was invented as a preamplification stage for micropattern gas detectors. It consists of a thin copper-clad polymer foil, perforated with a high density

of chemically etched holes, typically several ten thousands per square millimeter. The process starts with the raw material, an adhesiveless, 50 μm thick Kapton foil laminate with two 5 μm thick layers of copper, which is coated with a photosensitive film. Two identical masks containing the hole pattern are aligned with a microscope. Then the raw foil is slid in between and exposed to UV-light. After development of the photo sensitive layer, a copper etching process is carried out with conventional solvents. The next step consists of Kapton etching, in which the two copper layers serve as masks, and during a final copper-etching process, the remaining edges are removed. A detailed description can be found in [51].
GEM-holes are normally characterized by a double conical structure, which results from the volume etching of each side of the foil. In fig. 3.1 a microscope photograph of a GEM with *standard geometry* is shown.

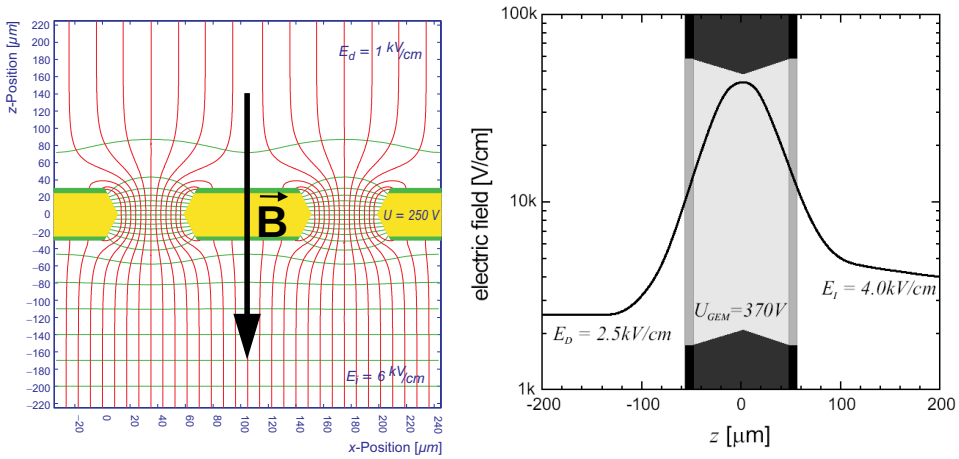

(a) (b)

Figure 3.2: *Operation principles and electric field configuration of a GEM. (a) The picture shows a vertical cut through GEM holes with the electric field lines included. (b) The picture shows the increase of the electric field strength reaches a maximum in the center of a GEM hole. The plot is computed for a standard GEM geometry with the software packages MAXWELL[52] and GARFIELD[53]. The plot is taken from [49]*

3.1 Operation Principles of GEM-Detectors

The application of a potential between the upper and lower GEM electrode produces a strong electric dipole field, which is built up inside the holes. Figure 3.2 illustrates the electric field in a standard geometry GEM with a potential difference of 370 V, a drift field of 2.5 kV/cm in front of the GEM and an induction field of 4 kV/cm. In this configuration the electric field strength in the hole center is 45 kV/cm.
When inserted in the drift field of a gas detector, electrons from the drift volume are guided into the holes of a GEM-foil, where they are multiplied in a gas avalanche amplification process. Most of the electrons are then released into the volume below the GEM-foil, where they can be collected by readout electronics or, in order to achieve higher total gains, transferred to another GEM. During drift and gas amplification, the electrons are subject to diffusion, which causes a fractional amount to be lost to the GEM-electrodes or the Kapton wall.
A single GEM-foil can reach gas gains above 10^3. By stacking several GEMs in cascades, multi-GEM detectors with even higher total gas gains can be built. The gain obtained with a GEM detector can be adapted to the needs of the application by choosing the number of GEM-foils and the voltage across each one. The big advantage of this detector type is the separation of gas amplification and readout stage. This separation provides not only a margin of safety in case of discharges occuring in the GEM-foils, it also allows high flexibility in the geometry of the readout structure. The distance between the GEMs is in the order of some millimeters, which leads to electric fields in the order 2-5 kV/cm. To achieve an efficient charge carrier transport, consecutive gaps should have slightly increasing values of electric field strength. Detailed studies of gain and charge sharing as a function of drift, transfer and induction field can be found in [54].

3.2 The GEM-Technology in the TPC

In figure 3.3 the different amplification principles of Multi Wire Proportional Devices and GEMs are illustrated. In the next two sections these different amplification techniques will be discussed.

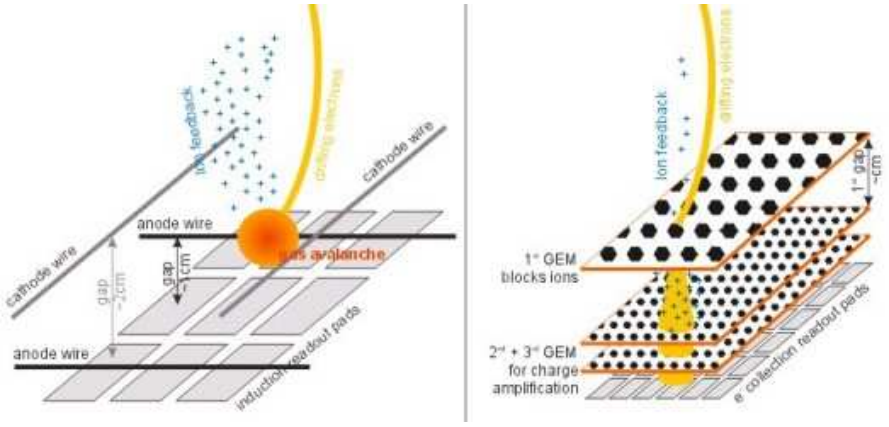

Figure 3.3: *The figure illustrates the gas amplification by wires (left) and a GEM-detector (right).*

3.2.1 Wire-based readout of TPCs

In conventional TPCs, the electrons from the drift volume are multiplied by anode wires. The huge ionization provides excellent energy resolution. The idea, on which this concept is based on is the Multi-Wire Proportional Chambers [55].
When the electrons from the drift volume are accelerated and amplified at the wires, they encounter a region of nonparallel E and B fields, so that they undergo deflections in the direction of the wires, the $E \times B$ effect. The distance between two wires defines the size of this effect, which can have an effect on the single point resolution. The electrons are absorbed at the wire. The ions remain at the wire and induce the signal on the readout stage. The distance between anode wires and the segmented readout plane is typically a few millimeter. The small areas of the segmented pad plane are called pads [33]. As the ions are much heavier than the electrons the ion cloud can be approximated in first order as constant in time. An induced signal covers a larger area of the readout stage compared to a direct electron signal. The electron signal distributes the charge due to the width of the charged cloud. The induced signal is not limited to the width of the ion cloud. This different behavior of direct and induced is illustrated in figure 3.3. A narrower charge distribution requires a smaller pad size. A smaller pad size should lead to a more accure determination of the point resolution of a track.
An induction signal requires a slow decay time of the electronic, as the decay of the ion signal is slow due to the slow ion drift velocity. This means, that a readout electronic with moderate sampling rate is sufficient. The size of the

voxel is thereby defined by the smallest measurable three dimensional space point in the detector.
The ions produced at the wires would drift slowly back to the drift volume, and could distort the next incoming track by producing locally ocurring space-charges. To prevent this effect gating wire grids are installed. These gating grids have an electric field that is vertical to propagation direction of the ions. All outgoing, but also all incoming charges are moving along the field until they are absorbed at the gating wires. The gating grid reduces the back flow of these ions with suppression factors of 10^{-4}.

3.2.2 GEM-based readout of TPCs

Detectors based on the GEM have already found numerous applications in particle physics. The GEM technology is a candidate for many future High Energy Projects, which use a TPC or gaseous detectors in general. High rate capability, good localization accuracy and multi track resolutions, together with robustness of operation make GEM-devices a well suited choice to replace the conventional wire amplification structures of a TPC. The amplification process takes place as described in chapter 3.1 for a single GEM. In case of a multi GEM-stack the broadening of the signal is determined by the width of the charged cloud before the amplification structure and by the electric fields between the GEMs respective GEM and pad plane. What reaches the pads is the direct amplified elctron signal.
There are a lot of improvements compared to the MWPC. Due to a very small distance between two GEM holes (see fig 3.1) of 140 μm $E \times B$ effects are by an order of magnitude smaller compared to a wire amplification system. The direct electron signal, which is read out on the pad plane, allows a fast readout on the pads, this should increase the separation capability between two tracks, which are nearby in z-direction. The separation capability should be in the order of the longitudinal width of the charged cloud. The same is also valid for the broadening of the charge cloud in $r\phi$-direction. The ratio between signal width and the width of the pads is optimal for much smaller pad sizes, which improves the single point resolution and the separation capability in this direction.
A significant improvement of the intrinsic ion suppression can be achieved by the voltage optimization of the multi GEM-stack. In the gas amplification process a big fraction of the produced ions is guided to the upper GEM electrode. Only ions produced in the center of the hole, close to the field lines which leads to the cathode, will be released to the drift volume. This means, that the ions produced in the GEM nearest to the drift volume play the greatest role in the case of space charge production.

3.3 Charge Transfer in GEM Structures

In this section the quantification of transport properties is defined as described in [49]. Important parameters, that determine these transport properties are the GEM design, the gas mixture, the voltage applied between the two electrodes and the electric fields on both sides of a GEM-foil. One also has to distinguish between the quantities of a single GEM and a GEM stack.

3.3.1 Charge Transfer Coefficients of a Single GEM

Transport and multiplication of electrons in the GEM are quantified by the transparancy τ, the gas gain g and the extraction ϵ, which are defined for a GEM-stage j as:

$$\tau_j = \frac{N_{e^-}\ reaching\ gas\ amplification}{N_{e^-}\ entering\ the\ GEM\ stage} \tag{3.1}$$

$$g_j = \frac{N_{e^-}\ leaving\ gas\ amplification}{N_{e^-}\ reaching\ gas\ amplification} \tag{3.2}$$

$$\epsilon_j = \frac{N_{e^-}\ leaving\ the\ GEM\ stage}{N_{e^-}\ leaving\ gas\ amplification} \tag{3.3}$$

In gas amplification mode it is impossible to disentangle τ, g and ϵ. A quantity which can be determined directly is the effective gas gain

$$G_j = \tau_j \cdot g_j \cdot \epsilon_j = \frac{I_A}{I_P} \tag{3.4}$$

where I_A is the anode current and I_P is the current from the ionization process.

$$T_j = \tau_j \cdot \epsilon_j \tag{3.5}$$

is the transmission. This quantity is most meaningful in the case unit gain, where it simply reflects the ratio

$$T_j|_{g=1} = \frac{N_{e^-}\ leaving\ the\ GEM\ stage}{N_{e^-}\ entering\ the\ GEM\ stage} \tag{3.6}$$

and directly indicates electron losses. In this regime, electron transmission can be determined by measurement of the electrode currents:

$$T_j|_{g=1} = \frac{I_A}{I_{TOP} + I_{BOT} + I_A} \tag{3.7}$$

The ion transmission is defined the other way around:

$$T_j{}^+|_{g=1} = \frac{N_{ions^+}\ leaving\ the\ GEM\ stage}{N_{ions^+}\ entering\ the\ GEM\ stage} \tag{3.8}$$

It can be defined by

$$T_j{}^+|_{g=1} = \frac{I_C}{I_{TOP} + I_{BOT} + I_C} \tag{3.9}$$

with the same setup and reversed electric fields. To characterize the ion back-flow of a GEM-foil in amplification mode, we define the fractional ion feedback

$$f_i = \frac{N_{ions^+}\ leaving\ the\ GEM\ stage}{N_{e^-\ ions^+}\ pairs\ produced\ in\ the\ GEM\ stage} \tag{3.10}$$

and the effective fractional ion feedback

$$F_i = \frac{N_{ions^+}\ leaving\ the\ GEM\ stage}{N_{e^-}\ leaving\ the\ GEM\ stage} \approx \frac{f_j}{\epsilon_j} \tag{3.11}$$

which can be approximated by

$$\frac{I_C}{I_A} = \frac{1 + F_j \cdot G_j}{G_j} \approx F \tag{3.12}$$

if $F_j \cdot G_j \gg 1$ with cathode current I_C and anode current I_A or exactly

$$F_j = \frac{I_C - I_P}{I_A} \tag{3.13}$$

in case the ionization current I_P is known.

3.3.2 Quantities of a GEM stack

In a multi GEM stack the total effective gas gain G is the product of the individual effective gas gains of the i GEM-stages:

$$G = \prod_{j=1}^{i} G_j \tag{3.14}$$

with the Number of produced electrons and ions after passing each GEM stage is:

- $N_1 = N \cdot \tau_1 \cdot (g_1 - 1) \approx N \cdot \tau_1 \cdot g_1 = \frac{N}{\epsilon_1} \cdot G_1$

- $N_2 = N_1 \cdot \epsilon_1 \cdot \tau_2 \cdot (g_2 - 1) \approx N \cdot G_1 \cdot \tau_2 \cdot g_2 = \frac{N}{\epsilon_2} \cdot G_2 \cdot G_1$
- $N_3 = N_2 \cdot \epsilon_2 \cdot \tau_3 \cdot (g_3 - 1) \approx N \cdot G_2 \cdot G_1 \cdot \tau_3 \cdot g_3 = \frac{N}{\epsilon_3} \cdot G_3 \cdot G_2 \cdot G_1$

Therefore the number of electrons and ions after passing the j^{th} GEM is approximated by:

$$N_j \approx \frac{N}{\epsilon_j} \prod_{k=1}^{j} G_k \tag{3.15}$$

The number of ions M released by a multi GEM stack of i stages in the drift volume is given by:

$$M = \sum_{j=1}^{i} f_j \cdot N_j \prod_{k=1}^{j-1} {T_k}^+ \tag{3.16}$$

with eq. 3.15 eq. 3.16 can be approximated:

$$M \approx \sum_{j=1}^{i} \frac{f_j \cdot N}{\epsilon_j} [\prod_{k=1}^{j} {G_k}^+] \cdot [\prod_{k=1}^{j-1} {T_k}^+] \tag{3.17}$$

and with 3.11 can be further approximated to:

$$M \approx \sum_{j=1}^{i} F_j \cdot N \cdot [\prod_{k=1}^{j} {G_k}^+] \cdot [\prod_{k=1}^{j-1} {T_k}^+] \tag{3.18}$$

The total effective ion fractional ion feedback defined as

$$F = \frac{number\ of\ secondary\ ions\ reaching\ the\ drift\ volume}{number\ of\ electrons\ leaving\ the\ last\ GEM} \tag{3.19}$$

can be calculated

$$F = \frac{M}{N \cdot G} = \frac{\sum_{j=1}^{i} F_j \cdot [\prod_{k=1}^{j} {G_k}^+] \cdot [\prod_{k=1}^{j-1} {T_k}^+]}{\prod_{k=1}^{j} {G_k}^+} \tag{3.20}$$

from the curves $F_j(G_j)$ and ${T_k}^+$ for the different GEM stages. It also can be determined in measurements with

$$F = \frac{I_C - I_P}{I_A} \approx \frac{I_C}{I_A} \tag{3.21}$$

if $I_C \gg I_P$ according to the case of a single GEM-foil in eq. 3.11 and 3.13. The resulting ion backflow of a GEM device, defined as the number of ejected ions per electron, is given by

$$\phi = \frac{M}{N} = G \cdot F \tag{3.22}$$

i.e. by the product of effective gas gain and effective ion feedback.

3.4 Discharges

The operation stability of a GEM detector is limited by the discharge propability. The mechanism which is most probably responsible for the breakdown is the transition from an avalanche to a streamer followed by a discharge between anode and cathode. This effect has been extensively studied in gas detectors working in parallel plate mode [56]. When a traversing particle releases a sufficiently high number of electron-ion pairs in the active gas volume of the detector, the total charge produced in the subsequent charge amplification process might exceed a number of 10^7 to 10^8 electron-ion pairs. This number corresponds to the Raether limit for the formation of streamer in the avalanche [57]. The streamer produces an ionised and therefore conductive channel between the anode and the cathode. Along this channel the discharge takes place.

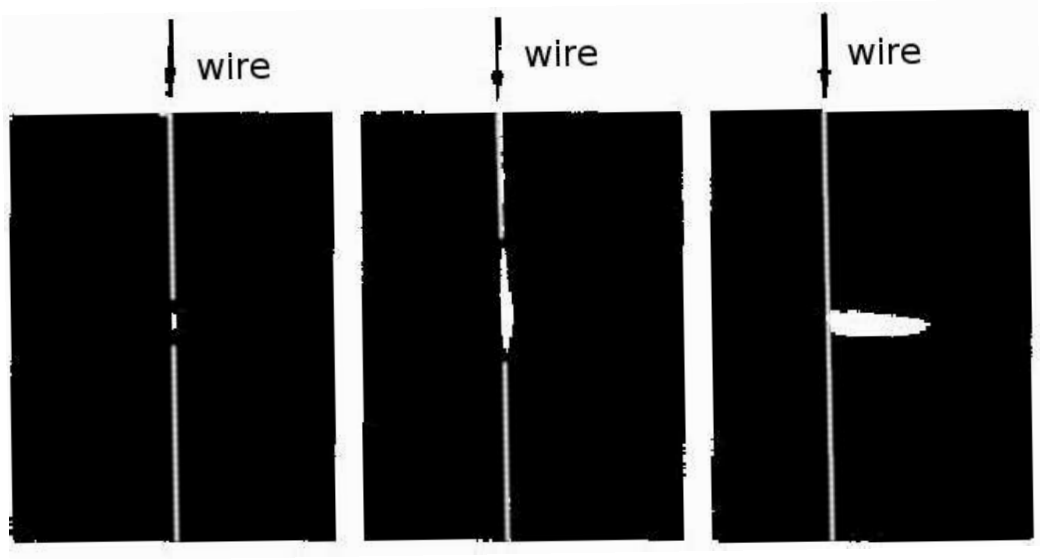

Figure 3.4: *In the left picture one can see the proportional region of gas amplification, the middle picture shows the Geiger-Müller region (no quench) and in the right picture a streamer occurs (with quench) [57].*

In Figure 3.4 the development from the proportional region of gas amplification to the production of a streamer is demonstrated.
Discharges in GEM detectors typically arise between the two electrodes of a GEM foil as local discharges. In rare cases the breakdowns involve neighboring GEM stages or the anode readout. Such breakdowns are called propagating discharges. A local discharge leads ordinarily to an increase of the dead

time or inefficiency of the detector, because the GEM-foil has to be ramped down in order to prevent it from permanent damage. In the time the detector has to recharge the voltage of the GEMs, there is no amplification. It is even worse if a propagating discharge occurs, as this could lead to a permanent damage of single GEM modules, or the complete readout structure itself. Therefore precise knowledge in terms of the expected discharge probability is crucial.
In this section two different methods to derive a discharge probability will be presented.

3.4.1 Discharge probability of GEMs in high intensity particle beams

Extensive tests of Double GEM detectors exposed to high intensity particle beams has been done to study the occurrence of discharges induced by beam particles. This studies has been performed in the preperation for the COMPASS experiment, which installed triple GEM detectors, using them as major part of the inner tracking system. The complete setup and the variety of measuring methods are described in [58].

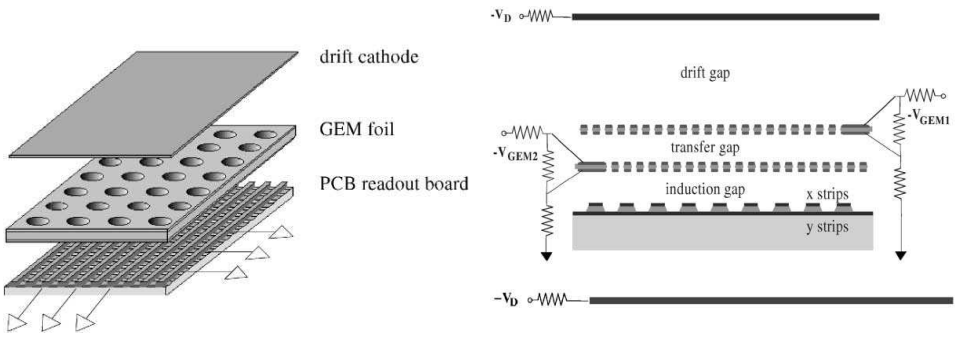

(a) (b)

Figure 3.5: *Schematics of a double GEM structure*

Two detectors have been built, which both consists of a small drift gap of a few millimeter followed by a Double GEM detector stack and finally a two-dimensional projective readout board. This two-dimensional readout board is two rows of strips with a pitch of 200 μm respective 400 μm between two strips. The first detector is assembled with two GEM foils of 10×10 cm^2. The second detector is a Double GEM prototype for the COMPASS experiment [59]. The active area of the GEM is 31×31 cm^2. The schematics of the

	Low fields	Medium fields	High fields
Transfer field (kV/cm)	2.	4.	4.
Induction field (kV/cm)	4.	4.	7.

Table 3.1: *Different field configuration used during the test beam experiments.*

Double GEM detectors are shown in figure 3.5.

Both setups have comparable transfer- and induction fields, which have been varied in different operational modes. The field configurations can be found in table 3.1. With these two setups measurments at the πM1 beam at the Paul Scherrer Institute (PSI) have been done. The πM1 beam provides either π^- with a momentum of 215 MeV/c and a rate of $10^7 \frac{\pi}{s}$ or π^+ with a momentum of 350 MeV/c with a rate up to $5{\cdot}10^7 \frac{\pi}{s}$. While pions of both charges at an energy of 300 MeV are minimum ionising, the π^+ beam is contaminated by protons of 63 MeV. At maximum π^+ intensity, the contamination is about 2 %. The protons have a significantly higher ionisation than the pions and change therefore the character of the π^+ beam.
The detectors have been operated for about 100 h, in equal proportion at low and high intensity. The choice of gas in all presented measurements was $ArCO_2$ in the proportions 70/30.

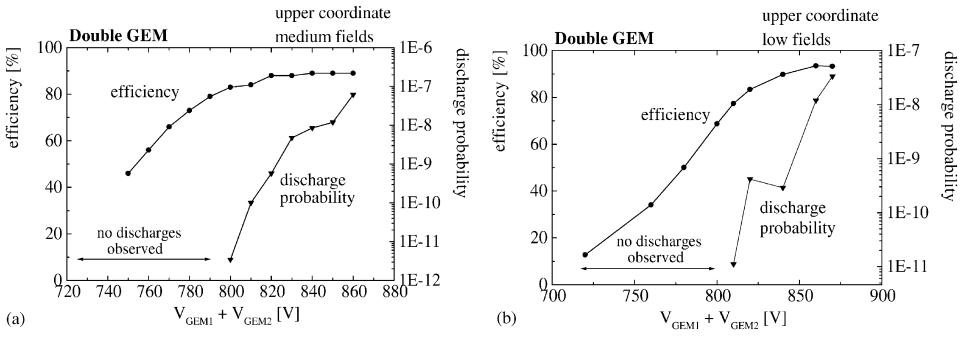

(a) (b)

Figure 3.6: *Discharge probability per incident particle and efficiency for the Double GEM at (a) medium and (b) low fields. The measurements were performed at the PSI πM1 beam [59].*

Knowing the rates of the particle beams, the actual measured particle

densities and the measured time between two discharges at a specific gain setting the discharge probability per incident particle and the efficiency can be calculated. The results are shown in figure 3.6.

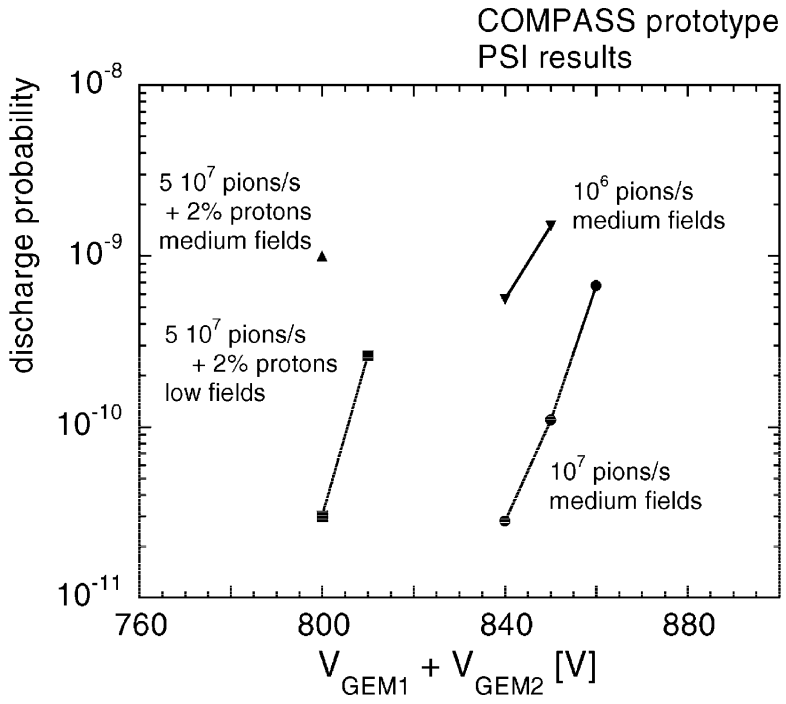

Figure 3.7: *Discharge probability per incident particle and efficiency for the Double GEM at (a) medium and (b) low fields. The measurements were performed at the PSI $\pi M1$ beam [59].*

The measured discharge probabilities for the COMPASS prototype are given in Figure 3.9. It shows that the discharge probabilities measured at paricle rates between 10^6 and $10^7 \frac{\pi^-}{s}$ are compatible to the results from the smaller size Double GEM detector. The results obtained at the maximum intensity $5{\cdot}10^7 \frac{\pi^+}{s}$ show significantly higher discharge probabilities at a lower gain, which is due to the 2 % contamination of protons, which represent a heavily ionising particle compared to minimal ionising pions. This example shows clearly, that the gain and the discharge probability has to be optimized in regard of different particle types.

3.4.2 Discharge probability of GEMs using radioactive sources

A complementary setup to determine the discharge probability of a GEM detector is to induce controlled discharges by radioactive sources. The complete method can be studied in [60]. Two methods were employed to generate the large ionization densities, emulating realistic operating conditions. In both cases the discharge probability is defined as the ratio between the observed frequency of breakdowns and the source rate.
The setup is very similar to the one presented in the previous chapter in figure 3.5, where one has a small drift gap of 3 mm followed by a GEM stack. The active area covered by the GEM foil is again the size of the standard GEM configuration, $10\times10\ cm^2$. For signal readout, a board with parallel anode strips with a pitch of 200 μm, connected in a group by wire bonding or conductive epoxy to an external grounding circuit. The measurements have been performed in $ArCO_2$ in the ratio 70/30.
In the first case an internal gaseous alpha emmitter, Rn^{230}(6.4 MeV), is added to the gas flow. The method has the advantage of uniformly exposing the sensitive volume of the detector with a 3 mm drift gap. The energy loss distribution has a broad spectrum with an average around 400 keV [61]. With a reasonable waiting time of a few hours for the occurence of a discharge a practical limit for discharges is around 10^{-4}.
In the second case a collimated Am^{241} source, emitting 5.5 MeV alphas, is mounted either internally, in contact with the drift electrode, or externally through a thin polymer window. In both cases, the drift electrode is made of a fine wire mesh, to allow penetration of the radiation into the drift volume. In this case energy loss spectrum is better defined, with a peak around 500 keV. With this collimated source discharge probabilities down to 6×10^{-6} can be achieved.

Discharge in single and multiple gem structures

The sequence of events that can lead to the propagation of a discharge throughout the detector begins with a sudden, radiation-induced breakdown of the gas rigidity in one GEM, normally the last in a cascade of multipliers. The probability of this initial discharge appears to depend on the primary ionization density and on the overall gain of the structure, but not directly on the external fields.

Figure 3.8 provides the discharge probability as a function of voltage for a single GEM detector, observed with the internal Rn^{230} alpha source added into the gas flow [62]. The measurement suffers from statistical limitations,

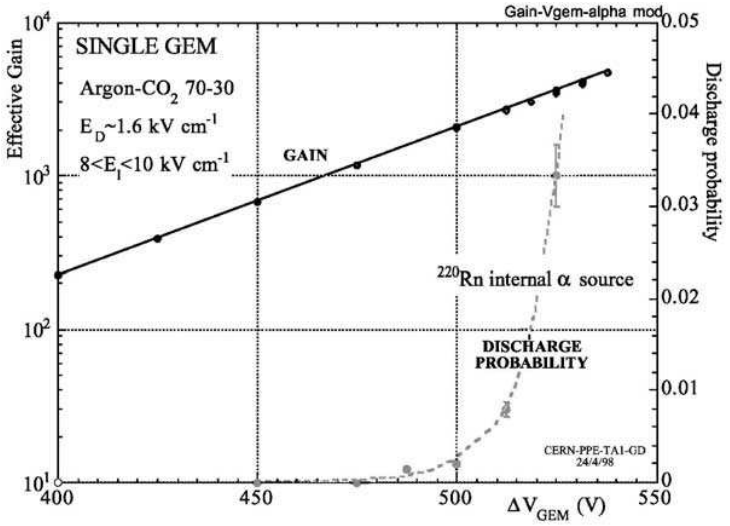

Figure 3.8: *Discharge probability with the Rn^{230} internal α source and gain as a function of a voltage for a single GEM detector [62].*

but has the particularity of corresponding to an isotropic track distribution in the narrow gap. The threshold for discharges is observed at a gain of one thousand.
Figure 3.9(a) shows the discharge probability measured as a function of multiplying voltage, in the single, double and triple GEM, exposed to the Am^{241} α source. For this measurement, the voltage applied to each GEM was identical. The induction and transfer field were fixed at 3.5 kV/cm, and the drift field at 2 kV/cm. The decrease in the discharge voltage is a reflection of the increasing avalanche size for multiple devices. In figure 3.9(b) the same data are plotted as a function of effective total gain of the structures. The maximum gain is increased by around an order of magnitude at each addition of a multiplier. In both measurements the statistical of the zero baseline corresponds to the observation of no discharges during a waiting time of 3000 s, or a probability of less than 6×10^{-6}.

3.4.3 Discussion of the results

The discharge probability for both methods show, that a safe operation is possible up to fields of about 420 V for each GEM of a double GEM structure and 380 V for triple GEM structures. The results for the double GEM structures are in good agreement.
In high intensity particle beams the discharge probability per passing par-

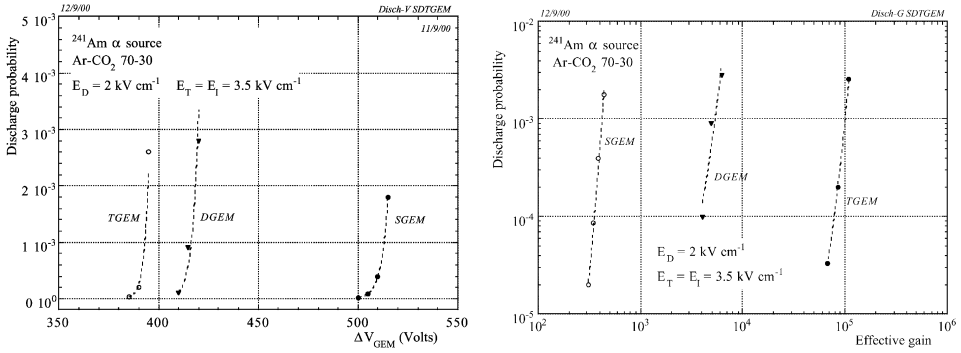

(a) (b)

Figure 3.9: *(a) Discharge probability on α particles in single, double and triple GEM detectors, as a function of applied voltage (equal on all GEMs). (b) Discharge probability as a function of total effective gain for single, double and triple GEM detectors [60].*

ticle shows a strong dependency on the radiation environment such as the particle identity, flux and energy. The results seem to be consistent with the idea that discharges are triggered by heavily ionising particle tracks releasing an exceptionally high amount of electron ion pairs in the active gas volume. This can be clearly seen in the results obtained with the COMPASS prototype. It has been shown, that in the case of MIPs low discharge rates can be expected. In the case of even small contributions of heavily ionising particles the discharge probability increases as the charecter of the beam is changed. From the results an upper limit of the discharge probability of 2×10^{-12} for 350 MeV π^+ can be derived.

The results of the studies with radioactive sources complement the view on the probabilities of discharges. In presence of moderate irradiation, proportional gains of about one thousand can be reached with a single GEM. A gain of 10^4 resp. 10^5 can be attained cascading two or three multipliers. The maximum gain, which allows a save operation, is however stongly reduced when the detectors are exposed to heavily ionising particles. Given the gain, the discharge probability depends both on the released amount of charge, density and on the angle of the track. With multiple structures the safe gain increases again by about an order of magnitude at each addition.

Studies to investigate the radiation environment of a TPC at the ILC concerning particle type, flux and density are in preparation. This should allow to approximate the discharge probability for an average occupancy of the TPC.

Chapter 4

Experimental Setup

This chapter explains the TPC detectors and detector components as well as all hardware systems, which have been used for the different data taking.

4.1 TPC Prototypes

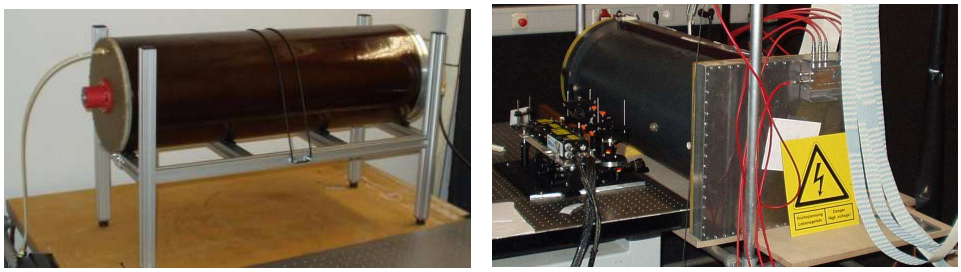

(a) (b)

Figure 4.1: *The TPC prototypes called (a) Medi-TPC and (b) Big TPC. The basic parameters of both prototypes can be found in Table 4.1*

Two TPC prototypes have been used (see Figure 4.1). The basic design parameters can be found in Table 4.1. The first prototype, here called Large TPC, was built for the Aleph TPC project with a wire amplification system at the anode plate. A new TPC endplate with a GEM amplification system was constructed for first investigations of the single point resolution. A detailed description can be found in [38]. The final design of the endplate was accomplished to investigate an alternative TDC readout electronics [63]
Neither the field cage nor the size of this TPC were appropriate to operate it

	Medi TPC	Big TPC
total length	80 cm	105 cm
diameter	27 cm	38 cm
length of the sensitive volume	66 cm	100 cm
columns, rows	16,8	8,8 (8,10)
pad size	2.2×6.2 mm^2	7×7 mm^2
sensitive area (xy)	35.2×49.6 mm^2	56×56 (56×70)mm^2
radiation length of the field cage	X_0 <1%	-
readout channels	128	64 (80)
Number of GEMs	3	2

Table 4.1: *Design parameter of the TPC prototypes*

under performance conditions similar to those required for the ILC. Therefore another prototype was constructed to achieve the requirements needed for a TPC at the ILC, here called Medi TPC. The basic design parameters can also be found in Table 4.1. The diameter of the TPC prototype was designed to fit into the bore of the high magnetic field facility as described in section 4.8.

4.2 Field Cage

The electric field cage has to be as uniform as possible, and ideally, similar to that of an infinitely large parallel-plate capacitor. The ideal boundary condition on the field cage is a linear potential varying from the potential of the high voltage cathode to the potential of the segmented anode.
This boundary condition can be achieved to a very good approximation by covering the field cage with high resistivity uniform material and the inner surface with a regular set of conducting strips perpendicular to the electric field. This provides a constant potential difference ΔV between two adjacent strips:

$$\Delta V = E\ d, \tag{4.1}$$

where d denotes the pitch of the electrode strips.
The electric field very near to the strips is not uniform and there are also field lines that go from one strip to the adjacent one. The transverse component essentially decays as $e^{\frac{-2\pi t}{d}}$ where t is the distance from the field cage. When t = d the ratio between the transverse and the main component of the electric field is about 10^{-3}. At larger distances it becomes completely

negligible.

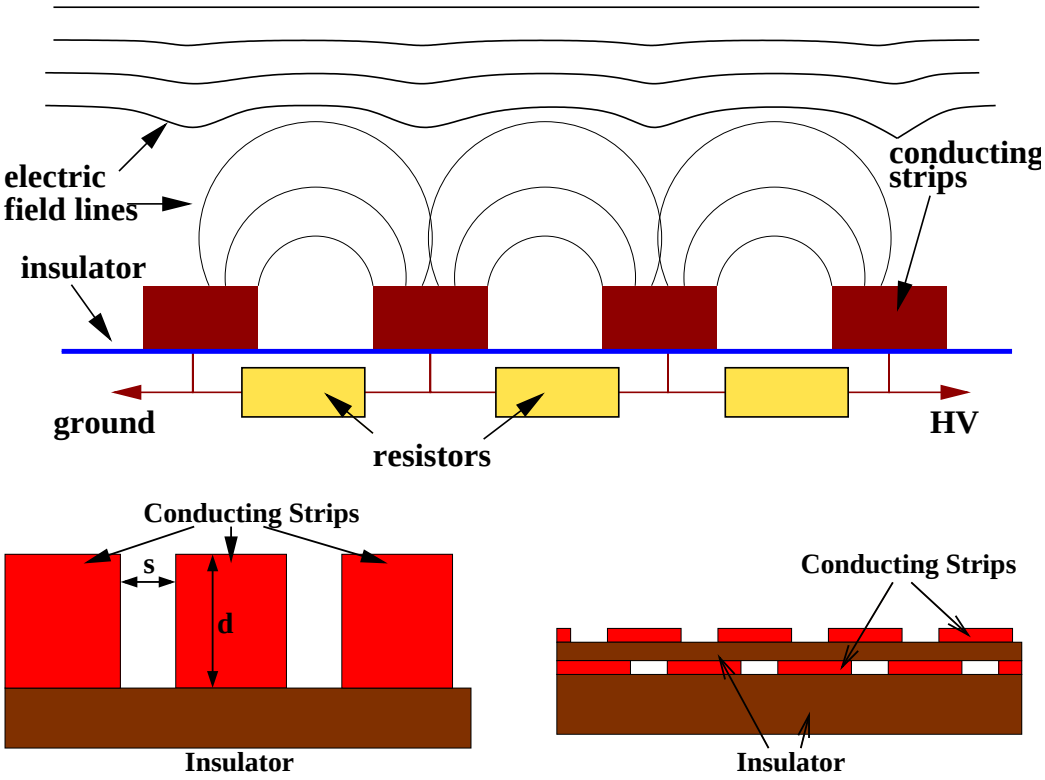

Figure 4.2: *The basic principles of the field cage strips are shown. The conducting strips are connected to each other by resistors. The cathode is located on the right and the anode on the left side [44].*

The use of conducting strips with an increasing potential makes insulator between them unavoidable. Free charges may settle down on these insulators and disturb the electric field. To avoid this several solutions are possible:

Controlled conductivity of the insulators: When a insulator has a conductivity, which leads to an equilibrium between charge deposit and transport to the next electrode, the disturbing effects are reduced.

Retracted insulator surface: If the field cage strips have the form as shown in fig. 4.2 the electric field caused by the charge deposited on the insulator between the two strips is damped by a factor of the order of $e(-\frac{\pi d}{s})$ at the top of the strips.

Shielding electrodes: The use of a second layer of electrodes separated from the first one by a small insulator as shown in 4.2 also reduces distortions. The best results are obtained if the staggered strips are at an intermediate potential of the two pads.

Depending on the experimental environment, the field cage has to satisfy a large number of requirements. It should work as a gas vessel, be mechanically stable, self supporting and must withstand the high potential difference between the conducting strips and the outer surface. This potential difference is of the order of several 10 kV around the cathode. On the opposite the field cage should have as little material as possible in front of the calorimeter to ensure the lowest impact on energy resolution. An important quantity to determine this is the radiation length X_0. The radiation length X_0 is the value by which the electron energy is reduced by $\frac{1}{e}$. A typicall radiation length of classical TPCs is about 7-15 % X_0 in total. Modern TPCs require a radiation length of about 3 % X_0.

4.2.1 Field Cage Design

Field Cage of the Large Prototype

The main cylindrical volume of the TPC is made of $Rohacell^R$ foam. The copper foil on the outer surface of the TPC wall is grounded, providing electro-static shielding of the TPC.
The uniformity of the electric field in the TPC is provided with the field cage formed on the inside of the outer wall TPC wall with 100 concentric copper strips of a width of 0.8 cm. A resistive divider of hundred 1 MΩ resistors supplies potentials to the strips. The high voltage applied to the field cage can be adjusted up to a maximal value of 22 kV.

Field Cage of the Medi TPC

The field cage of the Medi-TPC was designed to fulfill the requirements of a modern TPC for the ILC project. The whole process of development of the field cage is extensively described in the PhD work [64].

For the TPC prototype a sandwich structure for field cage walls was chosen. Fig. 4.3 shows the field cage design. The first inner layer is a Kapton foil coated on one side with copper strips, followed by three further layers of Kapton, a layer of carbon reinforced plastic (CFK) and a Nomex honeycomb structure. The field cage is completed in the radial direction

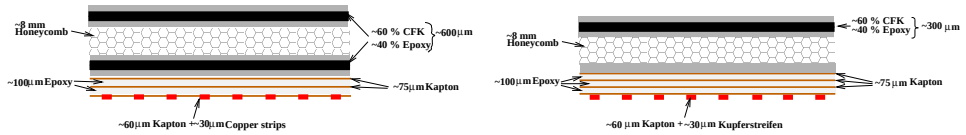

(a) (b)

Figure 4.3: *Field cage structure: original design (a) and design used for the construction (b)*

Material	X_0 [cm]	d [μm]	X_0 [%]
CFK	18.8	200	0.11
Epoxy	19.4	1000	0.36
Kapton	25	275	0.09
Nomex Hexacomb	1430	8000	0.06
Copper	1.43	30	0.21
Sum			$\approx$ 0.83

Table 4.2: *Material budget of the TPC prototype*

by a second layer of CFK. This CFK layer should act as a RF shield. To resolve to grounding problems, a copper coated Kapton foil was wrapped around the field cage.

The resistor chain between the strips was placed inside the gas volume. The width of each copper strip is 1.6 mm and the pitch 2.8 mm. Each resistor have a resistance of 810 kΩ. For reliability reasons not only one resistor chain was mounted, but four in parallel. This reduces the resistance between two strips to $\approx$ 200 kΩ. The total resistance between the shield and the cathode is $\approx$ 50 MΩ over almost 250 strips.

The material budget of the field cage was calculated. A total radiation length of $\approx$ 0.8 % was achieved and the results are shown in table 4.2. In the table an overview of the material used, the radiation length in X_0 in cm, the thickness d, and the relative radiation length X_0 in percent is given.

4.3 Anode and Cathode Plate

4.3.1 The Medi TPC

The cathode plate consists of a copper layer fixed to a G10 plate. In the middle of the cathode a 20 kV HV connector is mounted and connected through a wire to the copper plate of the cathode. The electrical connection between the cathode and the resistor chain is achieved by springs, which press against the field cage strip with the highest potential when the cathode is connected to the field cage. For the laser setup a new cathode was built, so that one can easily switch between a setup usable for cosmic particles and a setup for laser measurements which can be arranged by just choosing the appropriate cathode.
Complementary to the two separate cathodes, there are also two anode plates which can be exchanged to fit to the appropriate setup. The anode consists of a G10 layer coated with a gold nickel alloy. In the middle of the anode is a quadratic cut out where the GEM detector is located during the operation. The difference between the setup used for cosmic and laser operation modes is a Prism Positioning System (PPS), which is located on the anode to reflect the laser beams in the sensitive volume. A detailed description of the PPS is given in section 5.3.

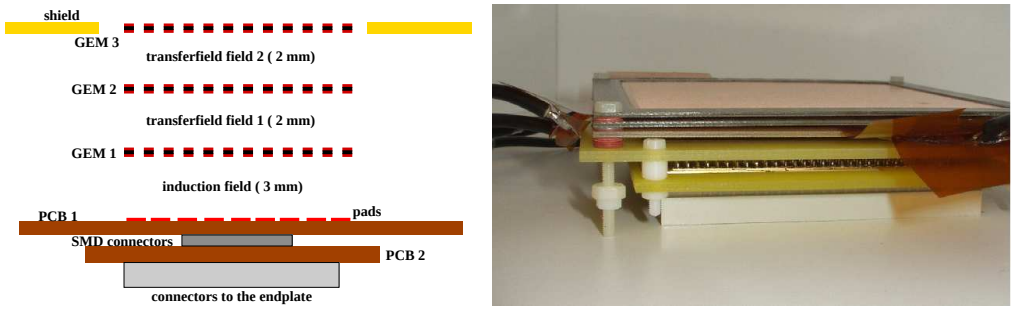

(a) (b)

Figure 4.4: *In plot (a) a sketch of the GEM detector setup is shown with the distances of the transfer and induction fields. Plot (b) shows a picture of this GEM detector.*

The anode similarly to the cathode is connected via springs to the field cage strip with the lowest potential. The GEM detector is placed in the center of the anode, where a quadratic piece is cut out to hold the GEM detector. The detector consists of a GEM tower with three $10\times10\ cm^2$ standard GEMs from the CERN workshop and 2 printed circuit boards connected by SMD

connectors. Figure 4.4 shows a schematic view of the GEM detector. The field between two GEMs is called *transfer field* and the field between GEM and the pad plane is called *induction field*. The transfer gaps are 2 mm, while the induction gap is 3 mm. The field strength is 1.5 kV/cm for the transfer fields and and 3 kV/cm for the induction field. On PCB1 the pads are coated, while on PCB2 the signal wires are grouped to simplify the pad mapping. Finally the signal is directed out of the chamber by two 96 pin connectors.

Pad Geometry

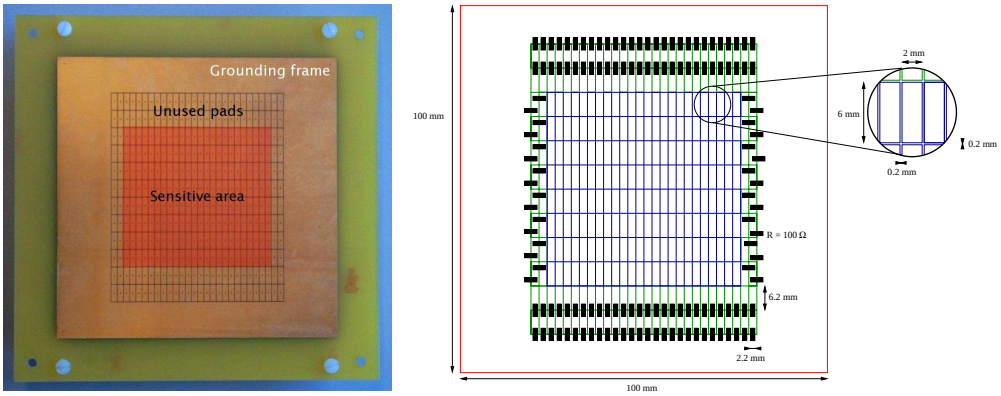

(a) (b)

Figure 4.5: *Picture (a) shows the non-staggered pad plane with an effective pad size of 6.2×2.2 mm^2. The maximal number of columns is 24, the maximal number of rows is 8. Picture (b) shows the schematic design of the pad plane including the connection of the outer pads to 100 kΩ resistors.*

For the measurement with the Medi TPC a non-staggered pad geometry is used. In the work of [64] and [65] the influence of staggered and non-staggered pad geometries on the single point resolution has been discussed. For cosmic particles, which traverse the pad geometry with small angle deviations to the y-axis the influence on the resolution is significant. For the tracks produced by our laser setup (see section 5.4.2) an intrinsic inclination angle is given due to the construction of the setup. Therefore only one non-staggered pad geometry was used as the intrinsic inclination leads to an staggering effect in both geometries. Figure 4.5 shows a picture of the pad plane. The pad geometry is based on rectangular conductive areas, which have a length of 6 mm and a width of 2 mm. The distance between two pads

is 0.2 mm, so that the effective size of the pad is 6.2×2.2 mm^2. The pad size was chosen from a simulation performed for the TESLA TDR [97]. 192 pads can be read out. Due to the fixed position of the laser tracks only 128 pads needs to be read out in 16 columns and 8 rows. The effective readout area is 35.2×49.6 mm^2. The remaining space of the pad plane consists of a large outer plane and two remaining lines of pads. These pads are connected via resistors of 100 kΩ respectively 150 kΩ to each other (see figure 4.5(b)). The aim of the these outer two pad rows was to guaranty a homogenous induction field and avoid cross-talk, which was not successful. The charge, which was deposited on these outer pad did not flow off fast enough, so that the remaining charge induced a lot of cross-talk on the neighboring pads.
The complete Anode is then connected to the endplate of the system. The endplate provides the connection to power the GEMs, the shield and the preamplifier tower. As the connection between the pads and the preamplifiers should be as short as possible, the endplate holds also the preamplifier tower where the signal is sampled and multiplied (see section 4.7).

4.4 HV System

(a) (b)

Figure 4.6: *(a) shows a FUG HCN 140-35 power supply, which provides a maximum voltage of 35 kV and a maximal current of 4 mA. (b) shows a CAEN SY 527 multi channel power supply to power each GEM channel indepedently.*

Several High Voltage power supplies are used to operate the TPC prototype. One type of power supply is used to power the cathode and the field

cage strips.
In case of the Medi-TPC a FUG HCN 140-35 [66] is used, which can provide a maximum voltage of 35 kV with a current of up to 4 mA (see figure 4.6(a)). To supply the GEM modules with HV a multi channel power supply from CAEN SY 527 [67] is used (see figure 4.6(b)). Each GEM channel was independently connected to the power supply. This has the advantage, that every GEM channel could be steered independently. This provides a good protection from an overcurrent, which can be a result of a discharge as discussed in Section 3.4. The discharge protection of an overcurrent could be set to a minimal value of 1 μ A. If one channel rise above this value the complete system is ramped down instantly. Additionally a 10 MΩ protection resistor is placed in front of each GEM. This also reduces significantly the probability of permanent damage of a GEM due to discharges. Without this resistors a spark might release enough energy to produce a permanent short circuit.
An important point is that the last field cage ring and the GEM surface nearest to the drift volume is at the same electrical potential U_{GS} to prevent the chamber from field distortions. To ensure this, for various field configurations, a steerable resistor (potentiometer) R_s is placed between shield and ground. R_s is calculated by:

$$R_s = \frac{U_{GS}}{U_c - U_{GS}} \cdot R_{cage} \tag{4.2}$$

R_{cage} is the total resistance of the field cage and U_c the voltage of the cathode.

4.5 Chamber Gas

The chamber was operated with a gas mixture of 93 % argon, 5 % CH_4 and 2 % CO_2. This gas mixture was optimized for operation of a TPC in the former linear collider project TESLA and proposed in the Technical Design Report [42]. In Section 2.5, a comprehensive gas mixture study is described in detail.

In Figure 4.7 the TDR gas is compared to an other standard gas, which consists of 95 % argon, 5 % CH_4 (P5 gas). Both gas mixtures are primarily based on argon with a contribution of 5 % CH_4, but the small contribution of 2 % CO_2 has a strong impact on the key parameters like the drift velocity and longitudinal and transverse diffusion.

4.6 Slow Control System

A slow control system has been built to measure, study and take into account the influence of the gas parameters temperature, pressure and the composition of the gas. A detailed description about the system can be found in the master thesis of [68]. With this system an accurate estimation of the drift velocity can be calculated and taken into account for data analysis. The slow control system consists of several measuring tools that will be described in the following.

4.6.1 Dew Point Measuring Instrument

The water content can be derived by the humidity of the gas, which is correlated with the temperature. If the temperature sinks below the dew (or frost) point the gas is saturated and the water condensates. In case of the dew point measuring instrument [69] the gas flows along a mirror, which is illuminated by a light source. The reflected intensity from the mirror is proportional to the amount of water in the gas. The cooling of the mirror is done by a peltier element. The related temperature T_{dew} of the mirror is measured and shown. The total range is -60 to +20 degrees, which corresponds to a water content of 10.5 to 20000 ppm. With T_{dew} the water $\Psi_{H_2O,gas}$ content is given by:

$$\Psi_{H_2O,gas} = \frac{6.11213}{1013.25hPA} \cdot exp(\frac{17.5043 \cdot T_{dew}}{241.2 + T_{dew}}) \cdot 10^6. \tag{4.3}$$

In case of a very small water content of some hundred ppm gas saturation occurs only at temperatures below 0 degree. Therefore Eq. 4.3 has to be modified to:

$$\Psi_{H_2O,gas} = \frac{6.11153}{1013.25hPA} \cdot exp(\frac{22.4433 \cdot T_{frost}}{272.186 + T_{frost}}) \cdot 10^6. \tag{4.4}$$

An automatic mirror cleaning system is included in the Dew Point Measuring Instrument to regularly clear the mirror from the condensed substances.

4.6.2 Oxygen Content Meter

The oxygen content is determined by an electro chemical reaction [70]. In this process gas and electrical substances produce a voltage. The voltage is proportional to the oxygen content of the gas.

$$O_2 + 2H_2O + 4^- \rightarrow 4OH^- \quad (Cathode)$$

$$2Pb + 4OH^- \rightarrow 2Pb^+ + 2H_2O + 4e^- \quad (Anode)$$

$$2Pb + O_2 \rightarrow 2PbO \quad (Sumreaction)$$

The reaction takes place in a cell, which has to be replaced after the oxidation of the lead. The total capacitance of the cell is $2.598 \cdot 10^7$ppm/h.

4.6.3 Pressure sensors

The pressure is an important parameter for several reasons. For pure mechanical reasons it is crucial to know the overpressure of the chamber compared to the outside pressure. It is necessary to keep the pressure below a certain limit of a few ten mbar to protect the field cage from permanent damage.
The effect on the density of the gas composition is described in section 2.4.4

To have a steerable overpressure control loop a 10 BP device from the company FAIRCHILD was used. The control loop operates in a region of 30 to 2000 mbar [71] [72].
For the measurement of the pressure differential and absolute pressure sensors from the company SETRA are used.

- Two sensors of type C280 [73] are used for the measurement of the absolute inner and outer pressure with a measuring range of 0 to 1720 hPa. The devices have an uncertainty of ± 0.11 %
- One sensor of type 267 [74] with a measuring range of ± 5 mbar and an uncertainty of ± 1 % is used for the measurement of the pressure fluctuation.

4.7 Data Acquisition System

For the readout a data acquisition system (DAQ) based on electronics used for the ALEPH detector at LEP [27] was adapted [75]. Each pad of the TPC is connected to a preamplifier, which integrates the charge deposited on the pad and converts it to a voltage signal. The integration time constant of the preamplifier is 2 μs. The voltage signal from the preamplifier is sent to a digitizing unit, the Time Projection Digitizer (TPD). The digitizer consists of a receiver/shaper, followed by an 8 bit Flash Analog to Digital

Converter (FADC). The sampling rate of the system is 12.5 MHz and it has a storage depth of 512 time slices (*approx* 41 μs). The digitized information is written in a memory bank of the TPD. The TPDs are placed inside a FASTBUS crate. The whole system is steered and read out by a Fast Intelligent Controller (FIC 8234), which is sitting in a VME crate. The FIC is connected to a FASRBUS-VSB-Interface (FVSBI 9210), where the FIC is the master and the FVSBI the slave.

In Figure 4.8 the system is shown. As the FIC has no storage memory of its own, it has to get the operating system from an external source. The FIC sends a broadcast via Ethernet to a connected Linux PC, which delivers the boot image of the OS9 operating system. With that boot image the FIC reboots itself to start OS9. The system is then connected via NFS to the Linux PC. This allows to run the data acquisition program, which steers the system and to access the raw-data output on the PC. The data acquisition program, which acts as a client sending the data to a daemon, which is the server. This daemon can be accessed by several other clients. An LCIO [83] (Linear Collider Input Output) client has been implemented to transform the raw-data format in an LCIO format. These files are basic input files for the reconstruction software, which is described in chapter 6.

4.8 High Magnet Field Test Facility

A superconducting solenoid magnet, which was formerly used in the ZEUS experiment, has been set up as a high field test facility for the detector development for a future linear collider. The magnet can be ramped up to currents of 1000 Ampere, which corresponds to a magnetic field of 5.25 T. The coil has a length of 1.2 m and consists of 5083 turns arranged in 18 layers. The surrounding cryostat has a length of 1.86 m and an inner diameter of 28 cm and an outer diameter of 104 cm.

The calibration curve in figure 4.9 shows the linear dependency between current and magnetic field in the center of the coil. The calibration curve was measured using several Nuclear Magnetic Resonance (NMR) probes.

Fig. 4.10 shows the measured homogeneity of the magnetic field in longitudinal and radial direction. In longitudinal direction the area of the uniform field is about 1 m, which corresponds to the length of the coil. The radial inhomogeneities increase significantly at the outer part of the coil. This suggests that only a limited region of approximately 1 m at the center of the magnet can be considered magnetically homogenous for the operation of a TPC.

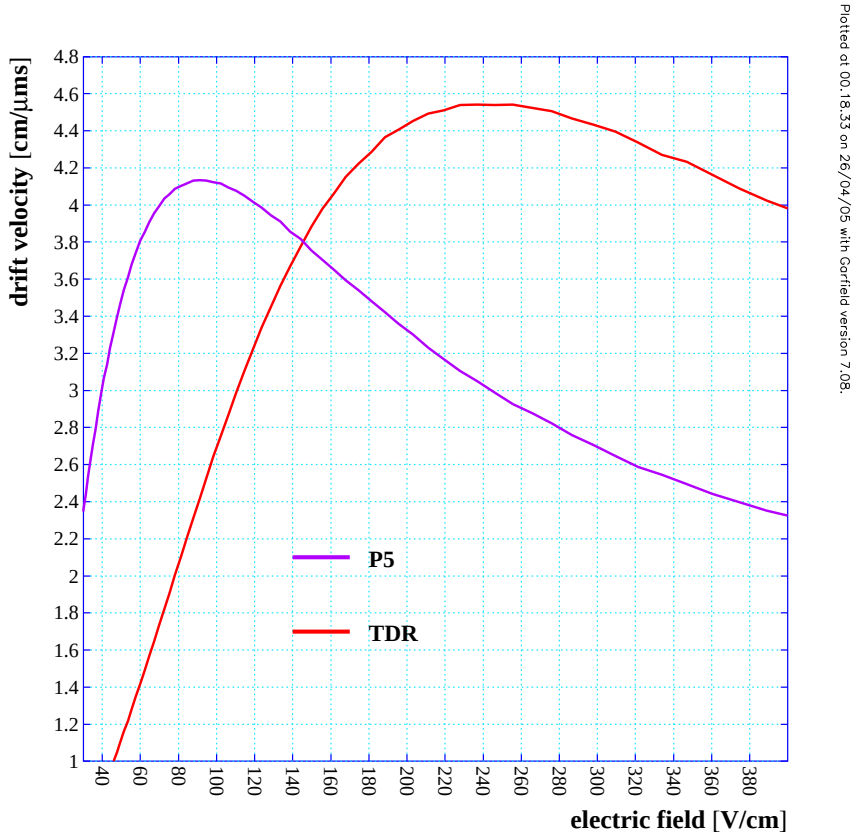

(a)

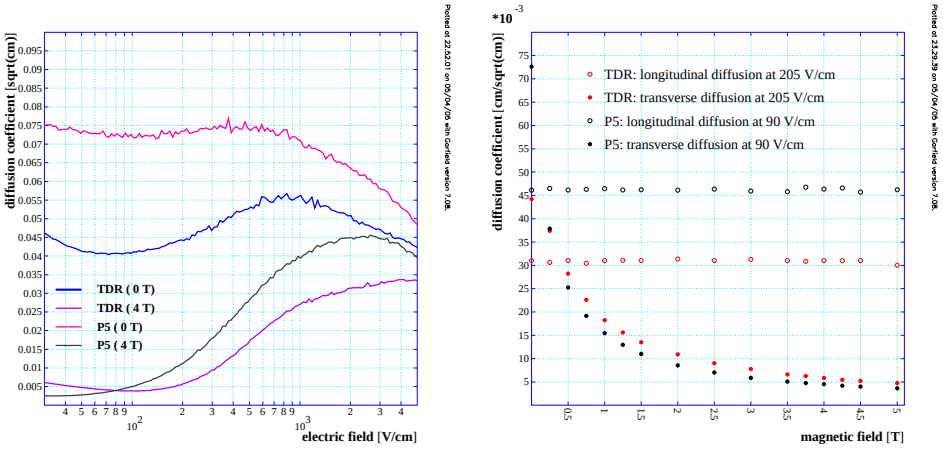

(b) (c)

Figure 4.7: *Comparison of TDR and P5 gas: (a) drift velocity as function of the electric field. (b) transverse diffusion coefficient as function of the electric field. (c) longitudinal and transverse diffusion coefficient as function of the magnetic field*

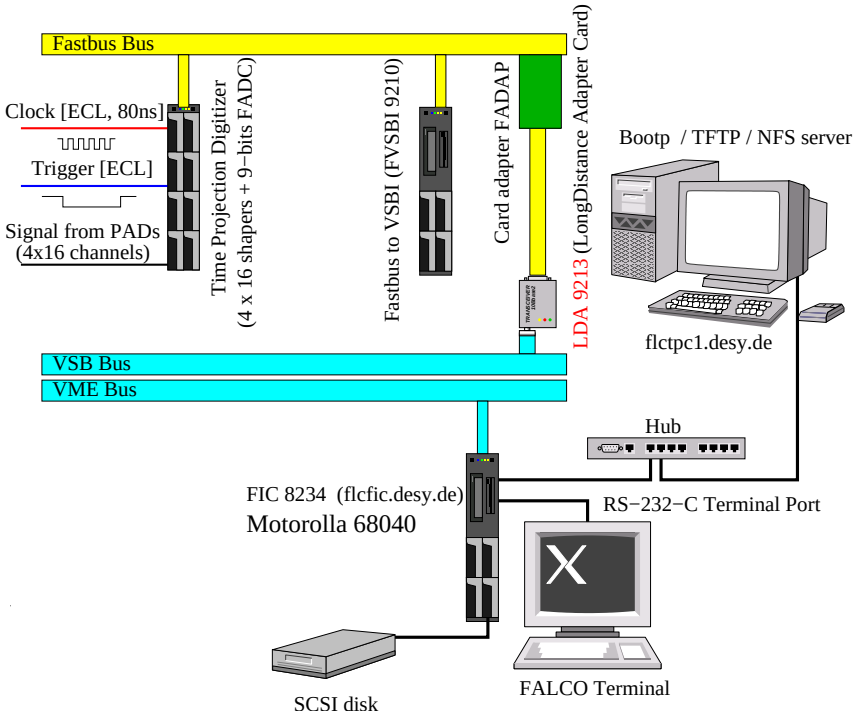

Figure 4.8: *Sketch of the DAQ system*

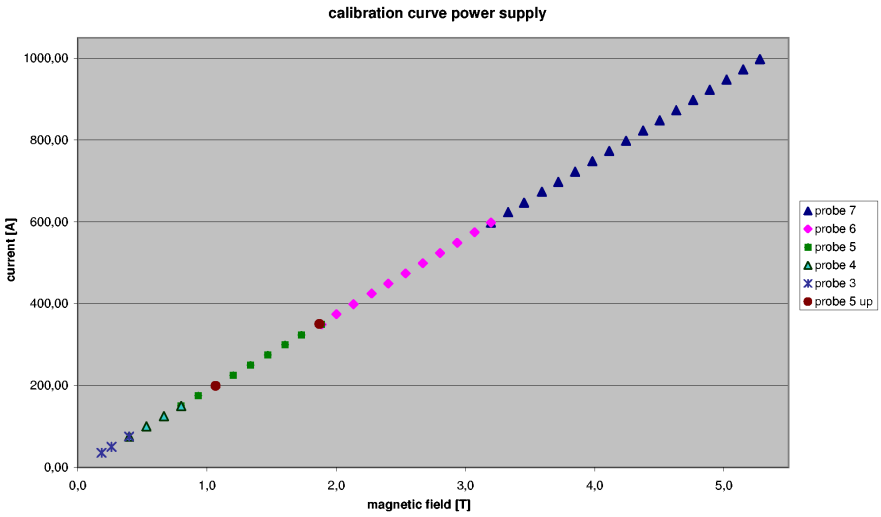

Figure 4.9: *Linear dependency between the current and the resulting magnetic field. Several Nuclear Magnetic Resonance (NMR) probes were used to measure the calibration curve*

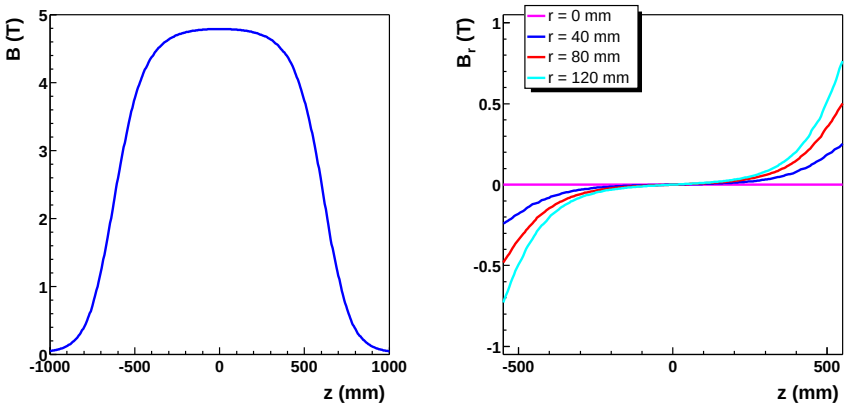

Figure 4.10: *Longitudinal and radial distribution of the magnetic field magnetic field.*

Chapter 5

The UV-Laser

In this chapter the operation principle of our NdYAG UV-laser is described. Afterwards the main components of the optical setup, the Galilean telescope and the wedge prism are explained. The impact they have on the waist of the laser beam is described. The estimate of the laser waist in connection with an energy calibration of the laser allows a statement about the estimated number of primary electrons. In the next sections the modifications to insert the laser in the Medi-TPC and the steering system, which allows the positioning of the laser, are described. To ensure that the electric field homogeneity of the sensitive volume is not influenced by the steering system, which is located at the anode field, electric field distortions are estimated by a simulation. Finally the laser setups for the drift velocity measurements and the two-track separation studies in x are presented.

5.1 The UV Laser

For the production of the laser beams an Ultra Compact Folded Resonator (CFR) Nd:Yag Laser System produced by Big Sky Laser technology was used [76]. The system consists of a laser head and a separated power supply, which has an integrated cooling system. Figure 5.1 shows the head of the UV-laser and the corresponding power supply.
The element Neodym (Nd) has the atomic number Z = 60 and belongs to the group of noble earths. These elements are characterized by their partially filled 4f-state (see Figure 5.1(b)). When Neodym is doped into another crystal structure, it releases three electrons to this crystal. In the newly generated Nd^{3+}-ion new dipole transitions of the 4f-state are allowed, which are weakly bound. These transitions have small energies and long lifetimes, which make such structures optimal for laser operation.

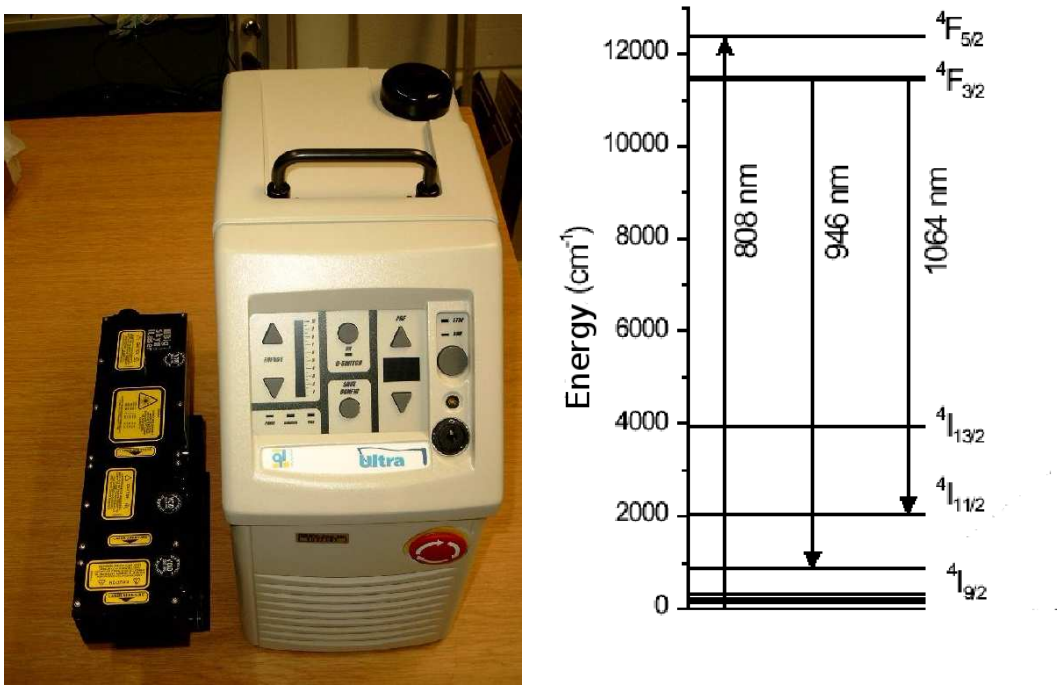

(a) The laser head and power supply of a UV CFR NdYag laser

(b) Energy levels of the NdYag crystal [77]

Figure 5.1: *The UV laser system with laser head and power supply*

The housing lattice is Yttrium Aluminum Garnet (YAG) $Y_3Al_5O_{12}$. It can be produced to a very good optical quality (Czochralski-grown) and a good heat conductivity. It is optically isotropic and has a strong Stark-effect.

The Nd-YAG laser is a four-level laser. Compared to a three-level laser, where the laser transition always ends on the ground state, the four-level laser has an additional state between the upper laser state and the ground state. In the case of the three-level laser, only by pumping more than half of the electrons into the upper laser level, one can obtain an inversion population. This requires a high pumping power for the three-level due to reabsorption caused by a stimulated emission. This process can be avoided with an additional laser state, which is given in case of a four-level laser, where the ground state and the lower laser level are separated.

The repetition rate and laser power of the laser can be steered electronically. The cooling keeps the Nd-YAG crystal in thermal equilibrium to prevent especially the ground state from thermal noise produced by power of the flash-lamp. A sketch of the laser optics placed in the laser head is

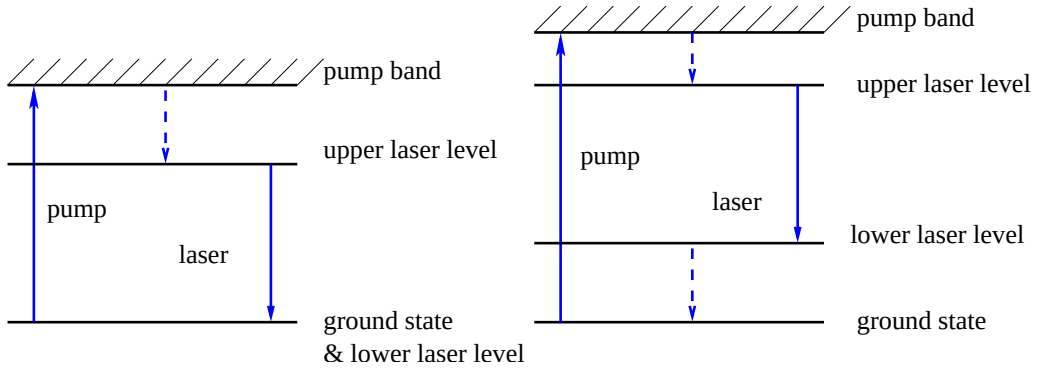

Figure 5.2: *Left side: a three-level system, where the laser transition ends on the ground state. Right side: a four-level system, where the laser transition ends on a level above the ground state, which is quickly de populated e.g. via phonons*

shown in Figure 5.3.

First a Nd-YAG laser rod is pumped by a gas flash-lamp. The flash-lamp excites the neodymium ion in the $F^4_{5/2}$ pump band, this decays into the $F^4_{3/2}$ state, which is metastable (see energy levels of Figure 5.1(b)). This state has a radiative lifetime of about 250 μs. Due to this long lifetime the population inversion can be achieved. From transition of level $F^4_{3/2}$ to $I^4_{11/2}$ a wavelength of 1064 nm is emitted. This is the main transition, which is afterwards used to produce the ultra violet wavelength of 266 nm. With the Nd-YAG crystal there is also a transition from level $F^4_{3/2}$ to $I^4_{9/2}$ possible. This transition is the reason for small contributions of additional wavelength to the laser output. The photons are extracted from the rod in the laser resonator through judicious control of the spontaneous emission (hold-off) and stimulated emission, which is achieved by a quality switch (Q-switch). The Q-switch is a important part of the laser for two reasons. Without the Q-switch the pulse length of the laser would be in the range of the combustion duration of the flash-lamp, which is about 100 μs and far away from the 5 ns pulse length, which should be achieved for the output pulse. This pulse length is important for the operation of a TPC to ensure a good resolution in the z-direction. To compress the laser pulse length in time to a few ns the Q-switch is needed. The Q-switch consists of a polarization device and an electro-optical switch, a Pockel cell. With a specific voltage the transmission is kept at a low loss. During the combustion duration the polarization plane is rotated such, that it inhibits the resonator. This prevents the laser from stimulated emission

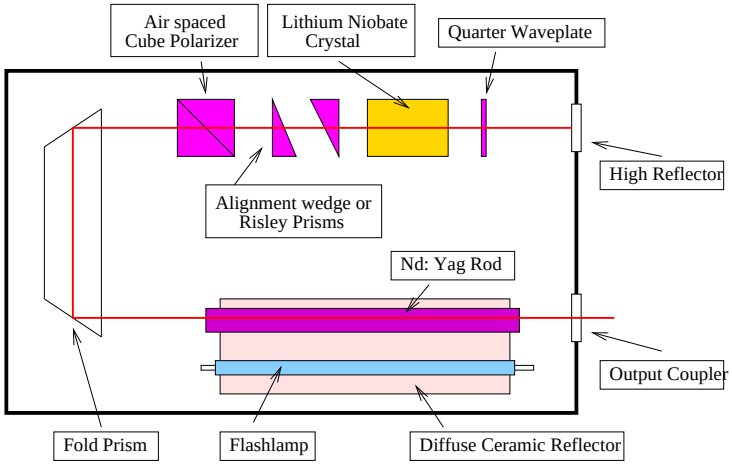

(a)

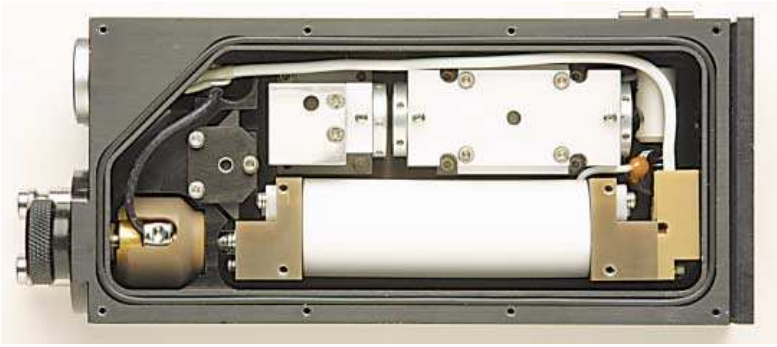

(b)

Figure 5.3: *Sketch and picture of the optics placed in the laser head*

before reaching its maximal population. With a fast high voltage pulse the transmission is changed from low to high energy loss, which releases a high energy pulse.
To produce laser light of Ultra Violet wavelength, two non linear crystals are placed in the optical path. Both consists of Potassium Titanyl Phosphate (KTP). These crystals generate higher harmonics. The wavelength is therefore converted first to 532 nm and afterwards to 266 nm. Of course the higher modes have a lower intensity. To reach a significant intensity for the laser output the incoming intensity has to be high. The correlation of the intensity curves is given by:

$$I_{2\omega} = 2KI_{\omega}^2, \tag{5.1}$$

with K the coupling constant of the frequency conversion. The factor 2 is

parameter	values
wavelength λ	266 nm
Energy of the single photon	4.66 eV
Max. Repetition Rate of the Laser	20 Hz
Max Energy of the Laser Pulse	3 mJ
Pulse length	< 6 ns
Diameter of the Laser Pulse y_0	1.5 mm
Divergence	< 1 mrad

Table 5.1: *The key parameters of the UV-laser. Some of the parameters as the repetition rate and laser power of the laser can be steered electronically.*

given by the fact, that the intensity $I_{2\omega}$ of the first harmonic is produced after passing back and forth inside the non linear crystal in the resonator. Equation 5.1 has two important effects. The first effect is, that the crystal has to withstand high incoming intensities to produce an acceptable intensity output. The second effect is, that small intensity fluctuations of the original laser wavelength can suffer huge fluctuations of the higher harmonic wavelength, as the intensity fluctuation propagates quadratically. A detailed sketch of the optical path of the photons starting from the Nd-YAG rod to the non linear Lithium Niobate crystals is shown in Figure 5.3.

In Table 5.1 the key parameter of the laser are given. These parameters have to be taken into account, and must be modified appropriately to make a track produced by a laser as comparable to a MIP as possible.

5.2 The Optical Setup

The optical setup has been chosen so that the laser beam fulfills the following criteria.

- The energy density has to be strongly diminished to achieve an ionization comparable to a MIP.
- The width of the laser spot should be negligibly small compared to the total width of the charge cloud after diffusion.

- The setup should provide the possibility to produce two tracks.

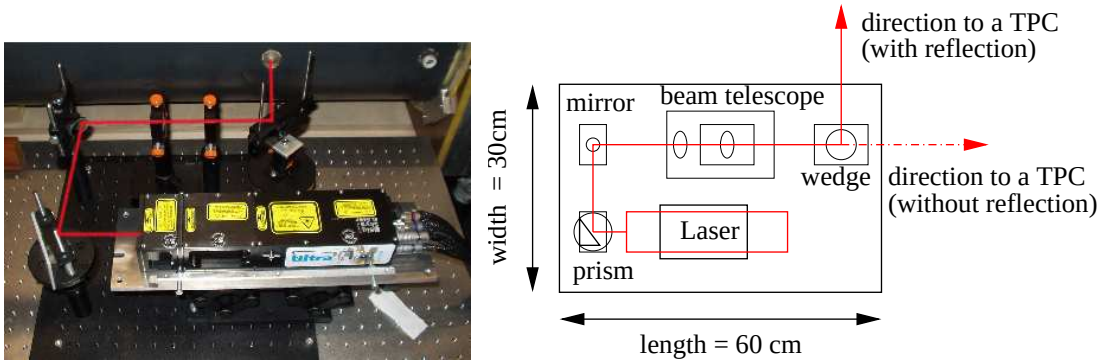

(a) (b)

Figure 5.4: *The Optical setup is mounted on a plate which is finally screwed on an optical table. The laser intensity is first attenuated by reflection at a prism. A mirror, whose position can be tuned, sends the laser beam to the Galilean telescope. Finally the laser can either be reflected by a second prism or send directly to the TPC. In (a) the picture and in (b) a sketch of the optical setup is shown.*

These criteria can be fulfilled by the laser setup shown in Figure 5.4. First a prism diminishes the laser beam intensity by one order of magnitude. Then a Galilean telescope focuses the laser waist, so that it is minimal at the sensitive volume. To produce a small angle between the two tracks a wedge prism is used. All optical components are mounted on a separate laser plate, which is afterwards screwed on an optical table. If the TPC is directly accesible as it was in our case in the laboratory, the wedge can be mounted on the plate. For the measurements in the magnet facility, where the beam has to be delivered over a longer distance, the wedge had to be placed inside the TPC. Both the Galilean telescope and the the wedge prism will be explained in detail in the following subsections. Also the different TPC installations for the calibration measurements in the laboratory and the track separation at the magnet facility are explained in detail in the following sections. For both measurements with the different TPC installations the general conception of the optical setup could be used. It was easily interchangeable between the laboratory and the magnet facility.

5.2.1 The Galilean telescope

A Galilean telescope [78] is used in our setup to reduce the width of the laser beam spot y_0 1.5 mm. The telescope is a combination of a convex and a

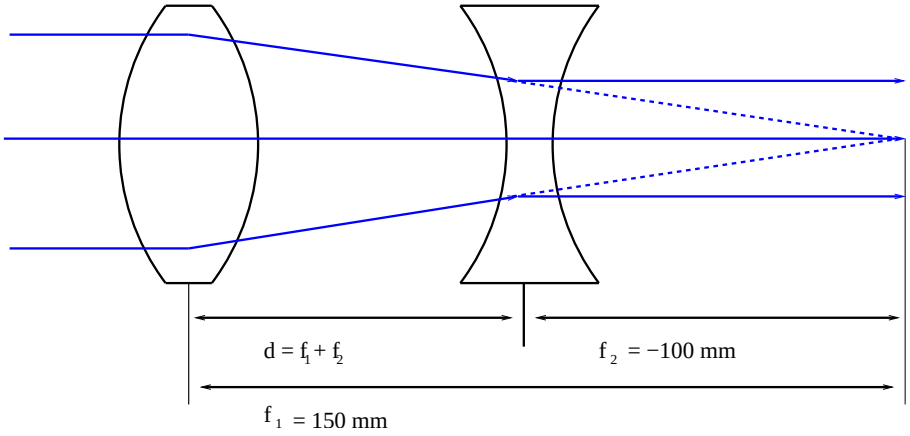

Figure 5.5: *Principle of a Galilean telescope. The second lens must have a distance of* $d = f_1 + f_2$ *to achieve an nearly parallel optical path.*

concave lens, with the convex lens having a positive focus point f_1 and the concave lens having a negative focus point f_2. The distance between the two lenses for the approximation of geometric optics is given by

$$d = f_1 + f_2. \tag{5.2}$$

This assumption is true if the subject, which is in our case the general laser beam diameter, is near to infinity. Figure 5.5 shows the principle of a beam telescope 5.5. Even a laser has not completely parallel beams, but a small divergence. This divergence can be understood as a lens with a big negative focus length and has to be taken into account to calculate the distance between the lenses correctly. Therefore the distance d between the two lenses increases. In practice one adjusts the two lenses roughly to each other and does the fine tuning with an adjustable stage, where the rod of the laser lens is mounted on.

The focus length of a combined system is given by:

$$\frac{1}{f} = \frac{1}{f_1} + \frac{1}{f_2}. \tag{5.3}$$

The magnification or demagnification of such a system is given by

$$M = -\frac{f_1}{f_2}. \tag{5.4}$$

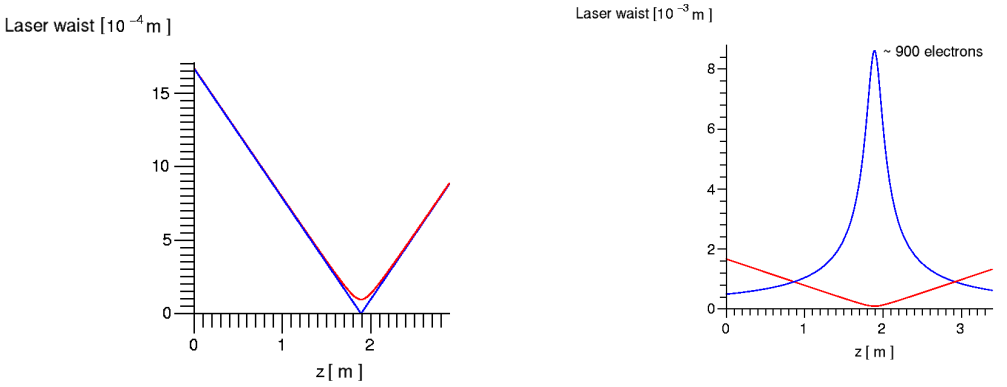

(a) (b)

Figure 5.6: *Laser waist for the beam-telescope with the settings f_1 = -100 mm, f_2 = 200 m and d = 125 mm. (a) Laser waist calculated for geometrical optic (blue) and Gaussian beam propagetion (red). (b) Laser waist (red) and the corresponding primary electrons (blue).*

The transformation of the beam by simple optical devices such as lenses and the space between them can be calculated easily with simple matrix multiplication. The matrices have a 2×2 structure:

The matrix defining free space is given by:

$$M_{fs} = \begin{pmatrix} 1 & d \\ 0 & 1 \end{pmatrix}. \tag{5.5}$$

The matrix defining a lens is given by:

$$M_{lens} = \begin{pmatrix} 1 & 0 \\ -\frac{1}{f_i} & 1 \end{pmatrix}. \tag{5.6}$$

With a matrix multiplication of every single optical device the matrix of the complete optical setup can be derived:

$$M_{tot} = M_n \cdot M_{n-1} ... M_2 \cdot M_1 \tag{5.7}$$

Here M_1 denotes the first and M_N the last optical device. The Matrix of the total optical system has to be multiplied with the beam spot vector:

$$M_{lw} = \begin{pmatrix} y_0 \\ \theta_{Laser} \end{pmatrix} \tag{5.8}$$

parameter	telescope 1	telescope 2	telescope 3
distance between Laser and 1st Lens [cm]	35	35	35
focus length 1st Lens f_1 [mm]	-100	-100	-100
focus length 2nd Lens f_2 [mm]	150	200	300
telescope focus measured [cm]	100	140	180
telescope focus calculated [cm]	150	190	290
d_2 distance between 1st Lens and 2nd Lens [mm]	68	125	235
Minimal waist $w_0[\mu m]$	102.3	96.1	101.3
Rayleigh Length z_R [mm]	2· 125	2· 110	2·121
Primary Ionization n_e [e-/cm]	760	861	775

Table 5.2: *Parameters of different beam telescopes used for the different laser setups.*

Here y denotes the width of the laser beam and θ its divergence. With

$$\vec{w} = M_{tot} \cdot M_{lw} \tag{5.9}$$

one gets the final vector of the optical system. The first element (1,1) of the vector provides the equation to determine the focal length of the system. With the element (1,2) of the vector the divergence θ_{tot} given by equation 2.38 can be derived. Figure 5.6 shows the waist of the laser beam depending on z after the last optical element. In Figure 5.6, the geometrical and the Gaussian beam propagation is plotted.

For different laser setups different telescopes have been used (see Table 5.2). The telescope 1 has been used for the drift velocity measurments of the TPC. In this case, also, a large TPC was used with the possibility of direct acces. Therefore the focus of the telescope could be shorter than in the setup used during the measurements at the magnet facility. The switch from telescope 2 to 3 becomes necessary to prevent the laser at the magnet facility from the influence of the strong magnetic stray field outside the cryostat. All setups have been optimized such, that a minimal laser waist of about 100 μm and a corresponding Rayleigh z_R (see Equation 2.37) with a length of about 2 times 12 cm are achieved.

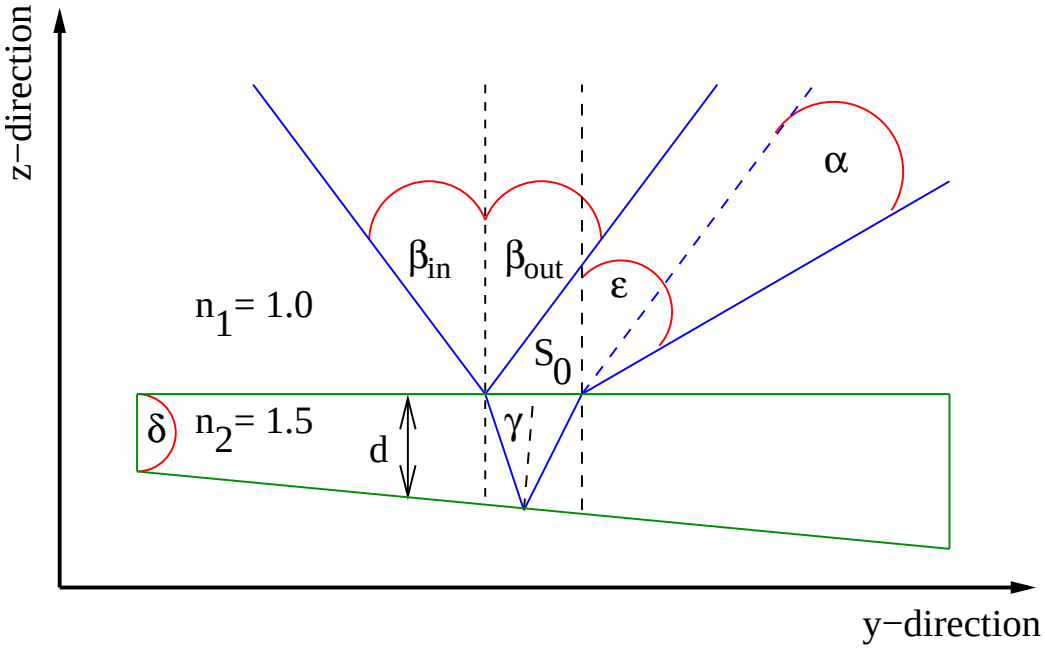

Figure 5.7: *The figure shows the optical path of an incoming laser beam in the wedge prism*

5.2.2 The wedge prism

In Figure 5.7 the principle to produce two tracks with a small angle wedge prism is shown. The main motivation for the usage of a wedge prism was to produce two tracks with a fixed angle between the tracks. Such a simple optical device allows it to compare the reconstructed angle with the expected. Due to the fixed angle it is also possible to calculate the expected distance and compare it to the measured distance between the two tracks in every pad row. The main advantage of such a system is to know the position of the two tracks and to avoid external calibration measurments. The relation of the angle between the tracks α and the prism angle δ will be explained in the following. An incident laser beam is hitting the quartz wedge prism and is treated by Snellius Law:

$$n_1 \sin(\beta) = n_2 \sin(\gamma^{|}) \Rightarrow \gamma^{|} = \arcsin(\frac{n_1}{n_2} \sin(\beta)). \tag{5.10}$$

Due to the small inclination of the wedge angle δ the reflection at the bottom side of the wedge is $\gamma = \gamma^{|} + \delta$. The wedge angle δ has to be taken into account twice. Once for the incoming and the reflected beam. The outgoing beam is therefore given by:

$$\epsilon = \arcsin^{-1}(\frac{n_2}{n_1}\sin(\gamma^{|} + 2\delta)) \tag{5.11}$$

The angle α between the two tracks is the difference between direct reflection β and ϵ

$$\alpha = \epsilon - \beta. \tag{5.12}$$

The orientation of the wedge prism plays an important role for the shift s_0. If the orientation of the wedge is as in Figure 5.7, the two beams have the same x-position. The distance between the two tracks in the z-direction increases with y. An offset s_0 is given by

$$s_0 = 2 \cdot d \cdot \tan(\gamma), \tag{5.13}$$

with d the thickness of the prism, which is 1.5 mm. This offset in the y-axis leads to an unavoidable displacement in the z-direction given by

$$z_0(\gamma) = \frac{s_0}{tan(90^o - \beta)}. \tag{5.14}$$

The displacement in z-direction has to be added to the distance of the two laser beams and leads to a distance between the two tracks of

$$\Delta_z = z_0(\gamma) + 2 \cdot \tan(\frac{\alpha}{2}) \cdot L. \tag{5.15}$$

If the wedge is rotated by 90 ° (see Figure 5.8), the offset s_0 is still not zero, but it does not lead to a displacement in the x-, but z-direction. This means the two tracks are not parallel in the z direction, but this orientation has the advantage, that the distance between the two tracks is linearly dependent on the angle α. The distance Δ_x is given by

$$\Delta_x = 2 \cdot \tan(\frac{\alpha}{2}) \cdot L. \tag{5.16}$$

In Figure 5.8 both orientations of the wedge prism are shown.

Another important feature of a wedge prism is the intensities correlation of both to each other. The refraction of the prism is R = 0.1, the transmission T = 0.9. The first beam has therefore 10 % of the incoming beam intensity. The second beam is transmitted before being reflected and is then transmitted again, so that it gets a contribution $T^2 = (0.9)^2$, which means it has 8.1 % the intensity of the incident beam. As described in eq. 2.28 the laser energy is related quadratically to the production of primary electrons. This means that a relation of I_1 to I_2 of 81 % means a relation of 64 % in the production of primary charge. This has to be taken into account by studying the charge distribution of the measured laser tracks and has also be included in the simulation tool (see section 6.5).

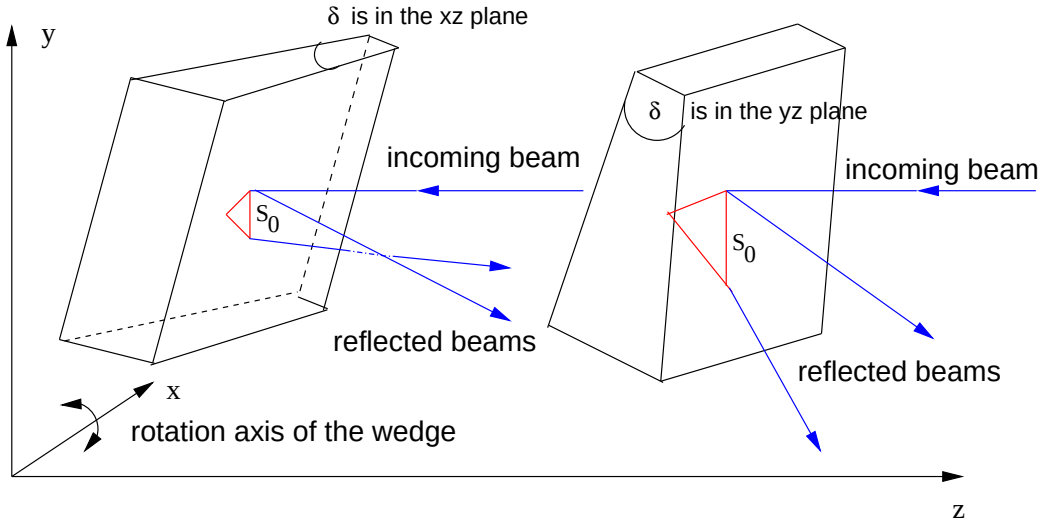

Figure 5.8: *The figure shows two possible orientation of the wedge prism. Both orientations of the wedge are rotated in the x-direction.*

5.2.3 Laser Power Calibration of the setup

As mentioned in section 5.1 the laser power can be steered. The energy is divided in power settings, which have a range from 0 to 20. To know the operation energy of a single laser pulse at a specific power setting, these power settings had been measured for several repetition rates. For the calibration measurement a photodiode and a corresponding readout device [79] for the photodiode had been borrowed from the Institute for Laser Physics of the University of Hamburg. In a simple setup the beam spot was enlarged with a lens, to prevent the photodiode from permanent damage. For high laser repetition rates the time to average the laser pulses is set to 1 minute. For low repetition rates of 1 and 2 Hz the average time is increased to five minutes. After this exposure time the system could be considered as stable from fluctuation of the laser itself.

In Figure 5.9 the laser energy is plotted versus different power settings. Below a power setting of 14 the laser intensity becomes unstable in energy. The laser was therefore never reduced below this setting. It is visible, that the maximal laser energy was reached only at the highest repetition rate of 20 Hz. In case of a repetition rate of 1 to 2 Hz the maximal laser energy was 1 mJ. The reduced energy output has been attributed to the stability of flash light, which seems to work only properly for high repetition rates. In our case, due to the slow readout speed of the data acquisition system and the fact that most of the laser energy has to be reduced to be comparable

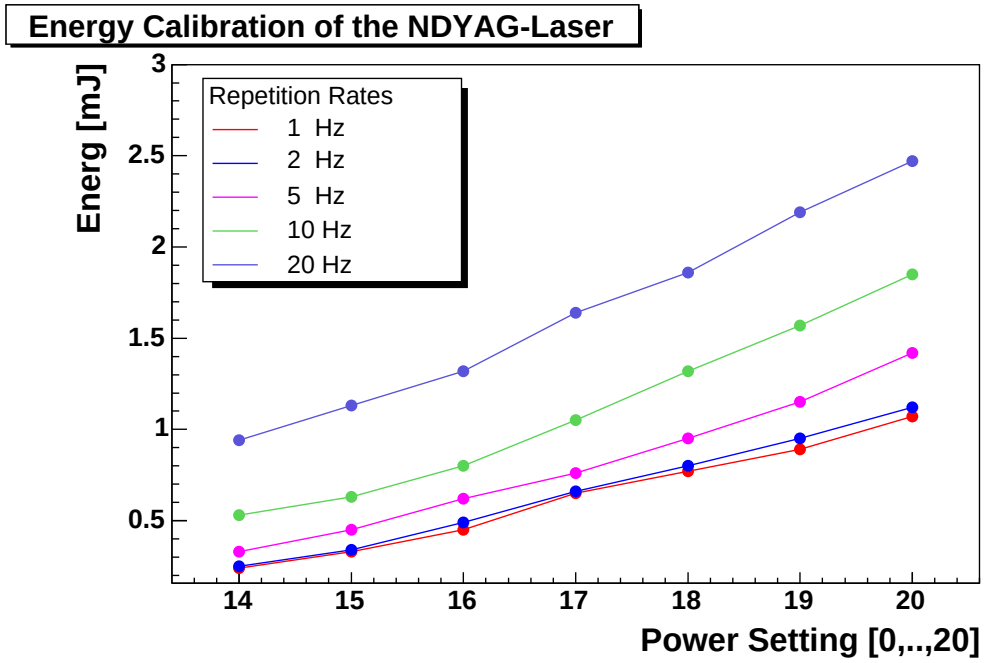

Figure 5.9: *The energy per pulse is plotted versus the power settings for different laser repetition rates. It shows, that at higher repetition rates the laser energy of a single shot is increased. The laser energy is about 2.5 mJ for a power setting of 20 and a repetition rate of 20 Hz. For a repetition rate of 1 or 2 Hz and the same power setting the laser energy is reduced by a factor of 2.5 to about 1 mJ.*

to a Minimal Ionizing Particle, the laser was mainly operated at repetition rates of 1 or 2 Hz with a power setting of 20.

5.2.4 Alignment of the Medi-TPC Cathode and Anode

A difference between a setup, which is used for measurements of cosmic particles and a setup, which is used for the measurement of laser tracks is the orientation of the cathode towards the anode. For the cosmic setup an alignment in the xy-direction of the cathode to the anode is not important. For the laser setup, which will be described in more detail in section 5.4.2 an alignment in xy-direction is necessary. The laser beam has to enter the TPC at a window of the cathode, passes along the field cage until it is reflected at the anode by a wedge prism. The whole system is described in Section

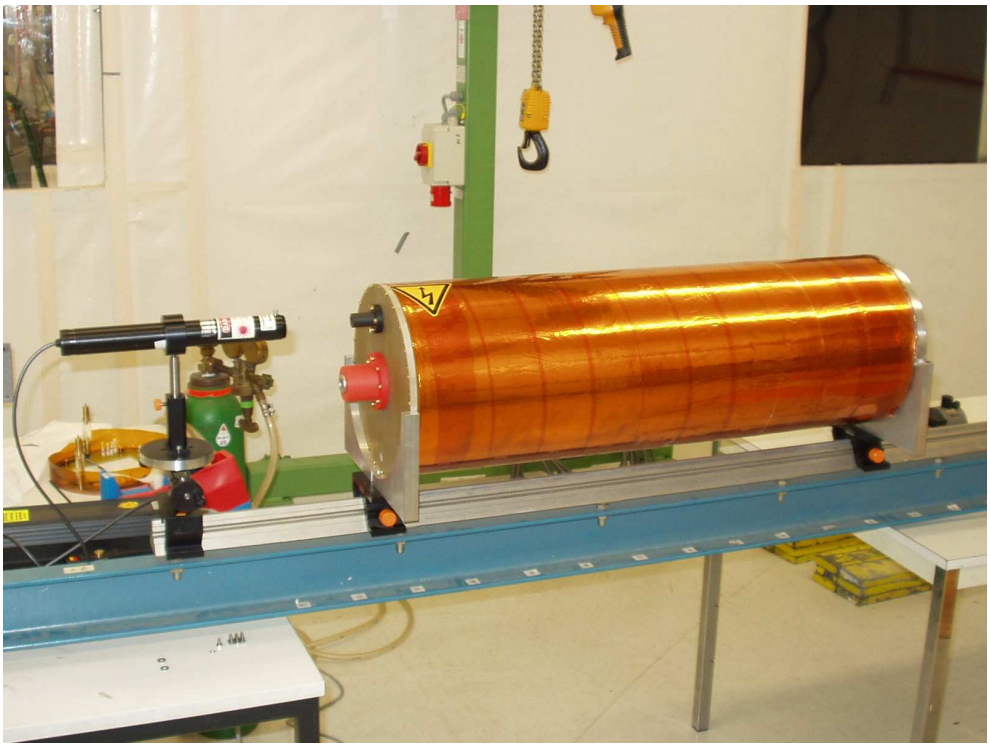

(a) The picture shows the assembled setup placed on a rail system. With a laser the alignment between the laser entry at the cathode and the wedge holder at the anode is tested.

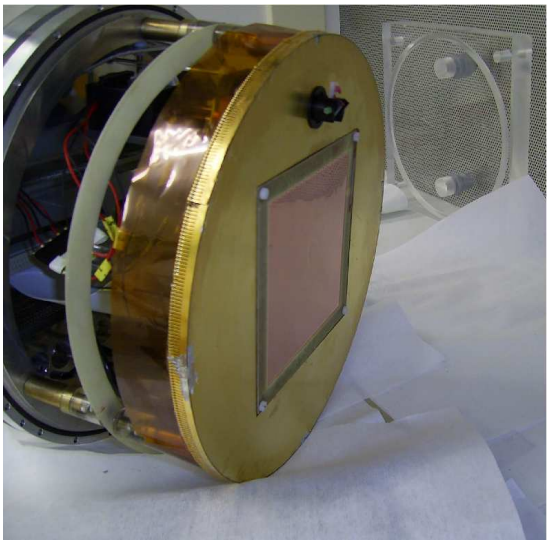

(b) Anode with the Prism Positioning System

(c) Cathode with the quartz window

Figure 5.10: *The picture show the alignment setup. The anode was arranged towards the cathode, that the mismatch between both was adjusted. As the laser setup was the second setup built in the Medi TPC, this new alignment was necessary as the positions of the holes for the screws were already fixed.*

5.3. This means the laser has to be aligned to the axis of the TPC. Every shift or tilt of laser entry and reflection position of the wedge makes it more difficult to get a reflection. As the TPC will be operated later in a magnet facility, which is not easily accesible, the alignment can only be reached with a limited precision. To have a good alignment between cathode and anode, both were connect to the field cage. A laser was placed on a rail system and aligned with an aperture torwards the rail. Then the TPC was placed on the rail. This guarantees, that both systems are parallel to each other. Figure 5.10 shows this setup to align cathode with anode. The position of the anode was determined by the inner threads for the screws, which were already fixed. With an additional flange the position of the anode could be rearranged. The flange consists of two parts, which can be tilted. The additional flange was preliminary fixed with clamps. With the alignment laser and a reticule, which was made from millimeter paper the positions of cathode and anode were tested. After reaching an acceptable agreement the two parts of the flange were glued together. The accuracy of this method was estimated to be within ± 1 mm.

5.3 Prism Positioning System (PPS)

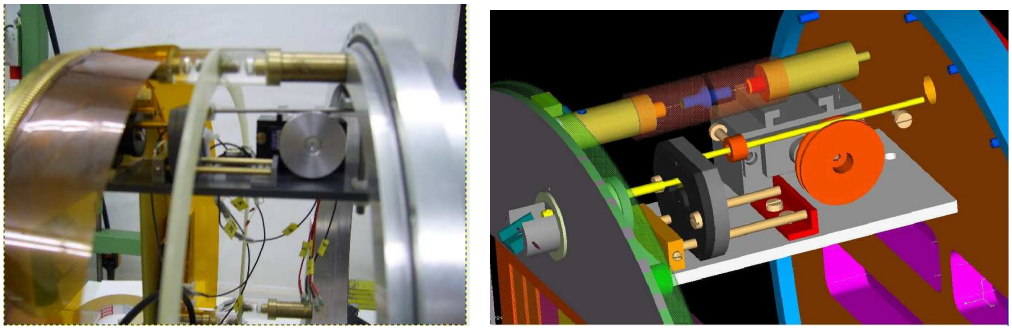

(a) The prism positioning system (PPS) (b) CAD drawing of the prism positioning system (PPS) provided by Karin Tröger

Figure 5.11: *The prism positioning system (PPS), which has been built and implemented at the anode plate of the Medi TPC.*

In Figure 5.11 the Prism Positioning System is shown as it is implemented at the anode plate of the Medi TPC. It consists of a PVC plate where a servo holder is attached. In this holder a standard servo is placed. The servo moves a rod, which is connected to a slider. If the rod is moved also the

slider is moved. The slider is mounted on the basic PVC plate by two sticks, which acts like a rail and forces the slider to move in a linear direction. The slider also moves a rod, which penetrates a PVC tower. The PVC tower is attached at a specific position of the anode shield, which is chosen such, that a distortion of the electric field homogeneity is avoided (see section 5.3.1). The tower holds a shell, in which a small wedge prism with a size of 8×8 mm^2 is placed.

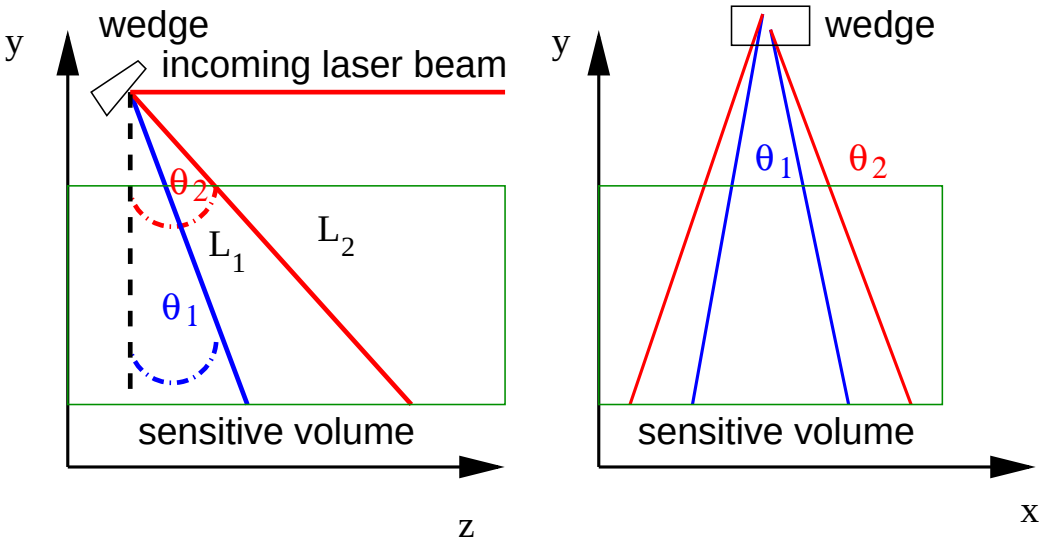

Figure 5.12: *The picture shows two different adjustments of the prism, that leads to different θ-angles in the TPC. Different θ-angles lead due to the relation* $\Delta x_i = \alpha \cdot L_{yi} \tan(\theta)$ *to different distances between the two tracks*

By moving the rod back and forth and changing the θ angle in the yz coordinate system of the TPC is changed. This leads to different lengthes and, therefore to different distances Δx due to the θ angle, which is shown in Figure 5.12. Δx is given by

$$\Delta x \approx \alpha \cdot L_y \cdot \tan(\theta). \tag{5.17}$$

5.3.1 Influence of the PPS on the electric field homogeneity

An important question to the setup is, whether it has an influence on the homogeneity of the electric field in the sensitive volume. Therefore a field cage simulation was made using the program CST STUDIO [80], which

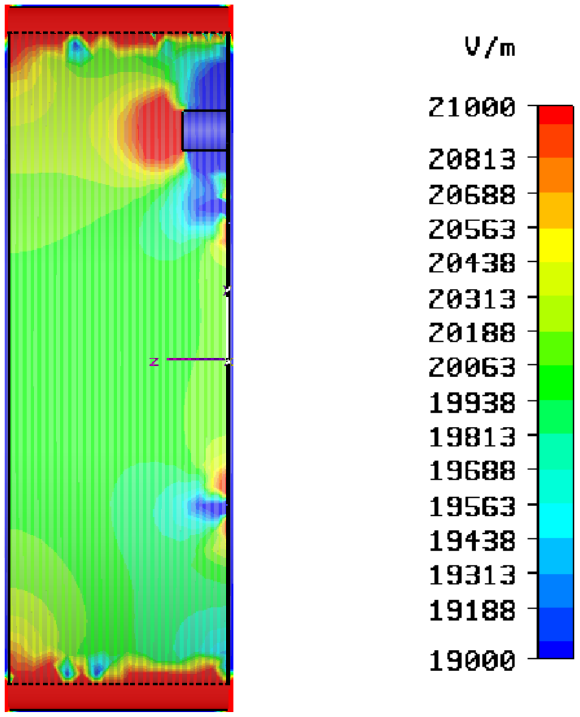

(a) Electric field deviations in the yz-plane of at x=0 of the system

(b) Color spectrum of maximal ±5 % field deviations.

Figure 5.13: *The influence to the PPS and the GEM frame in the yz-plane due to electric field inhomogeneities calculated with CST [80]*

performs a simple static electric field calculation based on a finite elements calculation. In Figure 5.13 the electric field deviations in the yz-plane are shown for the first 7.5 cm of the drift length in the TPC. It shows the influence of a 1.75 cm long object, which is placed 10.75 cm away from the center of the TPC and has a diameter of 1.5 cm. An object of this size was used as an approximation for the prism positioning system, which consists mainly on PVC material. Also the frame of the GEM has been simulated. The GEM of size 10×10 cm^2, is mounted in a 1 cm broad frame, which consists of G10 material. Both objects with the respective material have to be assigned with the appropriate dielectric constant to model the interaction with theelectric field. The color scale shows the size of the deviation, which ranges from 210 V/cm to 190 V/cm and represent a ± 5 % deviation to the

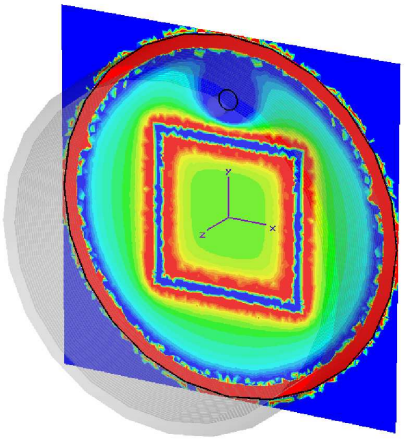

(a) distance to the shield 1 mm

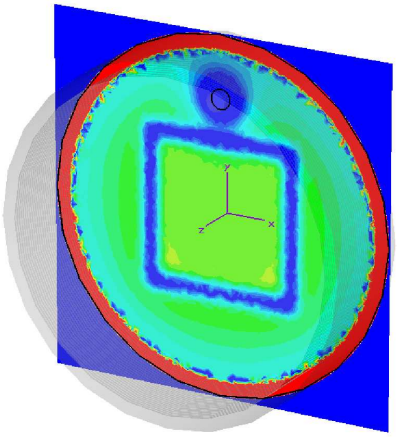

(b) distance to the shield 10 mm

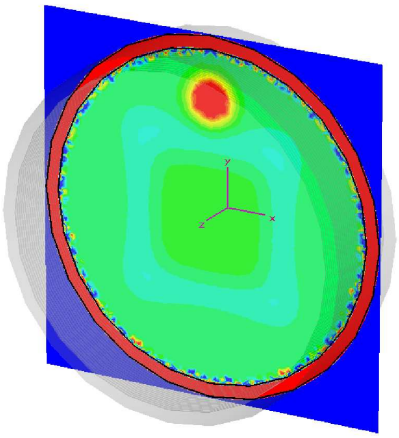

(c) distance to the shield 25 mm

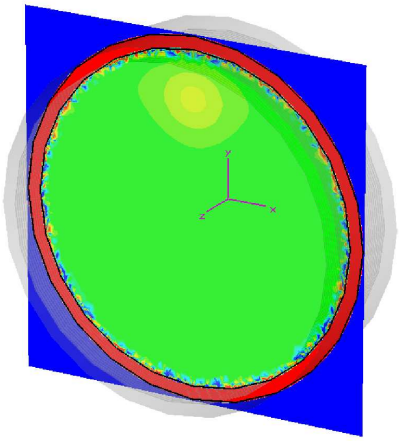

(d) distance to the shield 50 mm

Figure 5.14: *Electric field deviations in the xy-plane of the TPC at different projection stages. It is clearly visible, that the influence of the electric field deviations coming from the PPS is not affecting the region inside the region covered by the GEMs*

expected field of 200 V/cm. The deviations of the electric field are mainly located around the area of the prism holder and the GEM-frame. Here the maximal deviation of ± 5 % occurs. As the drift velocity is linearly dependent on the electric field the drift velocity deviation in this area are 5 %. The sensitive volume is defined by the size of the pad plane, which has a size of 5×5 cm^2 and is located in the center of the TPC. Here the influence of the electric field deviation of the prism holder is completely negligible. The influence of the electric field deviation of the GEM frame is in the order of 0.5 % for the first cm of the drift length.

In Figure 5.14 the electric field strength in the xy-plane of the TPC is shown at different z-positions. It starts with a distance of 1 mm between the shield and the projection plane and is then followed by distances of 10, 25 and 50 mm. At a distance of 1 mm the electric field deviations are maximal around the prism holder and the GEM-frame. Only in the inner 6×6 cm^2 the level of field deviations is about 0.5 %. At a distance of 10 mm to the shield the electric field deviations are - 5 % exactly around the position of the GEM frame. The electric field deviations at the position of the pad plane is about0.5 %. At a distance of 25 mm the electric field deviations decrease further and vanishes completely at a distance of 50 mm from the front of the shield. The prism holder has no significant influence to the homogeneity of the electric field in the sensitive volume and begins to vanish at a position of 50 mm before the shield.

5.4 Laser setups

Here the two different TPC installations with the different laser setups are described. The main difference between the TPC installations was the accessibility to the TPC, which required as a consequence also some modifications for the laser setup.

5.4.1 Laser setup for drift velocity measurement

In Figure 5.15 the laser setup for the drift velocity measurement is described. The studies have been done with the Large TPC prototype, which has three quartz windows placed at three different positions. An easy access of laser beams into the TPC was possible.
The laser beam is first reflected at a prism, that dimishes the laser intensity to 10 %. Then the laser passes the Galilean telescope. The parameters of this telescope are given in Table 5.2 for telescope 1. The laser hits the first

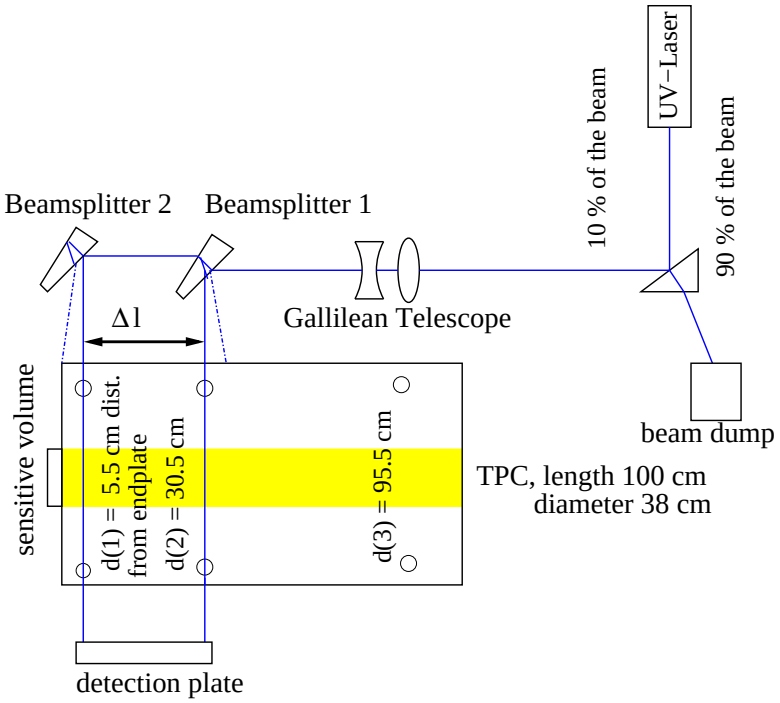

Figure 5.15: *Sketch of the Laser setup used for the measurement of the drift velocity*

wedge and is reflected in the laser window 2, which had a distance of 30.5 cm to the endplate. The transmitted beam hits another wedge, that reflects the beam into the laser window nearest to the endplate. The distance between the quartz window and the endplate is 5.5 cm. To guarantee the position stability of the laser beam in the TPC, the beam has to be aligned such that he leaves the TPC at the opposite site by a second quartz window, which is located at the same position. The outgoing laser beam could be easily detected with a sheet of paper. The two laser beams are attenuated in such a way, that both beams had the same intensity. As explained in Section 5.2.2 the intensity of the first and the second beam is correlated for the production of two beams using a wedge prism. The laser setup for the drift velocity measurements had a direct and easy handable access, so that it was possible to provide laser tracks with the same intensity for both tracks. With the known reflection and transmission coefficient of the wedge the intensity for both tracks is given by

$$I_i = (0.9)^2 \cdot 0.1 \cdot I_0. \tag{5.18}$$

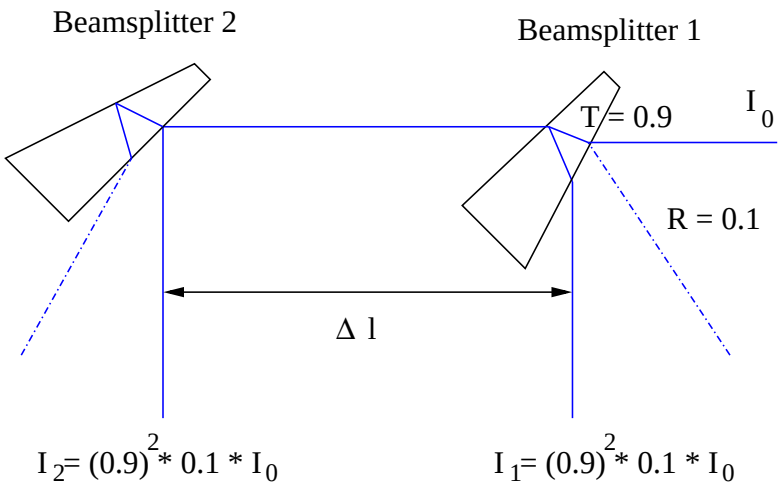

Figure 5.16: *Sketch of the two Beam splitters. In this application the two laser beams could have easily the same intensity. With the given Transmission and Reflection coefficient one can simply use the lower intense beam of Beam splitter 1 and the higher intense beam of Beam splitter 2*

In Figure 5.16 the optical path for the laser through the two wedge prisms is shown.

In general very similiar laser setup could be used to measure the separation in z-direction. It would be only necessary to get bouth laser beam reflections of a single wedge into the TPC. A high magnetic field would not be required for such a measurement, because the longitudinal diffusion is not depending on the magnetic field. However a appropriate elctronic was not available during the time of this PhD work. The two hit and two track resolution is strongly depending on the used electronic, which was in our case the ALEPH electronic, which was designed for a wire amplification system. So the rise time, decay and sampling time of the electronic was not appropriate for this measurement. So it would be only possible to confirm the results of ALEPH. A first investigation of a TDC electronic is given in [63], where basic elements of the proposed laser system was used to investigate the z resolution.

5.4.2 Laser setup for track separation studies in x

In Figure 5.17(a) a view inside a laser box and the bore of the magnet facility is shown. The laser box is an important tool to fulfill the safety

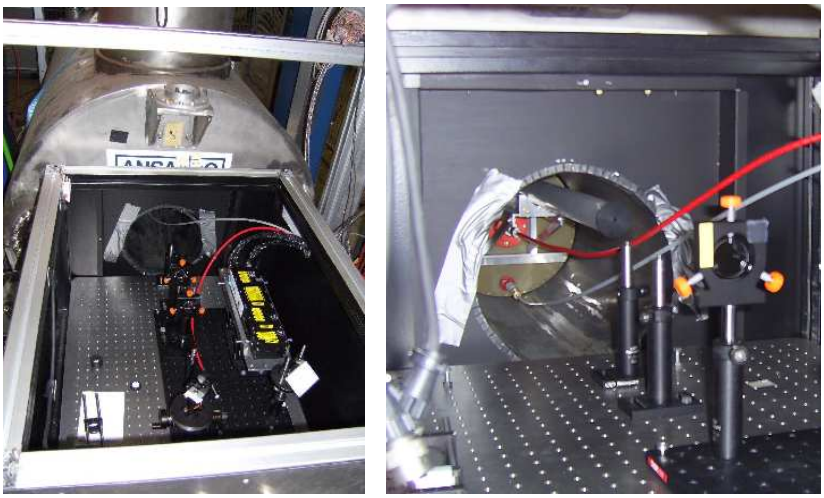

(a) View inside the Laser Box and the magnet bore

(b) View on the alignment system connected at the TPC

Figure 5.17: *Pictures of the setup and the placement of the TPC in the magnet facility*

requirements at the magnet facility. As a single laser shot is capable of permanently damaging the retina of the eye, it was necessary to operate the laser only within the laser box, which shielded the laser from the surrounding area.

Inside the laser box an optical table of size 60×90 cm^2 is placed. The optical table has to be adjusted such, that the heigth is appropriate for the quartz window at the cathode of the TPC. The optical setup has the same elements as the setup for the drift velocity measurements. Some of the elements have to be replaced, such as the beam telescope which has to operate this time over a range of about 1.4 to 1.8 m. Two beam telescopes where used. The parameters for telescope 2 and 3 are given in table 5.2. In Figure 5.18(b) a sketch of the laser box and the TPC placed in the magnet facility is shown. The difficulties of this setup is to align the laser beam from the last optical device with the wedge prism, which is located on the anode side of the TPC. The range between the last optical component and the wedge prism is about 1.0 m for beam telescope 2 respectively 1.6 m for beam telescope 3. The reason for the replacement of the first used beam telescope was to move the laser further away from the stray field of the magnet to protect the laser from its influence. Figure 5.17(b) shows a picture of the TPC placement in the magnet facility and the alignment system, which aligns the optical system placed in the laser box with the TPC. The alignment of the system is done

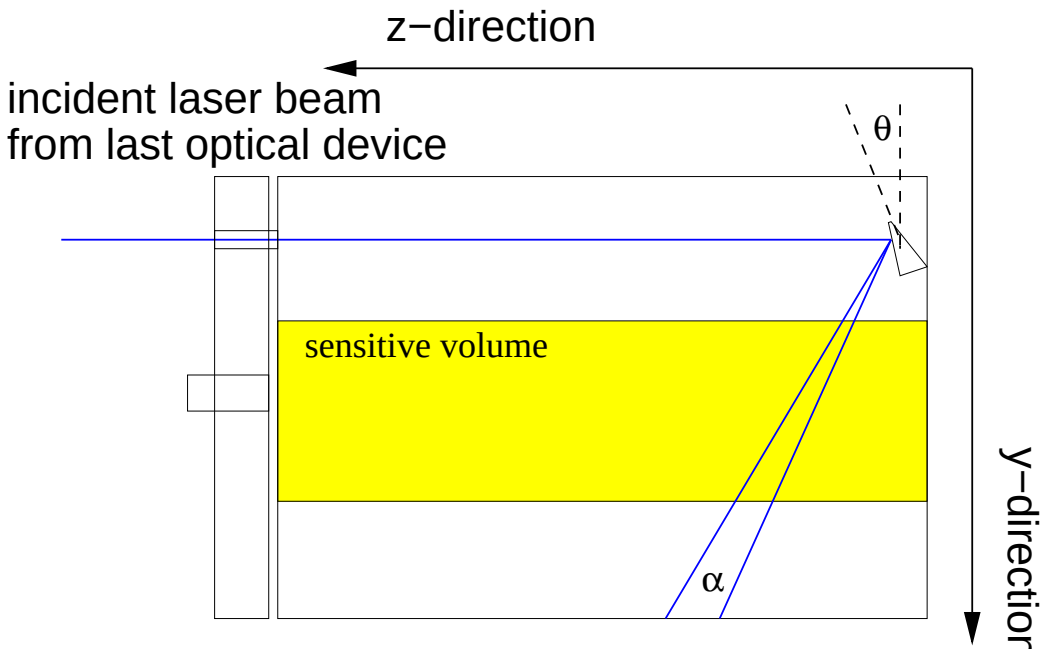

(a) Two-track production inside the TPC

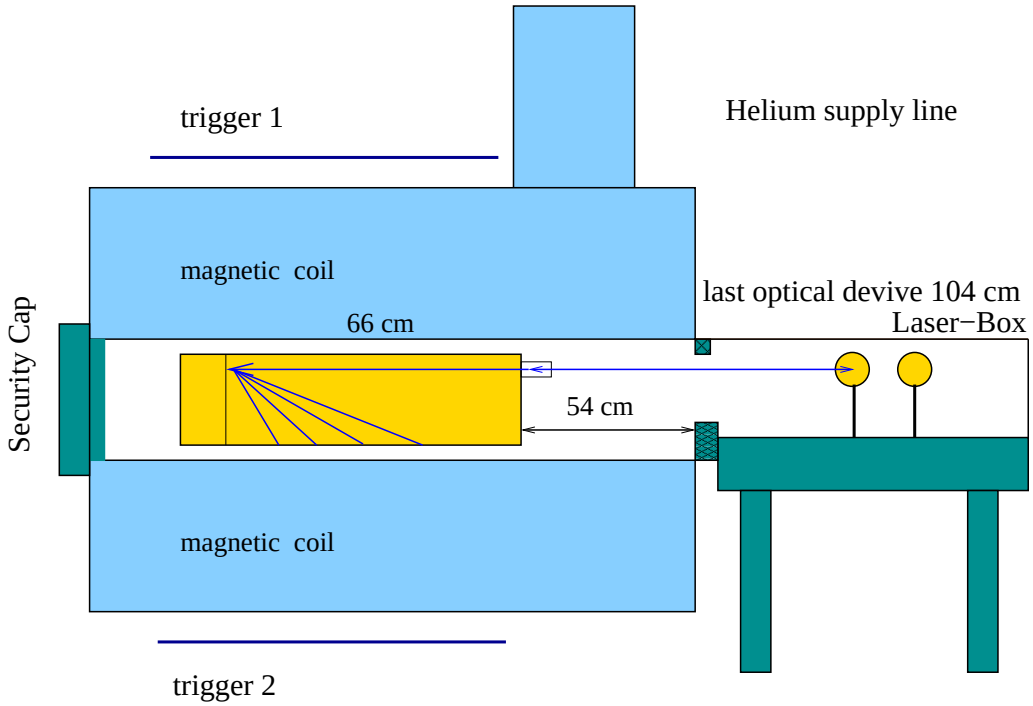

(b) Sketch of the optical setup at the Magnet Facility

Figure 5.18: *Sketch of the setup and the placement of the TPC in the magnet facility*

using two aperture. The two aperture are inside an aluminum tube, which is mounted on a supporting holding stage. Behind the last aperture a mirror reflects the beam outside, where it can be detected. After the alignment the device has to be carefully disconnected without changing the position of the TPC and the fine adjustment is then finally done by moving the laser beam with a micrometer positioning stage. If the laser is finally aligned with the TPC placed in the magnet. The wedge prism reflects the two tracks back in the sensitive volume with the production mechanism described in section 5.2.2 (see Figure 5.18(a)). The movement of the PPS leads to different θ_i angles, which corresponds to different Δx_i of the two tracks as described in the previous sections.

Chapter 6

Software for Reconstruction and Simulation

In this chapter the reconstruction software Multifit is described. As the name of the software package implies, Multifit does to not only reconstruct single, but also multi tracks events, which are investigated in the course of the TPC R&D activities. The methods to derive important track parameters like the single point resolution for multi track events will be described here. New methods are presented, which have been explicitly developed for the case of nearby tracks. A fast simulation tool has been developed, whose aim is to reproduce the data considering only the very basic principles of charge transportation in a TPC. It should especially help to understand and optimize the reconstruction software.

6.1 Basic Reconstruction of Clusters and Tracks

The software package MultiFit has been developed during the completion and data acquisition period of the Medi-TPC prototype. The program has been mainly developed by M.E. Janssen. A basic description can be found in his graduate work [81]. A significant contribution to the deeper understanding of an implemented Pad Response Correction and an more advanced Global Fit Method is gained in the graduate work of R. Diener [65].

The program is used to reconstruct the images of tracks produced in a TPC. It calculates all parameters, which can be derived from this track image and are used determine the detector performance. The software has therefore been designed to be applicable to several layouts of TPC prototypes.

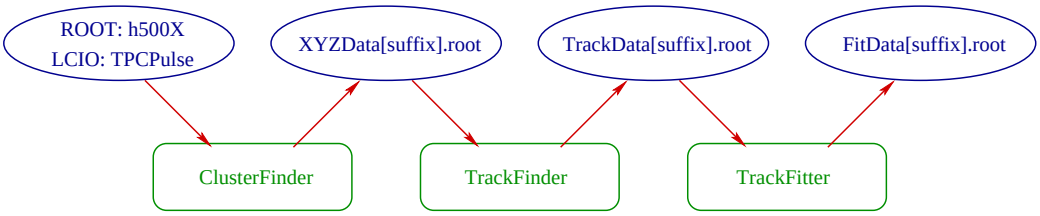

Figure 6.1: *The reconstruction programm MultiFit consists of three independent modules. First the clusters were built from a rawdata file. Afterwards the cluster are combined to form tracks. The quality of the track reconstruction is then quantified in a track fitting module. After each process a ROOT-tree has been produced to store the information of the previous process.*

The MultiFit software is written in C++ and makes use of the software packages ROOT [82] and LCIO [83]. The ROOT software package is used for all graphical output. Furthermore routines from the ROOT framework offer a broad opportunity of analytical methods, that are to some extend used in Multifit. LCIO is a data format developed for reconstruction and simulation of the detectors at the ILC. The idea is to use the same software for either the data analysis of stand alone detector prototypes or the simulation of physics events with the full detector chain.
Fig. 6.1 shows the reconstruction process, which is implemented in three steps:

ClusterFinder: The Clusterfinder reconstructs first a time integrated charge deposition on a every single pad. Afterwards it forms clusters from these charges seperately for each row. In this process both time and charge information is taken into account. It finally calculates a three dimensional position of the cluster.

TrackFinder: The Trackfinder combines these clusters to a track. It produces a first track hypothesis and adds all clusters, which fit both in time and the xy-plane to the track hypothesis. If suffiecient clusters could be assigned to the track hypothesis, it is defined and stored as a track.

TrackFitter: In the Trackfitter the quality of the tracks is calculated. With several methods the deviation of the clusters to the track is determined. All track parameters determining the track, such as track angles, curvature and the deviation of cluster to the track are finally stored. The output file can then be used for furher analysis.

Each software module produces a separate output file. It is possible to

investigate different track finding or track fitting routines. The different steering parameters needed for the reconstruction can be set in a configuration file. This file contains informations about pad geometry and layout, parameters and limits for the different algorithms used in the reconstruction process, data specific information like drift velocity and pedestals for each pad and even specific gas properties like diffusion and defocusing coefficients. A more detailed description can be found in [81].

To monitor the reconstruction process and examine single events, MultiFit provides the possibility to switch on a graphical display and save screen shots in various output formats.

6.2 Multifit ClusterFinder

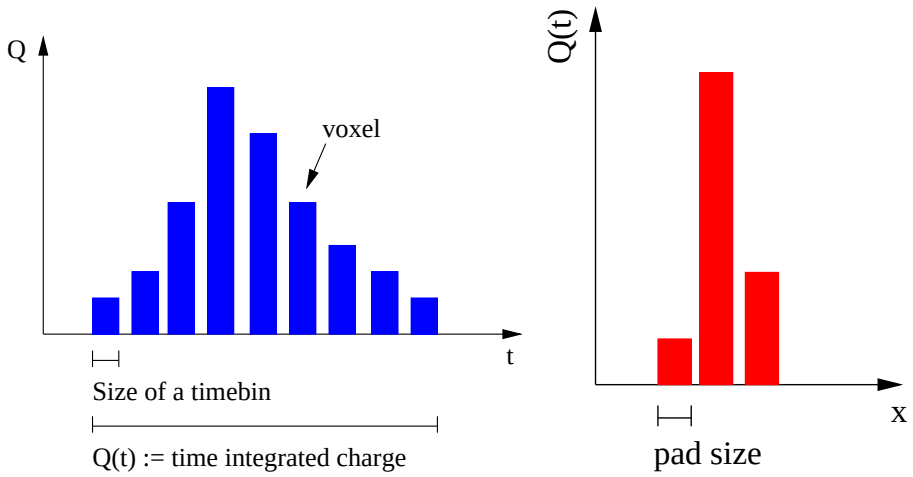

(a) Pulse (b) Hit

Figure 6.2: *In Figure (a) the composition of a pulse on a single pad is illustrated, in figure (b) the composition of a hit is shown.*

In the raw-data format the charge of every time bin with a certain channel ID is stored. The ClusterFinder reads the raw-data and in a first step reconstructs the measured charge on each single pad to a pulse (see Table 6.1). A pulse denotes a time integrated charge, which rises above and then falls again below a threshold. It is possible to choose different thresholds for the start and the end of a pulse. Additionally to the z bins that are between the two threshold, a selectable number of bins before and after the threshold can be added to the pulse. From this collection of bins both the integrated charge of the pulse and the time information are determined. The time assigned to the pulse is calculated by

Voxel	smallest possible three dimensional space point (Q, pad(x,y), t)
Pulse	Time integrated charge of a single pad
Hit	Sum of all puses, which belong together
Max. Hit Charge	Voxel with the biggest charge o a hit

Table 6.1: *The table shows the definition of parameters used for the reconstruction of points in the TPC.*

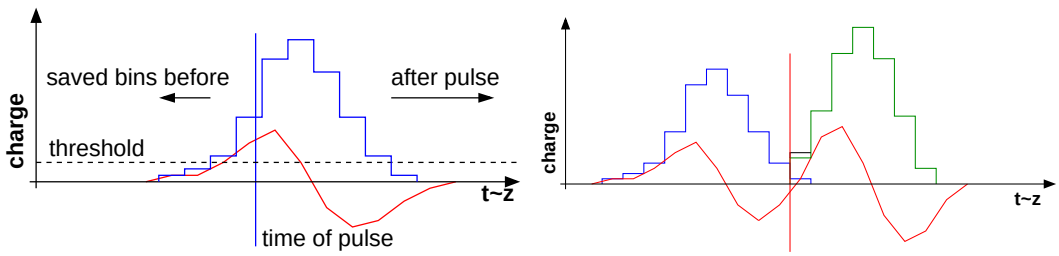

(a) Pulse reconstruction of a single pulse (b) Pulse separation of two pulses

Figure 6.3: *In Figure (a) the time integration of the charge for a single pad is shown. If the charge crosses a threshold the integration is started. The mean time is determined by the inflexion point of the rising slope. Figure (b) shows the separation of two pulses in time. If the slope rises twice the time bin with the zero crossing is taken as the starting point for the second iteration of charge integration.*

the inflexion point of the rising slope. This corresponds to the mean value of the positive derivative. This process is illustrated in fig. 6.3(a).

For events in which two pulses overlap in time, a separation algorithm is implemented. During the pulse search the change in the slope is detected and the time coordinate of the zero crossing of the derivative is taken to be the boundary between the two pulses. The process is illustrated in fig. 6.3(b).

The pulses are now merged to hits in every row of the pad plane. A hit denotes the integrated charge of the pulses in one row. Here the time position of the pulses is an important parameter as it prevents pulses to be merged which are not within a certain time window. The width of the time window can be chosen flexible. Two separation algorithms are available to separate charges, which do not belong to the hit. In the following two hit separation methods will be explained.

6.2.1 Hit Separation Method for Single Hits

For single tracks a hit search algorithm was developed starting with the pulse, which has the highest charge in a row. This pad which has the high charge pulse is defined as the central pulse. The algorithm searches the neighboring pads for pulses with less charge, that are not already assigned to a hit. The algorithm proceeds with the second highest pulse, which is not assigned to a hit until all pulses in a row are used. In this process the standard deviation σ of the pulse charge $Q_{pulse(i)}$ is taken into account:

$$Q_{i+1,pulse} - F \cdot \sigma_{Q_{i+1,pulse}} < Q_{i,pulse} + F \cdot \sigma_{Q_{i,pulse}}. \tag{6.1}$$

F is a factor, which can be set by the user and determines the multiple of the σ deviation. The number i is the running index, which proceeds from high to low charges. Charges that do not fulfill Eq. 6.1 are not assigned to the hit. When no more pulses can be added to the hit the search algorithm stops and the coordinates of the hit are calculated. The vertical center of the row is taken as y coordinate. The x coordinate of the hit is calculated by the Center of Gravity, using the charge informations $Q_{i,pulse}$ and the x position $x_{i,pulse}$ of the pulses:

$$x_{hit} = \frac{\sum_i^{pulses}[Q_{i,pulse} \cdot x_{i,pulse}]}{\sum_i^{pulses} Q_{i,pulse}} \tag{6.2}$$

A strong influence on the resolution is observed if the signal is distributed on to few pads. In cases of a narrow signal width, where the x position has to be derived by only a few pads, the signal is not reconstructed correctly by the Center of Gravity method. This problem is illustrated in figure 6.4(a). In the bottom of the figure the procuced signal on the pads is shown in two ways. The first diagram shows the charge, which is accumulated due to the size of the pads and

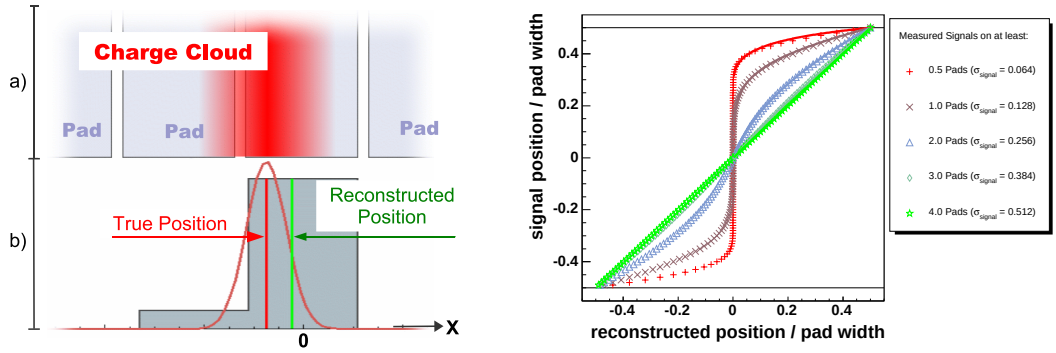

(a) Reconstructed and true position of a narrow signal

(b) Pad Response Correction functions for several widths σ of a Gaussian charge distribution

Figure 6.4: *In Figure (a) the need for a correction of the pad response is illustrated if the signal is distributed on too few pads. Figure (b) shows the influence of the pad response correction for different widths of the charge cloud.*

the second diagram shows the Gaussian distribution, which is responsible for the accumulation on the pads. It is clearly visible that true and reconstructed position are not the same. The reconstructed position is shifted to the pad with the higher charge. For a correct reconstruction of the x position of the hit a Pad Response Correction has to be taken into account. The Pad Response Correction is a function, that correlates the reconstructed with the true position signal position (see [84]). To get the Pad Response Correction the pad signal is simulated for a Gaussian distributed charged cloud with a specified width including a 1 % threshold. From this signal the x position of the hit is reconstructed by Center of Gravity (see equation 6.2). This is repeated for several positions relative to the center of the pad. The result is shown in figure 6.4(b). The values and fit functions are plotted for several widths σ of the Gaussian charge distribution. In the legend the corresponding minimal number of pads, which get a charge contribution from the signal are plotted.
There are two imporant signal widths: The width of 0.128 in units of pad width. This corresponds to the situation that the charge of the signal is at least reconstructed on one pad. Every larger width would therfore be reconstructed on at least more than one pad. This limits the occurence of indeterminacy in the recconstruction of the x position.
For the signal width of 0.512 units of pad width, which corresponds to a signal on at least four pads the function becomes astraight line. In this case the unfolding is not needed anymore to determine the correct x position of the signal. A more detailed description of the performance of this Pad Response Correction can be found in [65] and in [85].

6.2.2 Hit Separation Method for nearby Hits

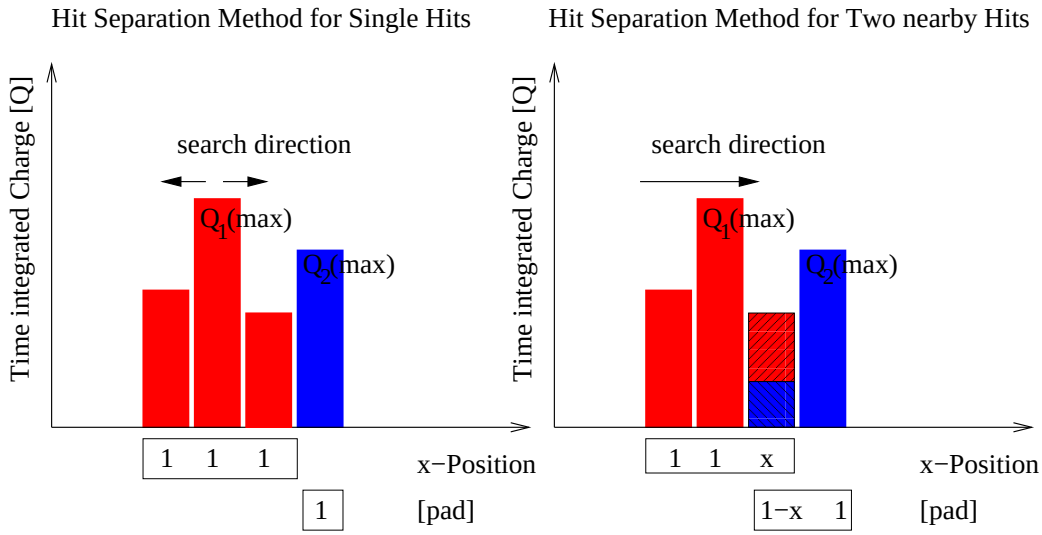

Figure 6.5: *Comparison of the two hit separation methods. The plot shows the hit separation in a row. The x-axis denotes the x-position determined by the pad. The y-axis denotes the corresponding charge. The hit separation method for single tracks only adds complete charges to a hit. The hit separation method for two tracks is looking for two local maxima and splits the charge in between the maxima by a weight factor, which is derived by ratio of the two charges* $Q_1(max)$ *and* $Q_2(max)$*.*

The previously described Hit Separation Method is a good approximation if mainly single hits have to be reconstructed. In this case equation 6.1 is a strong rejection criteria. If there are two maxima in one row a new hit separation method is needed as the charge on a pad can come from two hits. In Figure 6.5 the difference between the two methods is illustrated. The method does not need a distinguished direction. For the hit separation method for nearby hits the direction is needed to derive a local minima. If finding such a minima the charge of the pad had to be split in two charges. The two charges are split in the ratio of the charge of the two neighboring pads. With the previous separation method the complete charge is assigned simply to the hit with the higher maximal charge. To distinguish a minima from charges, which show small fluctuation the charges have to fulfill the criteria:

$$Q_{i-1,pulse} > Q_{i,pulse} + \sigma_{Q_{i,pulse}} < Q_{i+1,pulse} \tag{6.3}$$

Here only the uncertainty of the minima is taken into account, which is less strong than in the case of single hits (see. equation 6.1), where the uncertainty of both neighboring pads is taken into account. In the two hit case the motivation is different. One wants to split an already determined two hit candidate, but ensure that no hit splitting is done by small fluctuation of comparabel same charges. However this hit separation criteria might also be usefull in case of single tracks. A study to investigate the performance of the separation algorithm in case of single tracks would be needed.
The weighting factor for the intermediate pad is calculated with the charges Q_{max1} and Q_{max2}:

$$x = \frac{Q_{max1}}{Q_{max1} + Q_{max2}} \qquad 1 - x = \frac{Q_{max2}}{Q_{max1} + Q_{max2}} \tag{6.4}$$

Then a pulse collection is produced which stores the pulses from the charge before the minima and the intermediate pulse with the weighting factor x. From this pulse collection the position is calculated by Center of Gravity as described in the previous chapter. Afterwards the pulses are substracted and the search is repeated with the remaining pulses of the row, so that several hit separations can be executed. This procedure improves the x reconstruction significantly for the cases, where otherwise only one pad would remain. A hit, which consists of only one pad, can only be determined with an accuracy of $\sigma = \frac{d}{\sqrt{12}}$. The accuracy improves significantly if a second hit can be found.

6.3 Multifit Trackfinder

The second software module of MultiFit is the TrackFinder, which combines the hits to tracks and assigns them to a track collection. The algorithm assumes an straight track that enters the chamber from the top of the sensitive volume. This assumption is valid for small sensitive volumes since the particle tracks of the observed cosmic muon in our TPC prototype have a minimal radius of 900 mm, which corresponds to a curvature of about 1.1 m^{-1}. With a sensitive volume of size 50 mm a sagitta of 340 μm is given (seeAppendix B of [81]). Deviations of this size are negligible.

The search algorithm uses a track following method. The particle trajectories are assumed straight or vertical in the xy-projection, the implementation of this algorithm works row-wise. It is initialized by choosing two hits fitting a three dimensional straight track hypothesis to them. Based on the track hypothesis the algorithm searches for hits in the next row, that lie inside a three dimensional search windows around that position and are not already assigned to another track. The size of the search windows both in time and in x position can be set to different values.

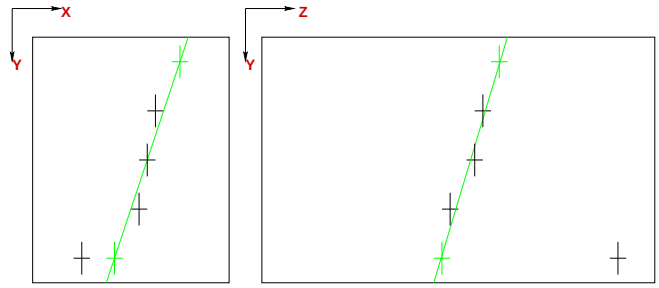

(a) Initialization of the track hypothesis by a hit in the first and last pad row

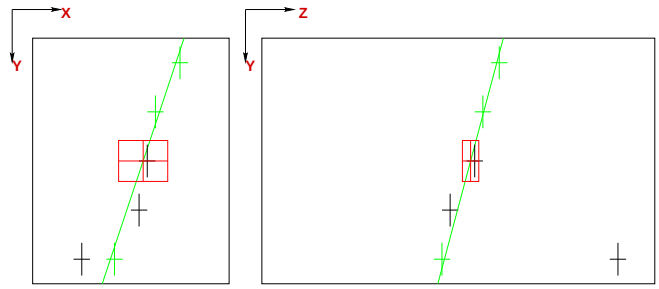

(b) In the second figure the algorith searches if a fourth hit fulfills the criterias given by two search windows in time and x-position.

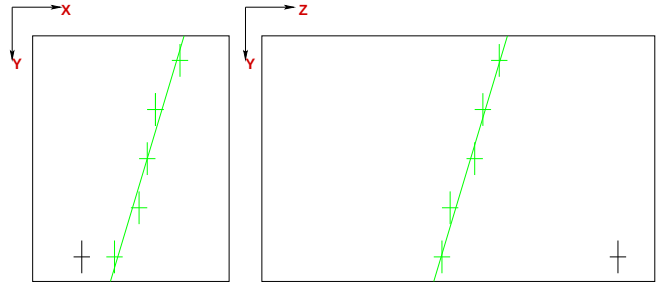

(c) Completed track collection

Figure 6.6: *The principle of the track following algorithm.*

The track following algorithm is illustrated in Figure 6.6. The hits are shown in the xy and the yz plane. The hit positions are illustrated by "+" symbols. Fig. 6.6(a) shows the initialization of the track hypothesis by a hit in the first and last pad row. In Figure 6.6(b) the track hypothesis has been extended by a hit, which falling within the defined search window and is therefore added to the track collection. The complete resulting track collection is shown in 6.6(c).

If more than one hit is found inside this window, the hit for which a straight line fit including the hit results in the smallest χ^2 is chosen:

$$\chi^2 = \chi^2_{xy} + \chi^2_{yz}, \tag{6.5}$$

with χ^2_{xy} being χ^2 of the xy-track projection and χ^2_{yz} being the χ^2 of the yz-track projection.
In the next step a new chisquared track hypothesis is calculated including the added hit. The algorithm searches in the next row for a new hit to be included. If no hit is found inside the search window or all hits that are found result in a probability below a specific limit, the algorithm counts this as a missing hit and continues its search in the next row. When the last row is reached, the algorithm starts again in the opposite direction to find hits above the upper initialization hit. The algorithm is started with any two hits, that meet the configurable boundary conditions of a maximum and minimum distance. Besides that, the maximum number of successive rows without a hit and the minimum number of hits a track must have can be set.

6.4 Multifit TrackFitter

In the TrackFitter module a selectable hypothesis for the track shape is fitted to the track collections from the TrackFinder. In MultiFit two different track fitting methods are implemented: The first method is the Chi Squared Method, which is based on the minimization of the least square method describing the track. The second method is the Global Fit Method, which optimizes the track parameters such as the angle in the xy-plane, the intercept, the width of the charged cloud and the curvature in the case of curved tracks by a likelihood function including all charges in the xy-plane at the same. Both methods are implemented for a straight track as well as for curved assumptions. In the case of tracks produced by a laser beam the curved assumptions can be ruled out as the magnetic field has no influence on photons. Therefore only the straight fit methods will be described. The implemented, selectable fit methods for straight tracks are:

ChiSquared: Analytical χ^2 minimization of a straight line fit both in the xy- and the yz-projection. Results: position of crossing point of the track and the xy-plane at $y = 0$ (Intercept) and slope in xy-

and yz-planes.

ChiSquaredRoot: Numerical χ^2 minimization of a straight line fit in the xy- as well as in the yz-projection using methods from the ROOT framework. Results: Intercept and slope in xy- and yz-planes.

GlobalStraight: Numerical log-likelihood maximization of a fit function describing the charge distribution of a straight track in the xy-projection and a χ^2 minimization of a straight line fit in the yz-projection using methods of the ROOT framework. Results: Intercept, slope in xy- and yz-planes, width of the charge cloud.

In this work only the Chi Squared and Global Fit method for straight tracks are used to calculate the point resolution. The method to determine the point resolution is described in the following section.

6.4.1 Point Resolution: The Geometric Mean Method

The parameters that have an influence on the achievable resolution of a TPC are the gas and field properties, the gas amplification and the readout system. In the rϕ plane the transverse diffusion and defocusing, which depend on the gas, the magnetic and electric field have an influence on the resolution. Additionally the pad size, geometry and layout are parameters that limit the point resolution. In the z direction the longitudinal diffusion is a crucial parameter, but mainly the resolution is determined by the electronic of the readout system.

Several points have to be taken into account considering the single point resolution. First in the TPC prototype no external reference from a hodoscope is available. Therefore the resolution estimates have been derived from the fitted track parameters and reconstructed hit positions.

A second point is that during the phase of R&D several definitions and methods determining the single point resolution were in circulation. A definition, which is used now as a standard definition is the Geometric Mean Method which will be explained in this section.

In the Geometric Mean Method one has to distinguish between two different terms. The first term is the *distance*, which denotes the difference between the x coordinate of a hit and the reconstructed track at the same y coordinate, when the hit is used in the determination of the track position. *Residual* denotes the difference between the x coordinate of the hit and the track, if the hit is not used in the determination of the track position. In the reconstruction excluding the hit all track parameter are fitted again. In Figure 6.7 the distance and residual

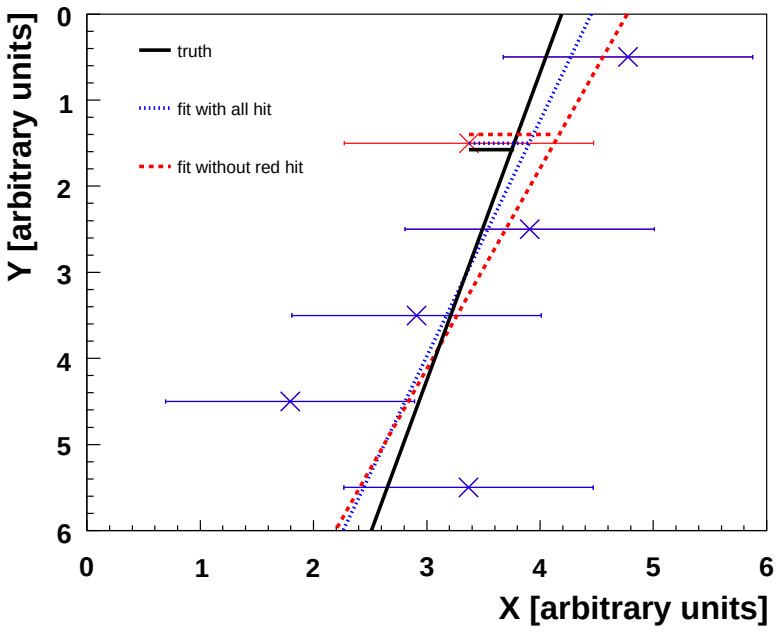

Figure 6.7: *shows the reconstructed track including all hits (blue dotted), the reconstructed track excluding the hit (red dashed) and with the known track parameters taken from the MC simulation (black solid)*

are illustrated. In this case the blue dotted track denotes the track reconstruction including all hits. The red dashed line denotes the track without the red marked hit. Using all hits for the track reconstruction the track is moving to the hit, as in case of the exclusion the track is moved away from the hit by the remaining hits. This calculation is repeated for each hit and all tracks in a data sample. It results in two Gaussian distributions. The distribution of the distances is expected to be narrower, than the one of the residuals. The calculation included in Appendix A of [86] proves analytically for straight tracks, that the geometric mean of both widths gives the true resolution:

$$\sigma = \sqrt{\sigma_{distance} \cdot \sigma_{residual}} \tag{6.6}$$

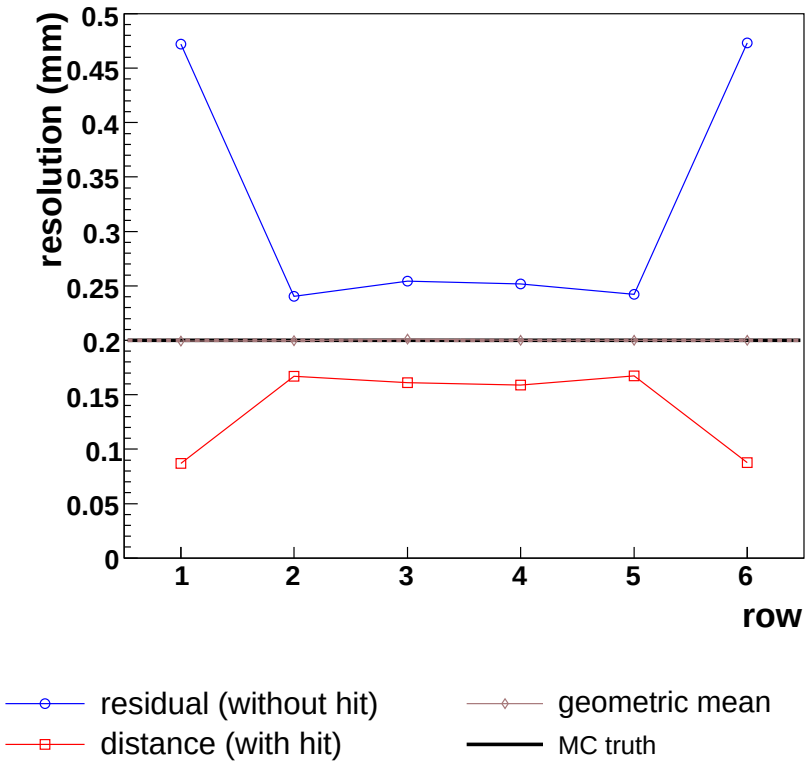

Figure 6.8: *Point Resolution: distance, residual and geometric mean for curved Monte Carlo tracks*

To quantify the validity of equation 6.6 for curved tracks a simple Monte Carlo simulation has been used. The simulation produces curved tracks with a radius between 500 and 2000 mm. The tracks go through the center of the sensitive volume and pad effects are not considered. The hit positions have been spread

with a σ of 200 μm. The result is shown in Figure 6.8. As expected the residuals are intrinsically larger while the distances are narrower. The geometric mean of both reproduces the Monte Carlo truth correctly. Figure 6.8 also shows, that the strongest effect on the distance and residual is at the outer rows. The effect is the result of the lever arm, which is greatest in the outer rows. The geometric mean method will be used in all track fit methods to determine the resolution.

6.4.2 Chi Squared Fit Method

In this section the principle of the Chi Squared Method is described, which is a conventional approach for track fitting. This fit is based on the *least square method*, which is often referred to as *chi-squared minimization*. The least squares method states that the parameter a_j for which the sum

$$\chi^2 = \sum_{i=1}^{n} \Big[\frac{x_i - f(y_i; a_j)}{\sigma_i} \Big]^2 \tag{6.7}$$

with x_i: measured values, with uncertainty σ_i taken at y_i, i = 1...n

a_j: parameters of the fit function:

$f(y; a_j)$, j = 1...m and m < n

is a minimum, are the values for which the function $f(y; a_j)$ best describes the measured data. The number of data points n have to be higher than the number of parameters for the fit function m. For the laser tracks the straight line fit is sufficient.

The straight line assumption is leads to the following equation for the least squares method:

$$\chi^2 = \sum_{i=1}^{n} \Big[\frac{x_i - a \cdot y_i - b}{\sigma_i} \Big]^2 \qquad \text{with} \quad x = f(y) = a \cdot y + b, \tag{6.8}$$

where a = Intercept X_0 and b = Slope X = $tan(\phi)$ denote the line parameters, x_i the measured x position of the hit with the associated uncertainties σ_i, y_i the vertical center of the hit in a certain row and n the number of measured hits (see figure 6.10).

The fit with the least square method used in the χ^2-method is a simple and well understood fit method. Since the maximum number of free parameters of the implemented fit functions is three and the minimal required number of active rows is set to at least five, the track fit with this method should work on almost all measured events.

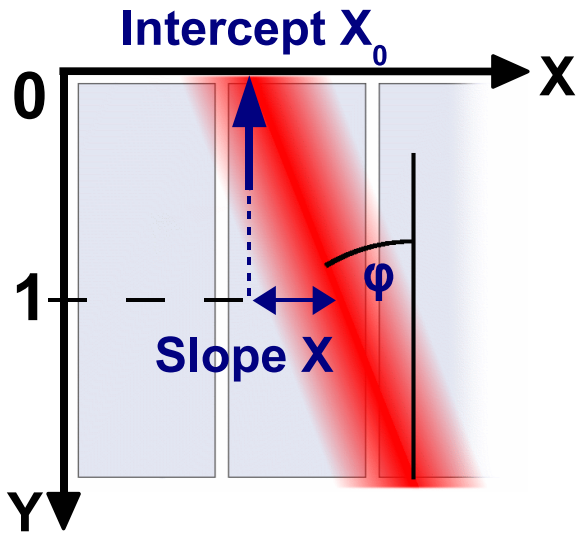

Figure 6.9: *Parameters of the straight line fit.*

A more detailed description of the least square method and the chi squared minimization can be found in [87]

6.4.3 The Global Fit Method (GFM)

An alternative approach to track fitting is the Global Fit Method (GFM), which is implemented in the MultiFit reconstruction software. The idea for this method has been developed by Dean Karlen and his research group [88] [89]. It was first implemented in a JAVA based simulation, fitting and analysis approach called JTPC. The program code can be downloaded at [89]. To understand the underlying fitting techniques, methods and reconstruction effects, the GFM has been implemented slightly modified as an additional fitting routine in the MultiFit reconstruction software. It was first implemented for single tracks. During the studies the routine was modified to use the method in the case of two or more nearby tracks.

Principle of the Global Fit Method (GFM)

The Global Fit Method is based on the maximization of a likelihood function describing the charge distribution on the pads. The difference to the JTPC implementation is, that only events, which have passed the criteria of Cluster- and Trackfinder of MultiFit, are fitted. These two modules work as a preselection of the events. This means only charge information, which is assigned to a track is taken into account.

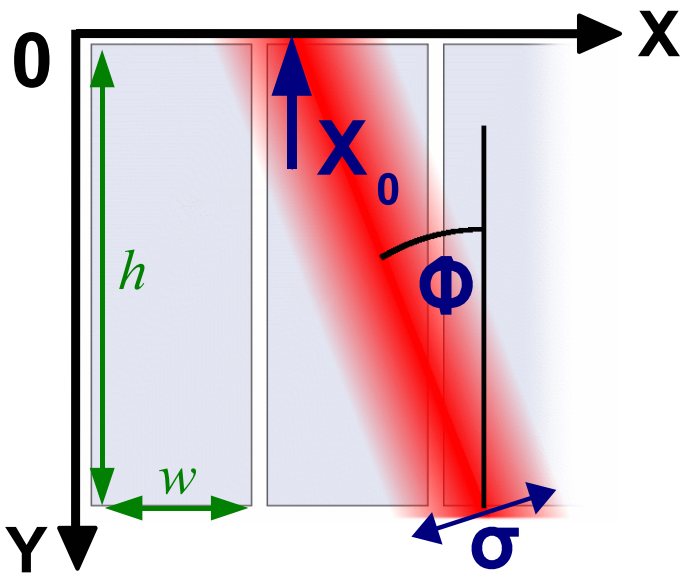

Figure 6.10: *Parameters of the likelihood function*

The parameters of the fit are the Intercept X_0, the angle ϕ and the width of the Gaussian describing the charge distribution along the trajectory σ. The parameter σ can either be set to a fixed value derived from the expected width of the charged cloud at a given z position or treated as a free parameter. The parameters are shown in figure 6.10.
In the model used by the Global Fit Method, the charge density function describing the distribution of the primary ionization along the track is assumed to be uniform in each pad row. Ionization fluctuations are not taken into account. The distribution due to diffusion is described by a two dimensional, isotropic Gaussian probability density function. The width σ for every hit is given by $\sigma_{hit}(z) = \sqrt{D_T^2 z_{hit} + \sigma_0^2}$. Three different cases can be distinguished:

- If there is no information describing the expected diffusion $\sigma_{hit}(z) = \sigma_0$ is assumed to be constant over the whole track length. In this case σ_0 is a free parameter, which is fitted together with the other track parameters.
- If the diffusion coefficient D_T is given $\sigma_{hit}(z)$ is calculated by this value, although σ_0 remains a free parameter, which is determined during the fit.
- In the third case, the diffusion information is completely determined by setting the defocussing coefficient σ_0. Here $\sigma_{hit}(z)$ is completely fixed and the fit has one free parameter less.

The charge deposition on a pad Q_{pad} is calculated by integrating the distribution function over the physical area of the pad and is proportional to:

$$Q_{exp} = \int_{-h/2}^{h/2} dy \int_{-w/2}^{w/2} dx \frac{1}{2\pi\sigma} \times exp\Big(\frac{\big[(x - X_d)\cos\phi_{row} + y\sin\phi_{row}\big]^2}{2\sigma^2}\Big), \quad (6.9)$$

where h is the height and w is the width of the pad. The integration variables follow the axis of the coordinate system, X_d is the horizontal distance between the pad center and the track position in that row. The azimuthal angle of the straight line in that row ϕ_{row}. In case of a straight track ϕ_{row} is simply given by ϕ_0, which is the track angle at the point where the track crosses the x axis.

The fit function is the product over all pads of the likelihood functions describing the charge deposition on each pad $\mathcal{L} = p_i^{n_i} \cdot p_i = Q_{exp}/\sum_{pads} Q_{exp}$ is the probability of the association of a primary ionization electron to the pad and $n_i = N_i/G$ is the number of primary electrons associated to the pad (N_i = number of measured electrons on the pad; G = gain value of GEM amplification). This leads to the following log likelihood function used in the track fit:

$$log\mathcal{L} = \sum_{m=1}^{rows} \sum_{n=1}^{pads/row} Q_{measured}^{n,m} \cdot log\Big[\frac{Q_{exp}^{n,m}}{\sum_{n=1}^{pads/row} Q_{exp}^{n,m}}\Big] \quad (6.10)$$

The log likelihood in $\mathcal{L}$ is maximized over all possible values of the parameters. The newly calculated parameters of X_0, ϕ and σ are then assigned to the track. The method does not work row-wise like the Chi Squared method, but takes all rows into account at once and includes angular effects. Due to the design of the fit function, the pad response is intrinsically taken into account and the unfolding of the hit positions using the PRC algorithm is not necessary. In the next step a fake track is produced, which includes these newly fitted track parameters, but consists of only one hit at a certain row position y_i. For this fake track the log likelihood function is maximized, but this time only the Intercept is kept as a free parameter, the other parameters are fixed. This procedure ensures that the information of the global track parameters gets into calculation, but only the hit position is recalculated and is finally assigned as new x position to the hit. This procedure is repeated for all hits belonging to the track at every row. In the MultiFit implementation of the Global Fit Method, the x position of the recalculated hits are saved for the calculation of the hit distances and residuals needed for the resolution analysis. A more detailed description of the derivation of the fit function can be found in [88].
So the Global Fit Method implemented in MultiFit is not able to produce new hits, it only can recalculate the distance and residual of the found hits due to the altered x position of these hits. This becomes important if applying the GFM for two tracks as described in the next subsection. In the current implementation

of the Global Fit Method it is not possible to separate one hit in two. A hit separation can only be done in the ClusterFinder. The GFM is no alternative or replacement of the ClusterFinder.
As mentioned before the, MultiFit has the possibility to set a fixed σ, which is calculated from the diffusion and defocusing coefficients in the configuration file. The values for this certain set of gas parameters are calculated using the simulationprogram MAGBOLTZ. With a fixed σ one parameter of the fit function is fixed. Therefore the total fit becomes more stable in the case when not many measurement points are available.

Modification of the Global Fit Method (GFM) for Multi Tracks

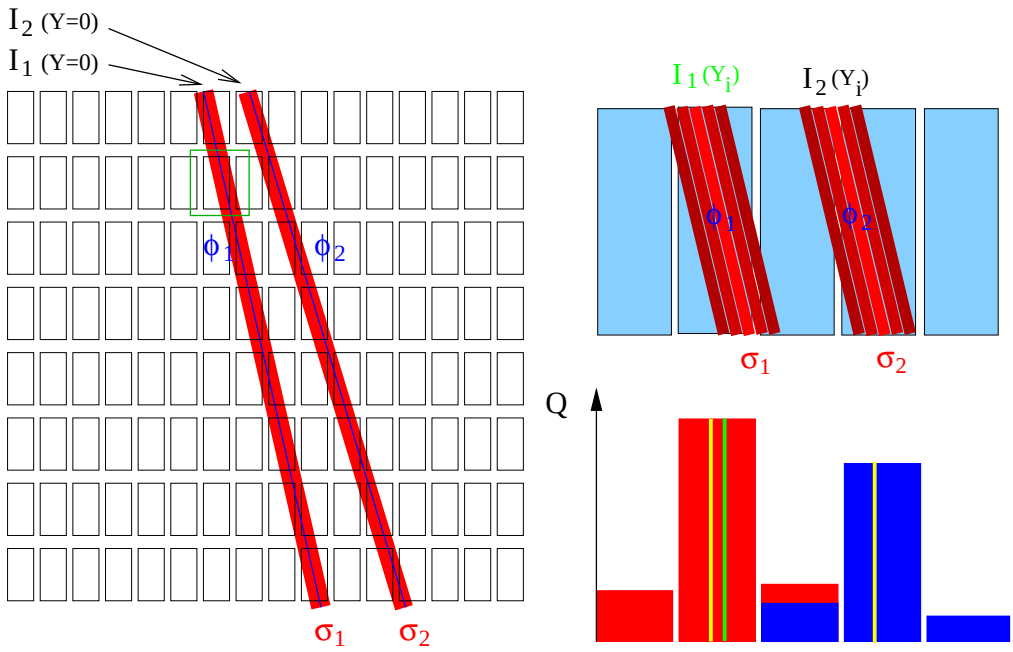

(a) Log likelihood ln L maximized for two tracks and two times the parameters

(b) Recalculation of the hit position of the first hit taking into account the charge of the second hit

Figure 6.11: *shows the GFM for two tracks. Figure 6.11(a) illustrates simultaneous optimization of both track parameters. In the bottom half of figure 6.11(b) the charge of a pad is histogramed. The yellow line represent the hit position before the green line the hit position after the recalculation. Only one hit position is changed, but the second intercept is taken into acoount in the fit as a fixed parameter.*

The Global Fit Method is used and optimized by investigating tracks from cosmic muons. The recent preliminary results of these studies have been presented

in [65]. In this work only single tracks have been studied. The rare multi track events have been ignored. The motivation of the laser studies, complementary to the investigation of single tracks, is to study the influence of a second nearby track. To investigate the two track performance with two different fitting routines the GFM has to be modified. Additional sets of parameters had been included, to gain the ability to fit the n tracks in an event simultaneously. The log likelihood function given by equation 6.10 has been extended to n times the total amount of parameters for a single track. Then again the likelihood function has been maximized for the charge deposition on the pads. The difference compared to the treatment of single tracks is that the parameters of all tracks are fitted and derived simultaneously (see an example for two tracks in Figure 6.11(a)).
In the next step two fake tracks are produced, which gets the track parameters derived from the likelihood function. Only one of this tracks gets a hit in one row. For the fake tracks the log likelihood function is maximized, keeping all parameters fixed except the Intercept of the fake track, which has the current assigned hit. This leads to a recalculation of the x position of the hit taking into account the complete track informations of both tracks. This procedure is repeated for all hits belonging to the first track. Then the algorith turns torwards the second track recalculate the single hit position of every row in the same way as for the first track. This procedure should ensure that the charge information and the global position of both tracks are taken into account simultaneously in the recalculation of the x position of the hit (see in fig. 6.11(b)).

6.5 Simulation Tool used for Laser Track Production

To understand the data taken from the measurement in more detail a simple, but fast simulation tool has been developed, which describes the basic processes of the signal production in a TPC. One big advantage of the simulation is, that all the main track parameters are known, so a comparison of the true and the reconstructed track position is possible. The data format of the simulation is the same as the one produced from the LCIO [83] client of the data acquisition system described in sec. 4.7. So the simulated events can treated with the same reconstruction software.
First all parameters to define the sensitive volume of the TPC have to be set. This includes the pad geometry with the size of the pads, the number of columns, rows and the number of time slices, which defines the length of the sensitive TPC volume. Then a gain factor is set, which convert the primary produced electrons on one pad in a FADC count. A pad mapping is implemented to assign the charge of a track to a pad. In a next step the input parameters resulting from the geometry of the prism positioning system related to the sensitive volume are introduced. It includes the possibility for two seed points, which have as input parameters

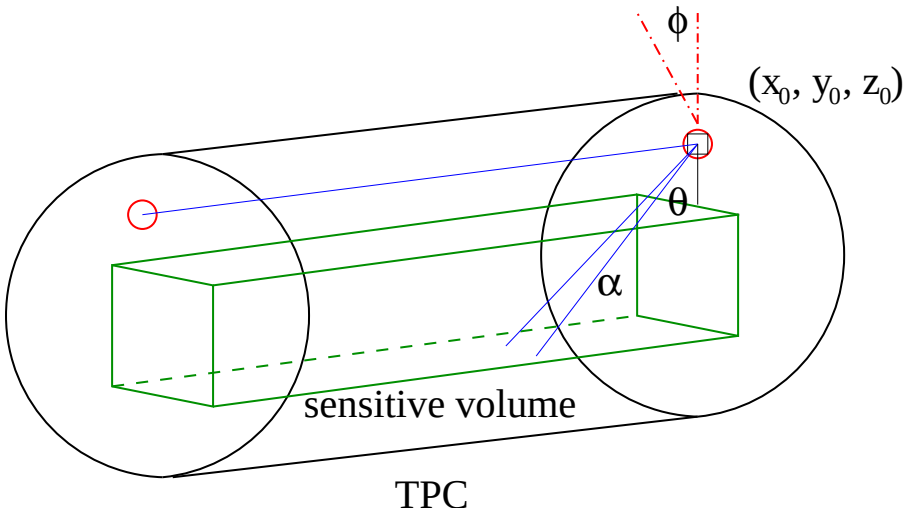

Figure 6.12: *shows the produced sensitive volume in the simulation and the input parameters for the two tracks*

$x_0, y_0, z_0, \phi, \theta$ and α. The coordinates x_0, y_0, z_0 determines the point of on the wedge prism, where the laser beam is reflected back in the sensitive volume, ϕ is the angle in the xy-plane, θ the angle in the yz-plane and α the angle between the two tracks as derived in sec. 5.2.2. A sketch of the input parameters is shown in fig. 6.12. As mentioned in sec. 5.2.2 the intensities of the two beams are correlated to each other. Therefore a correlation factor can be set, which relates the primary ionization of the two tracks to each other.
To get the correct charge broadening at the pads the diffusion is implemented, which consists of the diffusion coefficient and calculates the width of the charged cloud due to the position in z and a defocusing constant. The diffusion is determined by the choice of gas and the applied electric and magnetic fields. Then a Gaussian distributed primary ionization of the tracks is produced. Every pad row is convoluted with the corresponding diffusion due to the position $z[y_i]$. The assumption that the same diffusion factor is valid for all rows can not be obtained due to strong inclined θ angles, which are available with the prism positioning system.

Using the ROOT package it is possible to switch to a simple event display, which allows to monitor and store the simulated events. Fig. 6.13 shows an example of single event in the xy-projection. It is visible that both tracks are inclined by an angle ϕ, which represents the angle of the combined system of the two tracks. Every point represents a primary electron. The implemented pad structure is clearly visible.
The drawbacks of this simple simulation are at hand. There is no appropriate

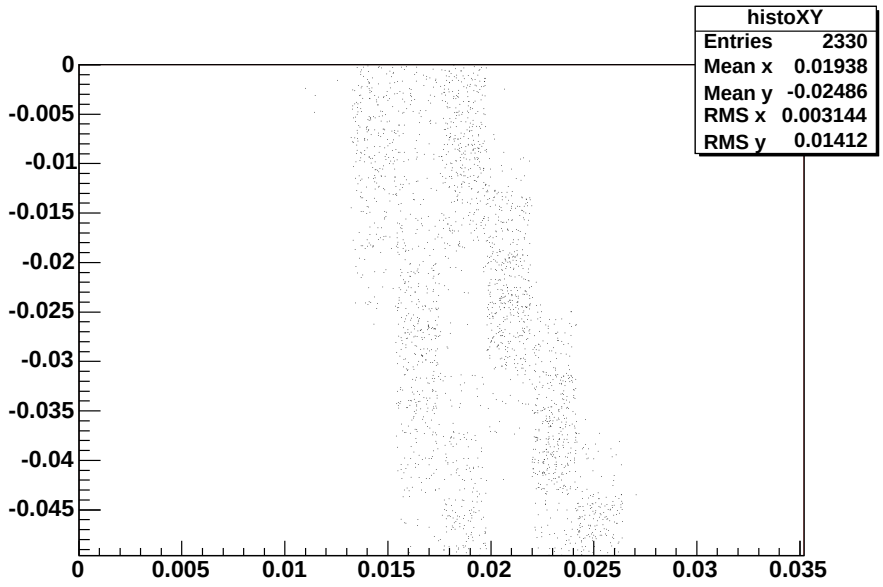

Figure 6.13: *shows an event display of the xy-projection*

implementation of other gas properties except the diffusion. Effects coming from an attachment coefficient of the drifting electrons in the gas volume or the influence of electric field distortions and their influence to the drift velocity are not taken into account. As mentioned no appropriate GEM-gain simulation is used, but only a gain factor, which does not include fluctuations of the GEMs. There is also no implementation of effects coming from the electronics. This means the z resolution is too good. A reliable interpretation of the single point resolution is only possible for the x direction. And as a last point only a very limited treatment of delta electrons is possible, which is not important in case of a laser, but limits the validity of conclusions for the cause of MIPs.

Despite this limitations the simulation is a useful tool to describe the features of the laser tracks on a basic level. An important point is that the charge distribution does not has to deal with the mentioned delta electrons which are responsible for the Landau-tail in the charge distribution of MIPs. This means especially the single point resolution is not affected by this effect. So the diffusion and the defocusing of the charged cloud in the amplification system should have the major impact on the resolution. Both effects are implemented in the simulation.

Although no electronic effects are included at least geometry effects, which are produced by the pad size and the fixed orientation of the track to the pad plane

can be investigated in detail. In comparison to the data the simulation can helps to disentagle this geometry from electronic effects.
The simulation was also very helpful in the development on the algorithm reconstruction. Especially in the case of GFM modifications for two nearby tracks the simulation provided an easy and fast accesible set of events, which helped to program and debug this routine.
Some problems occuring in the comparison of data and simulation are not caused by an simulation, which is not appropriate, but are caused by an incomplete knowledge of the system. For example the laser width could only be roughly approximated. Also an independent measuremnet of the track parameters, such as track angles and position of the track would determine the system more accurate.
Due to this limitations the simulation is quite fast. 1000 events can be produced in a timescale of a few minutes depending on the processor speed. Also the systematic effects coming from the pad width could be studied with the simulation. The performance and the results of the simulation are given in chapter 9.

Chapter 7

Drift Velocity Measurements in a TPC

An important parameter needed for the reconstruction of the 3 dimensional charge information is the amount of water, which is in the gas mixture. Even small contributions of water have a strong impact on the drift velocity, especially in the case of the used TDR gas. There are two different ways to treat the set of slowly changing gas parameters of a TPC.

- Measure the gas properties of the system and include the values later in the reconstruction and correct for it.
- Keep the gas properties of the system fixed within a margin of deviation to guarantee stable environmental conditions during the measurement.

In the current phase of research and development the first approach of measuring the gas parameters and to correct for them was used.

To test the reliability of an UV laser system extracting the drift velocity a systematic study was done. Two complementary methods to derive the drift velocity where tested and compared. In the first method the drift velocity was corrected by the amount of water, the pressure and temperature measured by the Slow Control System described in section 4.6. With the knowledge of these parameters and the strength of the electric drift field the drift velocity can be derived from the program MAGBOLTZ [90] and the visualization program GARFIELD [91]. In case of the slow-control measurement the water content is the observable and the drift velocity the corrected parameter. The second method measures the drift velocity directly with the laser setup described in section 5.4.1. The final aim was to test the agreement of both methods and determine the performance of the methods. Later the first method was used to determine the drift velocity with the dew slow control device. The slow control system can be connected to any TPC prototype and continuously record the gas parameters.

The drift velocity, which is an important parameter of the reconstruction can be extracted later from the stored slow control data-files. The following description is based on the work of [92].
To compare both methods a water enrichment device was built. With this device the gas could be enriched with a specific amount of water. This device was connected to the slow control system (see Section 4.6), that measures all relevant gas parameters to calibrate the drift velocity. Both systems were connected to the Big TPC prototype described in Section 4.1. The TPC has three quartz windows, that allows the laser to enter the TPC at a well defined distance to the readout plane. Finally the laser setup described in Section 5.4.1 used the first and second quartz window to produce two parallel tracks in the TPC.

In the following sections the experimental setup to measure and determine the drift velocity with both methods will be explained, compared and discussed.

7.1 Water Content Enrichment

To enrich the water content of the gas on its way to the TPC, the gas delivery system was partially replaced by a water permeable plastic tube. This plastic tube was placed in a water bath, so that the water could diffuse through it. Diffusion processes are described by Fick's first law:

$$\vec{j} = -D_F \cdot \vec{\nabla} c \tag{7.1}$$

with the particle flow density $\vec{j}$, the particle concentration c and the diffusion constant D_F, which is dependent on the used material. In the case of a permeable membrane of the thickness d, Equation 7.1 is modified to:

$$j = P \cdot A \cdot \Delta c, \tag{7.2}$$

with the particle flow j, the concentration gradient Δc, the surface of the membrane and the permeability coefficient P.
According to Equation 7.2 the particle flow through the membrane is proportional to the length of the plastic tube. The enrichment of the gas mixture with water is related to the exposure time of the gas in the tube and can therefore be controlled by the gas flow.

To verify the reliablity of this simple method of water enrichment a test setup was built, which can be seen in Figure 7.1. The used plastic tube has a length of 260 cm, a diameter of 6 mm and a thickness of about 1 mm.
The short term and long term behavior of the system have been tested to investigate the response time and the long term stability of the system. In Figure 7.2(a) the short term behavior is illustrated. It shows a clear anti correlation between gas flow and the measured amount of water of the dew point measurement device. The observed fluctuations are given by the precision of the device, which has an

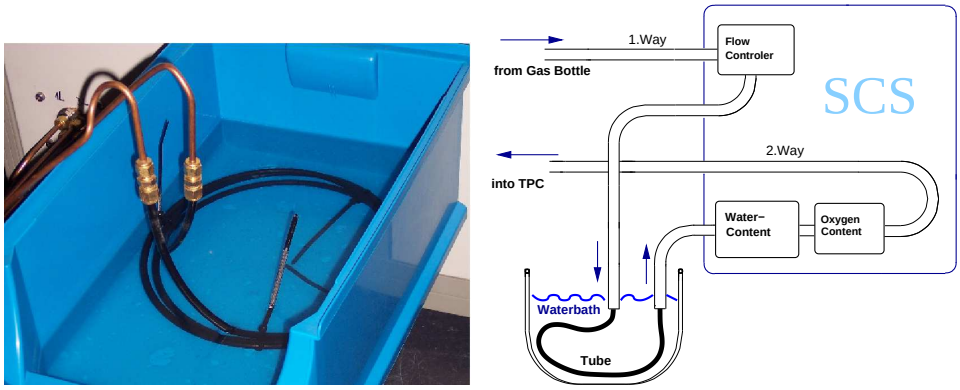

(a) Photo of the water bath with included plastic tube

(b) Sketch of the setup to test the reliablity of water enrichment

Figure 7.1: *The setup to enrich the water content of the gas. Figure (b) shows the water bath and the gas flow meter, located in the slow control system, that controls the exposure time of the gas to the water bath. With a homogenous flow the amount of water in the gas is constat.*

accuracy of $\pm 0.5°C$. Also the long term behavior (see Figure 7.2(b)) can confirm the anti correlation, which proves the long term stability of such a system.

7.2 Drift Velocity Measurement

For the drift velocity measurements the following components were used: A water bath, the Big TPC prototype, the slow control system and the laser setup. The laser beams were guided into the first and second window of the TPC. The TPC installation with the appropriate laser setup is given in Figure 5.16. With this setup the drift velocity could be easily calculated

$$v_{drift} = \frac{\Delta l}{\Delta t} \tag{7.3}$$

by measuring $\Delta\ l$, the distanc between the center of the first and second quartz window, which is $\Delta l = 24.6$ cm, and measuring Δt with the TPC. The whole system is shown in Figure 7.3.

The cathode voltage has been varied in the course of the measurements between 14 and 20 kV, which corresponds to a variation of the drift field between 120 to 210 V/cm. Due to the variation of the electric field one also had to change the potential at the shield given by Equation 4.2. For every measurement point the shield resistance R_S had to be newly aligned due to the current cathode voltage. To have a sample with sufficient statistic a data file with 250 triggers was stored.

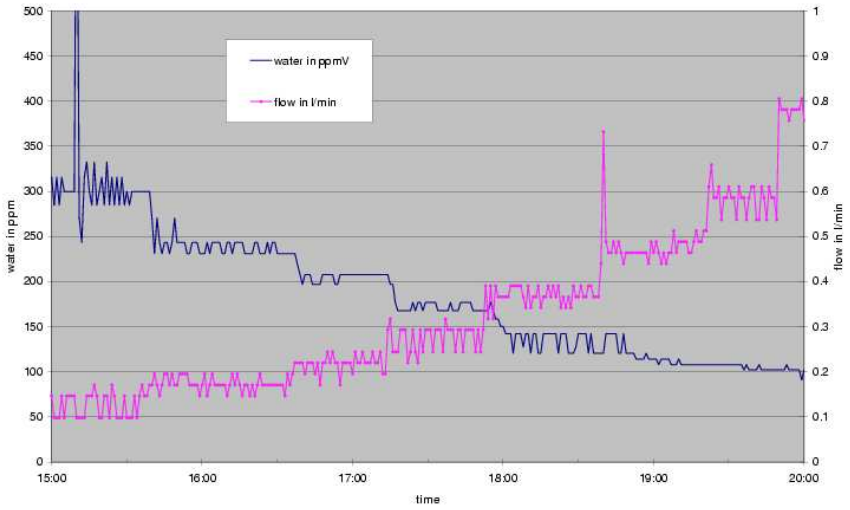

(a) Short term behavior of the gas-water enrichment system

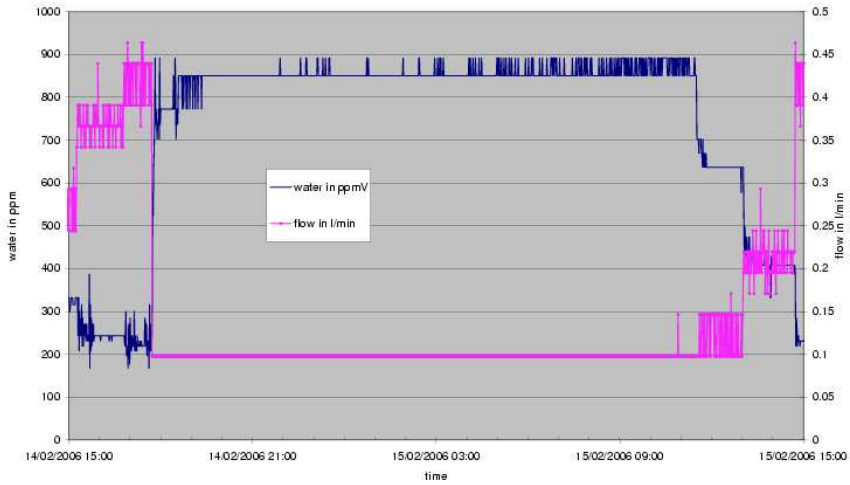

(b) Long term behavior of the gas-water enrichment system

Figure 7.2: *shows short term and long term behavior of the system. It shows the response time and the long term stability of the system.*

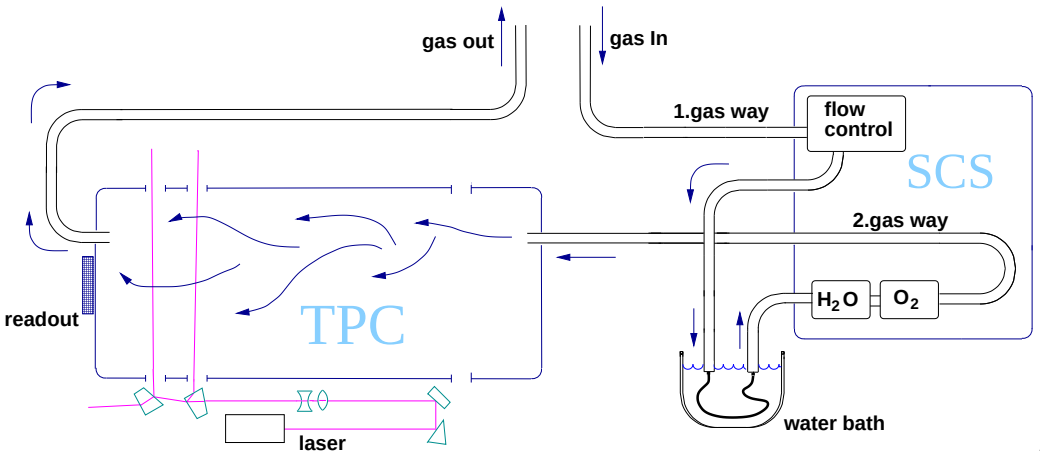

Figure 7.3: *shows the sketch of the complete setup used for the drift velocity setup, including the water generator, the TPC prototype and the laser setup.*

For the laser almost 100 % efficiency between trigger/event ratio was achieved. The complete measurement could be done in about one hour. During this time the fluctuations of the slowly changing pararmeters as water content itself, pressure and temperature are considered constant.
The data samples with flows of 4.8, 6, 9, 12, 15, 18 and 24 l/h had been investigated. This corresponds to a maximal water enrichment of more than 1200 ppm and a minimal enrichment of 300 ppm. After setting a new gas flow an exchange of about 3 to 5 gas volumes was needed to be sure that the gas and its containig amount of water had been completely replaced. The exchange time can be calculated by

$$t_{exchange} = \frac{x \cdot V_{chamber}}{f} \tag{7.4}$$

with the weighting factor x, which is about 3 to 5, the volume of the TPC $V_{chamber}$ of about 113 l and the gas flow f of the system, that varies between 6 and 24 l/h. With a factor x of 3 one has to wait between 56.5 h (6 l/h) and 14 h (24 l/h) until this gas volume is exchanged.
There could be contributions to the water content of the system, such as gas leakages of the TPC chamber, which allows water to infiltrate the TPC volume without detection. Also attachment of water on the surface of the TPC or the storage of water in hydrophil materials can be systematic uncertainties not covered by the water generator.

The drift velocity can be easily calculated from the raw data. In principle every hit with its time information can be taken into account, but to reduce the amount of noise hits, only hits, which are belonging to reconstructed tracks are taken into account for the calculation of the drift velocity. These hits with their reconstructed

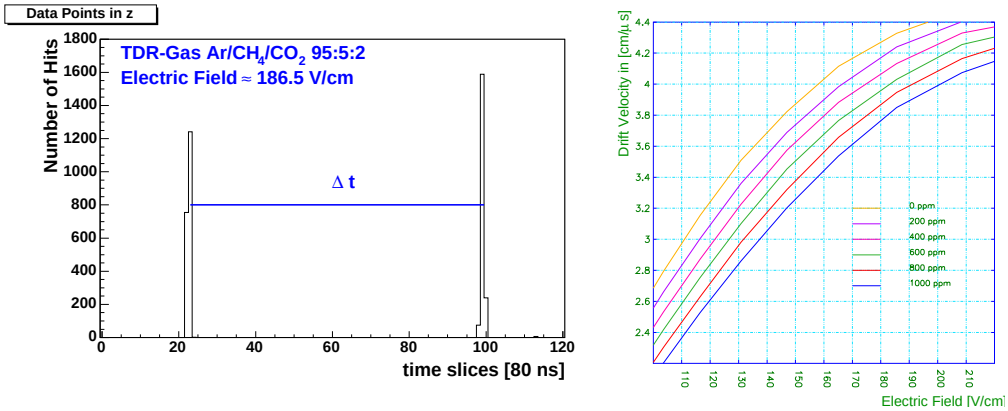

(a) Determination of Δ t at an effective electric field of 186.5 V/cm

(b) six hypothesis of gas mixtures with different values of water content

Figure 7.4: *shows the principle of measuring Δ t and the different hypothesis of MAGBOLTZ 7, the drift velocity is compared to.*

time information are filled in a histogram. In fig. 7.4(a) one can see the time information with the counted number of hits. From the derived time difference Δt of the two peaks and the measured distance between the two quartz windows one can easily derive the drift velocity. The expected statistical uncertainty of the mean value of a single peak is the width of the distribution σ divided by $\sqrt{N}$. This means the uncertainty of the time measurement is $\sqrt{(\frac{\sigma_1}{\sqrt{N_1}})^2 + (\frac{\sigma_2}{\sqrt{N_2}})^2}/\Delta t$. With Δt, which is in the range of about 100 timebins, dependent on the drift field and the uncertainty of the mean value, which is about 0.1 timebins, the total statistical uncertainty is below 1‰. To estimate the systematic uncertainty, which is determined by alignment errors and the external measurement of the distance between the quartz windows, an uncertainty of 1 % is assumed. An estimate for the systematic uncertainty is given in the Appendix of [92]. The calculated drift velocity $v_{drift}(E)$ is depending on the electric field. With the scan of the electric field between 14 and 22 kV one get nine electric field configurations, which allows an approximation to a gas mixture with a specific content of water. Various curves of gas mixture with different water contents are plotted in Figure 7.4(b). The strong decrease of the drift velocity at the same electrical field with increasing water content is clearly visible. The characteristic behavior of the curve is retained. It starts with an almost linear increase of the drift velocity due to the electric field. At higher electric fields a plateau is reached. With nine electric field configurations ranging from 120 to 210 V/cm it is possible to test, which water content hypothesis fits best to the MAGBOLTZ calculation.

7.2.1 The Effective Electric Field

To include all gas parameters in the calibration of the drift velocity an effective field strength E_{eff} has been derived. This field strength is given by:

$$\vec{E}_{eff} = \vec{E} \cdot \frac{p_0}{p} \cdot \frac{T}{T_0} \Rightarrow \vec{v}_{Drift} = \mu \vec{E}_{eff} \tag{7.5}$$

and can be derived from Equation 2.19. Here the parameters $p_0 = 1$ bar and $T_0 = 293$ Kelvin denote the pressure and temperature value used for MAGBOLTZ. The values p and T denote the measured pressure and temperature value of the slow control system. If pressure and temperature of the system changes, also the average time between two collisions of the charged particles with the gas molecules is affected.

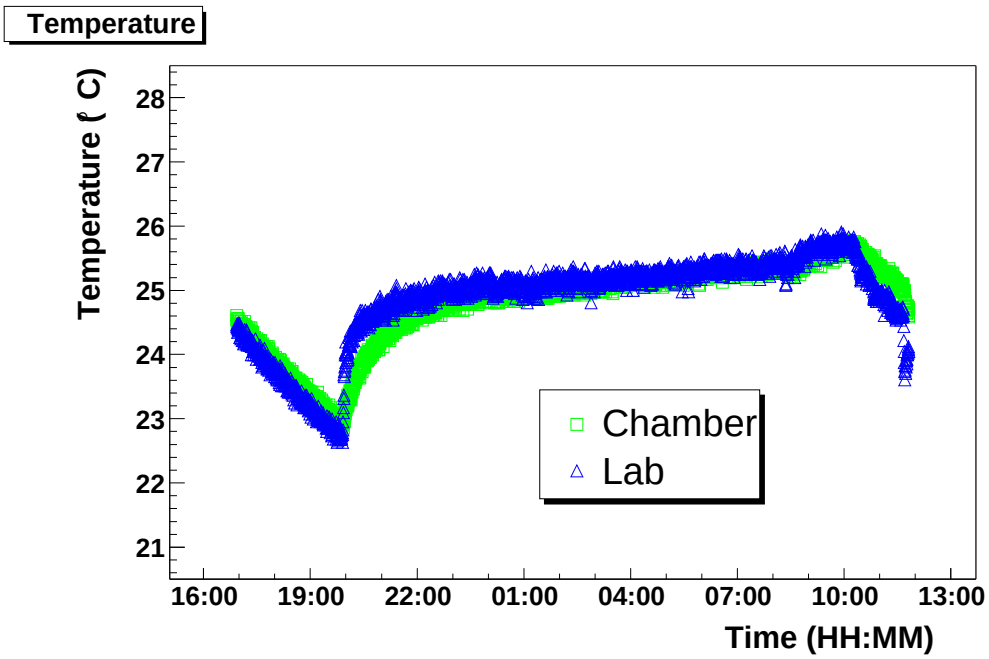

Figure 7.5: *shows the course of temperature in the chamber and in the laboratory. It is visible, that the temperature of the chamber follows the temperature of the laboratory very accurate.*

Both effects can be monitored by the slow control system, but only the pressure measurement was directly measured inside the chamber. The temperature was monitored only in the laboratory to included it in the calibration of the effective

Fig.	Water Content Slow Control [ppm]	flow [l/h]	pressure [mbar]	temperature [^{o}]
7.6(a)	300	24	1018.2	23.0
7.6(b)	500	18	999.2	22.5
7.6(c)	800	9	1025.3	22.0
7.6(d)	1200	4.8	1020.0	22.0

Table 7.1: *The water set of measured water content values.*

electric field $\vec{E}_{eff}$. From a study carried out from the TPC group of the RWTH Aachen it seems reliable to assume chamber and laboratory temperature as equal. In Figure 7.5 it is shown that the temparature of the chamber follows precisely the temperature of the laboratory. Therefore only the laboratory temperature was monitored by the slow control system.

7.3 Measurement compared with MAGBOLTZ 7 and 9

Four different gas flows were investigated, which correspond to four different water content. The parameters are given in Table 7.1. The anti-correleation between water content and drift velocity is clearly visible. The measured drift velocities were compared with two versions of MAGBOLTZ. The difference from MAGBOLTZ version 7 to 9 are improved calculations for cross-sections of different gases and small contributions of other gas ingredients. In Figure 7.6 the four water content hypothesis are plotted. The x-axis denotes the cathode voltage of 14 kv to 22 kV, y-axis denotes the drift velocity.

In Figure 7.6(a) the water content measurement of 300 ppm is illustrated. Both MAGBOLTZ versions fit fairly well to the measured values. This is also shown in Figure 7.7(a). Here the calculated values are subtracted from the measured ones. The deviation of the mean values stay below 1 % for both MAGBOLTZ versions.
In Figure 7.6(b) the next measurement point with a water content 500 ppm is plotted. Here a small shift appears for the MAGBOLTZ 7 versions compared to the measured values, which becomes clearly visible for U_{drift} above 18 kV. For this drift fields the deviation of the mean values rises significantly above 1 %, which becomes visible in Figure 7.7(b). The calculated values for MAGBOLTZ 9 do not show such a tendency. Here the deviation of the mean value stays significantly below 1 % (see Figure 7.7(b)).
This tendency gets more significant for a water content of 800 ppm (see Figure

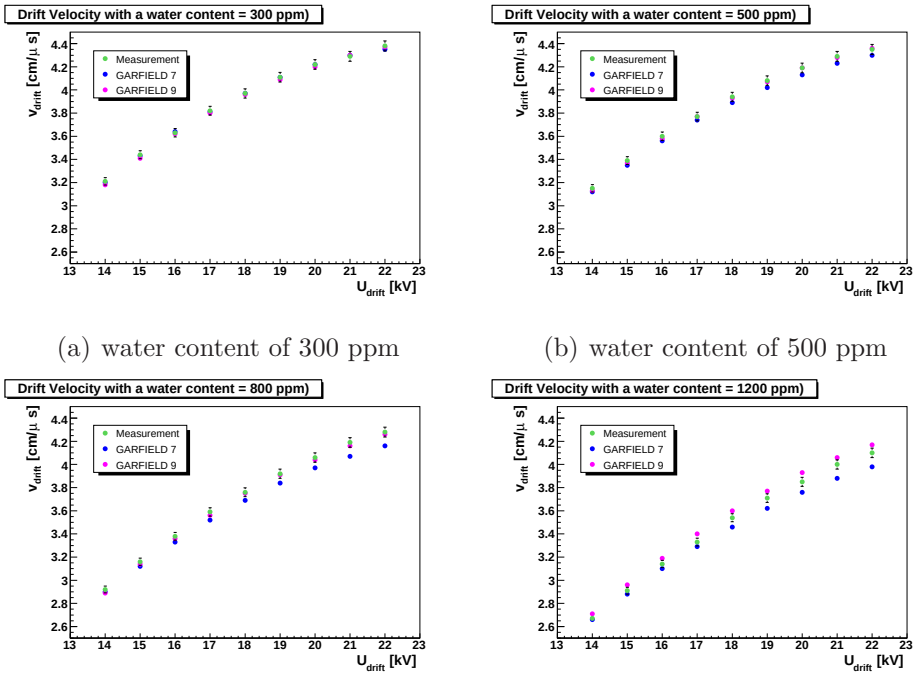

(a) water content of 300 ppm

(b) water content of 500 ppm

(c) water content of 800 ppm

(d) water content of 1200 ppm

Figure 7.6: *The measured drift velocity is compared with calculations of MAGBOLTZ version 7 and 9.*

7.6(b)). Also here the deviation between measured drift velocity and and the values calculated for MAGBOLTZ 7 increases for an increase of the drift field. It becomes clearly visible in Figure 7.7(c). The deviation of the mean values between data and MAGBOLTZ 7 calculations are of about 2 % at 20 kV for. Also for this high water content added to the gas mixture MAGBOLTZ 9 can describe the data very good. Comparing the values for the same electric fields, the prediction of MAGBOLTZ 9 stays still below 1 %.

For the measurement point with the highest water content of 1200 ppm also the discrepancy between MAGBOLTZ version 7 and 9 becomes maximal. In the Figures 7.6(d) and7.7(d) one can clearly notify the big discrepancy between measured drift velocities and the values of MAGBOLTZ 7, which increases dramaticaly with the drift field. For MAGBOLTZ 9 the deviation stays always below 2 % and has a constant shift to the mean value of the measurement. It might be, that due to the low flow of 4.8 l/h, which was the lower limit of the steerable gas flow meter, also the accuracy suffered from this limitation at this specific measurement point.

25. October, Water Content 300 ppm (SCS), pressure 1018.2 mbar, 23 ^{o}								
U_{Drift}	v_{Drift} Meas.	v_{Drift} GF9	v_{Drift} GF7	Deviation of GF9 to Meas.		Deviation of GF7 to Meas.		Deviation of GF7 to GF9
in kV	in cm/μs	in cm/μs	in cm/μs	in %	in cm/μs	in %	in cm/μs	in %
22	4.38	4.37	4.35	-0.35	-0.02	-0.72	-0.03	-0.37
21	4.29	4.30	4.30	0.04	0.00	0.02	0.00	-0.02
20	**4.22**	**4.20**	**4.22**	**-0.28**	**-0.01**	**0.03**	**0.00**	**0.31**
19	4.11	4.09	4.11	-0.41	-0.02	-0.09	0.00	0.32
18	3.97	3.96	3.97	-0.34	-0.01	-0.13	-0.01	0.21
17	3.82	3.80	3.81	-0.36	-0.01	-0.09	0.00	0.28
16	3.63	3.62	3.64	-0.29	-0.01	0.17	0.01	0.46
15	3.44	3.41	3.43	-0.73	-0.03	-0.12	0.00	0.61
14	3.21	3.18	3.20	-0.71	-0.02	-0.04	0.00	0.67

Table 7.2: *The measured and simulated drift velocities and the deviations for the 300 pm water content*

31. October, Water Content 500 ppm (SCS), pressure 999.2 mbar, 22.5 ^{o}								
U_{Drift}	v_{Drift} Meas.	v_{Drift} GF9	v_{Drift} GF7	Deviation of GF9 to Meas.		Deviation of GF7 to Meas.		Deviation of GF7 to GF9
in kV	in cm/μs	in cm/μs	in cm/μs	in %	in cm/μs	in %	in cm/μs	in %
22	4.35	4.36	4.30	0.19	0.01	-1.12	-0.05	-1.31
21	4.29	4.28	4.23	-0.08	0.00	-1.43	-0.06	-1.35
20	**4.19**	**4.19**	**4.13**	**-0.18**	**-0.01**	**-1.56**	**-0.07**	**-1.38**
19	4.08	4.07	4.02	-0.24	-0.01	-1.57	-0.06	-1.34
18	3.94	3.93	3.89	-0.18	-0.01	-1.34	-0.05	-1.16
17	3.77	3.77	3.74	-0.06	0.00	-0.98	-0.04	-0.91
16	3.60	3.58	3.56	-0.51	-0.02	-1.15	-0.04	-0.65
15	3.39	3.37	3.35	-0.52	-0.02	-1.03	-0.03	-0.51
14	3.15	3.13	3.12	-0.49	-0.02	-0.88	-0.03	-0.39

Table 7.3: *The measured and simulated drift velocities and the deviations for the 500 pm water content*

16. October, Water Content 800 ppm (SCS), pressure 1025.3 mbar, 22 ^{o}								
U_{Drift}	v_{Drift} Meas.	v_{Drift} GF9	v_{Drift} GF7	Deviation of GF9 to Meas.		Deviation of GF7 to Meas.		Deviation of GF7 to GF9
in kV	in cm/μs	in cm/μs	in cm/μs	in %	in cm/μs	in %	in cm/μs	in %
22	4.28	4.26	4.16	-0.43	-0.02	-2.76	-0.12	-2.34
21	4.19	4.16	4.07	-0.65	-0.03	-2.74	-0.11	-2.10
20	**4.06**	**4.04**	**3.97**	**-0.34**	**-0.01**	**-2.15**	**-0.09**	**-1.81**
19	3.92	3.91	3.84	-0.27	-0.01	-1.87	-0.07	-1.60
18	3.76	3.75	3.69	-0.37	-0.01	-1.74	-0.07	-1.38
17	3.59	3.56	3.52	-0.76	-0.03	-1.95	-0.07	-1.21
16	3.38	3.36	3.33	-0.66	-0.02	-1.63	-0.06	-0.97
15	3.16	3.14	3.12	-0.81	-0.03	-1.23	-0.04	-0.42
14	2.92	2.89	2.90	-1.12	-0.03	-0.92	-0.03	0.20

Table 7.4: *The measured and simulated drift velocities and the deviations for the 800 pm water content*

27. November, Water Content 1200 ppm (SCS), pressure 1020.0 mbar, 22 ^{o}								
U_{Drift}	v_{Drift} Meas.	v_{Drift} GF9	v_{Drift} GF7	Deviation of GF9 to Meas.		Deviation of GF7 to Meas.		Deviation of GF7 to GF9
in kV	in cm/μs	in cm/μs	in cm/μs	in %	in cm/μs	in %	in cm/μs	in %
22	4.10	4.17	3.98	1.70	0.07	-3.05	-0.13	-4.67
21	4.00	4.06	3.88	1.55	0.06	-2.99	-0.12	-4.47
20	**3.85**	**3.93**	**3.76**	**1.88**	**0.07**	**-2.44**	**-0.09**	**-4.24**
19	3.71	3.77	3.62	1.77	0.07	-2.37	-0.09	-4.08
18	3.54	3.60	3.46	1.73	0.06	-2.22	-0.08	-3.88
17	3.33	3.40	3.29	2.07	0.07	-1.46	-0.05	-3.45
16	3.14	3.19	3.10	1.62	0.05	-1.34	-0.04	-2.92
15	2.91	2.96	2.88	1.57	0.05	-0.86	-0.03	-2.40
14	2.67	2.71	2.66	1.47	0.04	-0.32	-0.01	-1.77

Table 7.5: *The measured and simulated drift velocities and the deviations for the 1200 pm water content*

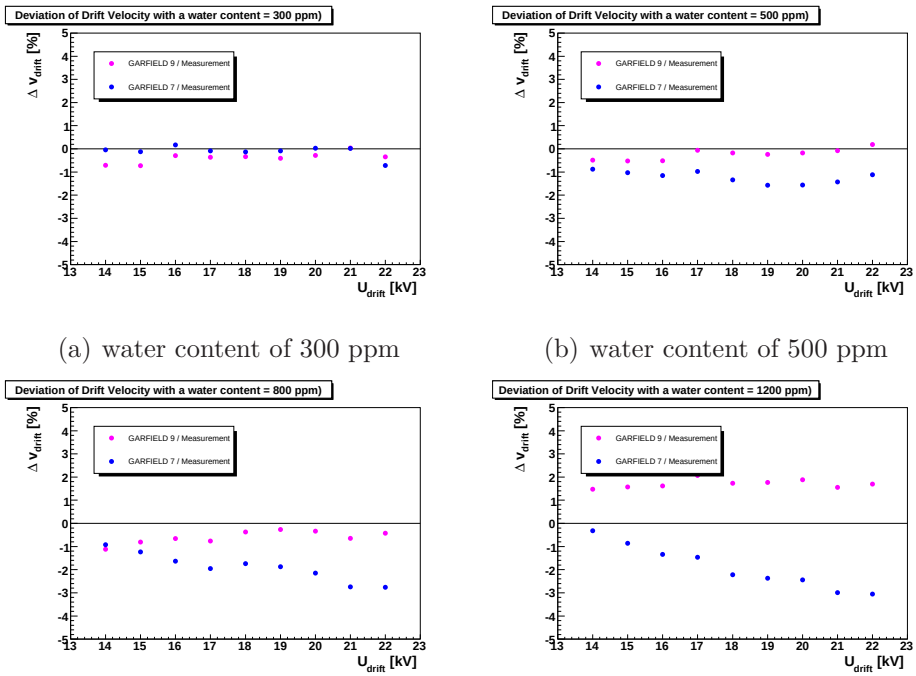

(a) water content of 300 ppm

(b) water content of 500 ppm

(c) water content of 800 ppm

(d) water content of 1200 ppm

Figure 7.7: *The deviations of the measured to the calculated drift velocity for MAGBOLTZ version 7 and 9*

7.4 Conclusion of the Drift Velocity Measurements

The measurments clearly demonstrated the strong limitation of the older MAGBOLTZ version 7, if concentrations of water higher than 500 ppm have to be added to the gas. To further improve the accuracy of the methods effects as attachment of water on the surface of the TPC or the storage of water in hydrophil materials had to be quantified. Such effects could be approximated more accurate, if a second water measurement device would be installed at the outlet of the TPC. This would quantify the difference between ingoing and outgoing water content. However the very good agreement of the comparison of measured drift velocities to the calculated values of MAGBOLTZ 9 is promising to finally determine drift velocities with an accuracy better than 1 % for water contens below 800 ppm.
It was shown that both an UV Laser and a slow control system are both appropriate tools to calibrate the drift velocity of a TPC. The study showed, that both methods are in agreement of about 1 % up to a water content of 800 ppm.

Both methods can be used as complementary methods to calibrate drift velocity. An easy cross-check of both methods is possible. This measurement increased significantly the reliability and the understanding of potential error sources of our TPC prototypes especially during the installation phases.
It also demonstrates the enormous importance to have a control system for the drift velocity, which is an absolutely mandatory parameter for all precision measurements with a TPC.
A nice feature of the UV laser was, that it is in principle easy applicable to a TPC if the accessibility is guaranteed. In our case the usage of simple optical devices as mirrors, lenses and beamsplitters was sufficient to achieve these first results. The whole method wass fast as one measurement needs only about one hour of data taking. With a faster electronic the drift velocity might be derived much faster. With readout speed of modern electronic this measurement could be done in minutes. The method is only limited by systematic not by statistical uncertainties, which is one of the main advantages of a laser system. Of course the operation of a laser system in a full detector would be questioned in terms of the accesibility.

The measurement of the drift velocity is not the only parameter, which can be derived from an UV laser system. It should be also possible to calibrate the electronic with such a system. It could also help to identify electric and magnetic field distortions. Espeially the magnetic field distortions should be easily detectable as a laser track would not be bended by the magnetic field. The laser could be an important calibration tool, especially in regard of a small magnetic field, which is needed in case of detectors of the ILC, which have to cope with large crossing angles.

Chapter 8

Performance Studies for the Simulation

The performance of the simulation discussed in Section 6.5 was investigated for the proposed reconstruction methods with single laser tracks. The reconsrtruction methods for single laser tracks do not suffer from limitations of the correct charge reconstruction in case of an other nearby track. All parameters, which are of importance to draw conclusions for the two track laser case are investigated. This concerns especially the ϕ angle, which denotes the angle in the xy-plane, the intercept, which denotes the reconstructed track position at y = 0 and the point resolution derived by the geometric mean method 6.4.1. The limitations of laser tracks, which are located on a fixed position on the pads and are therefore affected by the pad size, can be studied more easily for single laser track case. It is crucial for the following investigation of the two-track studies to know these systematic limitations of single tracks and take them into consideration for the interpretation of the results.
The performance of the two proposed reconstruction methods was investigated on the simulation level. As the input parameters of the simulation are known, the input and reconstructed values can be compared.
To demonstrate that the results of the Big TPC are transferable to the Medi TPC a comparison between these two detectors is done using cosmic particles.

8.1 Single Laser Track Studies

The data sample used for single laser tracks was taken during a measurement series in April 2005 with the Big TPC, whose parameters were given in Table 4.1. The laser entered the TPC at the second quartz window, but was not aligned to leave the TPC on the opposite side. Therefore the ϕ and θ angle are inclined. The components, for example the beam telescope of the setup were the same as the one presented in Figure 5.15 for the laser drift velocity measurement with the

Parameters of single laser track data sample	
Number of GEMs	2
Transfer Field	1350 V/cm
Induction Field	2670 V/cm
GEM 1	398.6 V
GEM 2	381.3 V
Pad Size	7×7 mm^2
Number of events	$\sim$ 2000

Table 8.1: *The table shows the parameters, that are different between the Big-TPC and the Medi-TPC.*

difference, that only the laser beam, which enters the second quartz window was used. The parameters of the Big TPC used for this data sample can be found in Table 8.1.

In Figure 8.1 the hit charge, the pulse charge and the maximal hit charge as defined in Table 6.1 are illustrated for the data and simulation sample. Both the mean value and the RMS of the hit charge distributions show an acceptable agreement (see Table 8.2). This is also valid for the pulse charge and the maximal hit charge distribution. It demonstrates, that the charge distributions on the pads can be modeled by the simulation.

Figures 8.2 and 8.3 show the reconstructed ϕ and intercept distributions. Both distributions agree for the mean value and the RMS for both reconstruction methods between data and simulation. The mean values and the RMS of the distributions can be found in Table 8.2. The Global Fit method reconstructs ϕ and intercept of the simulation sample closer to the true values as the Chi-Squared method. To investigate if this behavior depends on a specific set of parameters or is a general behavior, both methods are compared for three intercept and five different ϕ angles. The results are shown in the following section 8.1.1.

Figure 8.4 shows the number of active pads in a specific row averaged over the hits of the whole sample. The number of pulses for each row are illustrated for data and simulation samples. The hits of the first four rows of data and simulation consists mainly of two active pads per hit. The mean value for the number pulses in these rows are consistent for data and simulation samples. The next four pad rows show a different behavior. The amount of hits, which consists of only one pad, are significantly higher in the data than in the simulation. The inclination of the track in the xy plane, given by the ϕ angle, leads over the length of the pad plane of 56 mm to a shift of about 2.4 mm, if assuming a ϕ angle of 2.5 °. This shift is sufficient to position the charge in a row on only one pad.
Several reasons could be responsible for the difference of average number of active pads per row. It could be possible, that the diffusion and defocusing coefficient

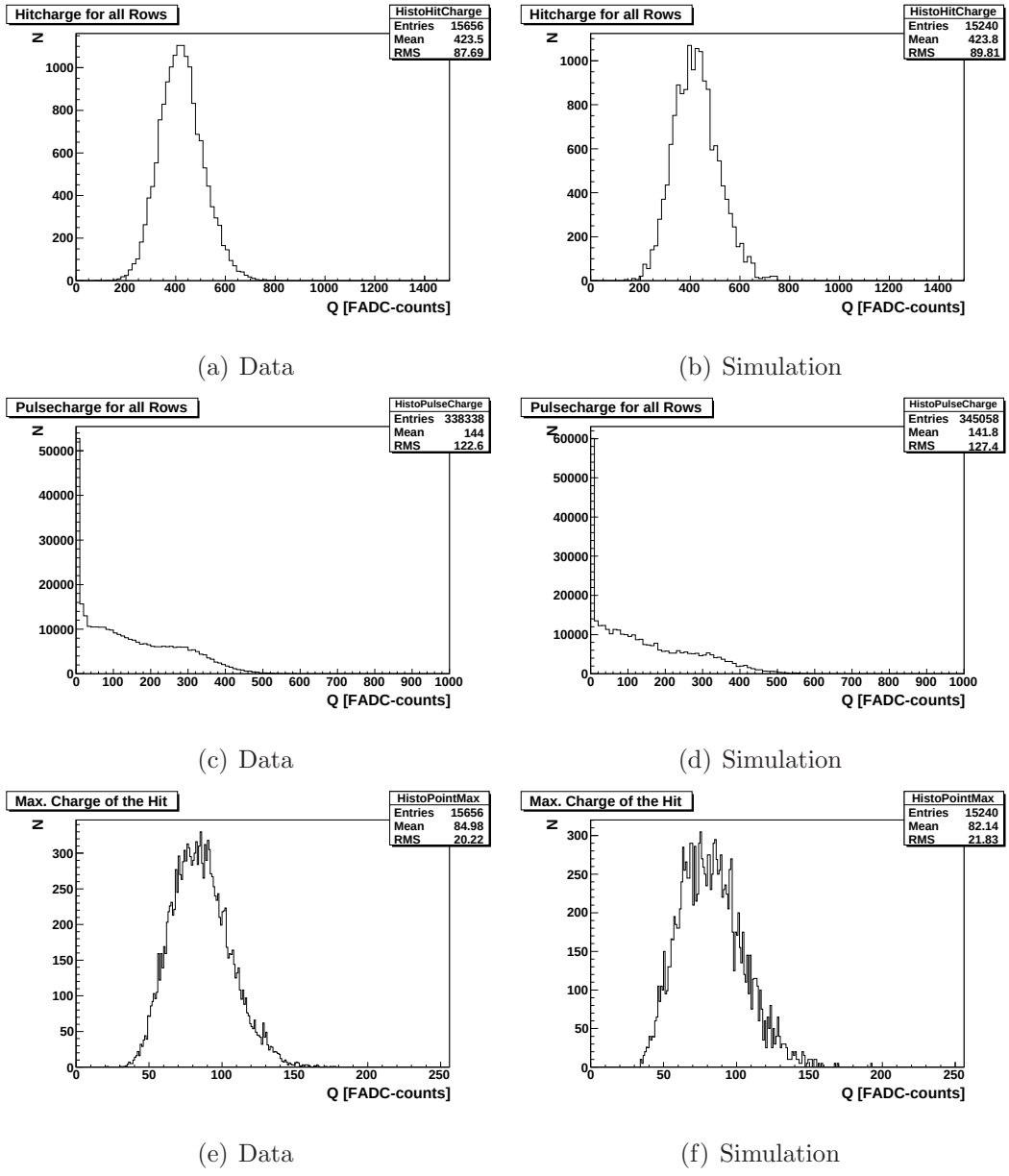

(a) Data (b) Simulation

(c) Data (d) Simulation

(e) Data (f) Simulation

Figure 8.1: *The figure illustrates the hit charge, the pulse charge and the maximal charge per hit for data and simulation. The simulation can describe the hit, pulse and maximal hit charge in mean value and RMS in good agreement with the data.*

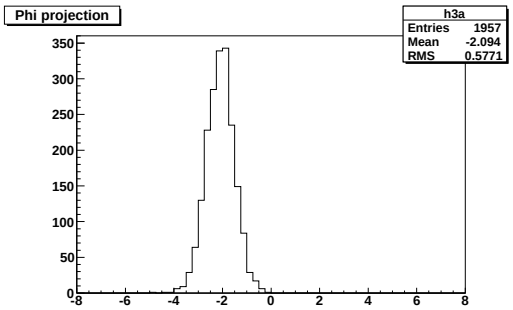

(a) Data / ϕ (Chi-Squared)

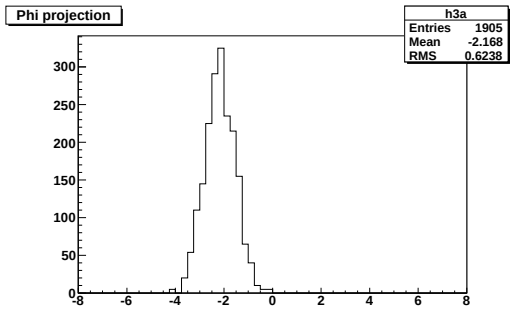

(b) Simulation / ϕ (Chi-Squared)

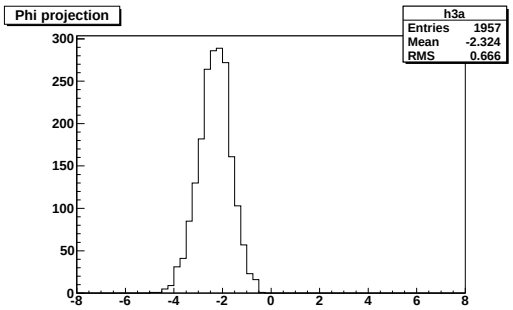

(c) Data / ϕ (GFM)

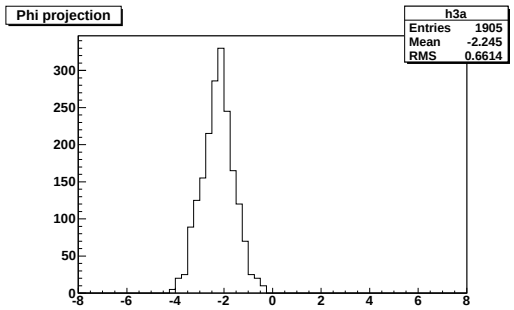

(d) Simulation / ϕ (GFM)

Figure 8.2: *The figures show the reconstructed ϕ angle for both reconstruction methods and. Data and simulation agree within a margin of 4 % for the mean values of both reconstructions.*

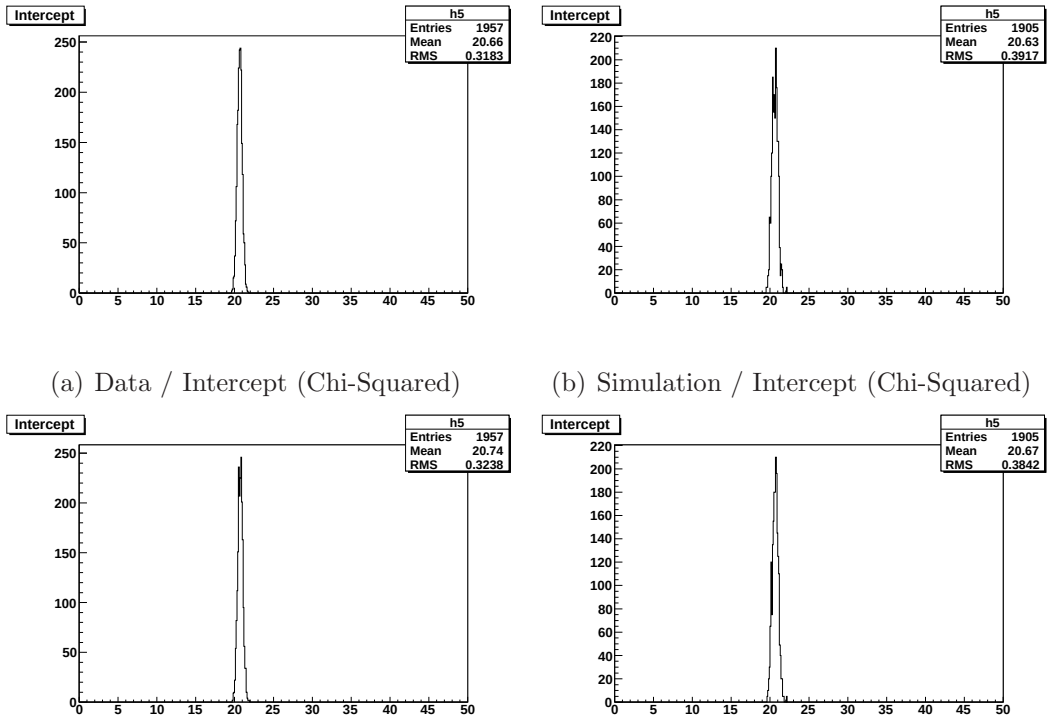

(a) Data / Intercept (Chi-Squared)

(b) Simulation / Intercept (Chi-Squared)

(c) Data / Intercept (GFM)

(d) Simulation / Intercept (GFM)

Figure 8.3: *The figures show the reconstructed intercept for both reconstruction methods and. Data and simulation agree within a margin of below 0.5 % for the mean values of both reconstructions.*

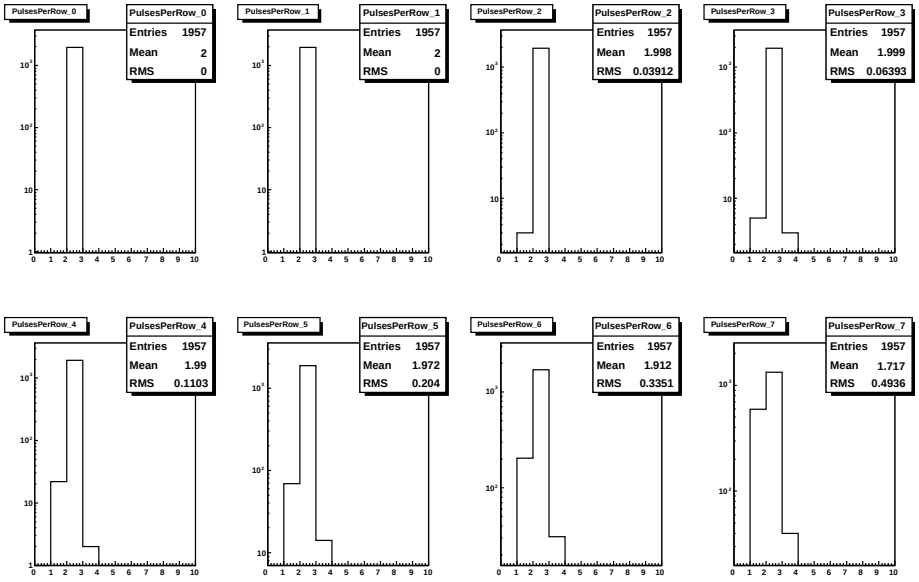

(a) Number of Pulses per Row / Data

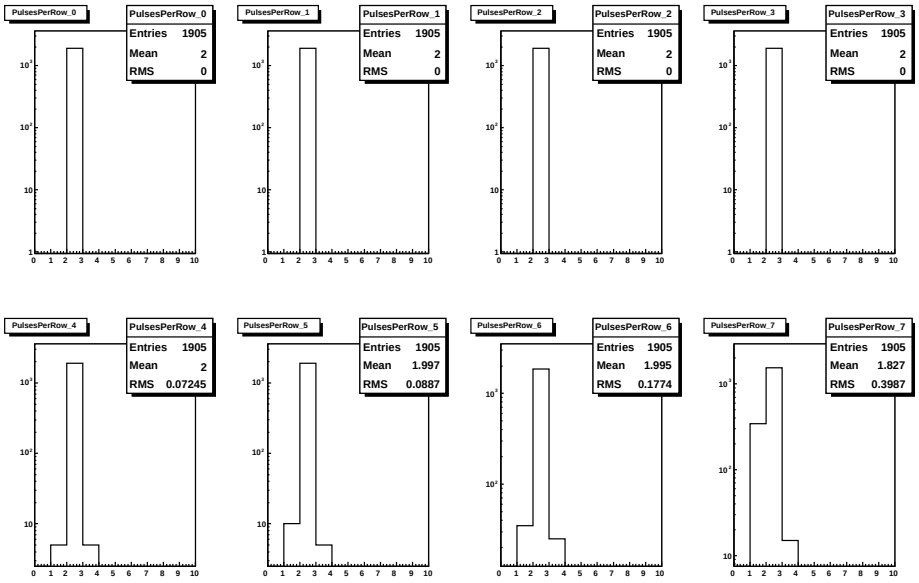

(b) Number of Pulses per Row / Simu

Figure 8.4: *The figure shows the number of active pads in each row for the data and simulation sample. A difference between both samples can be observed in the last two rows, where the data sample shows a significant higher number of one pulse hits than the simulation.*

are overestimated. Both parameters were taken from MAGBOLTZ 7 calculations, which are changed in the newer version 9 by about 10 to 15 %. Another effect could be laser intensity fluctuations, as the laser intensity enters quadratically in the primary charge production (see. Equation 2.27). The laser intensity fluctuations were estimated in the simulation by a correction parameter of ± 10 %. Measurement of the beam profile in future measurements will provide a more profound knowledge of the intensity fluctuations of the laser [93]. In combination with a fixed threshold these fluctuations are responsible for the increase of one and three pulse hits, which can be observed in the data (see Figure 8.5).

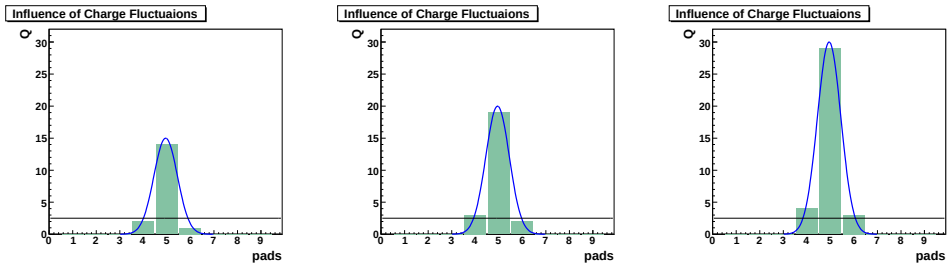

(a) (b) (c)

Figure 8.5: *The figure demonstrates the influence of the charge in regard of the number of pulses, that are found in a hit. In Figure (a) to (c) the maximum of the Gaussian distribution is varied from 15 to 30 counts. The threshold is set to 2.5. Due to the variation of the maximal charge 1, 2 or 3 active pads can be found.*

An effect, which was not included in the simulation was the changes of drift velocity caused by water, which can also alter the diffusion. This effect can be neglected as a variation of the drift velocity of 4.2 cm/μs by about 5 % would lead at a distance of about 30 cm to variation of diffusion by 63 μm. Compared to the total width of the charged cloud of 2.5 mm. This effect is negligible.

In Figure 8.6 the point resolution is plotted for each row. The filled dots show the result for the measurement, the unfilled dots the results for simulation. The triangles represent the theoretical limit, which can be calculated by the width of the charged cloud after diffusion divided by the number of primary electrons reaching the gas amplification stage. This gives the statistical uncertainty to the mean value of the true track position, which is the point resolution.
Several effects degrade the point resolution. Losses of primary electrons reaching the amplification stage will significantly degrade the point resolution. Losses of primary electrons can come from attachment by gas impurities (for example oxygen), as well as from electrons, which can not be forced into the GEM holes.

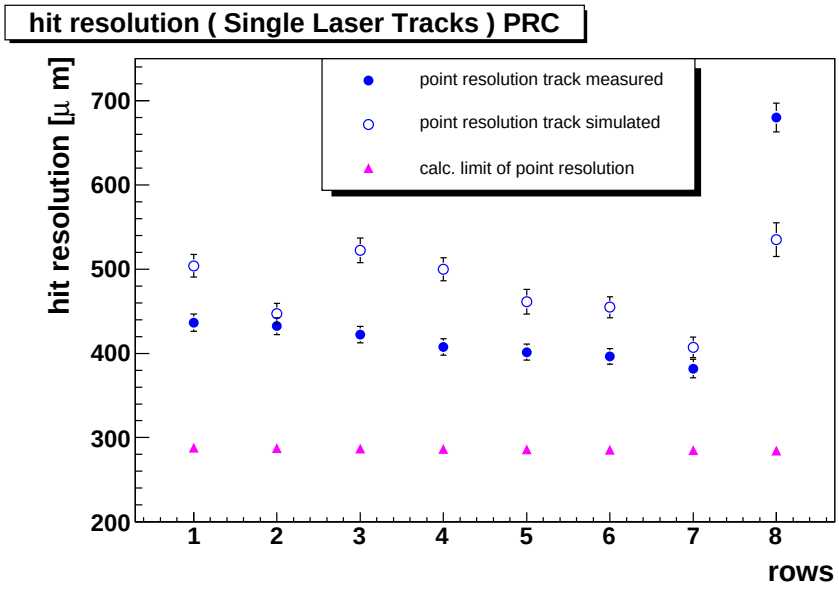

(a) Chi-Squared with PRC

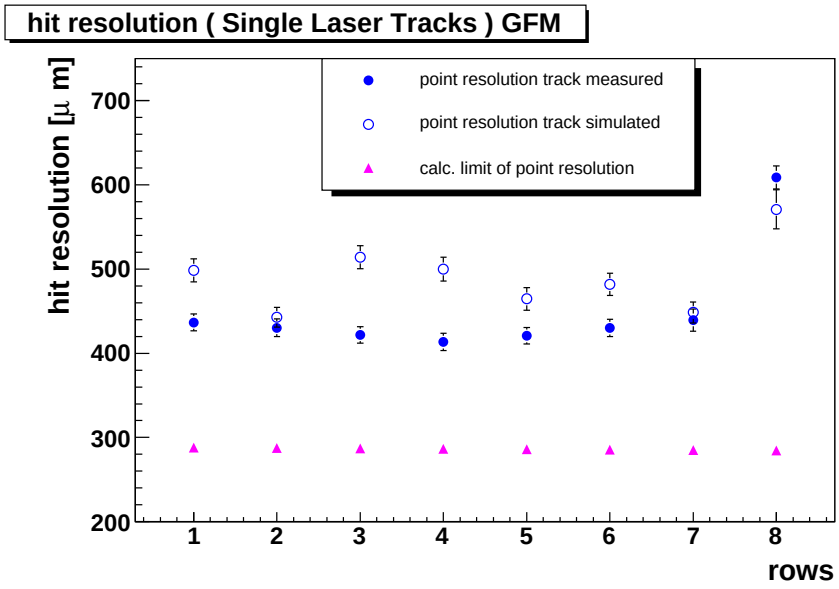

(b) Global Fit Method (GFM)

Figure 8.6: *The Figure illustrates the point resolution of data and simulation for both reconstruction methods. The blue filled dots represent the results for data the blue unfilled dots the simulation and the purple triangles the theoretical possible point resolution.*

The transfer and induction fields between the GEMs, the defocusing, broadens the width of the signal and can therefore add an uncertainty to the determination of the mean value of the track position.
A real detector has a finite number of pads with a specific size. Therefore the charge is sometimes distributed over few pads, which limits the accuracy to find the true position by center of gravity. The difficulties determining the true position are described in Section 6.2.
All these effects are responsible for a degradation of the theoretical possible point resolution. Two methods for the reconstruction of the point resolution are used. In Figure 8.6(a) the point resolution of measured and simulated tracks is illustrated for the Chi-Squared method, in Figure 8.6(b) the point resolution is illustrated for the Global Fit method. The point resolution reconstructed with the Chi-Squared method for all rows is $\text{res}_{data} = 423.3 \pm 3.6$ μm and $\text{res}_{simu} = 471.3 \pm 4.8$ μm. Data and simulation show similar characteristics for row 1 to 8. For both data and simulation the point resolution improves for increasing rows. Both curves show a strong degradation of the point resolution in the last row coming from a corresponding increase of single pulse hits in the last row. For the single pulse hits the hit position is located in the center of the pad, which pulls the track to this position. As this single pulse hits occur on the last row the lever arm to the track is maximal. The difference in the size of this effect is consistent with higher number of single pulse hits in the data than in simulation. The simulation has a worse resolution than the data. There is a difference of about 50 μm for the total point resolution between data and simulation. As the missing part of the point resolution has to be added quadratically, the missing contribution can be calculated by $\sqrt{(471.3\ \mu m)^2 - (423.3\ \mu m)^2} = 207.2\ \mu m$. This means an uncertainty of about 50 % deriving from the comparison of single laser tracks for the Chi-Squared method can estimated.
For the Global Fit method a similar behavior for the point resolution of data and simulation curves can be observed. Although the point resolution of data and simulation are more converged a difference of $\text{res}_{data} = 440.3 \pm 3.6$ μm and $\text{res}_{simu} = 479.8 \pm 4.9$ μm remains. The difference of about 40 μm corresponds to a missing contribution of the resolution of $\sqrt{(479.8\ \mu m)^2 - (440.3\ \mu m)^2} = 190.6\ \mu m$. This is an uncertainty of about 43 %.

Diminishing either the diffusion or defocusing coefficient in the order of 10-15 %, or both values at the same time did not significantly change the point resolution. The point resolution of the simulation could only be reduced by values of 10 μm. Neither the inclusion of an additional laser width of about 140 μm nor the exclusion of laser intensity fluctuations, leads to a significant reduction of the point resolution. None of these parameters could explain the difference in point resolution.

One general limitation of the simulation was the treatment of GEM-

amplification stage. The simulation scales the number of primary electrons arriving on a pad by a conversion factor, which translates the primary charge in FADC counts. The implementation of the gas amplification stage was too primitive to allow more detailed conclusions on the point resolution. A more sophisticated simulation, which was especially developed to include a more realistic modeling of the GEM gas amplification stage, might help to overcome this shortcomings in the future [94].

To demonstrate the major impact of single pulse hits to degradation of the resolution, the distribution for distances and residuals in each row are plottted. In Figure 8.7 the data events are illustrated for the Chi-Squared method with and without a cut on single pulse events. In the rows, where a significant number of single pulse hits was observed also a second peak occurs. Applying a cut, which removes the single pulse hits, a much more symmetric distribution around the zero value for distance and residuals appears.
The same effect can be seen for the simulation, which is shown in Figure 8.8. As a significant number of single pulse hits can only be observed in the last row, the cut effects only the distributions of distances and residuals for this row.
As more rows of the data samples have contributions of single pulse hits than the simulation the cut improves the point resolution also more significantly in case of the data samples. For the Chi-Squared method the point resolution res_{data} = 398.6 ± 3.4 μm and res_{simu} = 460.0 ± 4.7 μm, for the Global Fit method res_{data} = 416.4 ± 3.5 μm and res_{simu} = 467.1 ± 4.6 μm.
In the following the Chi-Squared and Global Fit method are compared on simulation level to investigate the performance of reconstructing basic track parameters.

8.1.1 Comparison Chi-Squared and Global Fit Method

To study the performance of both reconstruction methods, the simulation was used to produce 5 different ϕ angles for 3 different intercepts. Both reconstruction methods were applied to compare the reconstructed with the true input values. All other parameters such as number of primary electrons, diffusion and defocusing coefficient were kept constant. The three intercepts were chosen such that different charge sharing patterns were realized on the pads. The values for the intercept B1 are 19, 22.5, and 24.5 mm. If the values were divided by the width of the pad of 7 mm one gets a remainder of 5, 1.5 and 3.5 mm on a single pad (see Figure 8.9). With a σ of the charge cloud of about 2.5 mm, one expects for the ratio of σ charge cloud to pad width a signal, which is located on average on at least 2 pads (see Figure 6.4(b)).

In Figure 8.10 the number of pulses for each row is illustrated for the three intercepts. The distributions shows a ϕ angle of 2.0°. The same pad effects as mentioned in the previous section can be observed in the Figures 8.10(a) and 8.10(c). Here some of the rows show strong fluctuations between one and two

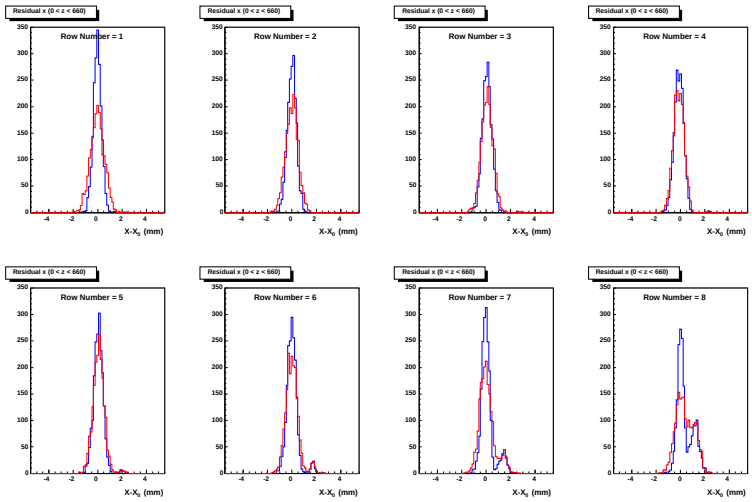

(a) without cut on single pulses

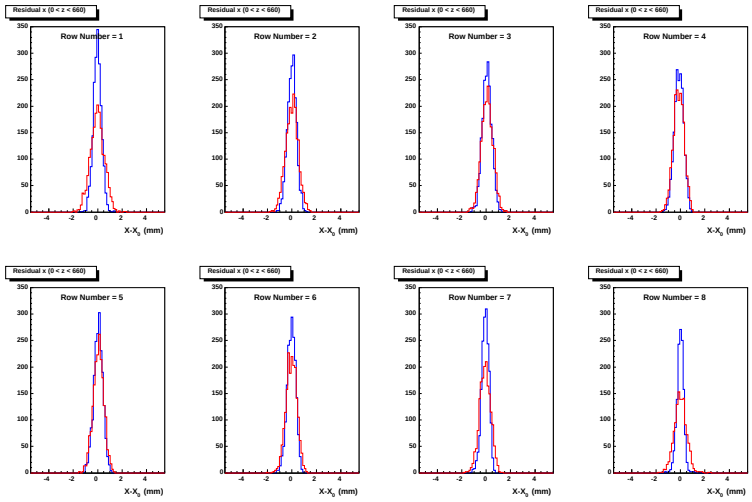

(b) with cut on single pulses

Figure 8.7: *Distributions for distances and residuals in each row. The data events were reconstructed with the Chi-Squared method. A clear improvement of the distributions for the last three rows can be observed, if applying a cut, which withdraws the single pulse hits. Thess rows had a significant number of single pulse hits.*

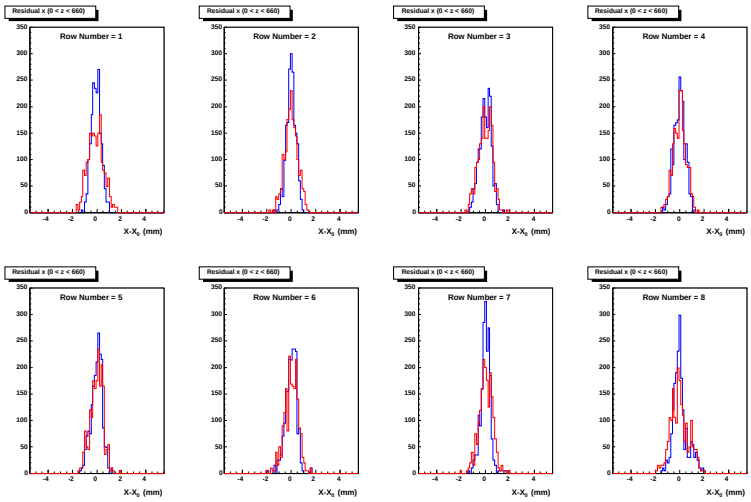

(a) without cut on single pulses

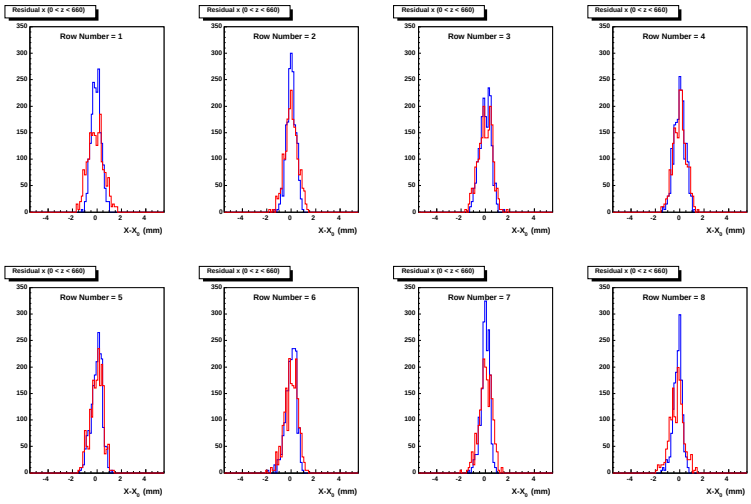

(b) with cut on single pulses

Figure 8.8: *Distributions for distances and residuals in each row. The simulation events were reconstructed with the Chi-Squared method. An improvement of the distributions for the last row can be observed, if applying a cut, which withdraws the single pulse hits. This row had a significant number of single pulse hits.*

Parameter	Data	Simulation	Dev. of the Mean (Sim./Data) [%]
Charge of the Hits [FADC-counts]	423.5 ± 87.69	423.8 ± 89.81	0.07
Charge of the Pulses [FADC-counts]	144.0 ± 122.6	141.8 ± 127.4	1.50
Maximal Charge of Hits [FADC-counts]	85.0 ± 20.22	82.1 ± 21.83	3.34
Phi reconstructed (Chi-Squared) [°]	-2.09 ± 0.577	-2.17 ± 0.624	3.8
Phi reconstructed (GFM) [°]	-2.32 ± 0.666	-2.25 ± 0.661	3.0
Input parameter of the Simulation [°]		-2.5	
Intercept reconstructed (Chi-Squared) [mm]	20.66 ± 0.318	20.63 ± 0.392	0.1
Intercept reconstructed (GFM) [mm]	20.74 ± 0.324	20.67 ± 0.384	0.3
Input parameter of the Simulation [mm]		20.74	
Point Resolution (Chi-Squared) [μm]	423.3 ± 3.6	471.3 ± 4.8	11.3
Point Resolution (GFM) [μm]	440.3 ± 3.8	479.8 ± 4.9	9.0
Point Resolution (Chi-Squared) [μm] (with cut)	398.6 ± 3.4	460.0 ± 4.7	15.4
Point Resolution (GFM) [μm] (with cut)	416.4 ± 3.5	467.1 ± 4.6	12.2

Table 8.2: *The table summarizes the important parameters for both data and simulation samples with the corresponding deviations of the mean value.*

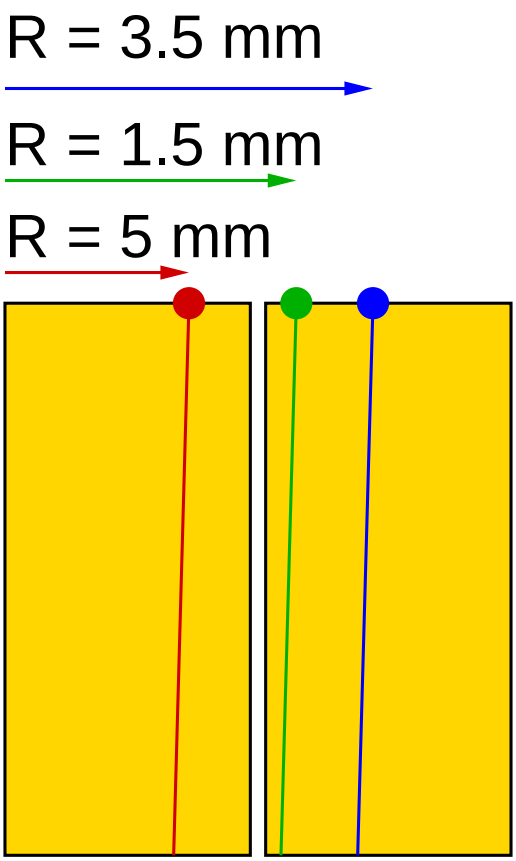

Figure 8.9: *The figure shows the three intercepts. The value R is the distance between the beginning of a pad and the the laser. The three intercepts were used to investigate the Chi-Squared and Global Fit method for the same* $\sigma_{diff./def.}$. *The intercepts were chosen such that three different charge sharing patters were realized on the pads.*

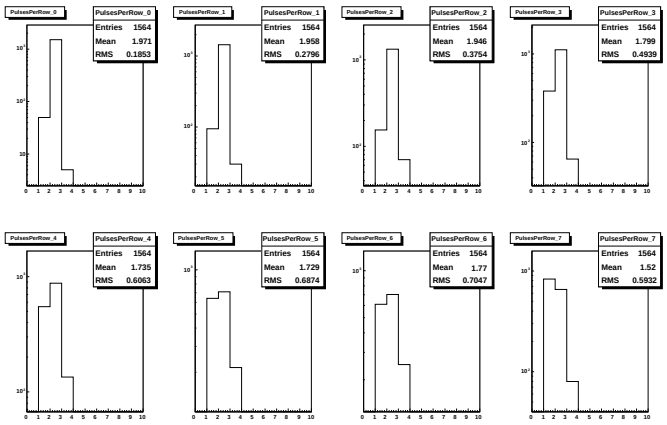

(a) Intercept = 19.0 mm, remainder = 5 m

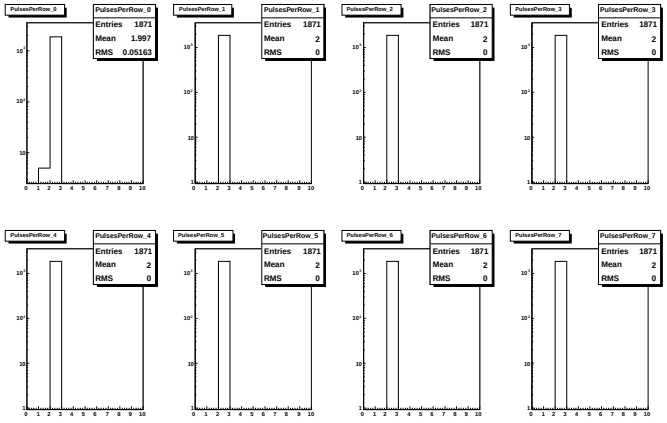

(b) Intercept = 22.5 mm, remainder = 1.5 mm

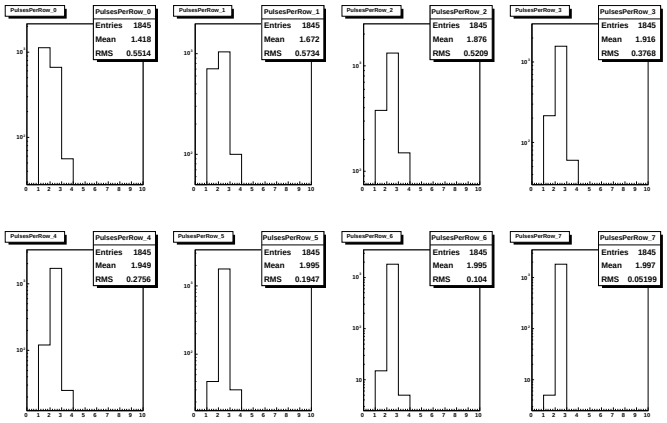

(c) Intercept = 24.5 mm, remainder = 3.5 mm

Figure 8.10: *The figure shows the number of pulses per pad for the three intercepts for a ϕ-angle of 2.0 °. Due to the track inclination the mean value of the charge is moving, causing a significant change of the number of pulses per row.*

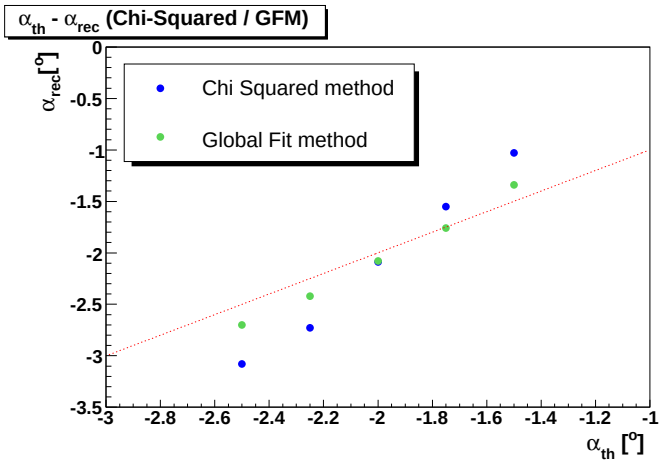

(a) Intercept = 19.0 mm, remainder = 5 mm

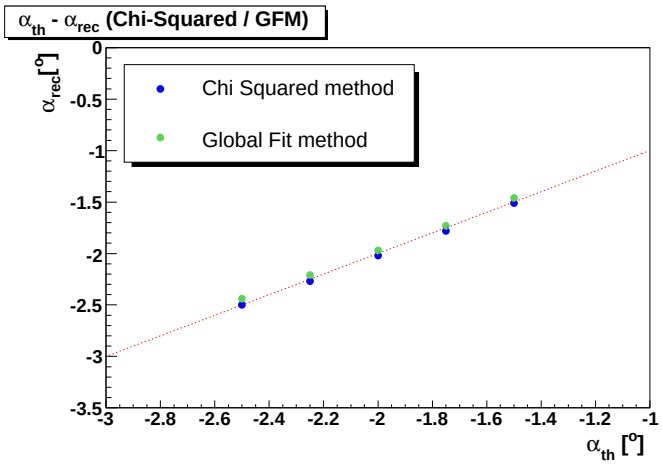

(b) Intercept = 22.5 mm, remainder = 1.5 mm

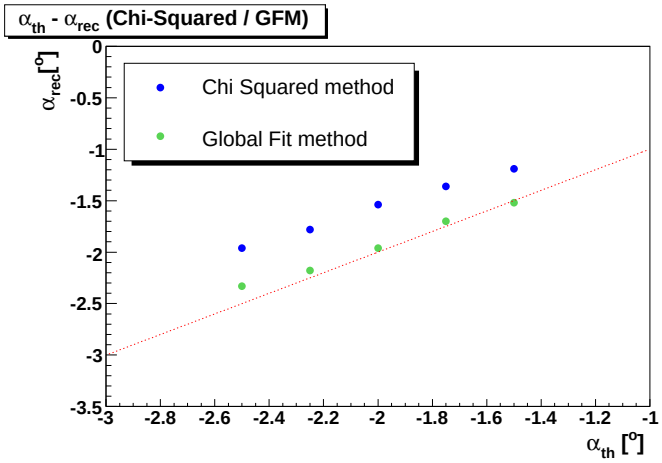

(c) Intercept = 24.5 mm, remainder = 3.5 mm

Figure 8.11: *The figure shows the reconstructed versus the input ϕ angle for the three intercepts. The general outcome of the comparison shows, that the GFM reconstructs for all three settings the ϕ angle closer to the input value than the Chi-Squared method.*

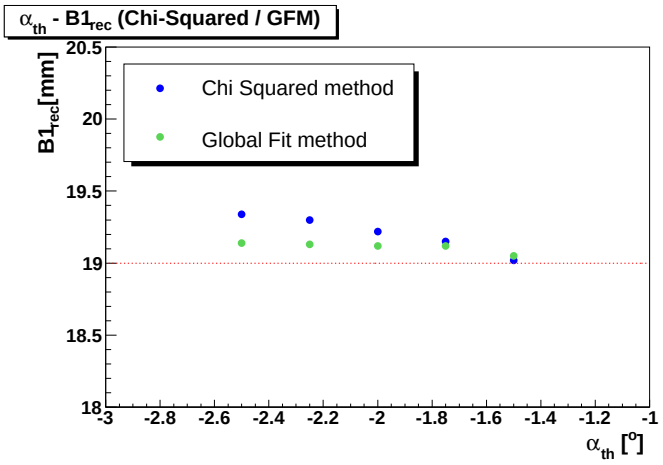

(a) Intercept = 19.0 mm, remainder = 5 mm

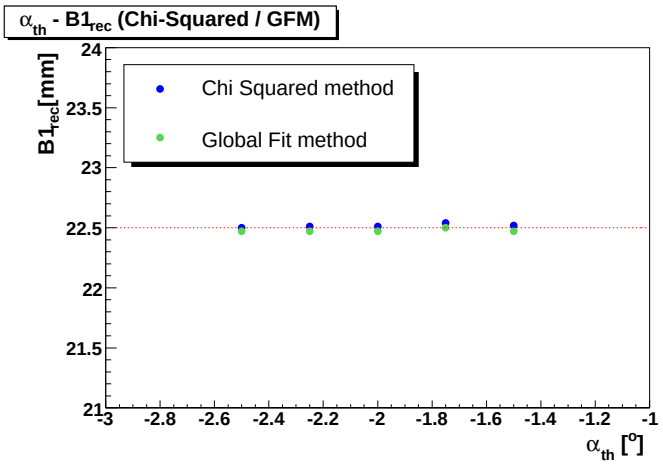

(b) Intercept = 22.5 mm, remainder = 1.5 mm

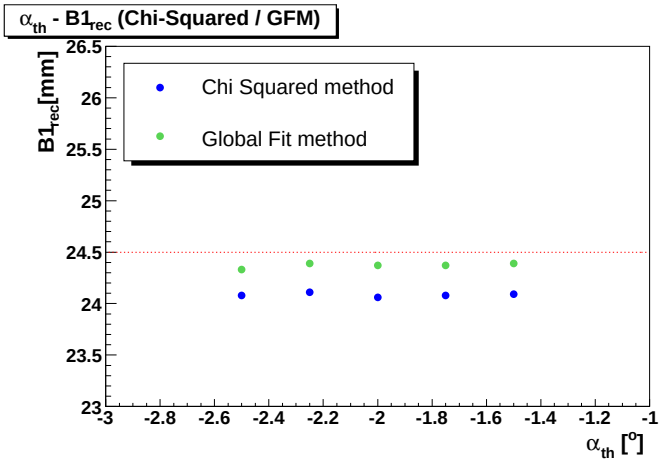

(c) Intercept = 24.5 mm, remainder = 3.5 mm

Figure 8.12: *The figure shows the reconstructed versus the input value for the intercept of the five ϕ angles. The results are consistent with Figure 8.11, where the GFM reconstructs this parameter closer to its input value.*

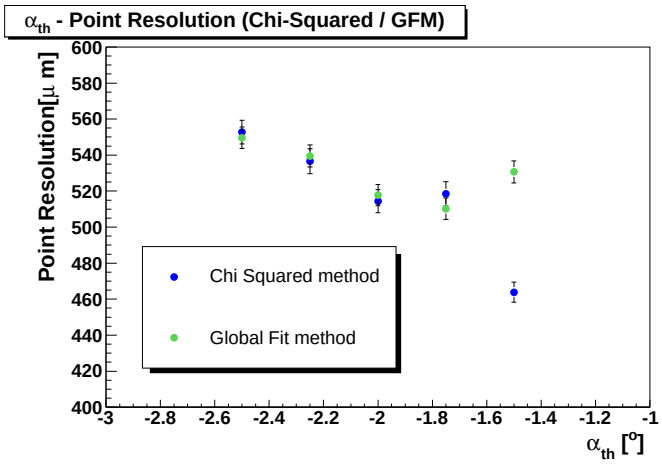

(a) Intercept = 19.0 mm, remainder = 5 mm

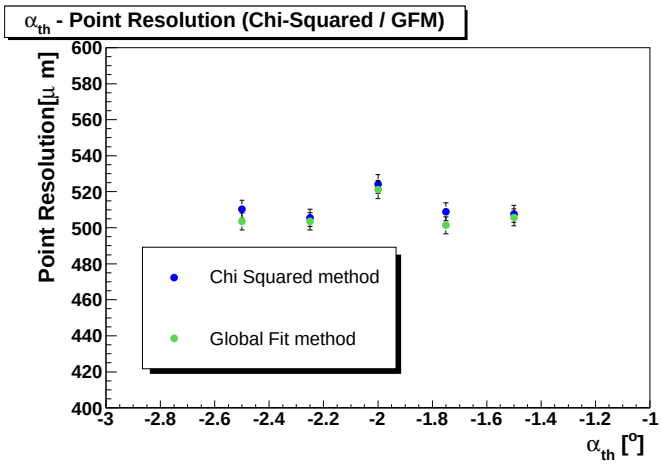

(b) Intercept = 22.5 mm, remainder = 1.5 mm

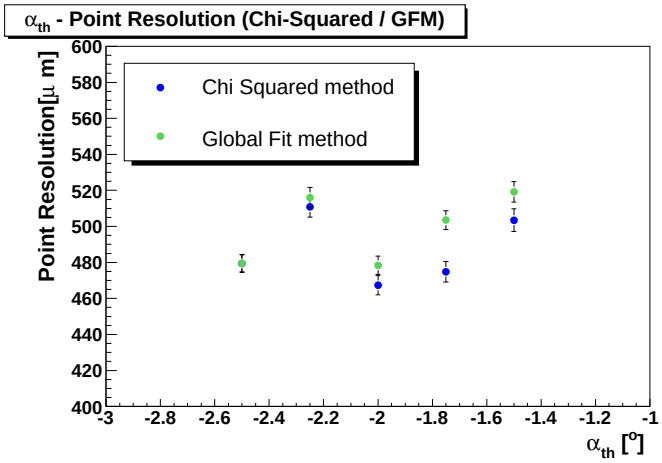

(c) Intercept = 24.5 mm, remainder = 3.5 mm

Figure 8.13: *The point resolution of the three investigated intercepts are plotted for the five different input angle of ϕ. Despite the obvious advantage of the GFM in reconstructing the basic input parameters, deviation of the point resolution for both reconstruction methods is rather exceptional.*

pulses per row, which is changing significantly due to the inclination of the ϕ angle along the y-axis. In Figure 8.10(b) where the inclined track starts almost in the center between two pads the one and three pulse hits vanish. This had a strong impact to the reconstruction of the parameters as the ϕ angle and intercept. In Figure 8.10(a) the pulses per row for an intercept of 19 mm are plotted, which leads to a remainder of 5 mm. The track inclination moves the mean value of the charge to the center of the pad. The consequence is a significant rise in the number of one pulse hits, which leads to limitations on the reconstruction of track parameters. Figure 8.10(b) shows the pulses per row for an intercept of 22.5 mm and a remainder of 1.5 mm. The track inclination moves the mean value of the charge between two pads. Here always two pulses per row can be reconstructed. Due to the complete absence of one pulse hits a good track parameter reconstruction is expected. In Figure 8.10(c) an intercept of 22.5 mm and a remainder of 3.5 mm. The track inclination moves the mean value of the charge from the center of the pad to its edge. Therefore the first rows show a significant contribution of one pulse hits. This contribution is reduced to zero for the last rows.

In the Figure 8.11 and 8.12 the ϕ angle and the intercept are reconstructed for three different intercepts and five different ϕ angles. As expected from the number of pulse distribution of each row the reconstruction of the track parameters for intercept = 22.5 mm are closest to the input parameters. For the intercepts = 19.0 and 24.5 mm, where a significant fraction of single pulse hits occur, the reconstructed values differ for both methods from the input values. However the Global Fit method has advantages in the reconstruction of these two globally reconstructed parameters. Even for the case of large contribution of single pulse hits the values for ϕ and the intercept reconstructed with the GFM are much closer to the input values than the ones reconstructed with the Chi-Squared method. Therefore the GFM seems for that specific case more appropriate to reconstruct these key parameters.

In Figure 8.13 the point resolution for all settings are plotted. Figure 8.13(b) shows the the point resolution for intercept = 22.5 mm. Here the point resolutions for both methods are in good agreement within their statistic uncertainties. The intercepts of 19.0 and 24.5 mm can not contain this good agreement for all ϕ angles. Nevertheless strong deviations between the two reconstruction methods concerning the point resolution seems to be the exception.

Two things should be kept in mind. First the basic production mechanism, is not the production mechanism of MIPs, which follow the Landau statistic, but of laser tracks, which follow the Gauss statistic. So the transferability to minimal ionizing particles (MIPs) might suffer from this difference in charge production. Figure 8.14 shows the hit charge distribution of the laser sample, which has already

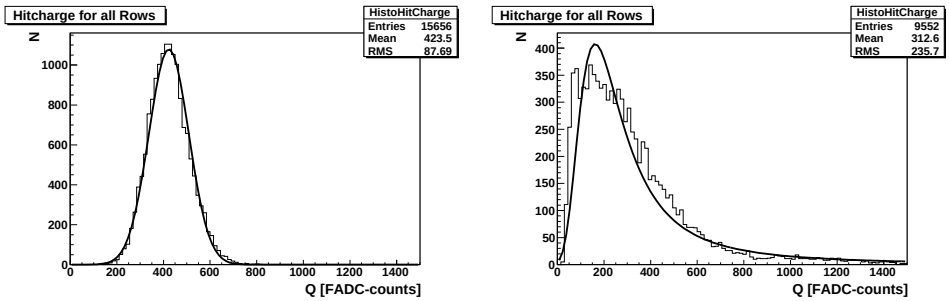

(a) Gaussian ionization of the laser (b) Landau ionization of MIPs

Figure 8.14: *The figure illustrates the difference in charge production between a laser and cosmic particles.*

been shown in Figure 8.1(a). This distribution fits perfectly to a Gaussian distribution. The hit charge distribution of cosmic particles measured with the Medi TPC at 3 T is shown in 8.14(b). The distribution fits to a Landau distribution. The difference in the charge production processes for both distributions is clearly demonstrated.
The simulation suffers from shortcomings as mentioned in the previous section. An agreement of data and simulation can not be achieved with regard of the point resolution neither with the Chi-Squared nor with the Global Fit method. This limitations have to be taken into account in the chapter about the track separation.

8.2 Transferability of the Results

The results of the single laser tracks using the Big TPC were compared to the Medi TPC to demonstrate, that both detectors are dealing with similar systematic limitations of the reconstruction. As laser tracks were not available for both detectors, the comparison was done with cosmic particles. 0 T data of the Big TPC were compared with 3 Tesla data of the Medi TPC. The reason for an comparison between these two settings was, that the ratio between the width of the charge cloud and the pad size should should be most comparable for these two settings. The design parameters of the Medi TPC are given in Table 4.1.
The result of this comparison for both detectors is illustrated in Figure 8.15, where the ratio of the charge cloud to pad width is plotted versus drift length. Despite all the differences between the two detectors Figure 8.15 shows an acceptable agreement between the mean number of hits. The blue points represent the values for the Big TPC in dependency of the drift length, the red points the values of the same drift length for the Medi TPC. Both curves show a significant difference

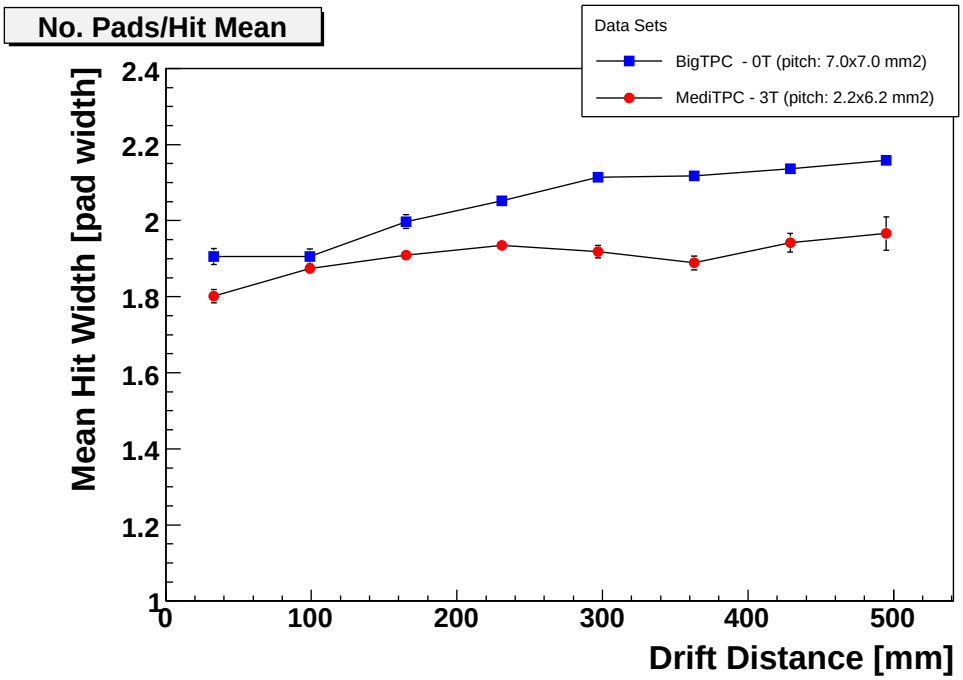

Figure 8.15: *The plot shows the mean hit width counted in pads for the Big (blue dots) and Medi TPC (red dots). Both detectors show a comparable hit width for drift length of 50 cm. The decrease of the hit width of the Medi TPC is caused by the trigger geometry.*

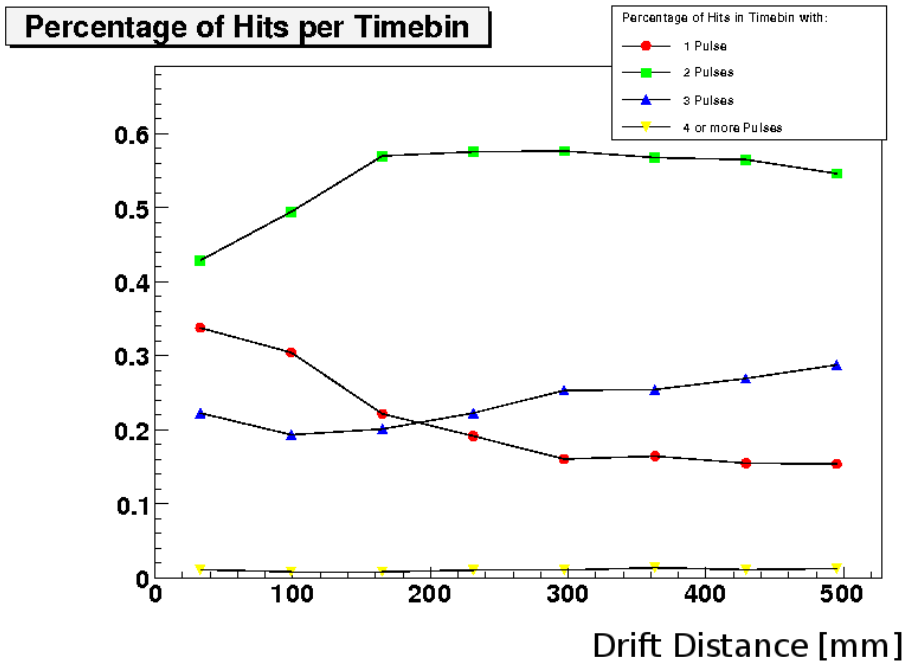

(a) Result for the Big TPC

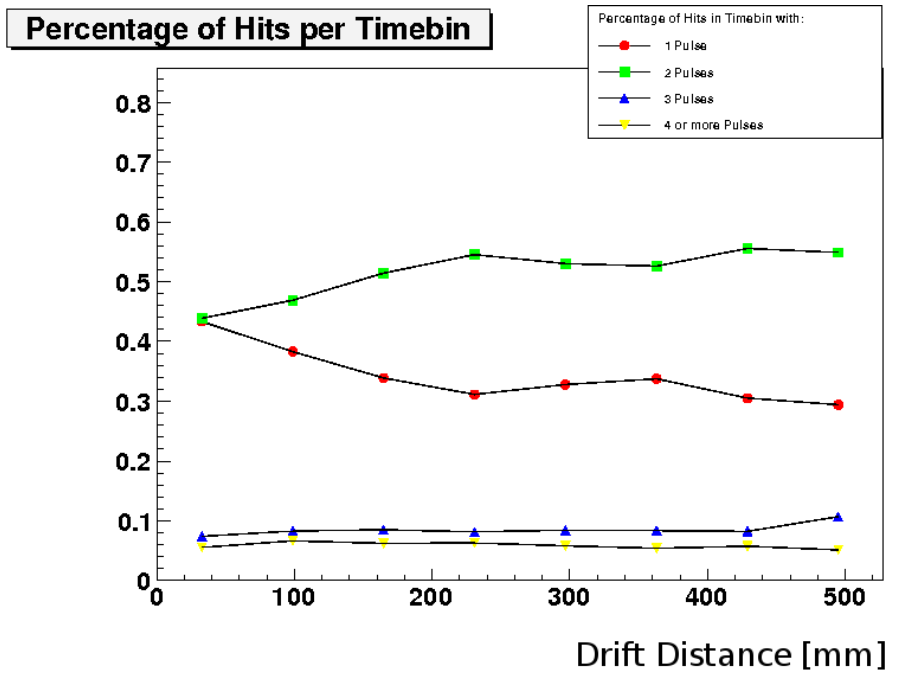

(b) Result for the Medi TPC

Figure 8.16: *The figure shows the fraction of single, double and triple pulse hits for the Big and Medi TPC. The significant fraction is the number of single pulse hits, which is the main limitation of reconstruction. Both detectors show a fairly comparable number of double pulse hits, but a fairly different number of single pulse hits.*

in dependency of the drift length. The values of the Big TPC rise constantly with drift length, which refers to the increase in diffusion at 0 T. For the Medi TPC this increase of the mean hit width can not be observed with increasing drift distance. The drop of the values at a drift length of 50 cm corresponds to the trigger geometry, which were not set properly during the measurement series as the main focus of the measurement were laid on the laser studies. This demonstrates, that at 3 T the mean hit width is limited by pad size and not by diffusion for the first 50 cm of drift.
The region, which is of interest for the laser studies of this and the following chapter, is between 15 and 30 cm. For this region the mean hit width of both detectors differs in the order of 5 to 10 %, which seems an acceptable agreement for two detector with the mentioned differences. To investigate the composition of the mean hit width the fraction of single, double and triple pulses per hit is plotted in dependency of the drift length in Figure 8.16. Figure 8.16(a) shows the composition of pulses for the Big TPC, Figure 8.16(b) the composition of pulses for the Medi TPC. The samples show a comparable fraction of 55 % for double pulse hits in the region of interest between 15 and 30 cm, but the number of single and triple pulse hits are significantly different for both detectors. The fraction of single pulse hits, which are the main limitation for the reconstruction is 22.5 % to 18 % for the Big TPC and is about 30 % for the Medi TPC.

This means the results of the single laser tracks for the Big TPC with a magnetic field of 0 T should be comparable to the Medi TPC layout at 3 T. However the limitations in reconstruction should be far more significant for the Medi TPC. The differences of both detectors are consistent with the expectations of the diffusion and defocusing coefficients. The Big TPC show a characteristic rise due to diffusion, which leads to a decrease of the one pad hits and an increase of the triple pad hits, with increasing drift length. For the Medi TPC, which is limited not by diffusion, but pad size, the values for single, double and triple pad hits stay constant, except for the first 10 cm.

Chapter 9

Two Track Separation Studies for a TPC

In this chapter the results of the track separation studies are presented. First a motivation for the study is given followed by a description of the data and the corresponding simulation samples. Afterwards the performance of both samples is tested by comparing some key parameters. The x separation performance is tested for the conventional Chi Squared and the Global Fit Method. Both are described in Chapter 6 in Sections 6.4.2 and 6.4.3. One has to distinguish here between separation performance of the total track on the one hand and the separation performance of the hits on the other hand. As the fixed position of the laser has a big influence to the performance of the separation, the influence of this systematic effect to the reconstruction has been investigated with the simulation tool.

9.1 Motivation

To achieve the required momentum resolution for the whole tracking system, the TPC needs a precision of:

$$\left(\frac{\sigma_{p_T}}{p_T^2}\right)_{TPC} = 1.5 \times 10^{-4} GeV^{-1} \tag{9.1}$$

The momentum resolution of a TPC is related to the point resolution by the Gluckstern formula [43] which has already been described in equation 2.21. The formula is repeated here as a short reminder $\left(\frac{\sigma_{p_T}}{p_T^2}\right)_{TPC} = \frac{\sigma_{r\phi}(B)}{0.3L^2B}\sqrt{\frac{720}{N+4}}$, where $\sigma_{r\phi}(B)$ denotes the point resolution, L the length of the lever arm, B the magnetic field and N the number of measurement points, which is maximal 200 pad rows. As mentioned in the introduction, this work is not based on the current pad size used for the LDC, but the previous detector layout of the TESLA detector. Therefore

Drift distance	10 cm	200 cm
rϕ point resolution	70 μm	190 μm
z point resolution	0.6 mm	1 mm
double hit resolution in rϕ	< 2.3 mm	
double hit resolution in z	< 10 mm	

Table 9.1: *Resolution requirements given for a TPC in the TDR concept [42]*

the requirements for the point resolution and the double hit separation for the TESLA detector are given in Table 9.1.

During the phase of TPC Research and Development, which can be done with small prototypes, the point resolution has been studied very extensively by several groups in the Linear Collider TPC community. This work will concentrate on the question if the observed results are also valid for multi track environment in the TPC. Considering equation 2.21 it is important to ask if the assumptions for $\sigma_{r\phi}(B)$ or N can be maintained in cases of nearby tracks.

A physical motivation for the need of the double hit resolution is given in [95]. Simulation studies show the influence of double hits in $e^+e^- \rightarrow d\bar{d} \rightarrow X$ decays for the TESLA detector design at a center of mass energy of 500 GeV. All multi track events have been examined, if they contain hits below a longitudinal and transverse limit for double hits. The longitudinal limimt was set to $\sigma_{long.} = 14$ mm, the transverse limit $\sigma_{trans.} = 3.3$ mm. The radius, where the hit of two nearby tracks exceed this limit is added to a histogram. Figure 9.1 shows the distribution of radii, which exceeds this limit. 8.8 % of the data sample (38011 tracks) were affected by double hits. The number of tracks with non resolvable double hit contributions drops significantly for larger radii of the TPC. The inner area of the detector does not seem suitable for the track reconstruction. Above radii of 1 m these double hits are almost negligible. This shows, that especially the hadronic decay modes, which produces a multi track environment might suffer from non resolvable double hits in the inner region of the TPC. It is therefore important to verify the requirements of the TPC also in terms of double hit resolution.

Questions which follows this motivation and should be answered with the existing TPC prototypes:

- How does the hit and track efficiency alter for the presence of nearby tracks?
- How is the reconstruction affected in regions of small distances between the tracks?
- How good can fundamental track parameters be reproduced with the used reconstruction methods?

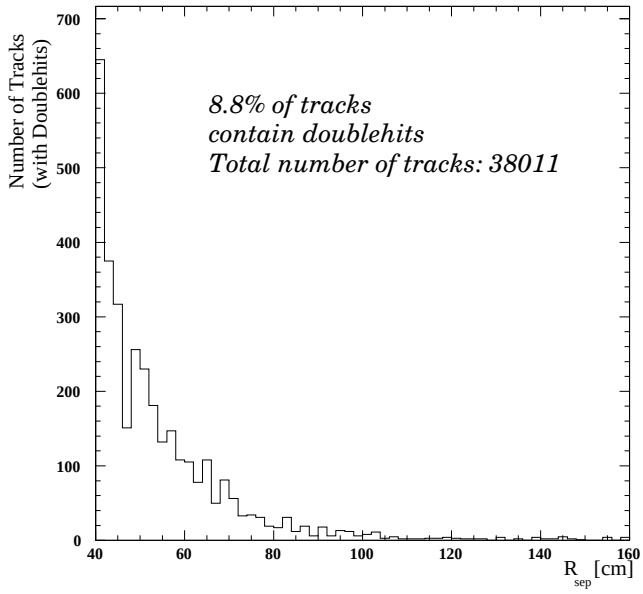

Figure 9.1: *The Figure shows the number of tracks for $e^+e^- \rightarrow d\bar{d} \rightarrow X$ decays, depending on the radii of nearby tracks, which do not suffer from non resolvable double hits [95].*

- Does the single point resolution of a track degrade in presence of a nearby track?
- How can the results be transfered into a prediction for the momentum resolution?
- Can the needed TPC requirements be fulfilled in terms of double hit resolution?

This work will start to answer these and related questions.

9.2 Influences on the Two Track Separation

In this section the parameters and effects, that have an influence on the two track separation are enumerated. Taking these parameters and effects into account a limit for the two hit resolution is estimated, which has to be validated for this work.

- The intrinsic two track resolution is limited by the width of the charged cloud itself. The transverse and longitudinal diffusion together with the charge

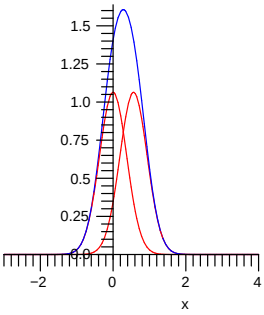

(a) $\mu_2 - \mu_1 = 1.5 \cdot \sigma_t = 0.5625$ mm.

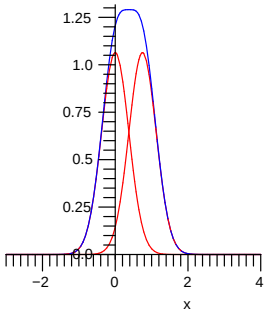

(b) $\mu_2 - \mu_1 = 2 \cdot \sigma_t = 0.75$ mm.

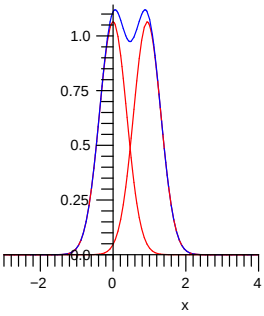

(c) $\mu_2 - \mu_1 = 2.5 \cdot \sigma_t = 0.9375$ mm.

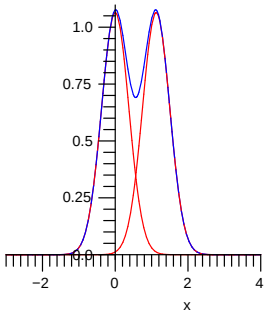

(d) $\mu_2 - \mu_1 = 3 \cdot \sigma_t = 1.125$ mm.

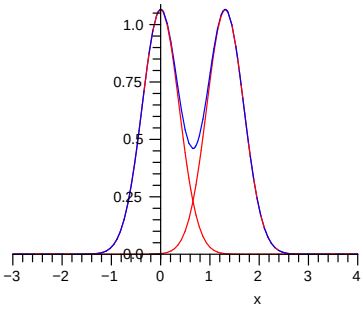

(e) $\mu_2 - \mu_1 = 3.5 \cdot \sigma_t = 1.3125$ mm.

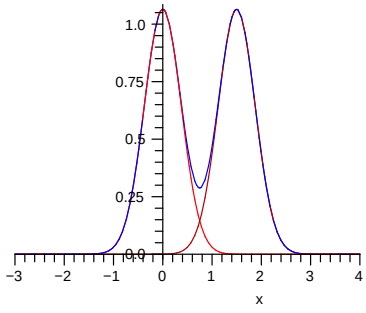

(f) $\mu_2 - \mu_1 = 4 \cdot \sigma_t = 1.5$ mm.

Figure 9.2: *The plots (a) to (f) show the width of two charged clouds. With a transverse diffusion coefficient of* $\sigma_t(3T) = 75\ \mu m / \sqrt{cm}$ *at* $z_0 = 25$ *cm (for TDR gas). The width of a charged cloud after 25 cm drift is* $\sigma_t(3T, 25\ cm) = 0.375$ *mm. The distance between the mean value* μ_1 *of the first Gaussian to the mean value* μ_1 *of the second Gaussian is plotted in units of* $\sigma_t(3T, 25\ cm)$*. The blue line shows the combined distribution for both Gaussians.*

broadening in the gas amplification system set the limit for the separation of two nearby tracks. This means the two track resolution is also depending on the drift length. See an example calculation in Figure 9.2.

- An other influence comes from the voxelsize of the detector. The two track resolution in $r\phi$ is depending on the width of the pad. The two track resolution in z is depending on the product of drift velocity $\times$ sampling rate of the electronics. It is obvious that the smaller this three dimensional channel size is, the more accurate two nearby charge distributions can be distinguished.

- The next influence comes from the separation algorithms of the reconstruction software. The definition of the separation criteria set the limits to distinguish two nearby tracks. If the algorithm is based on a simple row-wise reconstruction of hits it will be less efficient than algorithms, which take into account global information of the track.

- This study for track separation is done for small TPC prototypes with limited number of rows. In a large or full scale prototype the shortcomings due to a limited number of rows vanishes.

High energetic particle decays usually have more than one projection plane, which also limits the cases where the two track resolution of either $r\phi$ or z can be used. The two-track resolution of z is highly depending on the used electronic readout. For the Medi-TPC the electronic of the Aleph experiment was used, which is not appropriate as it was optimized for induced signals. Therefore the two track resolution in z is not investigated in this work. Only the two-track resolution in $r\phi$ direction provides realistic results.
With the pad size of 2.2×6.2 mm^2 used in the Medi-TPC and the separation algorithms used in our reconstruction software, which needs at least one pad with reduced charge between two maxima, a limit for the two hit resolution is expected for a distance of two tracks, which is above 2 times the pad width = 4.4 mm. With either smaller pad sizes or advanced separation algorithms, which take the information of the global track into account, this limit might be exceeded to the intrinsic limit given by the width of the charged cloud itself.

9.3 Data and Simulation Samples

With the setup described in chapter 5 in section 5.4.2 a measurement series was taken between July and September 2006. All data samples were taken with the same electric drift field and the same setting for the GEMs. Figure 9.3 shows the distances between the two tracks, which have been calculated for the three data samples according the propagation of the laser beam in the wedge prism. It can be clearly seen that two measurement series starts to enter a regime, which

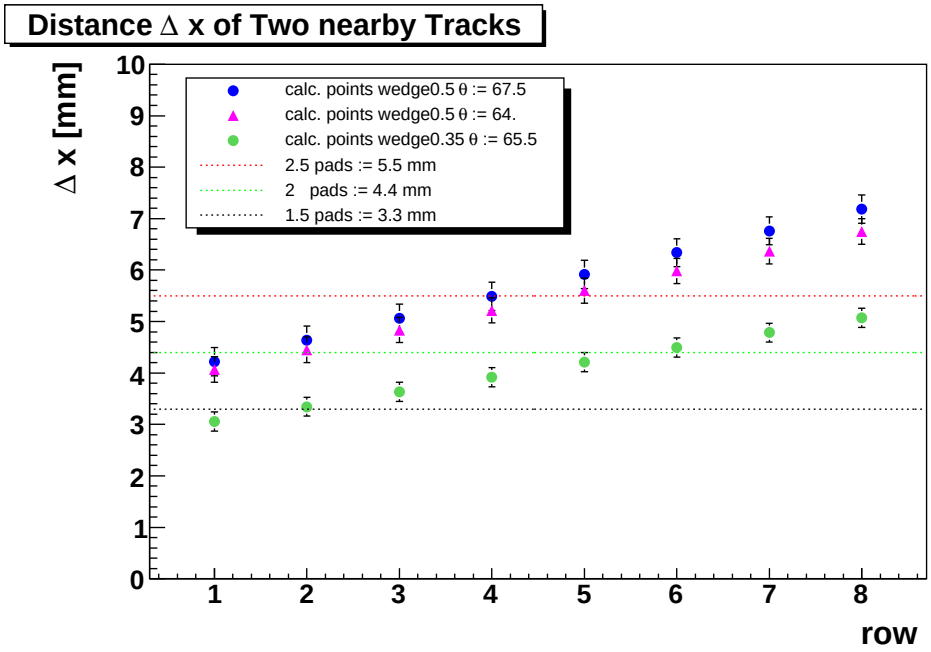

Figure 9.3: *The plot shows the three different settings, which were used in this work. The distances between the two tracks were calculated according to the propagation of a laser beam in the wedge prism (see section 5.2.2). The uncertainties of Δx derives from the uncertainties of the laser beam position on the wedge prism. The dotted lines translate Δx in units of pads.*

should be separable. One measurement series has a significant limitation as most of the pad rows have a Δx, which is below two pads.

All settings have been measured for magnetic fields between 1 to 4 Tesla. As described in Chapter 7 the drift velocity can be calibrated with the measurement of the water content to a precision of about 1 %, if the water content is below 500 ppm. So the data samples could be used with the appropriate drift velocity [1]. The water content is an averaged value of the measuring period during that day. The parameters for the data samples can be found in Table 9.2. Also the values for θ are reconstructed values.

In Table 9.3 the parameters of the simulation samples are given, which should

[1]Only for the 3 and 4 Tesla data samples of setting 1 a problem occured due to high water contents above 1000 ppm. In that case a gas bottle was running out during the night and a new gas bottle was connected in the morning.

Pad Geometry: Non-Staggered, 16 columns × 8 rows, Pad Size: 2.2×6.2 mm^2, Drift Field: 203 V/cm, $U_{GEM,i}$ 1/2/3: 315 V Transfer Field: 1.5 kV/cm, Induction Field: 3.0 kV/cm						
file-id	Setting	B-Field [T]	Wedge Angle [^{o}]	θ [^{o}]	Drift Velocity [cm/μs]	water content [ppm]
0025-01	1	1	0.5	68.24	4.285	361.48
0027-01	1	2	0.5	68.22	4.314	292.92
0028-01	1	3	0.5	67.62	3.883	1250.9
0029-01	1	4	0.5	66.34	3.883	1250.9
0033-01	2	1	0.5	64.54	4.285	361.48
0035-01	2	2	0.5	64.67	4.225	501.48
0036-01	2	3	0.5	64.78	4.244	459.09
0037-01	2	4	0.5	64.6	4.244	459.09
0041-01	3	1	0.35	65.12	4.27	397.78
0043-01	3	2	0.35	65.14	4.11	763.6
0044-01	3	3	0.35	65.44	4.243	459.45
0045-01	3	4	0.35	65.42	4.243	459.45

Table 9.2: *The table shows the investigated data samples of three different data points, which corresponds to three different distances between the tracks shown in fig 9.3*

Pad Geometry: Non-Staggered, 16 columns × 8 rows, Pad Size: 2.2×6.2 mm^2, Drift Velocity: 4 cm/μs, z_0: 0.0175 m Number of events: 3000					
file-id **B-Field**	Setting	PPS Position (x_0, y_0) [m]	Angles $(\alpha_{off},\ \theta)$ [^{o}]	Primary Electrons [$90e^-$/cm]	ratio I_1/I_2
simu-wedge0.5 dist3-**1T**	1	(0.0084, 0.058)	(7.0, 67.5)	4.5	0.6
simu-wedge0.5 dist3-**2T**	1	(0.0084, 0.058)	(7.0, 67.5)	4.5	0.6
simu-wedge0.5 dist3-**3T**	1	(0.0084, 0.058)	(7.0, 67.5)	4.5	0.6
simu-wedge0.5 dist3-**4T**	1	(0.0084, 0.058)	(7.0, 67.5)	2.25	0.6
simu-wedge0.5 dist2.5-**1T**	2	(0.008, 0.0575)	(6.9, 64.)	3.5	0.6
simu-wedge0.5 dist2.5-**2T**	2	(0.008, 0.0575)	(6.9, 64.)	3.5	0.6
simu-wedge0.5 dist2.5-**3T**	2	(0.008, 0.0575)	(6.9, 64.)	3.5	0.6
simu-wedge0.5 dist2.5-**4T**	2	(0.008, 0.0575)	(6.9, 64.)	2.0	0.6
simu-wedge0.5 dist2.5-**1T**	3	(0.0084, 0.063)	(7.1, 65.5)	3.25	0.64
simu-wedge0.5 dist2.5-**2T**	3	(0.0084, 0.063)	(7.1, 65.5)	3.25	0.64
simu-wedge0.5 dist2.5-**3T**	3	(0.0084, 0.063)	(7.1, 65.5)	3.25	0.64
simu-wedge0.5 dist2.5-**4T**	3	(0.0084, 0.063)	(7.1, 65.5)	2.0	0.64

Table 9.3: *The table shows the simulation parameters, which are used to reproduce the data samples of table 9.2*

reproduce the corresponding data samples of table 9.2. The use of the simulation is described in Chapter 6 in Section 6.5. The whole system can be described by the 3-dimentional position of the Prism Positioning System (PPS) with the set of parameters (x_0, y_0, z_0). As the TPC has to be moved out of the magnet to set a new position of the wedge, x_0, y_0 can be different within the size of the wedge. The center of the wedge is given by $x_0 = 0.0082$ m, $y_0 = 0.06$ m and $z_0 = 0.0175$ m. The wedge has a size of 8×8 mm^2, which means that x_0 and y_0 can have a possible inaccuracy of ± 4 mm measured from the center of the wedge. This can be transformed in an uncertainty for the determination of the distance between the two tracks of about ± 273 μm for setting 1, ± 240 μm for setting 2 and ± 170μm for setting 3. The position of $z_0 = 0.0175$ is considered fix. The second set of parameters are the offset angle in the xy plane α_{off} and θ the angle in the yz plane. The third set of parameters is given by the primary electrons of the high intense beam counted in units of 90 e^-/cm and the ratio of the higher and lower intense beam $\frac{I_1}{I_2}$.
An anomaly concerning the laser intensity appears in the data samples of 4 Tesla. The intensity of the laser was significantly reduced. As described in Table 9.2 the GEM Voltage was kept constant for all magnetic field configurations, so that the decrease of charge could not be explained by a change of the charge amplification system. A hypothesis is that at the high magnetic field and the corresponding high stray field an energy level of the laser was split, which reduces the laser intensity. The reduced intensity at 4 Tesla was taken into account for the simulation.

9.4 Performance of Data and Simulation Samples

Also for the case of two track events the variables of the data and simulation samples have to be compared to investigate the performance of the simulation. Table 9.4 shows the reconstructed values of data and simulation for the three different settings together with the statistical uncertainty $\approx \sigma/\sqrt{N}$ and the width of the distributions σ. As the laser produces identical tracks at the same position the statistical uncertainty of the mean value becomes negligible. The size of the samples is about 3000 events for data and simulation. To draw conclusions from the reconstruction of parameters for single events, it is more appropriate to regard the width of the distribution σ. All variables were compared at a magnetic field of 3 T, which was chosen as reference field. The 4 Tesla sample, which would naturally be the best choice due to the minimal diffusion, could not be used as a reference due to the mentioned drop in intensity.
The first three variables are the Q_1, the charge of the lower intense beam, Q_2 the charge of the higher intense beam and Q_1/Q_2 the ratio between both. The ratio should represent the reflection and transmission behavior described in Section 5.2.2. The next variables are the Intercepts$_{1/2}$ of the first and second track and

the difference between both Δ I. For the Chi-Squared method Δ I is correlated to the angle α, which denotes the angle between the two tracks. This will be discussed in section 9.4.1. For α the reconstructed and the theoretically expected values are shown. The angle θ denotes the angle in the yz-plane and α_{off} denotes the angle offset in the xy-plane.
The reconstruction and comparison of the parameters for data and simulation samples was more complicated in case of two track events than in the case of single track events. The reason therefore was the production of two tracks at the same time. The setup did not provide the possibility to switch on and off the particular beam to study the properties of each one at a time. This limits the conclusions one can make about the behavior of the two tracks.
At setting 1, where the distance between the two tracks is maximal almost all variables show a deviation below 10 % and are in good agreement. Setting 2 the next closer setting especially the charge Q_2 deviates and decreases the ratio between the charges. In setting 3 the two tracks are moved so near together, that all paramters, which require a distinction of the two tracks could not be reconstructed at all. Here the biggest deviations between data and simulation occurs, which limits the prediction capability of the simulation.

In Figure 9.4 the number of active pads is plotted. Figures 9.4(a), 9.4(c), 9.4(e) show the data samples of the three different settings and Figures 9.4(b), 9.4(d), 9.4(f). Generally the data samples have a broader distributed charged cloud represented by a higher amount of active pads, especially at setting 1 (see Figure 9.4(a) and 9.4(b)) and 2 (see Figure 9.4(c) and 9.4(d)). In the simulation the number of active pads, which lay in between the charges of the two tracks vanishes if the tracks proceed to a higher Δx. For the data samples a larger number of active pads is observed. A charge of such a pad is splitted and assigned to both tracks. It is therefore counted twice as expected due to the separation method introduced in section 6.2.2.
The larger number of active pads could be the result of several effects. One influence could be the width of the laser, which is not implemented properly in the simulation. As no beam profile measurement device was available during the measurement, it was only possible to estimate the size of the laser spot. Also crosstalk between neighboring pads and electronic noise can be a reason for the charge broadening of the charged cloud. Especially the cross-talk is difficult to implement in a simulation. Therefore this effect could not be investigated.
In setting 3 there were no inactive pads between the two tracks, neither in data nor in simulation. A minimal laser width was included in the simulation, because the tracks were so close together, that even small changes in the width of the charged cloud becomes important. The width was approximated with $\sqrt{2} \times 100$ μm. The minimal waist was assumed as 100μm and the factor $\sqrt{2}$ comes from the Rayleigh length z_R, which is the propagation length the laser width has increased by a the factor $\sqrt{2}$ (see 2.37). This setting was the most complicated to reproduce

	Setting 1			Setting 2			Setting 3		
Parameter	Data	Simu	Dev. [%]	Data	Simu	Dev. [%]	Data	Simu	Dev. [%]
Q_1 [FADC]	1067.5 ± 5.81 ± 257.	1064.3 ± 3.27 ± 189.	0.3	859.4 ± 1.49 ± 147.	814.4 ± 2.14 ± 142.	1.9	-	-	-
Q_2 [FADC]	1780 ± 5.80 ± 253.	1839.9 ± 7.56 ± 350.4	4.4	1853. ± 3.36 ± 266.	1326.6 ± 3.81 ± 311.	39.7	-	-	-
Q_1/Q_2 [%]	59.9	62.4	2.5	43.1	61.4	18.3	-	-	-
Intercept_1 [mm]	14.23 ± 0.002 ± 0.130	14.05 ± 0.002 ± 0.094	1.3	13.91 ± 0.002 ± 0.090	13.61 ± 0.002 ± 0.090	2.2	-	-	-
Intercept_2 [mm]	17.92 ± 0.004 ± 0.230	17.95 ± 0.001 ± 0.073	0.2	16.9 ± 0.003 ± 0.168	17.04 ± 0.003 ± 0.130	0.82	-	-	-
ΔIntercept [mm]	3.69 ± 0.027 ± 0.236	3.82 ± 0.016 ± 0.110	3.4	2.99 ± 0.027 ± 0.190	3.42 ± 0.012 ± 0.140	12.57	2.56 ± 0.016 ± 0.780	1.42 ± 0.016 ± 0.790	80.3
α [^{o}]	1.656 ± 0.008 ± 0.235	1.54 ± 0.002 ± 0.098	7.8	1.73 ± 0.006 ± 0.170	1.52 ± 0.002 ± 0.140	13.82	1.65 ± 0.010 ± 0.460	2.04 ± 0.009 ± 0.780	19.1
α [^{o}] (theo.)	1.5	1.5		1.5	1.5		1.05	1.05	
α_{off} [^{o}]	6.99 ± 0.010 ± 0.530	6.86 ± 0.005 ± 0.247	1.90	6.94 ± 0.005 ± 0.300	6.92 ± 0.006 ± 0.300	0.29	-	-	-

Table 9.4: *The table shows the comparison of some key observables of data and simulation at three different settings, but the same magnetic field of 3 T. From setting 1, which is the one with the biggest distance between the two tracks to setting 3, which is the one with the tracks closest together the deviations increase. In setting 3 only a limited number of values is reconstructable. The reconstructed values are assigned first with the statistical uncertainty* $\approx \sigma/\sqrt{N}$ *and the width of the distribution* σ*.*

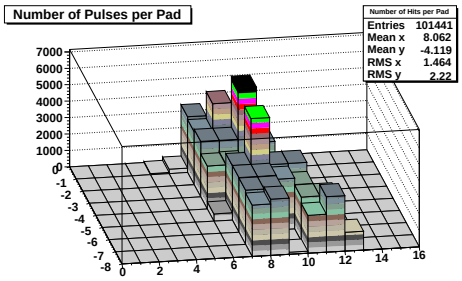

(a) setting 1 measurement at 3 Tesla

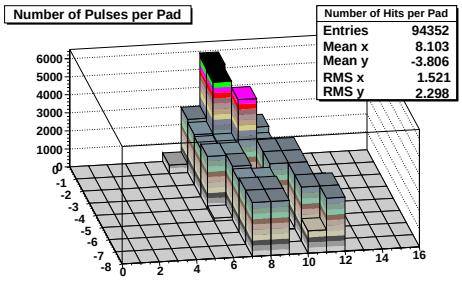

(b) setting 1 simulation at 3 Tesla

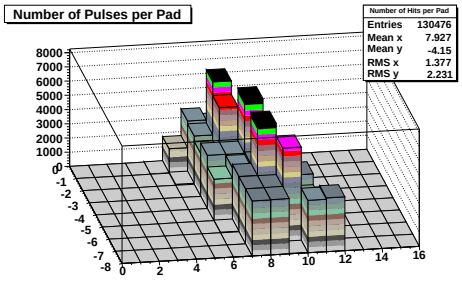

(c) setting 2 measurement at 3 Tesla

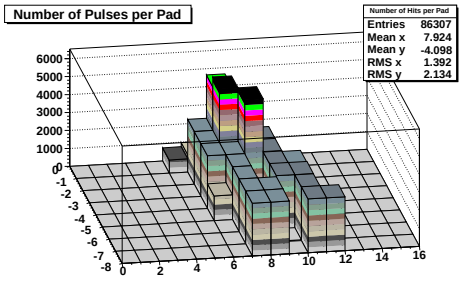

(d) setting 2 simulation at 3 Tesla

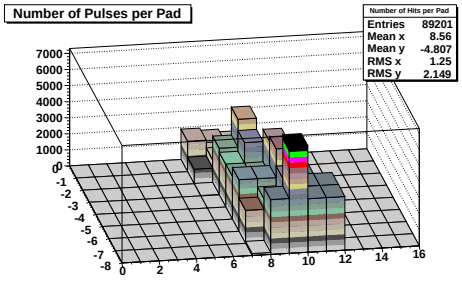

(e) setting 3 measurement at 3 Tesla

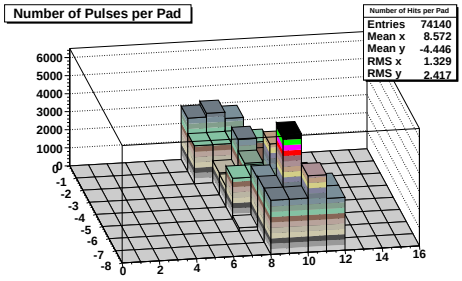

(f) setting 3 simulation at 3 Tesla

Figure 9.4: *In the figure the number of pulses per pad on the read out plane for the reference field of 3 Tesla. From setting 1 to 3 the two tracks are moving closer together. Due to the separation algorithm the charge on pads between two maxima is assigned to both hits. Therefore an increase of pulses between the two tracks can be observed. For the simulation these pulses are significantly reduced. In setting 3 both data and simulation show no free pad between the charges. In the simulation a laser width of about 140 µm is included.*

by simulation. Small changes of the input parameters have strong effects on the results and the whole system is very sensitive to small changes. As no additional measurements of these parameters were available an acceptable set of parameters were hard to find.

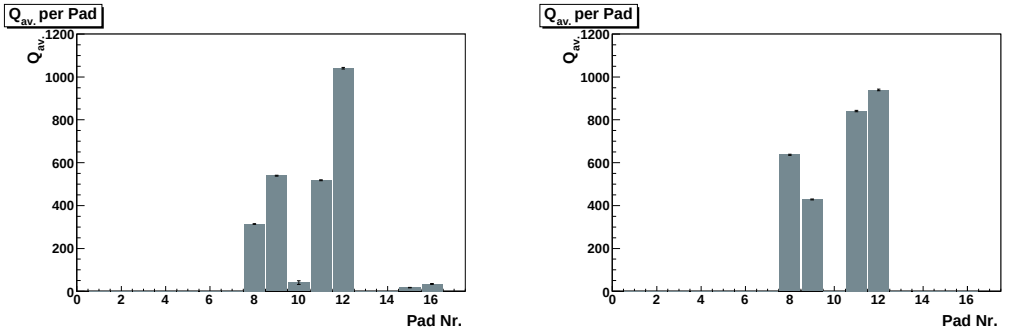

(a) Mean charge per pad (data) (b) Mean charge per pad (simulation)

Figure 9.5: *Average charge deposition of setting 1 in the seventh row. The x-axis denotes the pad numbers which starts from 1 and ends at 16. One can observe a charge dsplacement between data and simulation, which occurs for both tracks.*

As mentioned before an individual study of the laser tracks for this setup was not possible due to the simultaneous production of the two laser tracks. However single rows in a specific setting can be investigated, if the hits of both tracks can be clearly separated. In such a case one can be sure, that the hit charges and therefore the positions of both hits are at least not influenced by the reconstruction algorithm. In Figure 9.4 it is shown, that such a row is only existing for measurement series 1. The first and last row of the pad geometry would not be an appropriate choice, because both rows are suffering from cross-talk of the shield, which is explained in Section 4.3.1. In Figure 9.5 the mean value of the charge is plotted for each pad of this row. The first hit is located on pad 8 and 9, the second hit on pad 10 and 11. The charge distribution of both tracks in this row is displaced between data and simulation clusters. However the charge displacement is shifted for both hits in the same direction. In Figure 9.6 the reconstructed hit positions are plotted. The values for the reconstructed positions of the hits can be found in Table 9.5. It shows, that the absolute position of both simulated hits is shifted by 300 μm. The Δ x_{Row7} for both mean values is 6.67 mm in case of the data and 6.735 mm in case of the simulation, which is a of 65 μm. This means the distance Δ x between the two tracks is approximated correct for the simulation and is in agreement within the uncertainties.

Another important value is the ratio between the two hit charges (see Table

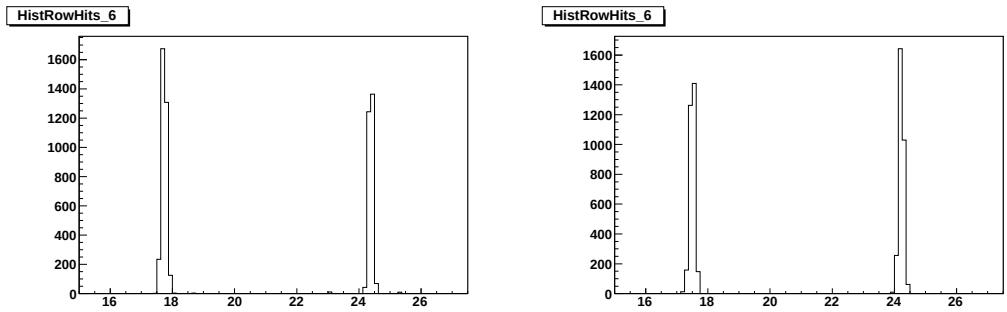

(a) Hit positions for row 7 (data) (b) Hit positions for row 7 (simulation)

Figure 9.6: *Average hit position of setting 1 in the seventh row. The positions derive directly from the average charge deposition of Figure 9.5. The Δx between both hits is 6.67 mm (data) and 6.735 mm (simu.), which is a difference of 65 μm. This is in agreement with the uncertainties. However one can observe, that the absolute position of both tracks is shifted by about 300 μm.*

9.5). This ratio correspond to the intensity ratio $Q_1/Q_2 = (I_1/I_2)^2$. For the simulation a ratio of Q_1/Q_2 of 60 % was assumed (see Section 5.2.2). The charge ratio of row seven is 54.7 % for the data and 59.85 % for the simulation. The result for the data is inconsistent by 5 % with the value measured later for several rows in Figure 9.7(a). It is not clear, if it is an effect of this specific row or if the transmission and reflection coefficients defined in Section 5.2.2 have to be modified. If the charge ratio Q_1/Q_2 is changed to an input value of the simulation of 55 %, the reconstructed value is 54.8 %, which leads to a $\Delta\ x_{Row7}$ of 6.74 mm. In this specific case the deviation of the charge ratio by 5 % have no significant influence.

In Figure 9.7 the hit charge is plotted for the three settings. The x-axis denotes the charge given in units of FADC-counts and the y-axis denotes the number of entries. In the histograms each hit is taken into account. In some of the rows of the data samples electronic artefacts were observed. These electronic artefacts apears if the charge of a voxel exceeds the limit of the FADC spectrum of 256 FADC counts. The preamplifier is operating in saturation. In Figure 9.8 the hit charge of setting 1 is plotted for each row. In row 1, 4 and 6 an extremely narrow charge distribution appears, which is shows a significantly increased number of entries. In the other rows the charge can be separated as expected. If the rows with electronic artefacts were excluded for the filling of the hit charge histogram, also the number of charges in one time bin above the FADC spectrum limit were significantly reduced. Rows, which show this electronic artefact in the other two settings of the data are also excluded.

Figures 9.7(a) and 9.7(b) show the hit charge distributions for setting 1. Here the best agreement between measurement and simulation can be observed (see table

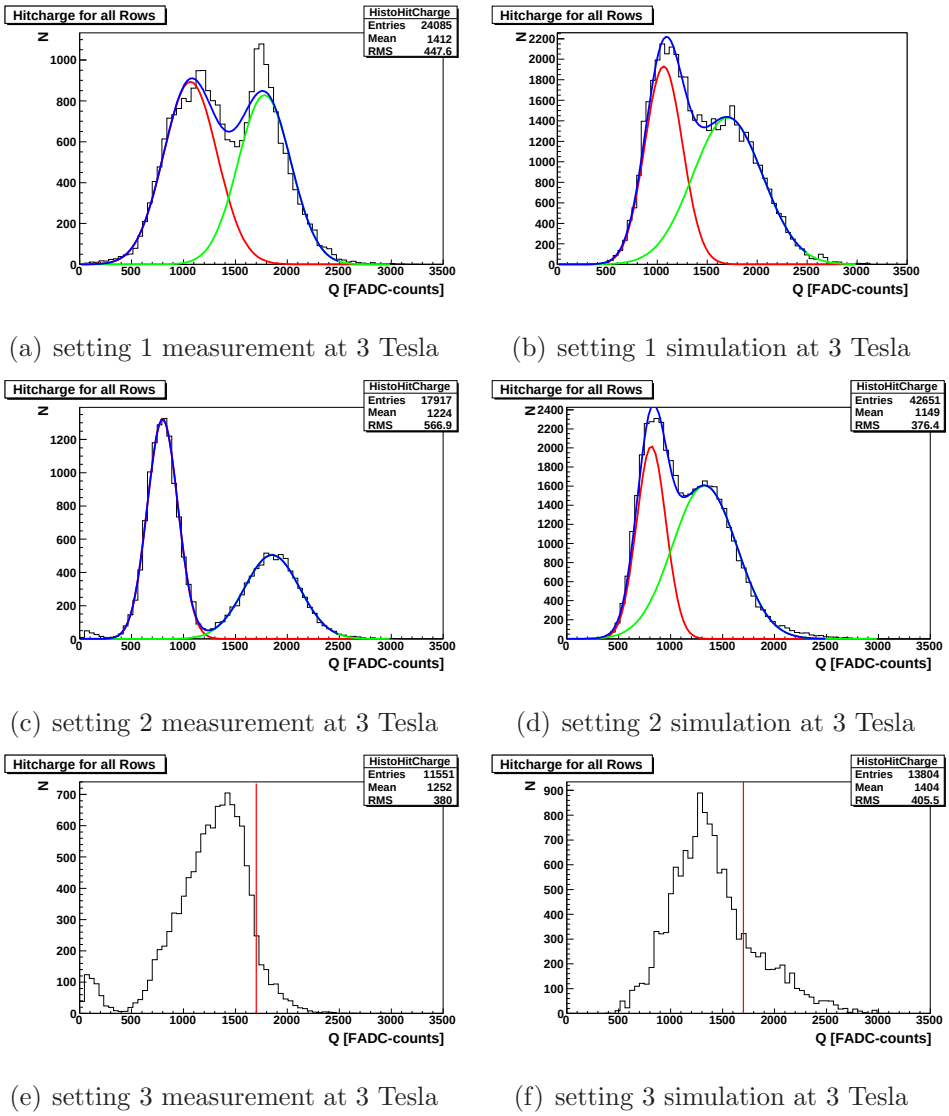

(a) setting 1 measurement at 3 Tesla

(b) setting 1 simulation at 3 Tesla

(c) setting 2 measurement at 3 Tesla

(d) setting 2 simulation at 3 Tesla

(e) setting 3 measurement at 3 Tesla

(f) setting 3 simulation at 3 Tesla

Figure 9.7: *The figure shows the hit charges of the three settings for a magnetic field of 3 Tesla. For setting 1 the best agreement between data and simulation is achieved. For setting 2 the ratio between the charges of the tracks is degrading in case of the data. The charge of the higher energetic track can absorb charge from the lower energetic one. The increase of charge for one beam would decrease the charge of the other. In setting 3 the charges of the two beam can not be separated anymore. The tail in both distributions comes from rows where both hits are reconstructed as one charge (see figure 9.9). Single rows of the data sample were excluded if electronic artefacts were observed (see figure 9.8).*

Parameter	Data	Simulation Q_1/Q_{2input} (60 %)	Simulation Q_1/Q_{2input} (55 %)
x-pos$_{hit1}$ [mm]	17.77 ± 0.076	17.45 ± 0.102	17.45 ± 0.102
x-pos$_{hit2}$ [mm]	24.44 ± 0.142	24.185 ± 0.142	24.19 ± 0.142
Δ x-pos [mm]	6.67 ± 0.161	6.735 ± 0.175	6.74 ± 0.176
Q_1 [FADC-counts]	853.2	1065.3	972
Q_2 [FADC-counts]	1558.3	1779.8	1782
Q_1/Q_2 [%]	54.7	59.9	54.6

Table 9.5: *The table shows the reconstructed charge and hit position information for the seventh row of setting 1. The row could be used as a reference row as both data and simulation have an inactive pad in between. It allows a clear assignment of charges and therefore an undisturbed reconstruction of hits.*

9.4). Both values for Q_1, the mean charge of the lower energetic track and Q_2, the mean charge of the higher energetic track, are in good agreement and show deviations below 5 %.
In setting 2 the agreement for Q_1, Q_2 and the ratio $\frac{Q_1}{Q_2}$ begins to deteriorate. As the ratio between the two hit charges stays constant, one possible explanation is, that in the reconstruction of the higher energetic track charge from the lower energetic track are assigned to the more energetic one. This explains the strong deterioration of the ratio between Q_1 and Q_2. The increase of Q_1 automatically decreases Q_2. As seen in the Figures 9.4(c) and 9.4(d) the simulation has a narrower charge distribution. Therefore the charge could be separated without wrong assignment of charges from the ClusterFinder. The simulation is adjusted to Q_1. As the value for Q_1 is not reconstructed properly also Q_2 is affected. which is probably underestimated. This explains the high deviation of the values Q_2 for data and simulation.
In setting 3 the distribution of measurement and simulation can not separate the hit charge anymore. The shape of the distributions show similarities. Both start at about 500 FADC counts. The mean value of the measurement is at 1297 FADC counts, the simulation of 1404 FADC counts, which is a deviation of 7.6 %. Both charge distributions contain a tail, which starts at about 1700 FADC counts. This tail is much more distinct in the simulation (see figures 9.4(e) and 9.4(f)). The tail comes from hits, where the charge of both track has been reconstructed as one hit. These behavior has the highest probability in the first rows, where the distance between the two tracks is minimal. In Figure 9.9 this is shown for the simulation. In the first two rows the mean value is significantlly higher than in the remaining rows.

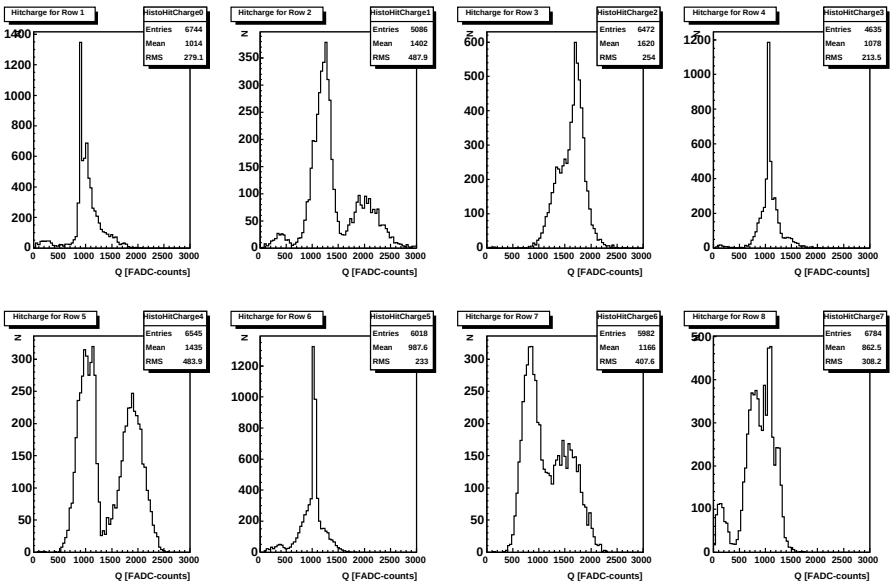

Figure 9.8: *The measured hit charge for every row of setting 1 is shown. In row one, four and six a spike appears, which are electronic artefacts. This electronic artefact appears when the charge of a voxel exceeds the total limit of the preamplifier. Rows, which shows this behavior were excluded for the determnation of the total hit charge distribution in figure 9.7.*

9.4.1 Correlation between α and Δ Intercept

The next two performance parameters have to be considered together as these parameters are highly correlated, if reconstructed with the Chi-Squared method. In the figures 9.10 the angle α, which denotes the angle between the two tracks, is plotted. Here it is very important to know that setting 1 and 2 are different from the one in setting 3 as in the first two a wedge prism with an angle of $\delta = 0.5\ ^\circ$ was used, which leads to an angle α between the two tracks of 1.5 °. In setting 3 a wedge prism with an intrinsic wedge angle of 0.35 ^{o} was used, which leads to an angle of 1.05 ^{o} between the two tracks. In Figure 9.11 the intercepts of the two tracks are plotted in the left histogram and ΔI of all event are plotted in the right histogram. The intercept is here defined as the position of the reconstructed track in the first row (y=0). Therefore ΔI denotes the distance between the two tracks in the first row.
The parameters are anti-correlated if using the Chi Squared fitting method, because both track parameters are fitted independently of each other. If for one track the angle and intercept deviates, this deviation is significant for these parameters, which have to be derived from both tracks. This means if the angle α

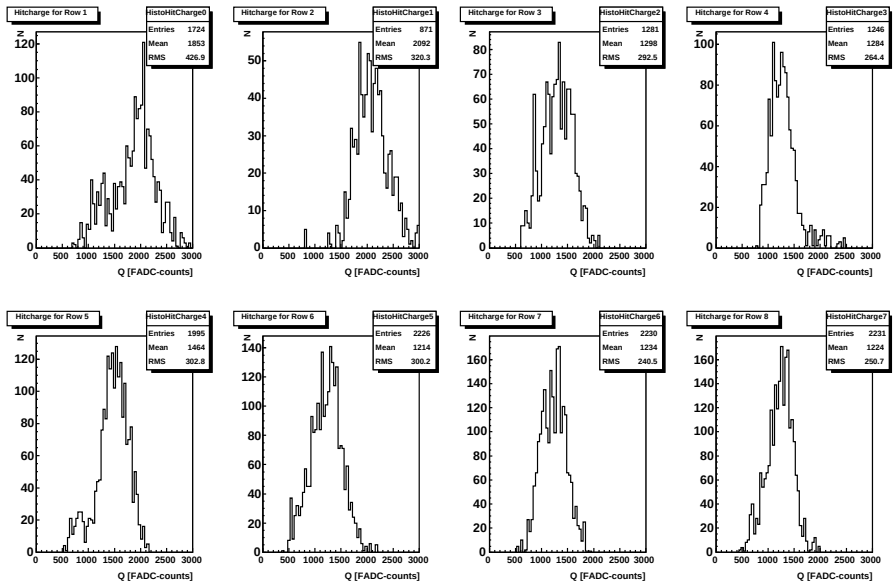

Figure 9.9: *The simulated hit charge of setting 3 for each row. The hit charges of the first two rows is significantlly increased compared to the remaining rows.*

is reconstructed too big the corresponding ΔI will be reconstructed too small. If using the Global Fit method, the track parameters are optimized in regard of the other track and the anti-correlation vanishs (see section 9.6).
This anti-correlation can be observed in setting 1 for the reconstructed α and ΔI of the data sample. In Figure 9.10(a) there is a small side peak at a value of 2.5 ^{o} next the expected peak of 1.5 ^{o}. The same small side peak is visible in the right plot of Figure 9.11(a) at small values for ΔI. A similar behavior is missing in case of the simulation. A reason for this side peak is shown in the Figures 9.4(a) and 9.4(b), which show the number of active pads for this setting. Especially in the first rows of the data one can observe a huge amount of active pads between the two expected hit positions. This means the highest probability for a limited hit reconstruction is for these rows. If the charges are for example wrong assigned or even merged, the reconstructed hit position will be moved in the middle between the true hit position. As a consequence the whole track will be moved in this direction, if such a hit is included in the track reconstruction. The angle between both tracks will be reconstructed too big respectively the ΔI too small.
The correlation of α and Δ intercept is also visible in setting 2. In Figure 9.10(c) there is also a small tail visible shifting α to bigger values and is responsible for the small shift to smaller intercepts in Figure 9.11(c). Nevertheless both settings agrees fairly well with the expected value of 1.5°. The deviation of the mean value

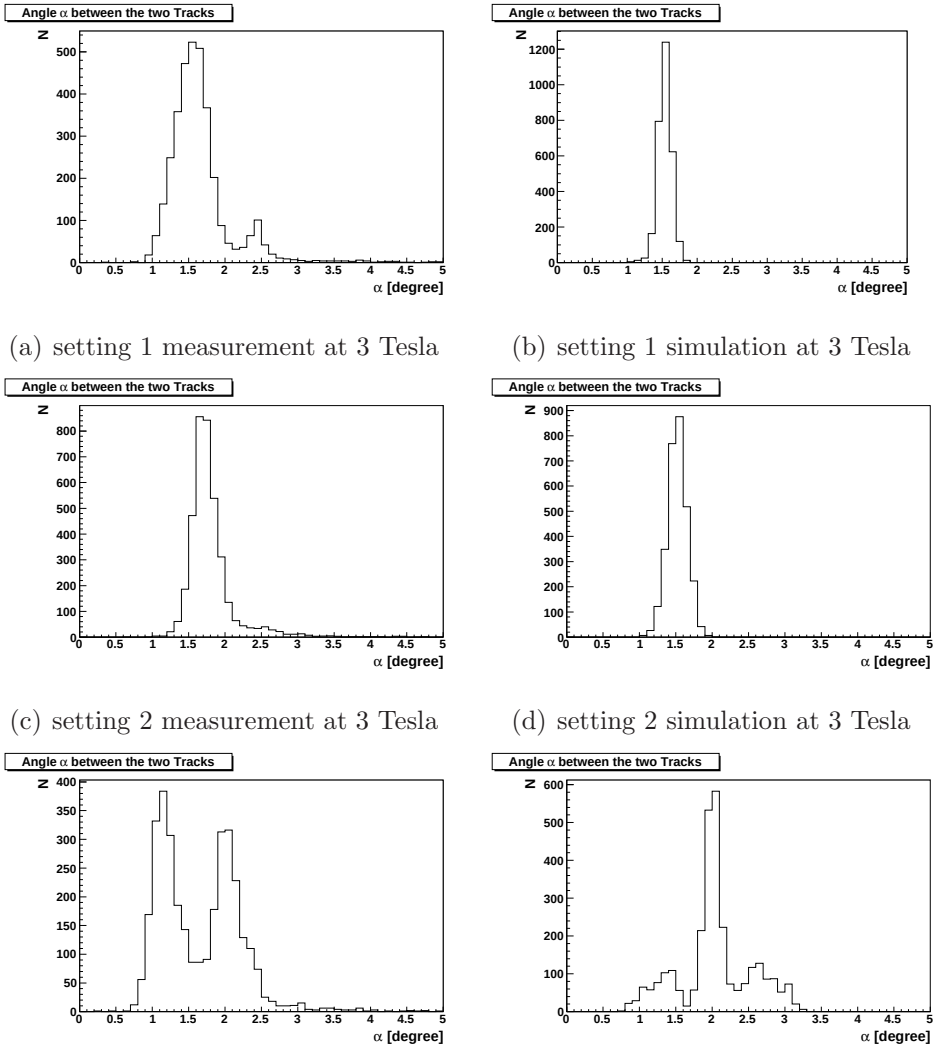

(a) setting 1 measurement at 3 Tesla

(b) setting 1 simulation at 3 Tesla

(c) setting 2 measurement at 3 Tesla

(d) setting 2 simulation at 3 Tesla

(e) setting 3 measurement at 3 Tesla

(f) setting 3 simulation at 3 Tesla

Figure 9.10: *The figures illustrate the distribution of α. The angle α denotes the angle measured between both tracks. This angle is determined by the angle of the wedge prism (see Section 5.2.2). For the setting 1 and 2 a wedge prism, which leads to an α of 1.5° is used. For setting 3 a wedge prism with an α of 1.05° is used. It is a key element of the analysis, that due to a precise knowledge of α the reconstructed values can be compared to this input value. In the first two settings the reconstruction is fairly good for data and simulation. Only a small tail appears in case of the data. In setting 3 α is reconstructed closer to the input value in data than in simulation. In the data one of the two stable positions shows the correct value. In the simulation only a small percentage of the events are reconstructed properly.*

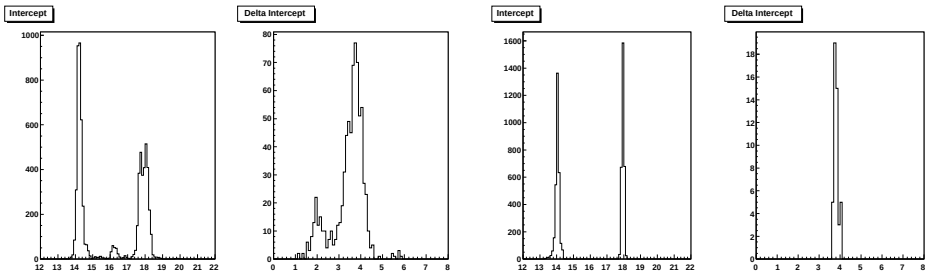

(a) setting 1 measurement at 3 Tesla (b) setting 1 simulation at 3 Tesla

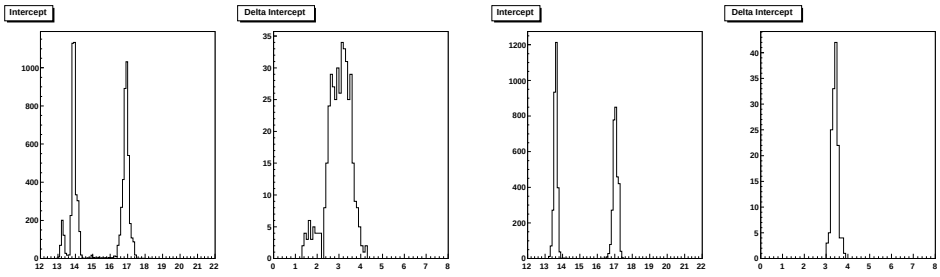

(c) setting 2 measurement at 3 Tesla (d) setting 2 simulation at 3 Tesla

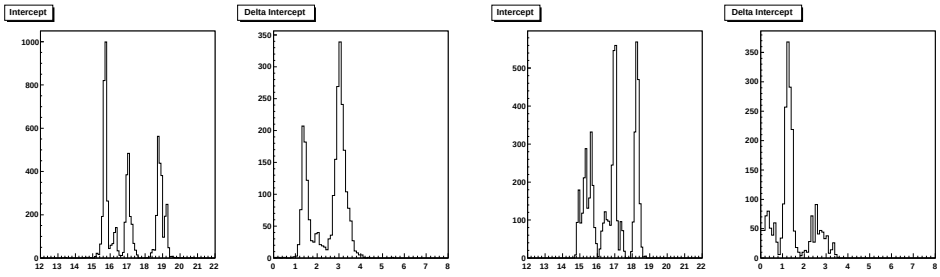

(e) setting 3 measurement at 3 Tesla (f) setting 3 simulation at 3 Tesla

Figure 9.11: *The figure shows the intercepts of the tracks respectively the difference between two intercepts for the three settings. In the left plot the two intercepts of the laser tracks are shown, in the right plot the* Δ *intercept. The intercept is strongly correlated to the angle alpha. In the first two settings the reconstructed intercepts for both tracks and the corresponding* Δ *intercept is clearly visible. In the corresponding* α *plots, which showed a tail at higher values, in the* Δ *intercept a side peak at lower values can be seen. At setting 3 the intercepts and* Δ *intercept can not be reconstructed clearly anymore.*

for setting 1 is 10.4 % respective 15.3 % for setting 2. The simulation is here much more precise and only shows deviations to the expected value of 1.3 % for both cases.
For setting 3 the expected value for α is reconstructed better for the data than in the simulation. Here α shows a two peak structure. The first peak is reconstructed at the expected position. The second peak can be clearly separated from the first one. In the simulation α is always reconstructed twice as large as expected at about 2.0° . Only a few events are reconstructed correctly at the expected position of 1.05°. The effect for the wrong reconstruction is the same as for setting 1. Only rate and weight of the wrong reconstruction is extremely increased. As mentioned especially in the first two rows the charge of both hits are merged (see Figure 9.9). If a hit of these rows is included in the reconstruction the wrong reconstructed hit position pulls the whole track to bigger angles α. In the measurement the influence of the first rows seems to be reduced, so that a stable point with the correct angle information can be reconstructed using the last 6 rows. In case of the measurement a mean value for α 1.65 ^{o} could be reconstructed or 1.19 ^{o} if only the first peak is considered, which is a deviation of 57.1 respective 8.4 %. For the simulation the angle is 2.04 and the deviation about 100. %.

9.5 x-Separation Performance of the Chi Squared Method

In this section the results of the Chi Squared method are presented and compared for several magnetic fields. First the two track efficiency $\varepsilon^{2,track}$ is determined in regard of the number of minimal reconstructed hits per track. For a fixed two track efficiency definition a two hit efficiency $\varepsilon^{2,track}$ is derived. The reliability of the reconstruction is investigated using the knowledge about the angle α of the two track system as introduced in the previous section. Finally the point resolution of both tracks is considered for the different magnetic fields.

9.5.1 Track Efficiency

A definition of the two track efficiency, as it is used in this work, composes by a measured two track efficiency $\varepsilon^{meas}_{2,track}$ and an optimal two track efficiency $\varepsilon^{opt}_{2,track}$ to which the measured one is normalized.

The optimal efficiency is defined as:

$$\varepsilon_2^{opt} = \varepsilon_{st(1)}(1-\psi_1) \times \varepsilon_{st(2)}(1-\psi_2) \tag{9.2}$$

with

$\varepsilon_{st(i)} := \frac{N_{\geq 1}}{N_{tot}}$ denotes the efficiency to reconstruct one track if only one primary particle is present

presence of the other track.

$\psi_i := \frac{N_{\geq 1}}{N_{tot}}$ denotes the probability that a single track is reconstructed wrongly as two tracks due to other mis-reconstruction effects

For the case of a limited number of pad rows the efficiency to find a single track $\varepsilon_{st(i)}$ is strongly depending on the minimal number of hits, which are used for the track. Track definitions for single tracks efficiencies were tested and compared to find an acceptable value for the minimal number of hits. The fake rate as defined above can have several reasons. If for example the level of noise hits is increased due to an unsufficient threshold of the pads, these noise hits can produce fake tracks. Also crosstalk can induces charge on neighboring pads and produce fake tracks. Another possibility is if the minimal number of hits defining a track is too low, fake tracks can occur. In the case of this work the fake rate is mainly dependent on two effects: A decrease of the minimal number of hits defining a track in combination with electronic effects. The electronic effect occurs if the maximal charge of the preamplifier is exceeded above its total range and therefore runs in saturation. This produces an artificially long tail, which can be reconstructed falsely as a fake hit. If the minimal number of hits defining a track is reduced a set of fake hits can be reconstructed as a fake track. As the samples for the different magnetic fields have always the same GEM setting, the gain should be of the same order of magnitude. This means the effect is dependent on the width of the charge cloud, which is dependent on the strength of the magnetic field, which prevents the charge cloud from diverging. The highest amount of charge is therefore concentrated in a single voxel for a magnetic field of 3 Tesla[2]. Therefore the technique to derive the fake rate must be to measure two single track data samples at the same position and with the same gain as the two track setting. This would require a setup, where the laser beams can be switched on and off individually. As this feature was not implemented in the setup, the efficiency for $\varepsilon^{opt}_{2,track}$ has been derived from simulation. In the simulation this electronic effect is not implemented. Therefore the fake rate ψ_i is always zero.

The two track efficiency is then defined as:

$$\varepsilon_{2,track} = \frac{\varepsilon^{meas}_{2,track}}{\varepsilon^{opt}_{2,track}} \tag{9.3}$$

In Figure 9.12 the two track efficiency for setting 1 is shown as a function of the minimal number of hits defining a track. The minimal number of hits defining a single track were varied from 5 to 8 hits. 8 is also the total number of rows of the readout plane, which requires a hit in every row. The filled dots

[2]Normally 4 Tesla would be the choice, but due to the mentioned decrease of laser intenity at 4 Tesla the 3 Tesla sample has the highest fake rate probability

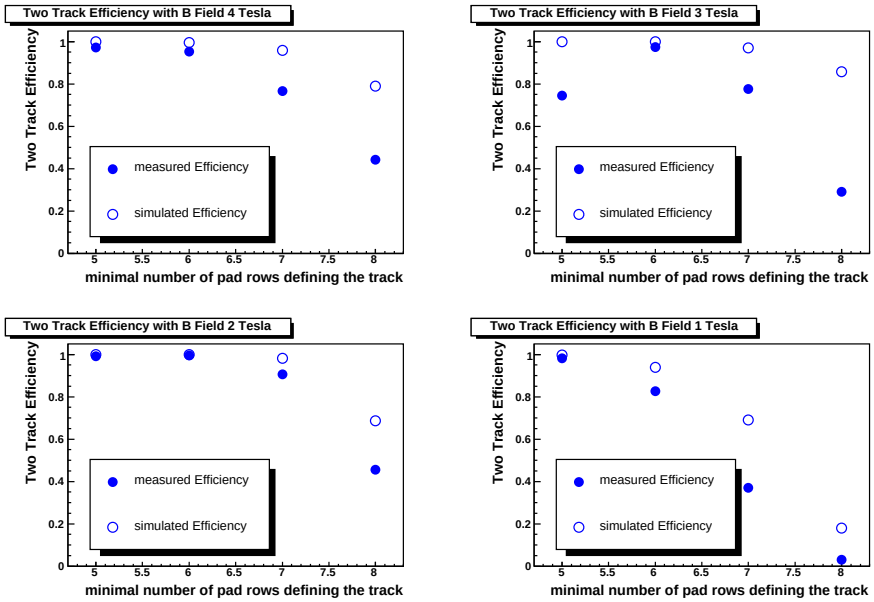

Figure 9.12: *Two track efficiency for setting 1. The efficiency is investigated for magnetic fields of 1, 2, 3 and 4 Tesla.*

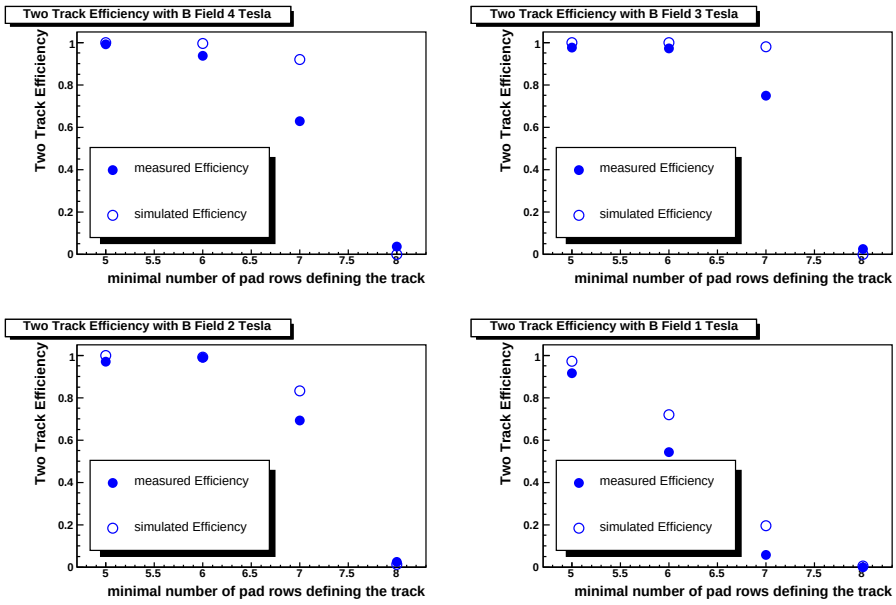

Figure 9.13: *Two track efficiency for setting 2. The efficiency is investigated for magnetic fields of 1, 2, 3 and 4 Tesla.*

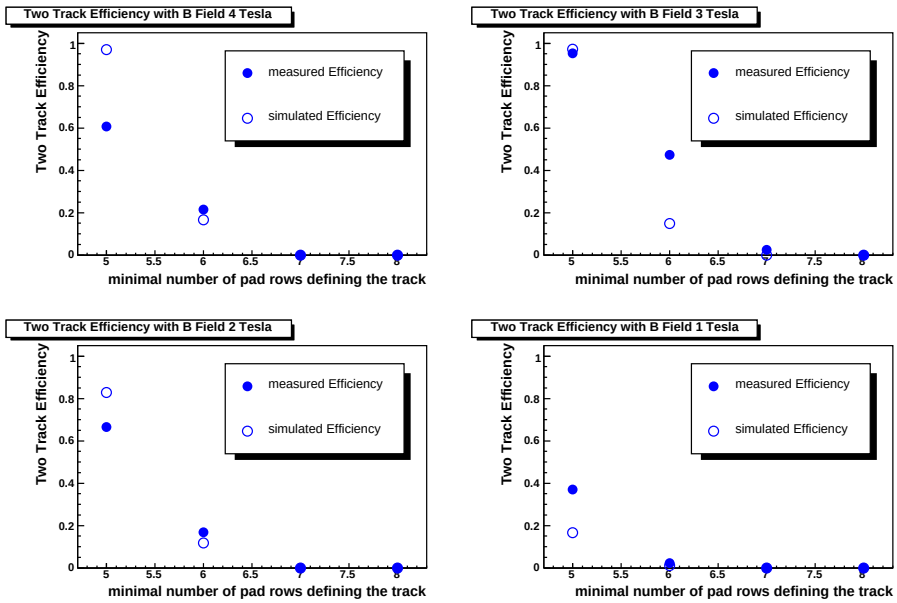

Figure 9.14: *Two track efficiency for setting 3. The efficiency is investigated for magnetic fields of 1, 2, 3 and 4 Tesla.*

represents the measurement, the open dots the Monte Carlo simulation. It is clearls demonstrated, that an increasing number of hits is decreasing the two track efficiency. For magnetic fields above 2 Tesla the maximal $\varepsilon_{2,track}$ is nearly 100 % if a track consists of 6 hits. It drops if 7 or 8 hits are required. In the 1 Tesla case $\varepsilon_{2,track}$ drops earlier, which indicates an more unfavorable width of the charged cloud for separation. The plots always show a stronger decrease in the data than in simulation. One reason for this behavior is crosstalk between the shield and the the first and last pad row. This phenomenon is known and have also been reported in the work of [81, 64, 65]. The 3 Tesla sample shows a slight decrease at a value of 5 minimal pad rows compared to the value of 6 minimal pad rows, which is caused by an increasing fake rate, as defined in this chapter. For this setting the best track definition seems to be if at least 6 pad rows are assumed to determine the track.

For setting 2 the two track efficiency $\varepsilon_{2,track}$ is shown in Figure 9.13. As setting 2 is only slightly smaller than setting 1, also in this setting an optimal value for $\varepsilon_{2,track}$ is reached for a single track definition of 6 hits. The efficiency of data and simulation vanishes if the minimal number of pad rows is extended to 8. Again the sample for 1 Tesla shows a stronger decrease of efficiency for all track definitions.

setting	B-Field [T]	$\alpha_{meas.}$ [^{o}]	Dev. [%]	$\alpha_{simu.}$ [^{o}]	Dev. [%]
1	4	1.59 ± 0.006 ± 0.283	6.0	1.48 ± 0.003 ± 0.154	1.3
1	3	1.54 ± 0.004 ± 0.235	2.7	1.53 ± 0.002 ± 0.098	2.0
1	2	1.56 ± 0.005 ± 0.222	4.0	1.46 ± 0.002 ± 0.122	2.7
1	1	1.63 ± 0.004 ± 0.208	8.7	1.47 ± 0.003 ± 0.184	2.0
2	4	1.72 ± 0.003 ± 0.179	14.6	1.46 ± 0.004 ± 0.170	2.7
2	3	1.73 ± 0.003 ± 0.169	15.3	1.52 ± 0.003 ± 0.136	1.3
2	2	1.68 ± 0.003 ± 0.183	12.0	1.65 ± 0.004 ± 0.201	10.0
2	1	1.52 ± 0.009 ± 0.243	1.3	1.51 ± 0.008 ± 0.285	0.7
Setting 3 using mean value					
3	4	1.98 ± 0.012 ± 0.609	88.6	2.20 ± 0.008 ± 0.458	109.5
3	3	1.65 ± 0.010 ± 0.559	57.1	2.04 ± 0.009 ± 0.489	94.3
3	2	2.02 ± 0.009 ± 0.472	92.4	1.77 ± 0.010 ± 0.489	68.6
3	1	2.12 ± 0.015 ± 0.559	101.9	1.61 ± 0.025 ± 0.564	53.3
Setting 3 with a cut					
3	4	1.12* ± 0.022 ± 0.269	7.0	-	-
3	3	1.20 ± 0.006 ± 0.184	14.3	1.42* ± 0.028 ± 0.259	35.2
3	2	1.20* ± 0.017 ± 0.220	14.3	1.32 ± 0.014 ± 0.269	25.7
3	1	1.16 ± 0.032 ± 0.228	10.5	0.97 ± 0.012 ± 0.106	7.6

Table 9.6: *The table show the reconstructed angle α for data and simulation. The track definition for setting 1 and 2 was, that a track consists of at least 6 hits. For setting 3 the track definition was 5 minimal hits. From setting 1 to 3 the deviation from reconstructed to predicted values increase. The values for α are shown for the uncertainties on the mean value and the RMS.*

For setting 3 the two track efficiency is near to 0 % for a minimal row requirement of 7 or 8 hits to both in measurement and simulation. For a track definition of 6 pad rows a non zero two track efficiency can be observed for magnetic fields above 2 Tesla. For 1 Tesla the unfavorable two track reconstruction capability remains. Even for a single track definition of 6 hits one still has a $\varepsilon_{2,track}$ of zero. Therefore for this setting a all further sudies have been done for a track definition of 5 minimal hits per track. In figure 9.3 it is shown that this setting has a distance between the two tracks, which starts at 3.3 mm and ends at 5.5 mm, which can be expressed in pad sizes of 1.5 to 2.5 pads. This setting is expected to show the highest limitations for the reconstruction of two track events. Investigation of this region should provide important answers to the hit separation and the quality of the reconstruction referring to the known angle between the two tracks and the resolution.

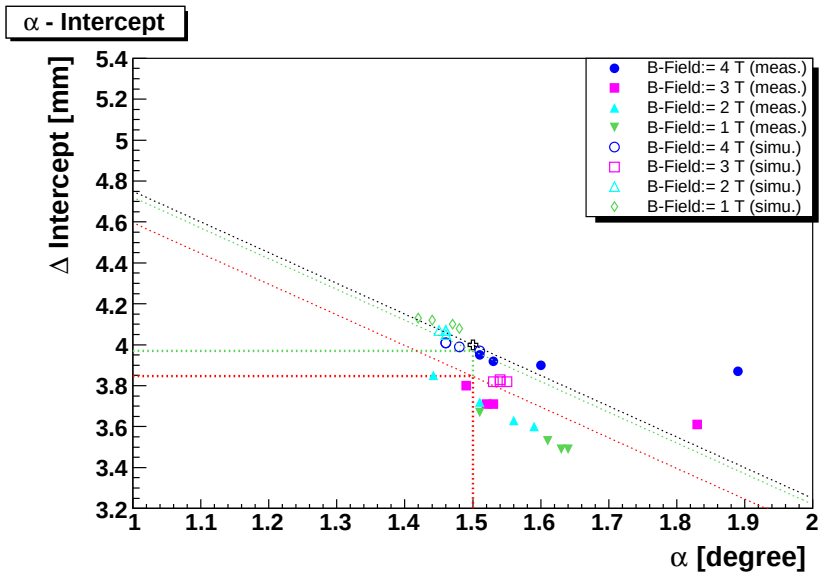

Figure 9.15: *The figure shows the anti-correlation of* α*, the angle between the two tracks and the difference between the intercepts* Δ *I for setting 1. For lower magnetic fields* α *is reconstructed at higher values. If one distinguishes between data and simulation samples, one can get the correlation factor for both. A straight line is fitted, where the slope is a fixed and* Δ*Intercept a free parameter. At the expected position for* α *the value for* Δ*Intercept is read out. The red line is the straight line assumption for the reconstructed data points, the green line for the reconstructed simulation points and the black line is the MC truth. The simulation obviously reproduces a too big* Δ *Intercept.*

9.5.2 Performance of Two Track Reconstruction

To investigate the reconstruction performance of the two tracks the reconstructed value angle α can be compared to the calculated prediction. The reconstructed values for α can be found in Table 9.6. For setting 1 and 2 a track definition is used, which demands at least 6 minimal hits per track. For setting 3 a track definition of minimal 5 minimal hits per track is used [3]. The difference between the reconstructed and and calculated prediction of α is smallest for setting 1. For all measured magnetic α is reconstructed within a range below 10 % to the prediction. For the simulated magnetic fields the range is even below 3 %. For setting 2 the α reconstruction of the measurement degrades slightly above a 10

[3] except the values with *, which consists of minimal 6 hits, because only this value was available.

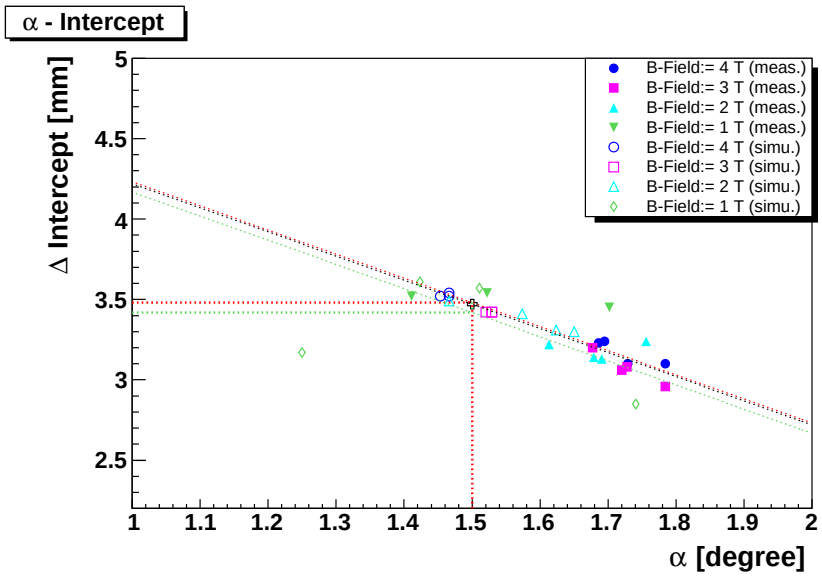

Figure 9.16: *The figure shows the α-Δ I anti-correlation for setting 2. The figure show a fairly good agreement between data and simulation. Also the straight line fits and the determination of Δ I for both show a very good agreement of this parameter.*

% level for investigated magnetic fields. For the simulation the deviation is still below 10 %. For both data and simulation the reconstruction of α degrades extremly if the two tracks are moved as close together as in setting 3. Here the reconstruction fails completely to achieve the calculated prediction. Therefore two different methods have been applied. The first method takes all reconstructed events into account an takes the mean value. The second method is applied if a clear peak at the predicted α position could be determined (see figure 9.10(e)). If such a distinct peak can be found, which can be clearly distinguished from a peak reconstructed at a false position, a cut is placed around the correct position. Afterwards the mean value of the Gaussian distribution is taken describing the peak. For the first method the reconstructed angle α deviates between 50 to 100 % from the prediction for data and simulation. The second method can reconstruct α in a range of 7.0 to 15 % in case of the measurement and 7.0 to 35 % for the simulation. This demonstrates clearly, that the separation algorithm is reaching its limits. Even if the two tracks can still be separated, the parameters, which can be derived, have to be treated with care.

In Section 9.4 the anti-correlation between the angle α and the distance ΔI is discussed. Therefore these two parameters can be plotted against each other.

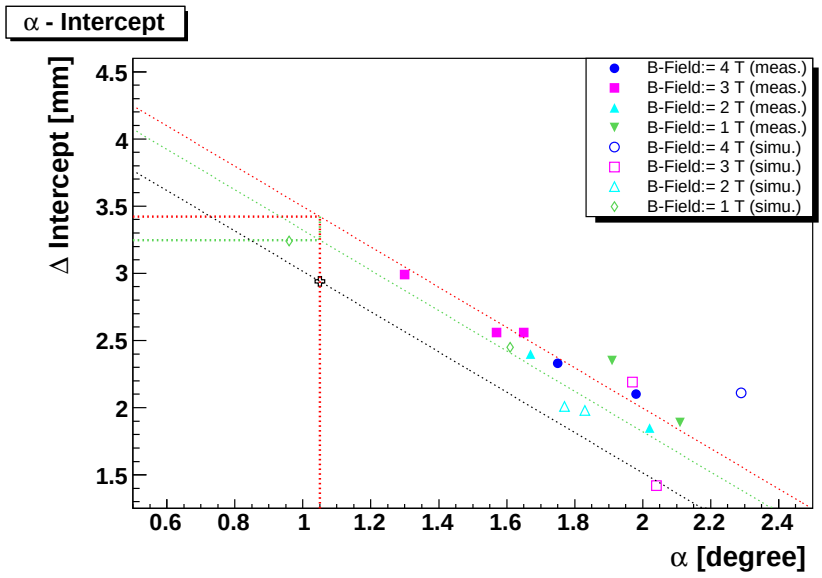

Figure 9.17: *The figure shows the α-ΔIntercept anti-correlation for setting 3. The figure show the results if the complete sample is taken into account. The reconstruction fails to reconstruct α the theoretical prediction.*

For the plots the statistical uncertainty was used. In the Tables 9.4 and 9.6 one sees, that the statistical uncertainty is below 1 % and can be neglected. The RMS of these two values is of course much larger and describes more accurately the uncertainty for the reconstruction a single event. As one wants to know the general detecor performance on a statistical base the uncertainty of the mean value is more appropriate to describe these parameters. For the following plots always the statistical uncertainty of the mean value is included in the plots.

To quantify the dependency between the two parameters a correlation factor is given by:

$$|\rho_{xy}| = \frac{|\sigma_{xy}|}{\sqrt{\sigma_x^2 \sigma_y^2}} \leq 1 \tag{9.4}$$

with the covariance σ_{xy} and the standard deviations σ_x and σ_y. If x is independent from y the correlation factor $\rho_{xy} = 0$. If $\rho_{xy} = \pm 1$, there is a complete correlation between the two variables. The expected correlation between the two parameters α and ΔIntercept is a linear dependency. Due to the size of the pad plane a wrong reconstruction of α by 0.1 ^{o} corresponds to a shift of ΔIntercept by 150 μm. With these two parameters it is possible to fix the slope of the correlation.

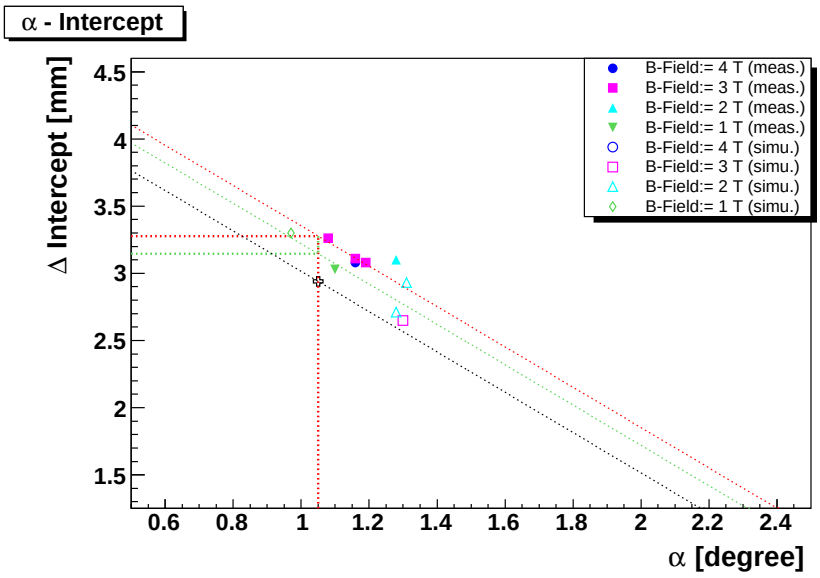

Figure 9.18: *The figure shows the α-ΔIntercept anti-correlation for setting 3 if a cut on the α distribution can be placed. For example in Figure 9.10(e) a clear two peak structure can be observed. Only samples with such a distinct two peak structure are taken into account for the determination of α. These values fit much better to the theoretical prediction for α.*

In Figure 9.15 α and ΔI are plotted for all measured and simulated magnetic fields of setting 1. There are four entries for every magnetic field. These four entries correspond to the four different track definitions. Also the true point of the simulation is added as a reference. This point is connected with the predicted slope. All points of the simulated magnetic fields fit perfectly to the slope. This is also expressed in the correlation factor in Table 9.7, which is -0.99. The points from the measurement also show a correlation, but the whole curve is shifted to smaller values of ΔI. The 1, 2 and 3 Tesla samples agree to the straight line assumption. The entries of 4 Tesla differ most from the straight line, which is demonstrated by the correlation factor. If including the 4 Tesla samples the the $\rho_{xy,with4T}$ = -0.22 without the 4 Tesla samples $\rho_{xy,without4T}$ = -0.66. This confirms the assumption to treat the 4 Tesla data with care. One reasons to treat the 4 Tesla data was the strong reduction of the laser intensity, which leads to a strong reduction of the primary ionization, which was mentioned in 9.3.
In Figure 9.15 the straight line assumption is fitted with the slope as a fixed and ΔI as a free parameter. At the expected position for α the value for ΔI is read out. The red line is the straight line assumption for the reconstructed data

setting	ΔIntercept reconstructed [mm]	ΔIntercept from MC-truth [mm]	Correlation Factor ρ_{xy}
Data 1	3.85		-0.2
Data 1 (without 4 T)	3.76		-0.66
Simulation 1	3.97	4.0	-0.99
Data 2	3.48		-0.78
Simulation 2	3.42	3.47	-0.44
Simulation 2 (no outlier)	3.49	3.47	-0.92
Data 3 (Mean Value)	3.42		-0.95
Data 3 (with cut)	3.27		-0.33
Simulation 3 (Mean Value)	3.24	2.94	-0.53
Simulation 3 (with cut)	3.15	2.94	-0.61

Table 9.7: *The table shows the reconstructed values for the difference of two intercepts at the known position for α. The values are derived for all settings and both data and simulation. It also shows the correlation factor ρ_{xy}, which describes the degree of correlation between α and ΔI. A correlation factor ρ_{xy} $= \pm 1$ means complete correlation and a value of 0. means no correlation at all.*

points, the green line for the reconstructed simulation points and the black line is the MC truth. The reconstructed ΔI of the simulation is in complete agreement with the MC truth. The reconstructed value ΔI show a deviation of about 200 μm between data and simulation. This deviation can occure if the y-position of the wedge holder, where the laser is reflected back in the sensitive value is not correct. The maximal possible uncertainty of the wedge holder is about $\pm$ 4 mm. This leads to a maximal uncertainty for ΔI of $\pm$ 273 μm.
In Figures 9.16 the samples of setting 2 are illustrated. A good agreement between data and Monte Carlo simulation to a common straight line fit can be observed. The points of the simulation reconstruct α and therefore also ΔI more precise at the predicted position of $\alpha = 1.5°$. The points of the data samples reconstruct α at higher value than the predicted respective smaller values for ΔI. Nevertheless both simulation and measurement fit to the same straight line assumption. The red line with the straigt line assumption of the data and the green of the simulation points are in very good agreement. The correlation factor $\rho_{xy,data}$ of the data samples is with -0.78 compared to -0.44 nearer to -1. This of course seems to be the result of two outlier at 1 Tesla. After removing these outliers $\rho_{xy,simu}$ = -0.92. Also the reconstructed ΔI, which are derived in Figure 9.16 are almost equal, with ΔI_{meas} = 3.48 mm and ΔI_{simu} = 3.42 mm (respective 3.49 mm after removing the outliers).
For setting 3 the two different methods have been applied. The first method takes all reconstructed events into account. The mean values of the α and ΔI histogramms are plotted in the Figure 9.17. For the second method a cut is applied if a clear peak at the correct position for α is found. This is illustrated in Figure 9.18.
In Figure 9.17 the angle α is reconstructed far too big as discussed in section 9.4. The range for α is between 1.6 ° and 2.2 ° for data and simulation. This is far away from the theoretical prediction of 1.05°. Here the correlation factor of the data ρ_{xy} = -0.95 and ρ_{xy} = -0.53 for the simulation does only show, that the anticorrelation between the two parameters is still valid, also the values itself are reconstructed falsely.
In Figure 9.17 it can be observed, that the simulation, which could reproduce the reference point in the previous settings perfectly, shifts ΔI to higher values. The ΔI of the measurement is 3.42 mm and 3.27 mm for the simulation, which is comparable to setting 2. The value for ΔI is reduced, if the second method is applied, which leads to more realistic values for ΔI (see figure **??**). Here the difference of the intercepts is 3.24 mm for data and 3.15 mm for the simulation, which is closer to the value expected from the Monte Carlo truth. The values for all settings can be seen in table 9.7.

9.5.3 Hit Efficiency

In this section the two hit efficiency and the hit resolution of nearby tracks is studied for all three settings. The aim is to investigate the requirements for a TPC at the ILC concerning the double hit resolution, which is one of the main motivation of this work as described in Section 9.1 of this chapter in Table 9.2.

The two-hit efficiency as used in this work is defined:

$$\varepsilon_{2\ hits,norm}(i) = \frac{N_{2\ hits}(i)}{N_{tot}} / \frac{N_{2\ tracks}}{N_{tot}} = \frac{\varepsilon_{2\ hit}(i)}{\varepsilon_{2\ track}} \tag{9.5}$$

where $N_{2\ hits}(i)$ denotes the Number of counted double hits for a row i and N_{tot} the number of events which have passed the ClusterFinder of Multifit as a candidate for a track. This efficiency is normalized to the to the two-track efficiency $\varepsilon_{2\ track}$ as defined by eq. 9.3. The track definition for single tracks is the same for each setting as described in the previous chapters.

In Figure 9.19 the two hit efficiency $\varepsilon_{2\ hits,norm}(i)$ for setting 1 is illustrated. Due to the sufieciently high number of events the statistical uncertainties are negligible. The error bars, which are included for the simulation, coming from systematic uncertainties of the two track efficiency $\varepsilon_{2\ track}$ of each setting (see section 9.7). As pointed out in section 9.5.2 the two tracks are probably closer together for the measurement than for the simulation. This has also an impact to the two-hit efficiency. The two hit efficiency of the simulation for all magnetic fields is supposed to be much higher than of the measurement. This behavior was also described in section 9.4, when comparing the number of active pads (see figures 9.4(a) and 9.4(b)). For the data sample many more active pads especially between two charge maxima were observed. As mentioned before also the missing electronic effects in the simulation such as noise of the pads or cross-talk can have an impact to this. This active pads between two charge maxima can lead to a failure of the separation algorithm (described in Subsection 6.2.2).
All these effects limits the agreement between measurement and simulation seriously. Even considering the the range of the systematic uncertainty there are huge deviations for the hit efficiency between data and simulation in each row. For all magnetic fields of this setting one can see strong deviations in single rows, although a decrease of the $\varepsilon_{2\ hits,norm}(i)$ is not explicitly seen in the first rows, where the hits are closer together than in the last ones. This means above a $\Delta\ x$ of 4.5 mm one does not expect problems with the separation algorithm to separate 2 hit positions.

Figure 9.20 shows the two hit efficiency of setting 2. As we have seen in Figure 9.13 in this setting a strong decrease of the two track efficiency appears if a track has to consist of 8 rows. The decrease is caused by the first row where the hit separation algorithm fails to separate the hits. This is confirmed in figure 9.20, where a significant drop of the two hit efficiency can be seen in the first row for all magnetic fields. In general there is a good agreement within the

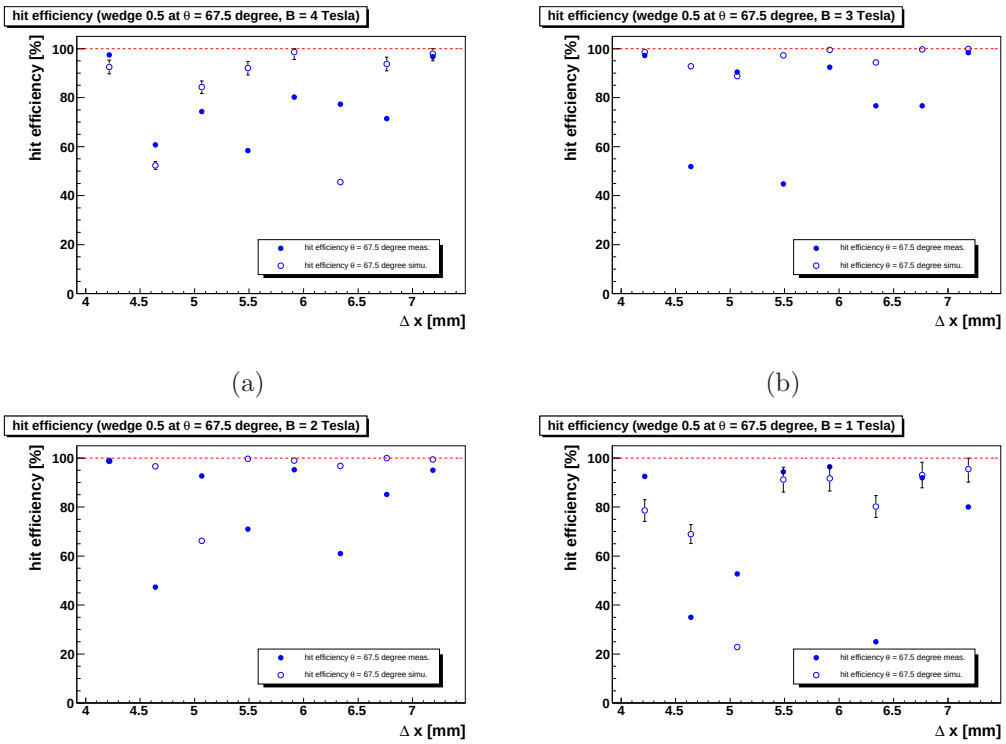

Figure 9.19: *The plots shows the efficiency to find exactly two-hits in a row for setting 1. The track definition for a single track is, that it has to consist of at least 6 hits. From figure 9.19(a) to 9.19(d) the hit efficiency for 4, 3, 2 and 1 Tesla are shown.*

systematic uncertainties of data and simulation for all magnetic fields. Especially for 2 Tesla (Figure 9.20(c)) the curve follows a clear systematic decrease. In the range of 4.5 to 3.5 mm, which corresponds to a pad width of 2 (Δx = 4.4 mm) respective 1.5 (Δx = 3.3 mm) a drop of the two hit efficiency from 60 % to 20 % appears. Above this value the two hit efficiency rises to 100 %. Only the second row shows an increase in efficiency for the data and simulation, which is probably an binning effect caused by the pad size. The 3 Tesla data curve shows the same behavior only that the decrease is more step and the maximal efficiency is reached earlier. For the simulation the decrease appears as an edge at 4 mm. The 4 Tesla samples show more fluctuation of the two hit efficiency, but also here the efficiency drops significantly at 4 mm. For the 1 Tesla samples, which has the most unfavorable ratio between width of charged cloud to pad size, one can clearly distinguish the first four and the last four rows. The last four rows reconstruct almost every time two hits. The first four rows show a

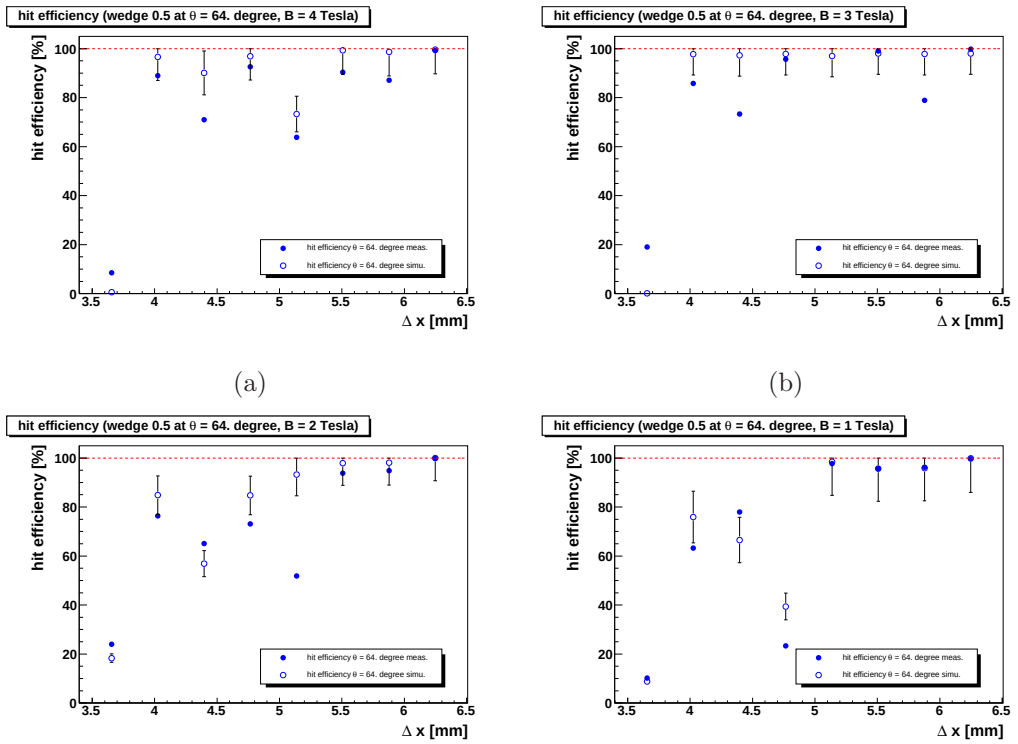

Figure 9.20: *shows the hit efficiency for setting 2.*

clearly identifiable limitation. This suggests that the hit separation limit, which is about 4.4 mm for the sample above 1 Tesla gets shifted to about 5 mm for 1 Tesla.

The two hit efficiency of setting 3 is plotted in Figure 9.21. The setting is a continuation of the previous setting, where the two-hit efficiency drops at about 4.4 mm. A significant drop of $\varepsilon_{2\ hits,norm}(i)$ in regard of each row for all magnetic fields (see Figure 9.21(a) (4 T sample) to 9.21(d) (1 T sample)). This shows that the limitation of the two hit reconstruction is not dominated by the width of the charged cloud, but by the distance between the two tracks. The seperation algorithm can only reconstruct the last three rows sufficiently. For the first five rows a serious drop in the two hit reconstruction capability can be observed. The data samples show the same behavior, although single rows can show deviations. Below a pad width of 1.5 (Δx = 3.3 mm) and below the two hit efficiency is around 20 % or less. This allows to set a limit to the two hit separation and reconstruction algorithms, which is about 4 mm.

The study of the two-hit efficiency confirms the assumption, that according to the size of the pads and the condition of the separation algorithm, a limit of the

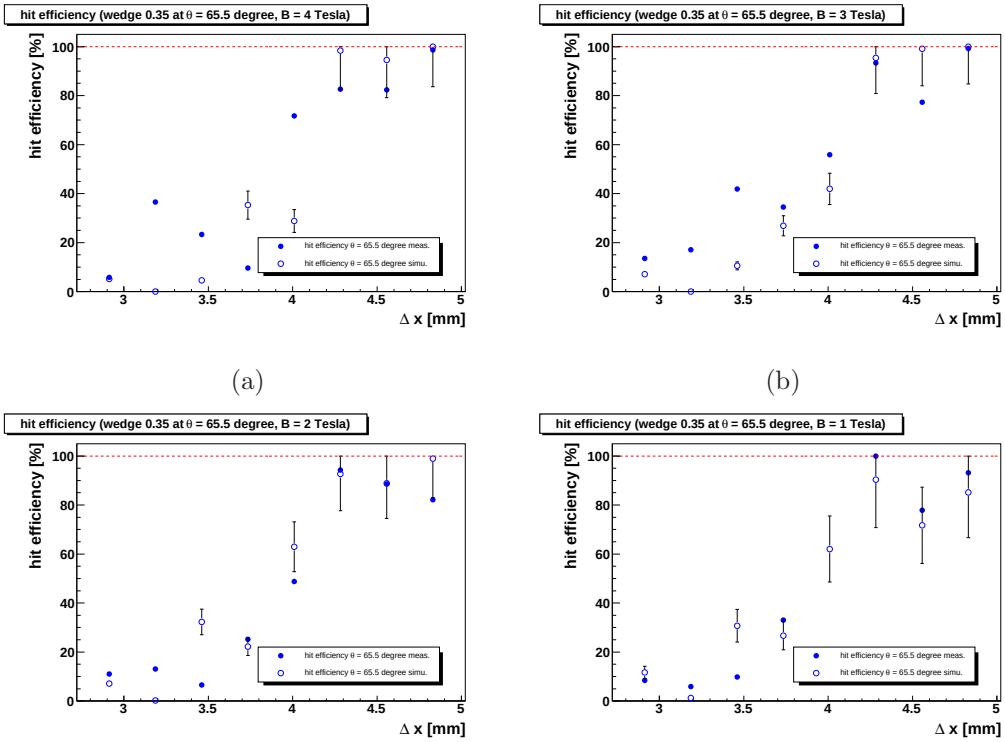

Figure 9.21: *The Figure shows the hit efficiency for setting 3.*

separation capability of two times the pad width was valid. The drop in two-hit efficiency at setting 2 and 3 around this limit also shows, that the needed tracking requirements proposed in Table 9.1 concerning the two-hit resolution could not be reached for the used pad width and the proposed reconstruction software.

9.5.4 Point Resolution of Nearby Tracks

To gain a deeper understanding also the average point resolution of both nearby tracks is studied in dependency of the magnetic field. Together with the hit efficiency of the previous section this should provide information on the the parameters $\sigma_{r\phi}$ and N and the impact these parameters have on the momentum resolution (see Equation 2.21).

In Section 6.4.1 the point resolution derived by the geometric mean method was introduced. In case of two nearby tracks, one has to ensure, that the point resolution calculated by Multifit is is assigned to the right track. The residuals and distances of the first and second track should not mix. This is very important because the assignment which is the first and the second track, which is done by

MultiFit, is not depending on angular information. This information has to be added afterwards by hand in the analysis scripts.
To calculate the resolution of the track the point resolution of all rows have to be taken into account. The point resolution of the track is given by:

$$\bar{x} = \frac{\sum_{i=1}^{n} \frac{x_i}{\sigma_i^2}}{\sum_{i=1}^{n} \sigma_i^2} \tag{9.6}$$

with x_i the single point resolution of the row i and and σ_i the uncertainty of x_i. In equation 9.6 the point resolution is weighted with the size of the uncertainty, so that points with larger uncertainties are neglected.
Also here the data and simulation samples are investigated for the same single track definition as defined in the previous chapters.

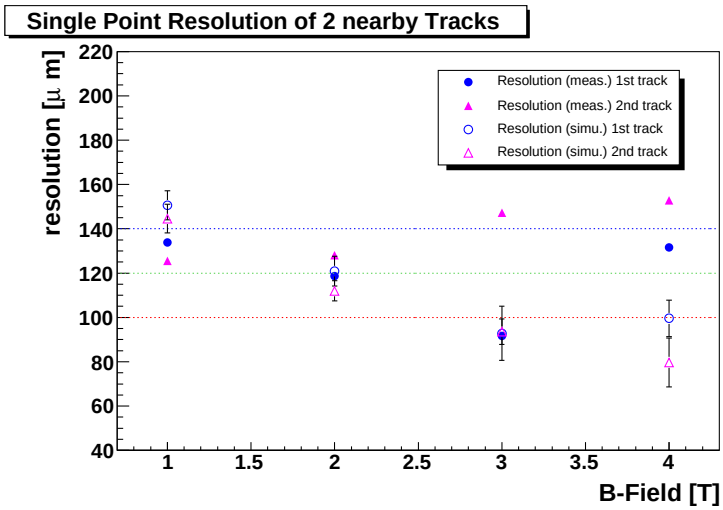

Figure 9.22: *The point resolution $\bar{x}$ of both tracks is plotted for the 4 investigated magnetic fields of setting 1. As track fitting method the Chi Squared method was used.*

In Figure 9.22 the point resolution of setting 1 for both tracks is plotted as a function of the magnetic field. The point resolution of the simulation follows the expected behavior, that the resolution improves with an increase of the magnetic field. This is not the case for the measurement. For 1 and 2 Tesla the point resolution of measurement and simulation is in good agreement, which is not the case for the 3 and 4 Tesla. The second track at 3 Tesla shows a strong deviation to the simulation. The second track is also the one with the higher intensity. Due to this high intensity and an unfavorable topological position to the read-out

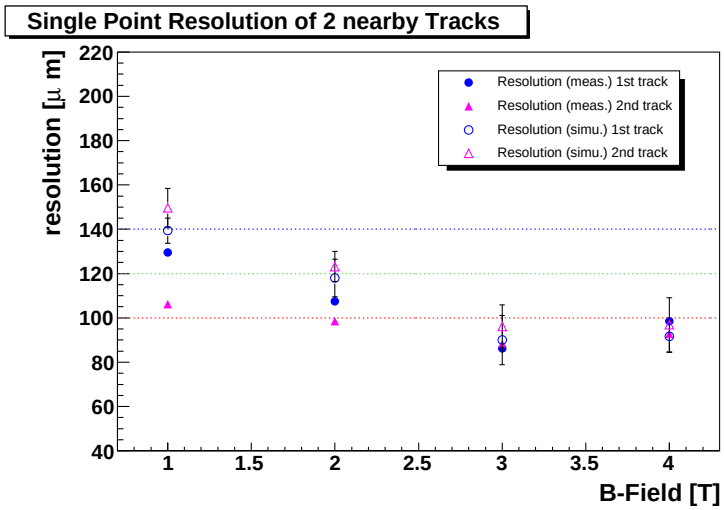

Figure 9.23: *The point resolution $\bar{x}$ of both tracks is plotted for the 4 investigated magnetic fields of setting 2. All 8 rows are included for the determination of the point resolution. As track fitting method the Chi Squared method was used.*

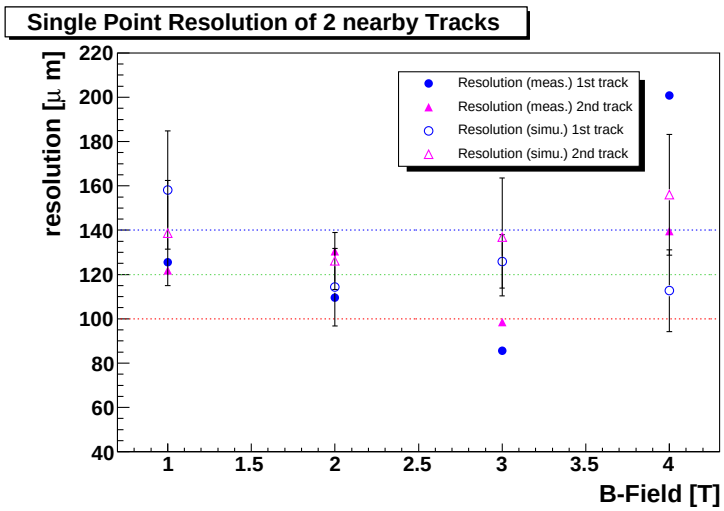

Figure 9.24: *The point resolution $\bar{x}$ of both tracks is plotted for the 4 investigated magnetic fields of setting 3. All 8 rows are included for the determination of the point resolution. As track fitting method the Chi Squared method was used.*

plane, tha charge of this pad is collected mainly on one pad. This exceeds the total dynamic range of the preamplifier and the 8-bit FADC. This might be an explanation for the degradation of the point resolution for the second track at 3 Tesla (see B). At 4 Tesla for both tracks of the measurement a serious degradation of the resolution can be observed. An explanation for the rise of the point resolution could be related to the drop in intensity, which also drops the production of primary electrons. If the amount of primary electrons, that determines the track position in front of the charge amplification system, is high also the point resolution is improved. A further explanation for the degradation of the resolution at 4 Tesla is, that also the point resolution of single tracks degrade for short drift distance and high magnetic fields. The main reason for the degradation is the charge, which is distributed mostly on one pad. This effect is studied in detail in [65, 85]and is illustrated in the Figures 9.25(a) and 9.25(b) for the Chi-Squared and Global Fit method. As the tracks are inclined in the yz-plane the charge, which is deposited on the first rows is produced at a drift length, where this effect can occur. A third explanation was discussed in section 9.5.2. Here one could see the difference of ΔI for data and simulation. This can of course change significantly the distribution of charges on the pads, what is also seen for an investigation of row 7 of setting 1. This shift of the charge distribution would have the highest influence at 4 Tesla, where the transverse diffusion has the lowest possible value for the investigated magnetic fields.

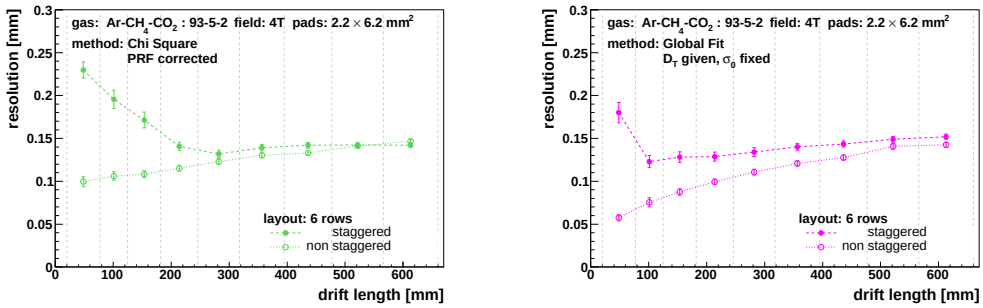

(a) Chi-Squared method

(b) Global Fit method

Figure 9.25: *In figure (a) the point resolution of single tracks reconstructed with the Chi-Squared method, in figure (b) the point resolution of single tracks reconstructed with the Global Fit method is shown. For both methods a degradation of the resolution for short drift distances is observed. Both figures were taken from [85]*

In Figure 9.23 the point resolution of setting 2 is illustrated. This setting shows an impressive agreement between data and simulation for both tracks at all magnetic fields except the second track at 1 Tesla, which has a deviation of about

45 μm. Here the topological position of the high intense track is much better than compared to the previous setting.
In Figure 9.24 the point resolution of setting 3 is shown. For 1 and 2 Tesla there is an acceptable agreement between data and simulation, but for 3 and 4 Tesla a big discrepancy of data and simulation is observed. This time also the simulation show the rise of the resolution for high magnetic fields. One explanation for the disrepancy could be, that the track position is determined without considering the influence of the charge of the other nearby track. In the Chi Squared method the nearby charge of the other track is only taken into account in the ClusterFinder of the reconstruction software (see Section 6.2). If the two tracks are moved together systematic errors from a wrong charge separation can occur. A wrong charge separation would have a stronger impact at high magnetic fields due to the limited number of charges per pad used for the reconstruction of the hit position. A wrong charge assignment on a single pad, puts a higher weight on the hit position reconstruction. This might also explain the big discrepancy between data and simulation. If the width of the charged cloud is not modelled accurate enough, the charge per pad, which determines the the hit position is not determined properly. This can lead to a strong replacement of the hit position. The replacement of the simulation is carrying a heigher weight, because it was already shown in Section 9.4, that the simulation has a smaller number of active pads. It might be also an advantage if the track and the track parameter are optimized globally (see Section 6.4.3). This might help to stabilize the track with the rows, that are well seperable in charge. This two effects were studied in the next section.

9.6 x-Separation Performance of the Global Fit Method

An alternative approach of a fitting algorithm has been used to compare and cross check the results of the Chi Squared method. This approach is the Global Fit method (described in section 6.4.3). The Global Fit Method does not produce new hits, but recalculates the resolution for the already existing ones. One gets the same hit and track efficiencies as for the Chi Squared method, but the values for the reconstructed track parameters α and ΔI and the recalculated point resolution can change. Therefore only plots of these paramters are shown. The Global Fit method is used with the same track definition as the Chi-Squared method for setting 1, 2 and 3.

9.6.1 Performance of Two Track Reconstruction

The angles α reconstructed with the GFM are shown in Table 9.8. These results can be compared to the values, which have been reconstructed with the Chi-

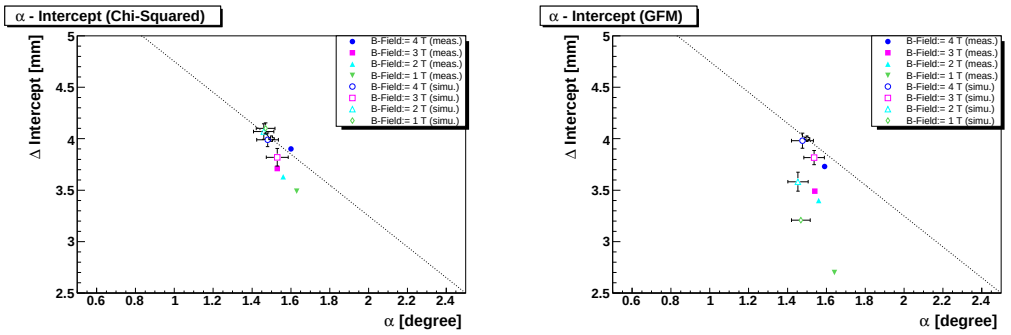

(a) Chi Squared method for setting 1. The track consists of at least 6 hits.

(b) Global Fit method for setting 1. The track consists of at least 6 hits.

Figure 9.26: *In the plots the α-ΔI correlation is shown for setting 1. In Figure (a) the values for α and ΔIntercept follow the expected straight line prediction. In Figure (b) this correlation is not valid anymore. A clear difference between Chi-Squared method and the GFM can be observed.*

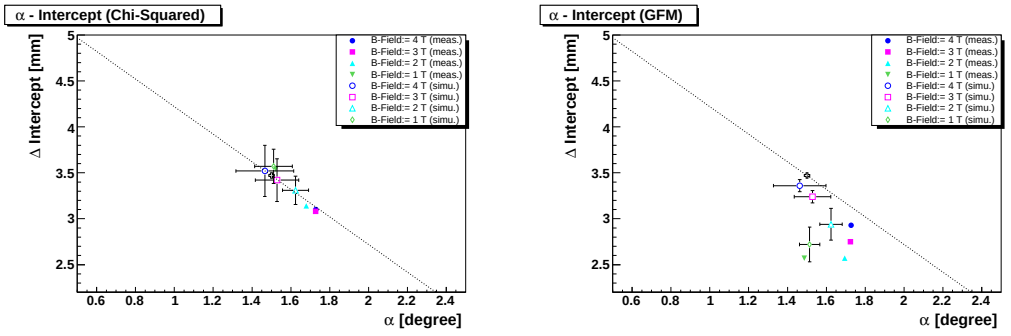

(a) Chi Squared method for setting 2. The track consists of at least 6 hits.

(b) Global Fit method for setting 2. The track consists of at least 6 hits.

Figure 9.27: *The same behavior as for the α-ΔIntercept correlation of setting 1 can also be observed for setting 2 between (a) the Chi-Squared method and (b) the GFM.*

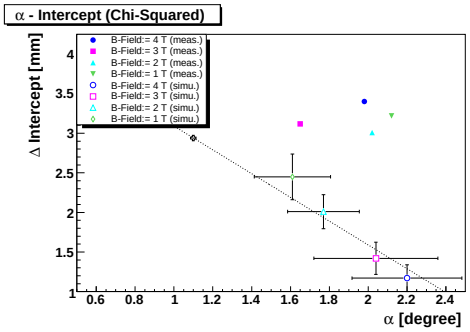

(a) Chi Squared method for setting 3. The track consists of at least 5 hits.

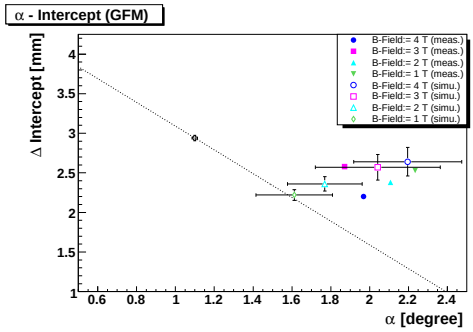

(b) Chi Squared method for setting 3. The track consists of at least 5 hits.

Figure 9.28: *The behavior of the GFM method changes significantly compared for the previous settings. The GFM reconstructs ΔI more or less at a fixed position, also the the strong α deviation for the different magnetic fields remains.*

setting	B-Field [T]	$\alpha_{meas.}$ [^{o}]	Dev. [%]	$\alpha_{simu.}$ [^{o}]	Dev. [%]
1	4	$1.59 \pm 0.006 \pm 0.283$	6.0	$1.38 \pm 0.002 \pm 0.112$	8.0
1	3	$1.54 \pm 0.004 \pm 0.235$	2.7	$1.49 \pm 0.002 \pm 0.103$	1.3
1	2	$1.56 \pm 0.005 \pm 0.222$	4.0	$1.49 \pm 0.002 \pm 0.109$	0.7
1	1	$1.64 \pm 0.004 \pm 0.208$	8.7	$1.44 \pm 0.003 \pm 0.169$	1.3
2	4	$1.73 \pm 0.003 \pm 0.179$	14.6	$1.46 \pm 0.004 \pm 0.170$	2.7
2	3	$1.72 \pm 0.003 \pm 0.169$	15.3	$1.53 \pm 0.003 \pm 0.136$	2.0
2	2	$1.7 \pm 0.003 \pm 0.183$	12.0	$1.62 \pm 0.004 \pm 0.201$	8.0
2	1	$1.49 \pm 0.009 \pm 0.243$	1.3	$1.51 \pm 0.008 \pm 0.285$	0.7
Setting 3 using mean value					
3	4	$1.97 \pm 0.012 \pm 0.601$	87.6	$2.20 \pm 0.008 \pm 0.457$	109.5
3	3	$1.87 \pm 0.014 \pm 0.809$	78.1	$2.04 \pm 0.009 \pm 0.489$	94.3
3	2	$2.11 \pm 0.012 \pm 0.631$	101.	$1.77 \pm 0.010 \pm 0.488$	68.6
3	1	$2.23 \pm 0.020 \pm 0.724$	112.4	$1.61 \pm 0.025 \pm 0.564$	53.3
Setting 3 with a cut					
3	4	$1.29 \pm 0.022 \pm 0.269$	22.9	-	-
3	3	$1.20 \pm 0.006 \pm 0.184$	14.3	-	-
3	2	-	-	$1.23 \pm 0.008 \pm 0.184$	18.1
3	1	$1.14 \pm 0.040 \pm 0.232$	8.6	$0.97 \pm 0.012 \pm 0.106$	7.6

Table 9.8: *The table show the values for α reconstructed with the Global Fit method. Comparing these values with the values of Table 9.6, the differences for α are negligible.*

Squared method (see Table 9.6). The α values of setting 1 and 2 are within a 1 to 2 % level the same between Chi-Squared and GFM method. This is valid for data and simulation. This changes for the α data values of setting 3.
In Figure 9.26 the α-ΔIntercept correlation is compared for the two track fitting methods of setting 1. In Figure 9.26(a) the results of the Chi Squared and in Figure 9.26(b) the results of the Global Fit method are shown. A clear difference for the two methods can be observed. For the Chi Squared method the two tracks are calculated independently of each other, therefore a deviation of α is strongly correlated to the intercept (described in Section 9.5.2). For the Global Fit Method these two track parameters are optimized simultaneously in a Likelihood function. Therefore this relation between α and ΔI is not valid anymore. This can be clearly seen in the plots. The Chi Squared method follows the straight line assumption. A shift of α by 0.1 $^\circ$ corresponds to a shift of ΔI by 150 μm. For the Global Fit method α also shows a total deviation of 0.1 ^{o} , but ΔI is changes here by about 1 mm. The simultaneous optimization of both tracks has only a negligible effect on the reconstruction of α, but shows a significant influence on the reconstruction of ΔI as a function of the magnetic field.
The same behavior comparing the two track fitting methods is seen in Figure 9.27 for setting 2. In Figure 9.27(a) the Chi Squared method shows a good agreement for data and simulation with the straight line assumption. The Global method shown in Figure 9.27(b) still distributes the values around the correct α position, but have a strong variation especially for different magnetic fields of ΔIntercept.
For setting 3 the behavior changes. In Figure **??** one can observe, that although α is reconstructed with huge deviations to the theoretical predicted value the straight line assumption for the correlation of α-ΔIntercept is still valid. The reconstruction of α with the Global Fit Method is shown in Figure 9.28(b). The values for α are almost the same as for the Chi-Squared method, but the reconstruction of ΔIntercept differs significant between the two methods. For setting 3 ΔIntercept deviates only in a range of 300 μm for different magnetic fields, which is much more stable than in the previous settings. It seems that either α or ΔIntercept is reconstructed stable for the different magnetic fields, but not both at the same time.

9.6.2 Point resolution of nearby Tracks

In Figure 9.29 the point resolutions in dependency of the magnetic field is shown for the Global Fit method. Both tracks are illustrated for setting 1. The course of the point resolution is comparable to the one given in Figure 9.22. Also for the GFK a drop of the single point resolution for an increasing magnetic field can be observed. Especially the resolution of 1 and 2 Tesla calculated for the GFM is higher compared to Chi Squared method. Also the increase of the resolution at 4 Tesla is less strong than seen for the Chi Squared method. Nevertheless there is a significant difference to the results of the Chi-Squared method. In the GFM the

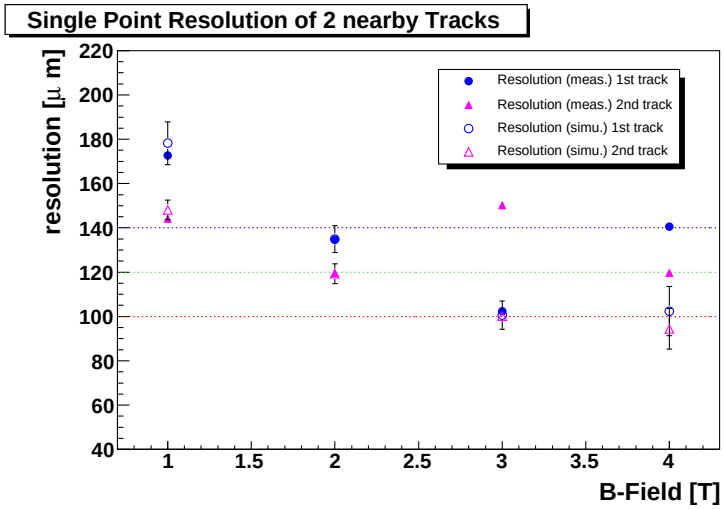

Figure 9.29: *shows setting 1. The point resolution $\bar{x}$ of both tracks is plotted for the 4 investigated magnetic fields. As track fitting method the Global Fit method was used.*

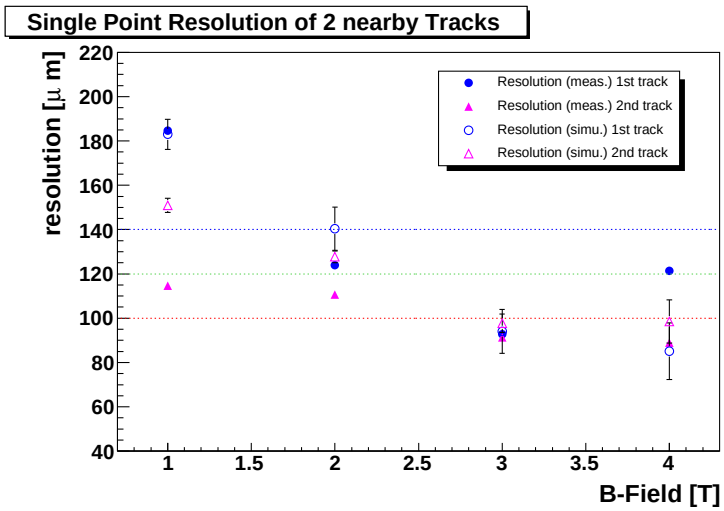

Figure 9.30: *shows setting 2. The point resolution $\bar{x}$ of both tracks is plotted for the 4 investigated magnetic fields. All 8 rows are included for the determination of the point resolution. As track fitting method the Global Fit method was used.*

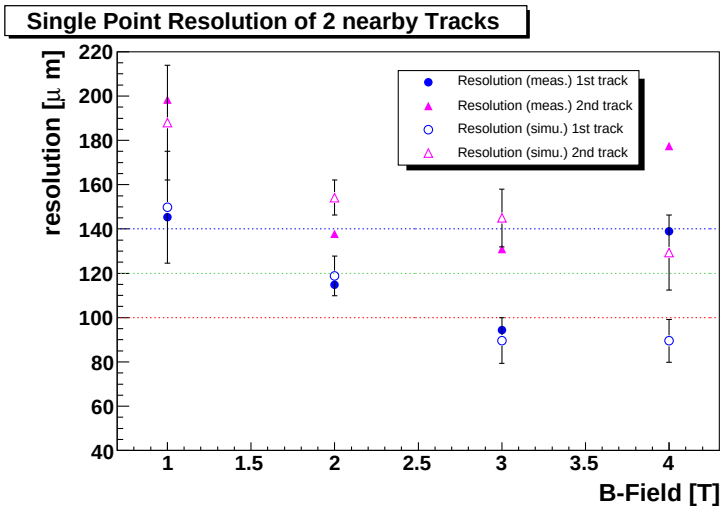

Figure 9.31: *shows setting 3. The point resolution $\bar{x}$ of both tracks is plotted for the 4 investigated magnetic fields. All 8 rows are included for the determination of the point resolution. As track fitting method the Global Fit method was used.*

value for the point resolution for the first track is always higher except for the 3 Tesla case. This is closer to the expected behavior of tracks with strong differences in primary ionizations. One can observe a better resolution for the higher energetic track and a worse resolution for the lower energetic track. Also here the 3 Tesla case is different for the same reasons as mentioned in Section 9.5.4. This means for setting 1, where both tracks have the highest separation, that the influence of the point resolution is significant. A method, which optimizes the charge of one track in dependency to the other, seems to describe the results more reliable.
For setting 2 the same effects as in setting 1 can be observed. One can see a clear improvement of the point resolution for an increase of the magnetic field. Also here the lower energetic track shows a worse resolution than the higher energetic one. The remarkable effect of the GFM is that in comparison to the the Chi-Squared method it worsens the point resolution, but also makes the results more consistent to the expectation.
The strongest influence of the fitting routines on the data and simulation samples can be observed for setting 3. In Figure 9.24 the Chi Squared method shows a degradation of the point resolution for the simulation at 3 Tesla. This behavior changes completely for the Global Fit method (see figure 9.31). One can observe a good agreement between data and simulation for first and second track up to 3 Tesla. Only for 4 Tesla the tracks of the data sample deviates from the simulation assumption. A Global Fit method with the possibility to optimize the charge dis-

tribution of two tracks at the same time seems to be more appropriate to calculate the point resolution of nearby tracks.

9.7 Influence of the Pad Size

The advantage of a laser system, which produces tracks at a specific position, can also have the disadvantage of systematic effects caused by the fixed position of the laser track to the pad. Especially the width of the pad is an important parameter in regard of the separation capability. It is important to know if the separation is limited by the pad size or by the width of the charged cloud. Therefore the influence of the pad size has been investigated with the simulation. This allows to move the laser tracks under exactly the same conditions along a pad. Two different pad sizes have been investigated. First the pad size used for the measurement has been examined for the three settings. Also a smaller pad size has been investigated for setting 2 and 3, where the two tracks have been moved together. The results of the simulation for smaller pads are considered as an outlook for measurements with such smaller pad sizes. Future measurements with pad sizes as proposed in [8] have to answer also the important question of this intrinsic limit of track separation.

The first pad size used has the size of $2.2 \times 6.2\ mm^2$. The same parameters of table 9.3 have been used for the simulation except (x_0, y_0). These parameters have been replaced by a x_{01}, which denotes in this case the starting point of a the first track position. The value Δx is kept fixed, so that the starting point for the second track can be easily calculated by $x_{02} = x_{01} + \Delta$x. The starting point x_{01} is scanned with 220 μm along a pad, which is one tenth of the pad pitch. After 11 steps the same position as the original position is reached, which means that the track parameters should be comparable to the starting point. For each step point a sample of 1000 events is generated. The single track definition is the same as previously definitions. The analysis for the $2.2 \times 6.2\ mm^2$ pad size is done for the Chi-Squared and GFM fitting method to derive the systematic uncertainty for both reconstruction methods. This uncertainty is included in the error description of the previous sections about the point resolution as well as for the description of the α-ΔI correlation. A sketch of the scanning process is illustrated in figure 9.32.
Three set of parameters are tested regarding the deviations. The relation α-ΔI, the track efficiency and the point resolution of both tracks. In the figures 9.33 and 9.34 these relations are illustrated for all magnetic fields of setting 1. The x-axis always denotes the position of x_{01} on the pad starting with 0, which is the beginning of the pad. The blue vertical lines represent the step size of 220 μm. The red vertical lines mark the beginning of the pad ($x_{01} = 0$) and the position, when the original position is reached again ($x_{01} = 2.2$ mm).

Setting 1 is the one, which has the biggest distance betweent the two tracks at

Rec. method	B-Field [T]	RMS α [^{o}]	RMS ΔI [mm]	RMS efficiency [%]	RMS Res. 1^{st} track [μm]	RMS Res. 2^{nd} track [μm]
Setting 1						
Chi^2	4	0.056	0.067	3.0	8.2	11.
Chi^2	3	0.056	0.085	0.0	12.2	5.7
Chi^2	2	0.052	0.076	0.6	6.7	4.6
Chi^2	1	0.048	0.053	5.5	6.6	6.5
GFM	4	0.056	0.074	3.0	11.1	9.2
GFM	3	0.053	0.068	0.0	6.4	2.2
GFM	2	0.052	0.092	0.6	6.1	4.4
GFM	1	0.048	0.021	5.5	9.7	4.4
Setting 2						
Chi^2	4	0.149	0.278	9.9	7.1	12.2
Chi^2	3	0.112	0.232	8.7	11.1	9.7
Chi^2	2	0.067	0.154	9.3	8.5	6.8
Chi^2	1	0.097	0.186	10.5	5.7	8.9
GFM	4	0.135	0.065	9.9	12.8	9.8
GFM	3	0.094	0.068	8.7	9.9	4.2
GFM	2	0.058	0.173	9.3	9.7	2.6
GFM	1	0.052	0.190	10.5	6.8	3.2
Setting 3						
Chi^2	4	0.283	0.169	15.8	18.5	27.3
Chi^2	3	0.319	0.203	14.8	12.1	26.6
Chi^2	2	0.185	0.215	13.4	17.5	12.8
Chi^2	1	0.196	0.288	3.6	26.7	23.7
GFM	4	0.278	0.180	15.8	9.7	16.9
GFM	3	0.322	0.161	14.8	10.3	13.0
GFM	2	0.192	0.091	13.4	9.0	7.9
GFM	1	0.197	0.068	3.6	25.3	25.9

Table 9.9: *The table shows the RMS for all investigated parameters and magnetic fields for Chi-Squared and GFM reconstruction method. One can clearly see, that the systematic uncertainty to determine the parameters rises significantly with smaller distances between the tracks.*

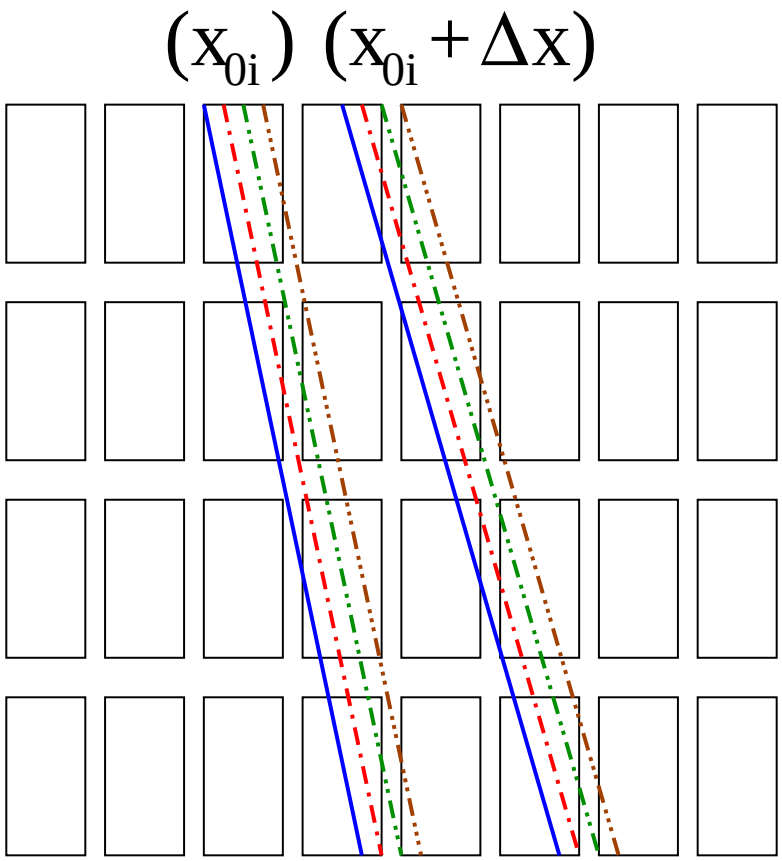

Figure 9.32: *The figure shows the how the laser was moved along the pads. Only the parameter x_0 of the first track was shifted by 220 μm, a tenth of a pad size, until the same position as the original is reached. All other parameters of the two tracks stay unmodified.*

the beginning of the sensitive volume. The $\Delta\ x = 4.0$ mm at y = 0 between the tracks. This also means, that the fluctuations of the three parameter sets should be minimal. The α-ΔI relation is plotted for 4 (figure 9.33(a)), 3 (figure 9.33(b)), 2 (figure 9.34(a)) and 1 Tesla (figure 9.34(b)). The black dots show the deviation between the true and the reconstructed values of α. The red dots show the same deviations for ΔI. The full dots represent the Chi-Squared method, the unfilled the GFM method. All magnetic fields show a very good agreement between real and reconstructed values when moving along the pad. Both α and ΔI show a deviations below 0.2 ^{o} and 0.2 mm.
The efficiency of this setting, which is given in the figures 9.33(c), 9.33(d) and 9.34(c) for 4, 3 and 2 Tesla is at about 100 %. Only for 1 Tesla a decrease can be observed in figure 9.34(d).

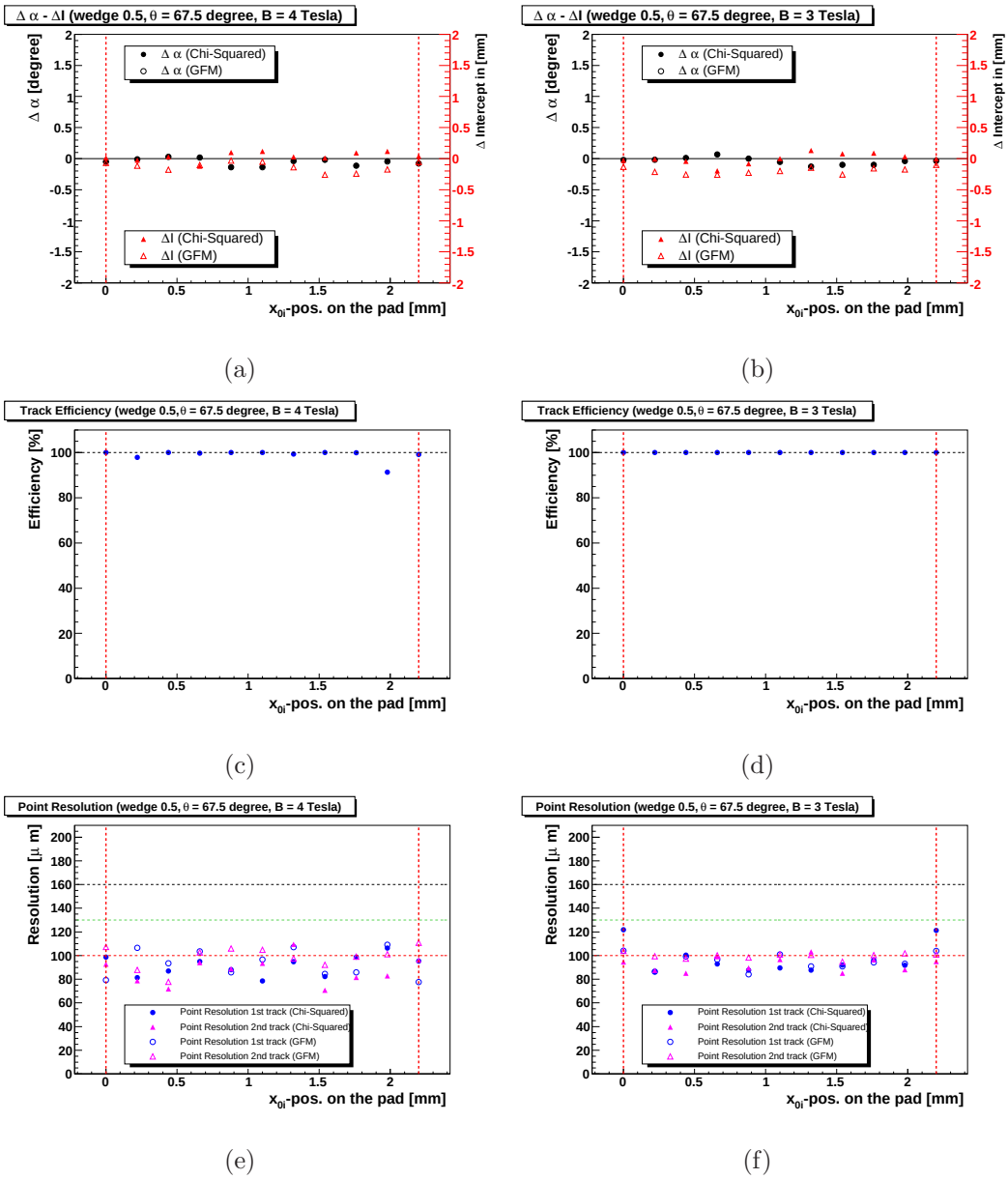

Figure 9.33: *shows the systematic effects on key parameters caused by a fixed position of laser tracks to the pad geometry with a pad size of* $2.2 \times 6.2\ mm^2$. *The plots show the margin of fluctuations of the reconstructed parameters for the 3 and 4 Tesla case of setting 1. The Chi Squared method was used as fitting routine.*

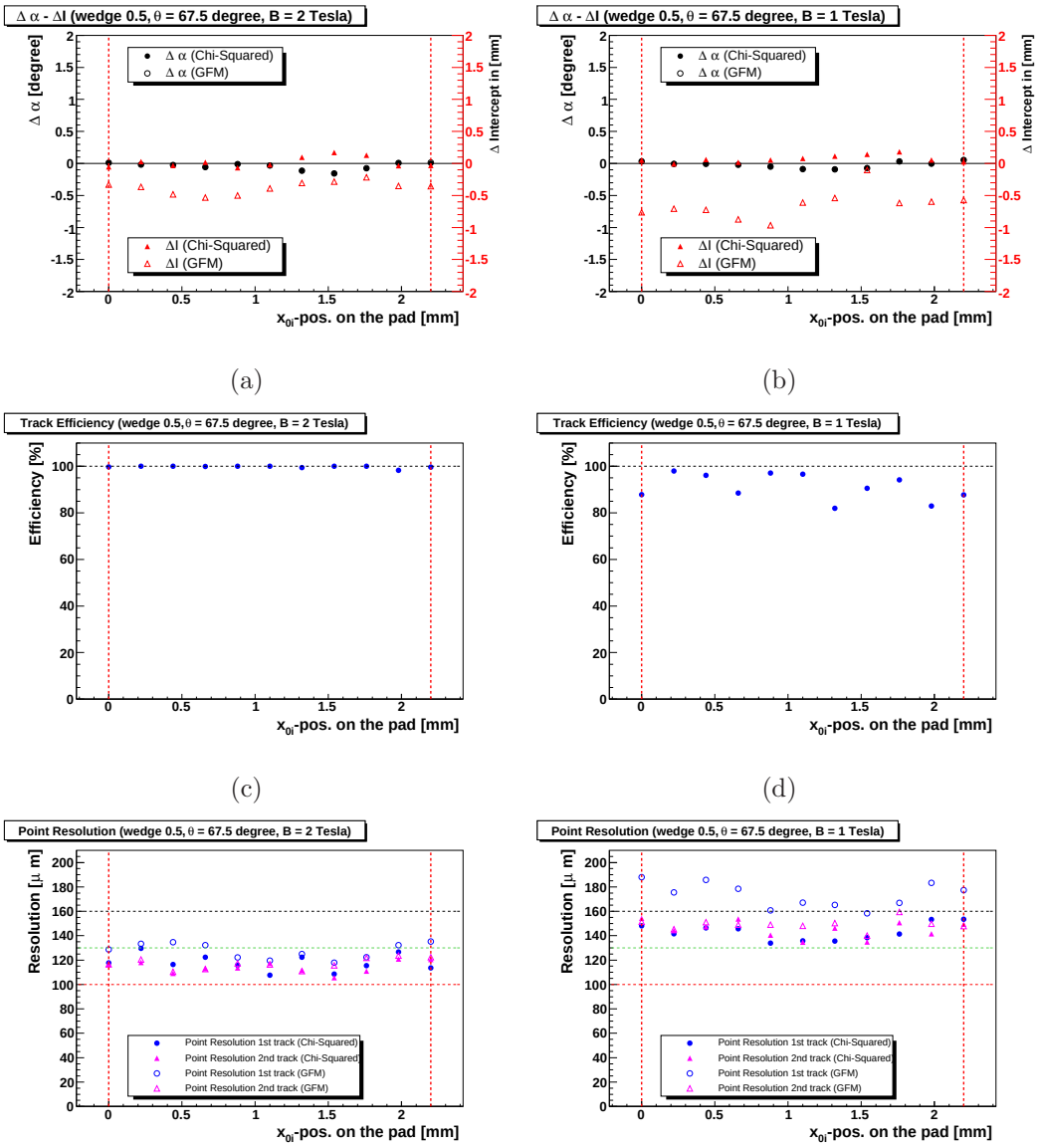

Figure 9.34: *shows the systematic effects on key parameters caused by a fixed position of laser tracks to the pad geometry with a pad size of* $2.2 \times 6.2\ mm^2$. *The plots show the margin of fluctuations of the reconstructed parameters for the 1 and 2 Tesla case of setting 1. The Chi Squared method was used as fitting routine.*

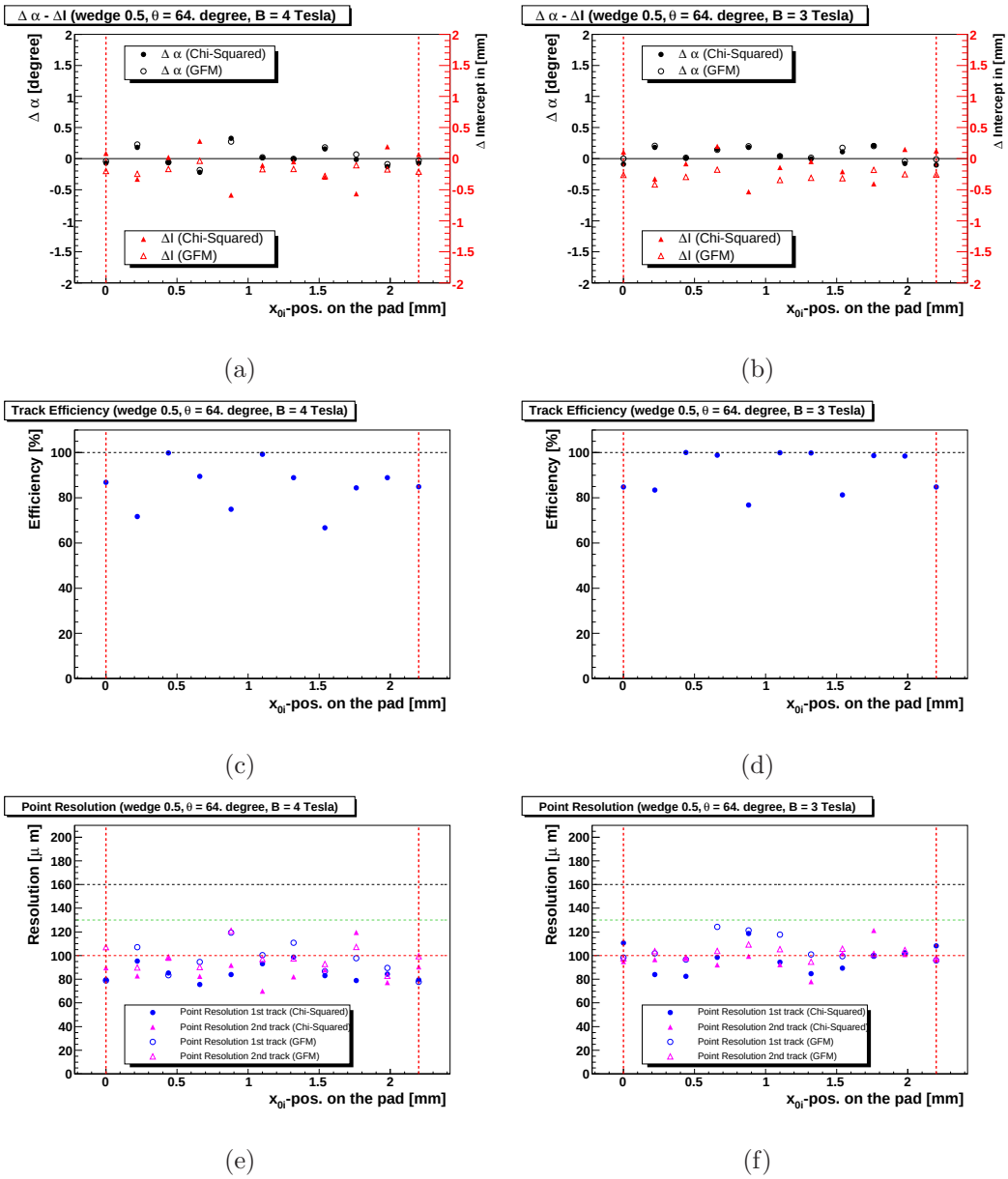

Figure 9.35: *shows the systematic effects on key parameters caused by a fixed position of laser tracks to the pad geometry with a pad size of* $2.2 \times 6.2\ mm^2$. *The plots show the margin of fluctuations of the reconstructed parameters for the 3 and 4 Tesla case of setting 2. The Chi Squared method was used as fitting routine.*

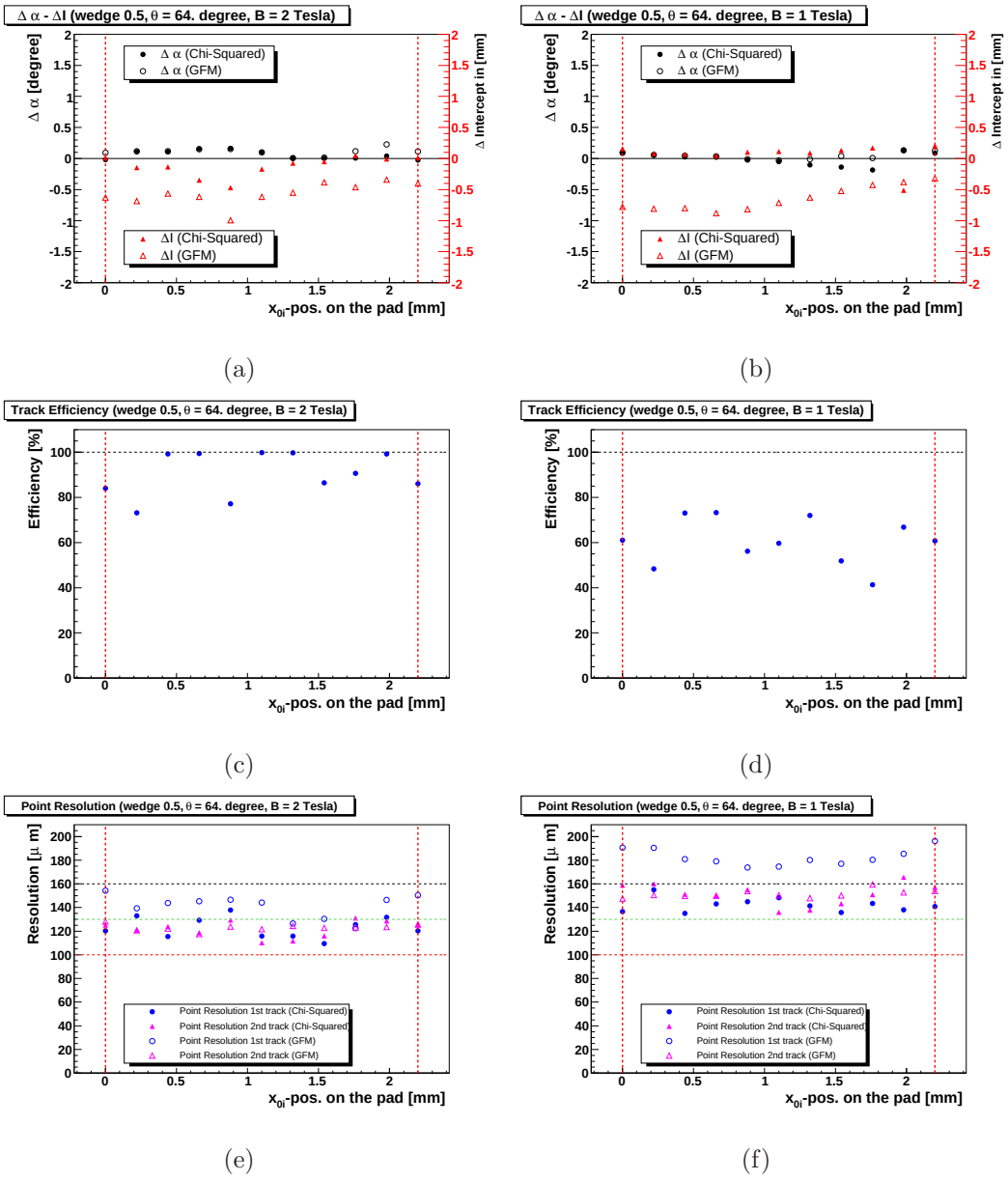

Figure 9.36: *shows the systematic effects on key parameters caused by a fixed position of laser tracks to the pad geometry with a pad size of* $2.2 \times 6.2\ mm^2$. *The plots show the margin of fluctuations of the reconstructed parameters for the 1 and 2 Tesla case of setting 2. The Chi Squared method was used as fitting routine.*

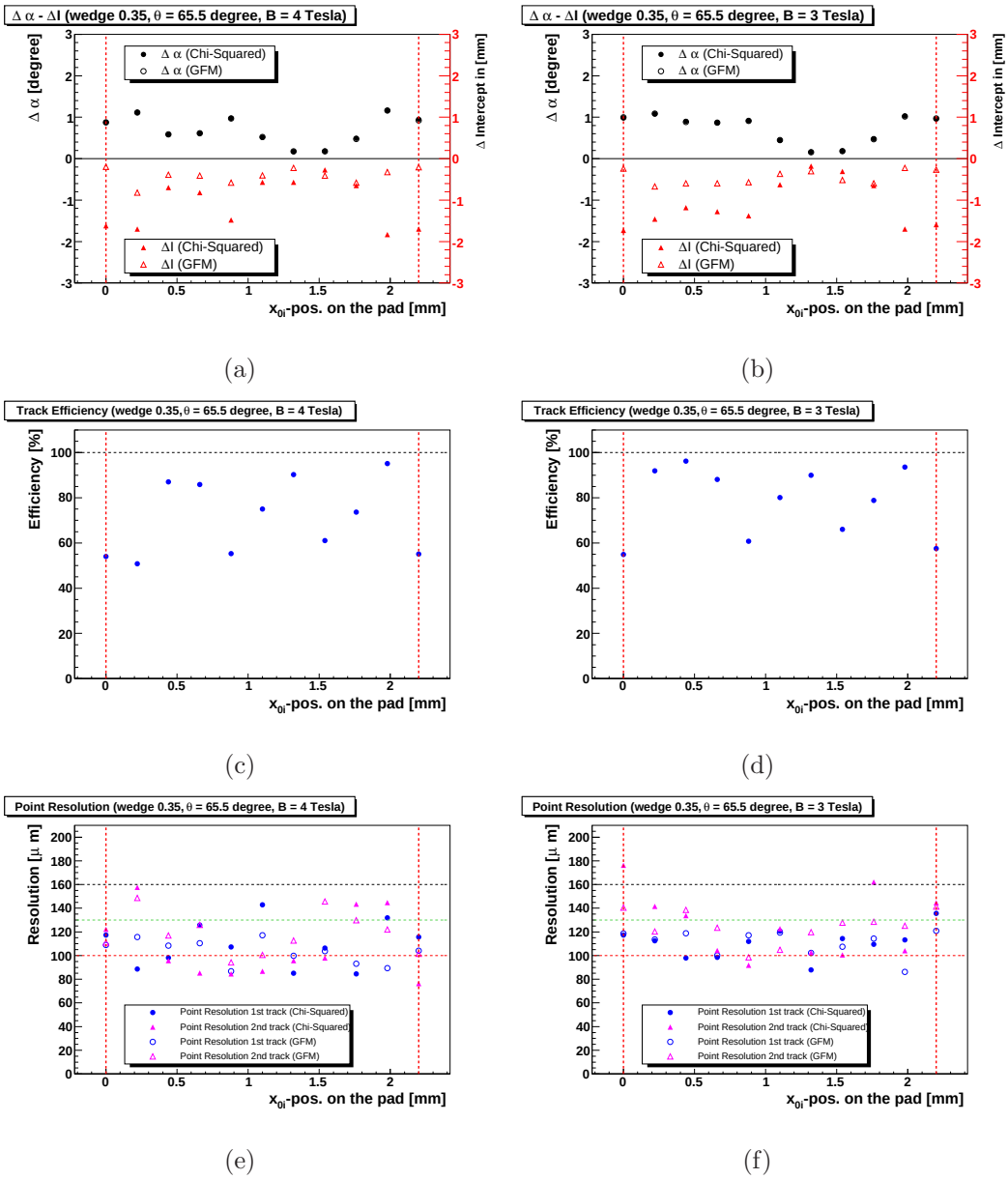

Figure 9.37: *shows the systematic effects on key parameters caused by a fixed position of laser tracks to the pad geometry with a pad size of* $2.2 \times 6.2\ mm^2$. *The plots show the margin of fluctuations of the reconstructed parameters for the 3 and 4 Tesla case of setting 3. The Chi Squared method was used as fitting routine.*

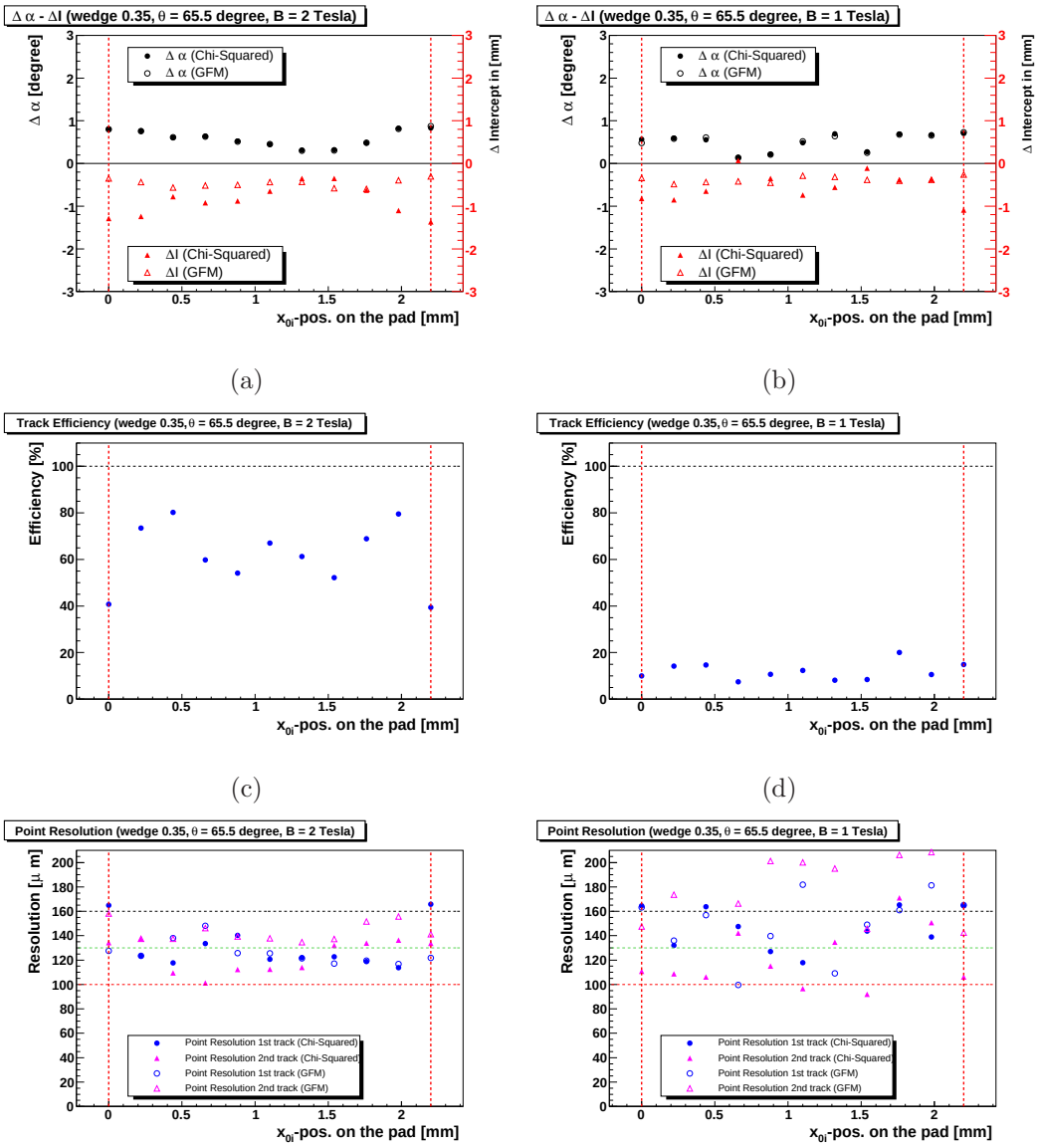

Figure 9.38: *shows the systematic effects on key parameters caused by a fixed position of laser tracks to the pad geometry with a pad size of* $2.2 \times 6.2\ mm^2$. *The plots show the margin of fluctuations of the reconstructed parameters for the 1 and 2 Tesla case of setting 3. The Chi Squared method was used as fitting routine.*

The point resolutions for all magnetic fields, given in the figures 9.33(e), 9.33(f), 9.34(e) and 9.34(f). In Table 9.10 the RMS values for all investigated parameters are given. One can clearly see, that for this setting the influence of the pad size is minimal for all magnetic fields.

In setting 2 the distance between the tracks is reduced to $\Delta\ x = 3.47$ mm at y = 0 between the tracks. Here one can already see an increase of the deviation between true and reconstructed value for α respectively ΔI. In the figures 9.35(a), 9.35(b), 9.36(a), 9.36(b) α and ΔI for the magnetic fields of this setting are plotted against the different pad positions. Again one can observe, the expected anti-correlation of α to ΔI for the Chi-Squared method. The deviations are unstable if the width of the charged cloud is small, as for the 3 and 4 Tesla case. For 1 and 2 Tesla the deviations follows a more predictable course, which indicates that with an increase of the width of the charged cloud the reconstruction is much less sensitive to small changes of the laser position. The GFM shows a different behavior. For 3 and 4 Tesla the uncertainty of α is large and small for ΔI. For 1 and 2 Tesla it is the other way around.
The track efficiency is decreased for this setting now even for higher magnetic fields, where the tracks are expected to be much better separable. In the figures 9.35(c), 9.35(d), 9.36(c) and 9.36(d) the track efficiencies of 4, 3, 2 and 1 Tesla are plotted. The resolution of the two tracks show a comparable fluctuation as for the previous setting (see Figures 9.35(e), 9.35(f), 9.36(e) and 9.36(f)). A clear increase of the uncertainties for all parameters can be observed for this setting in Table 9.10. This shows the growing influence of the pad size, which has to be taken into account and can not be neglected anymore.

In setting 3 the distance is further reduced to $\Delta\ x = 2.94$ mm at y = 0 between the tracks. This also leads to a further increase of the deviations between true and reconstructed value for α respective ΔI (see the figures 9.37(a), 9.37(b), 9.38(a) and 9.38(b)). The deviation of α reaches a value of 1 $^\circ$ and ΔIntercept exceeds 1.5 mm. In all plots there is a small area, where the deviation between true and reconstructed values becomes minimal. This is for a value of x_{01} between 1.1 and 1.76 mm and can be observed for 2, 3 and 4 Tesla. Here the strong influence of the pad size to the reconstruction becomes clearly visible.
The track efficiency of this setting is illustrated in the figures 9.37(c), 9.37(d), 9.38(c) and 9.38(d). The total range of the fluctuations are of the order of 40-50 % for 2, 3 and 4 Tesla. For 1 Tesla the maximal achievable efficiency is diminished so strong, that the possible range of fluctuations is shrinked either.
The resolution for both tracks show a strong degradation for all magnetic fields. In the figures 9.37(e), 9.37(f), 9.38(e) and 9.38(f) one can see that the maximal range of the deviations is about 60-80 μm for all magnetic fields. The course of the point resolution between two steps becomes unstable and unpredictable. Here also one important difference between the two reconstruction methods occur.

Rec. method	B-Field [T]	RMS α [^{o}]	RMS ΔI [mm]	RMS efficiency [%]	RMS Res. 1^{st} track [μm]	RMS Res. 2^{nd} track [μm]
Setting 2						
Chi^2	4	0.019	0.037	0.0	6.6	2.1
Chi^2	3	0.027	0.055	0.0	3.0	1.8
Chi^2	2	0.008	0.009	0.2	2.8	2.6
Chi^2	1	0.011	0.02	3.2	2.0	2.3
Setting 3						
Chi^2	4	0.02	0.034	0.2	2.0	3.0
Chi^2	3	0.019	0.035	0.4	2.0	2.1
Chi^2	2	0.005	0.01	1.6	2.6	2.4
Chi^2	1	0.01	0.016	6.5	5.7	5.2

Table 9.10: *The table shows the RMS of all investigated parameters and magnetic fields for a pad size of* 1.27×7.0 mm^2. *Only setting 2 and 3 were investigated with the Chi-Squared method. Compared to the larger pad size one can clearly see, that the systematic uncertainty is significantly smaller.*

For the previous two settings the RMS of all parameters were approximately the same. In setting 3 the point resolution of first and second track shows a much better performance for the GFM than for the Chi-Squared method for all magnetic fields except 1 Tesla. This is consistent with previous observations. The strongest difference between the reconstruction of the GFM and the Chi-Squared method is observed for setting 3.
The RMS of all parameters have the highest values in setting 3. This shows the huge limitation due to either the pad size or the reconstruction methods. This limitation is responsible for the huge uncertainties of the track parameters, which have been included in setting 3.

These last two settings are also investigated with smaller pad size in x-direction. The used pad size is 1.27×7.0 mm^2, which is the pad geometry, which will be used for a upcoming data taking with the Medi-TPC. The number of steps and the step size was kept unchanged. In the figures 9.39, 9.40, 9.41 and 9.42 the results are shown. Both settings show clearly, that for this pad size all relations and therefore both tracks are optimally separable. The values for α and ΔIntercept agrees very good between input and reconstructed parameters. The track efficiency is nearly 100 %, except for the 1 Tesla case of setting 3 (see figure 9.42(d)). The resolution of both tracks show fluctuations of about 20 μm. Therefore settings with a $\Delta\ I <$ 2.94 mm at y = 0 and smaller wedge angle should be used to test the limits of the track separation defined by the pad geometry.

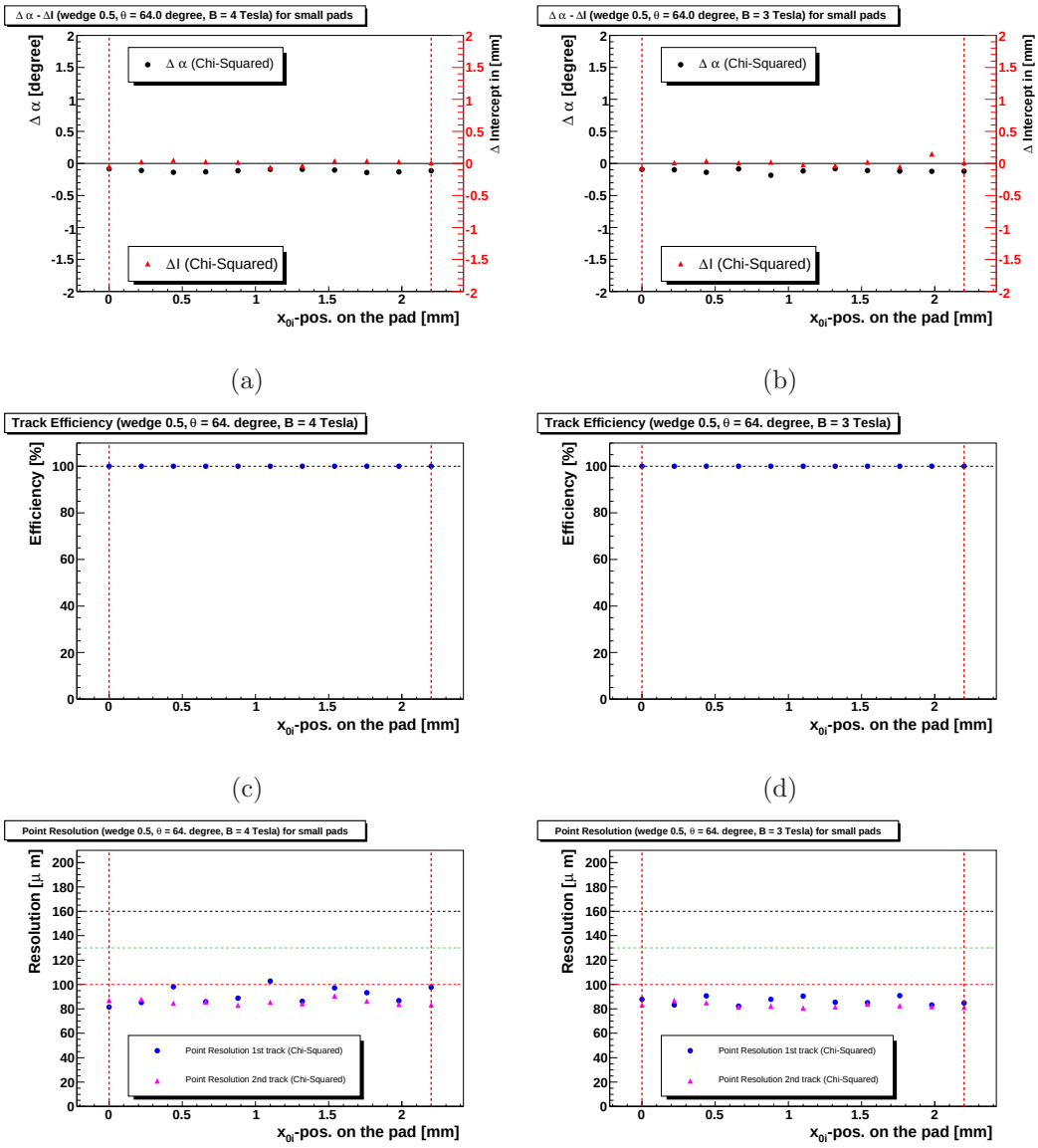

Figure 9.39: *shows the systematic effects on key parameters caused by a fixed position of laser tracks to the pad geometry with a pad size of* $1.27 \times 7.0\ mm^2$. *The plots show the margin of fluctuations of the reconstructed parameters for the 3 and 4 Tesla case of setting 2. The Chi Squared method was used as fitting routine.*

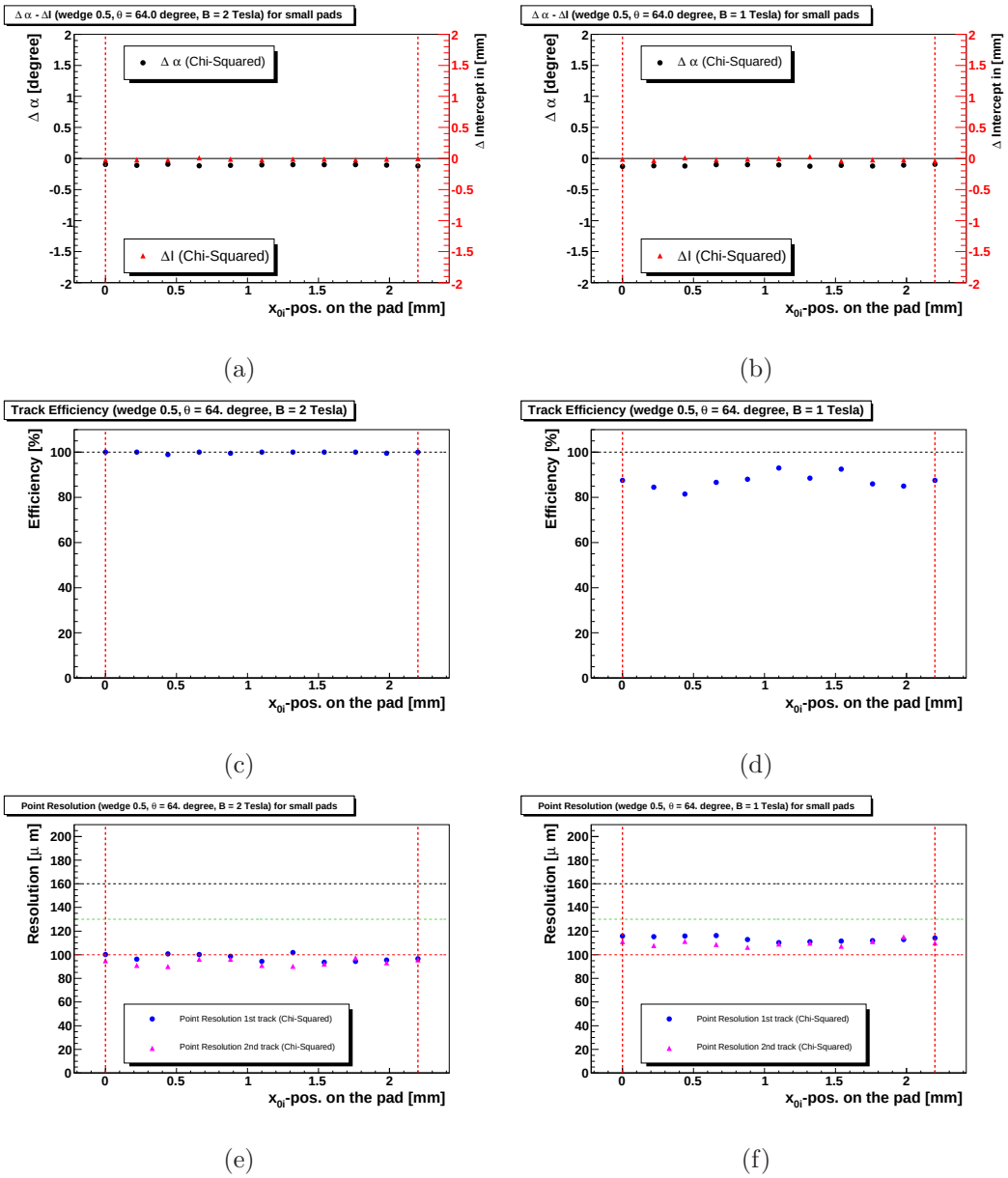

Figure 9.40: *shows the systematic effects on key parameters caused by a fixed position of laser tracks to the pad geometry with a pad size of* $1.27 \times 7.0\ mm^2$. *The plots show the margin of fluctuations of the reconstructed parameters for the 1 and 2 Tesla case of setting 2. The Chi Squared method was used as fitting routine.*

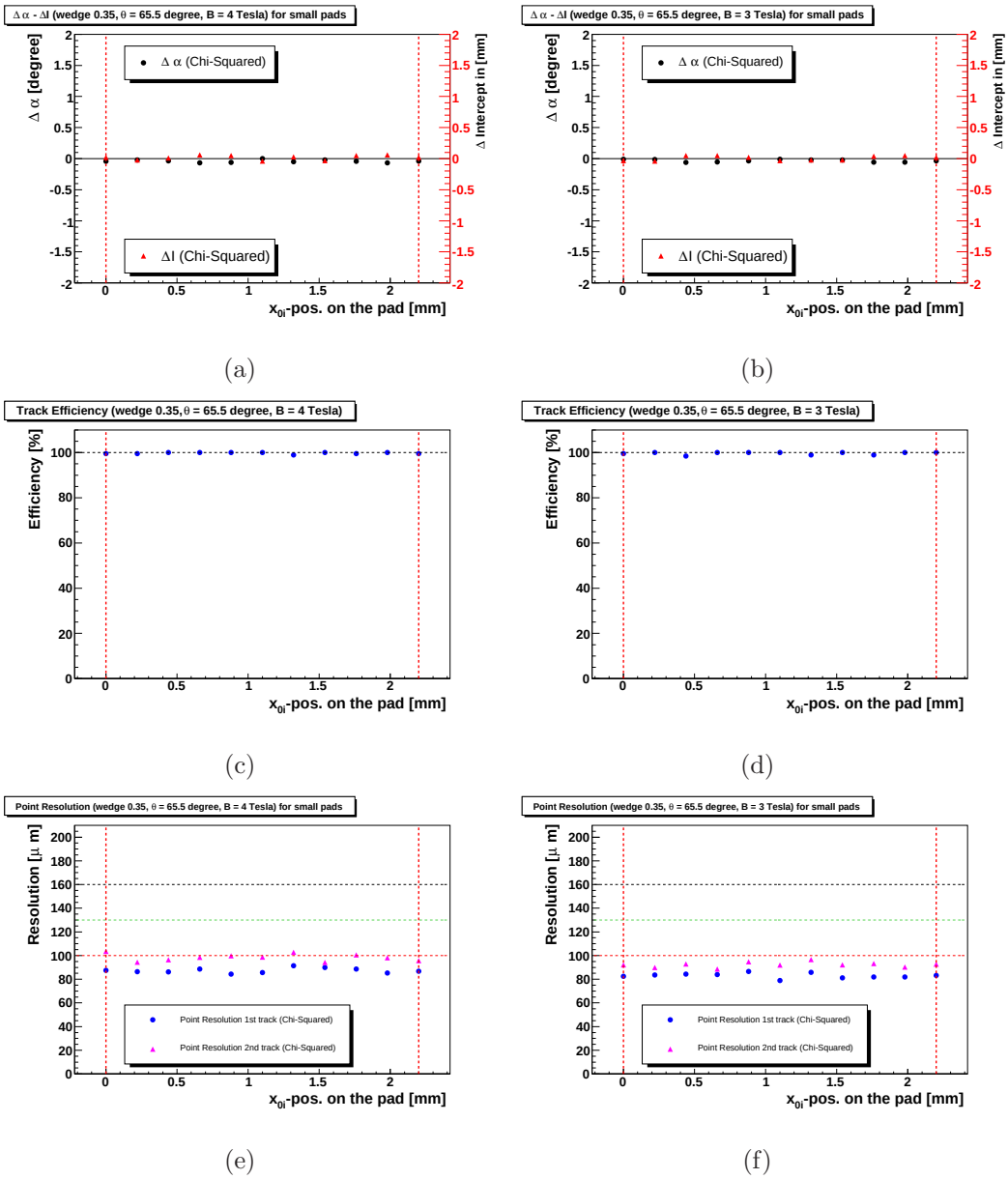

Figure 9.41: *shows the systematic effects on key parameters caused by a fixed position of laser tracks to the pad geometry with a pad size of* $1.27 \times 7.0\ mm^2$. *The plots show the margin of fluctuations of the reconstructed parameters for the 3 and 4 Tesla case of setting 3. The Chi Squared method was used as fitting routine.*

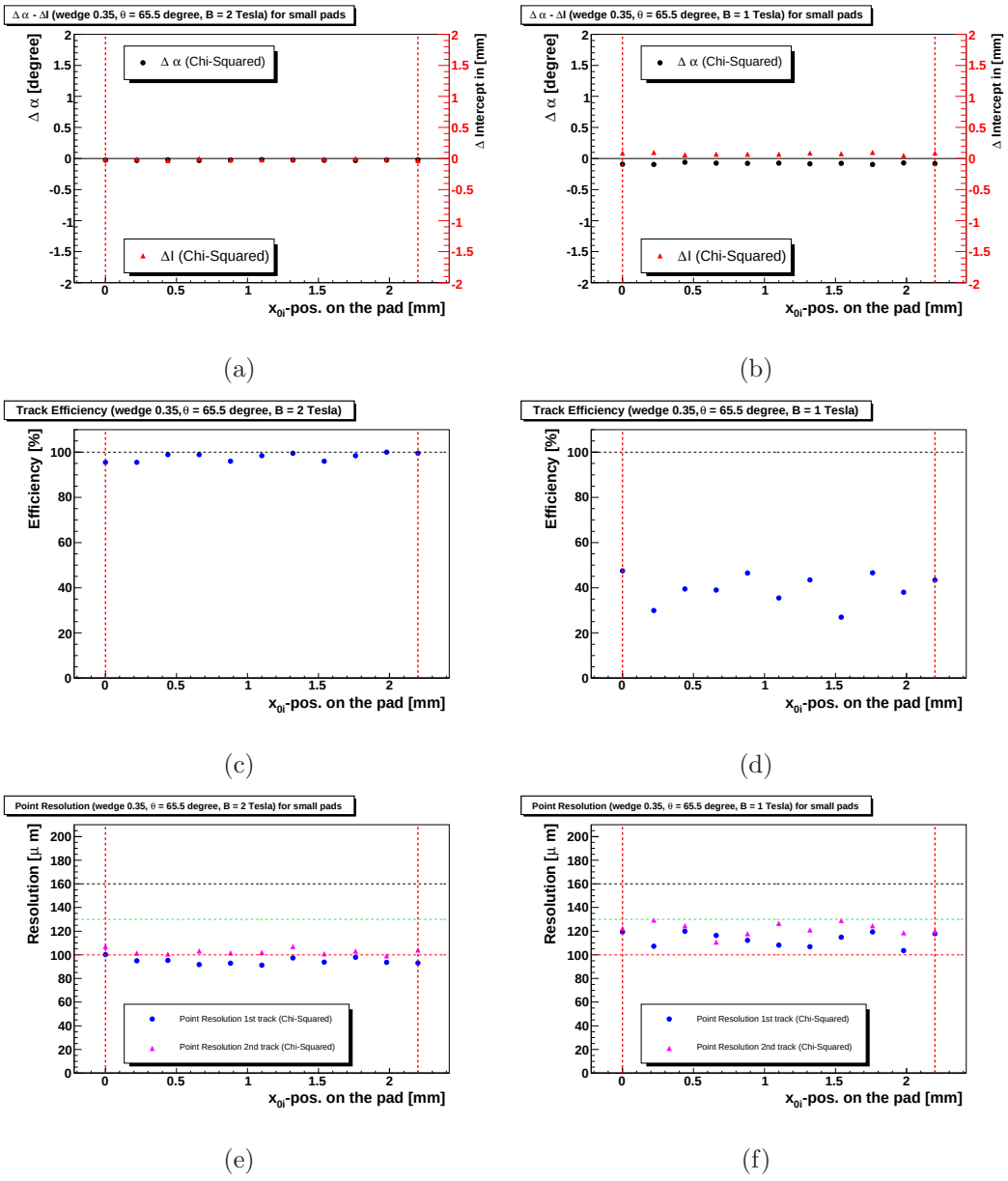

Figure 9.42: *shows the systematic effects on key parameters caused by a fixed position of laser tracks to the pad geometry with a pad size of* $1.27 \times 7.0\ mm^2$. *The plots show the margin of fluctuations of the reconstructed parameters for the 1 and 2 Tesla case of setting 3. The Chi Squared method was used as fitting routine.*

Chapter 10

Conclusion and Outlook

In this thesis first results for calibration and track separation of a GEM based TPC for small pads were presented using an ultra-violet laser. For this studies a laser setup was planned and built. An older TPC prototype was used to study the performance of the laser system. This setup was also used to perform calibration studies using the laser to measure the drift velocity. A slow control system, which has been developed in the group, was attached to the TPC. With these two tools it was possible to study the major influence of the water content on the drift velocity for a gas mixture of argon (93 %), methane (5 %) and carbon dioxide(2 %). The slow control system has been successfully used to compare water content measurements with predictions from the program MAGBOLTZ 9. The predictions from MAGBOLTZ 9 are consistent with the measurements on a level of 1 % up to water content of 800 ppm. As the water content in a TPC is normally significantly smaller the limit on the determination of the drift velocity could be set to this precision.

To use the developed laser setup for track separation studies in high magnetic fields a TPC prototype was significantly modified to enable laser operation. The laser positioning system, which produces two tracks, had to be implemented and its operation was tested in magnetic fields up to 4 T. With this TPC a successful data taking was performed to investigate the track separation performance for magnetic fields of 1, 2, 3 and 4 T. The gas was a mixture of argon (93 %), methane (5 %) and carbon dioxide (2%). The readout plane was the same as used for the point resolution studies of single tracks, which had a pad size of 2.2×6.2 mm^2. The distance between the two tracks in the xy plane was systematically reduced to study the limitations of the reconstruction in presence of another track. Two different reconstruction approaches were tested. The first approach is a conventional Chi squared approach, which determines the track and the track parameters one after another. The second one is a more advanced Global Fit method, which determines the track parameters simultaneously. It was presented, that the main track parameters such as track angles, intercept and point resolution deteriorate

strongly, if a significantly number of hits is below a distance of 4.5 mm. It was also demonstrated, that a reconstruction method, which is capable of optimizing the track simultaneously has a clear advantage over a method, which optimizes the tracks one after another.
These results were confirmed by a simulation, which was developed in course of this work. This simulation was compared to measured single laser tracks to check the validity of the simulation and afterwards used to prove the agreement of the two track measurements. The simulation shows an acceptable agreement to the measurement. It was further used to estimate the systematic influence of the pad size to the reconstruction. It was shown, that the systematic uncertainties rise significantly with the reduction of the distance between the tracks.
However the hit separation for x as given in the Technical Design Report of 2.3 mm could not be confirmed with the proposed setup and methods. Two possible direction or a combination of both can be recommended to achieve this requirement.

- **Further improvement of the reconstruction software:** Two improvements have been investigated and discussed. The improvement of the hit separation algorithm as well as the extension to a simultaneous multi track optimization are first steps to an appropriate multi track reconstruction algorithm. The next improvement would be an algorithm, which includes track information as for example average charge per row and angles in rϕ or rz from well separated multi track regions to separate the tracks in limited separation regions.

- **Reduction of the pad size:** An alternative or combination to the improvement of the reconstruction software would be a reduction of the pad size. As indicated by the studies of the systematic pad effects, the separation of the tracks is not limited by transverse diffusion, but by the pad size. As pointed out in [8] for a possible TPC at the ILC the pad size is already be reduced to a pad size of 1×6 mm^2. This will not only improve the point resolution, but also the track separation capability.

The presented results provide first answers and point out a direction for further studies to the important questions of the track separation. As a good multi track separation is crucial for the particle flow concept (PFLOW) of the detectors at the ILC, it is mandatory to investigate the track separation. A lot of work has been done to measure and improve the point resolution for single tracks. It should be demonstrated that some of the methods and tools to improve the point resolution are not inconsistent with the aim to achieve also a good track separation.
It should also be mentioned, that this work only considers the track separation in xy direction. It is crucial to investigate also the separation in z direction as soon as an appropriate electronic is available. The single point and the two track resolution is highly influenced by the proper choice of the electronic. The lack of

such an electronic made it impossible to use the setup also for this purpose, which is in principle possible.
In the framework of the newly founded ILC TPC collaboration this work as well as the described open questions can be a starting point to study the track separation on large scales. Both the knowledge of implementation of a laser system in such a TPC as well as the methods to measure and investigate the track separation can and should be included in a scientific program for a larger TPC prototype.

Appendix A

Servo Operation Tests in High Magnetic Fields

In this chapter the operation priciple of a servo motor is described. A servo motor is the main device of the prism positioning system (PPS). It was

A.0.1 Operation Principle of a Servo Motor

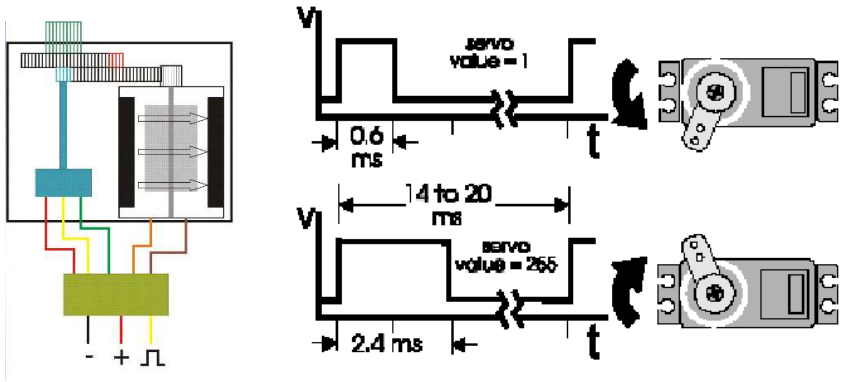

(a) General setup of a servo motor

(b) Steering principle of the servo

Figure A.1: *General setup of the servo and the principle to steer the servo with a rectangular pulses*

A servo is a simple small power motor, which is widely used in model electronics. It consists primarily of three components. A circuit board, which steers a potentiometer. The potentiometer gives a feedback signal, which then moves the motor. The motor is connected to several cogwheels. The cogwheels move

a final cogwheel, which is responsible for the movement of the PPS as explained in chapter 5.3 and additionally moves the potentiometer. If the resistance of the real potentiometer is equal to the resistance assumption, which is set at the circuit board, the movement stops. The circuit board needs a repetitive rectangular signal with a repetition frequency between 14-18 ms and an operating voltage between 4.8 and 6 V. If the signal width is of a length of 0.6 ms, the servo is moved to the first maximal position, if its 2.4 ms the servo is moved to the opposite maximal position. The servo is a S-811 model produced by Conrad Electronic [98]. It is steered by a Servo Motor Controller Board produced by Pontech [99], The board is capable of steering up to eight servo motors in parallel. In fig. A.2 the operation principle of such a servo is shown. The basic question when using a servo motor was if the motor could withstand high magnetic fields. This question is answered in the next section.

A.0.2 High Magnetic Field Tests

The test measurements of servo motors in high magnetic fields is based on the summer student report [100]. In a first test the servo motor was put in the the DESY Magnet facility described in chapter 4.8. There the servo was destroyed after applying a small field of 0.25 T, small compared to the required maximal field of 4 T. It turns out that even at this low field the circuit board implemented in the servo gets broken. As a first counter-measurement the servo was opened and the cable connection to the circuit board is by-passed, so that the circuit could be placed outside of the magnet. After tests with such a modified servo placed in the magnet facility the short term behavior showed that the servo is steerable even after applying high magnetic fields. Magnetic fields of 1, 2, 3 and 4 Tesla were tested. The magnet was ramped up to the specific field and was kept there for 15 minutes before ramped down again. The servo was steerable even if exposed to a magnetic field of 4 Tesla. Also the long time behavior was tested. These tests were not successful. After leaving the the servo for at least 12 hour in a high magnetic field of larger than 1.5 Tesla, the servo gets broken even with the modification. It turned out that the the motor and the potentiometer were still operating, but if the servo is connected to a power source some of the plastic cogwheels are permanently damaged. Therefore a closer look to the motor itself was needed.

In fig. A.2 the operation principle is shown. The servo motor consists of a permanent magnet and three coils, which produce a magnet field. If the current is applied correctly the motor is moved in the appropriate position. As a working hypothesis it has been assumed that the polarity of the permanent magnet has been reversed. If switched on the servo steering board gets the information that the resistance of the real resistance is not aligned with the one set at the board. The board tries to move the resistance by the motor to get the expected position. If the maximal position of the potentiometer is reached the gear hits a mechanical

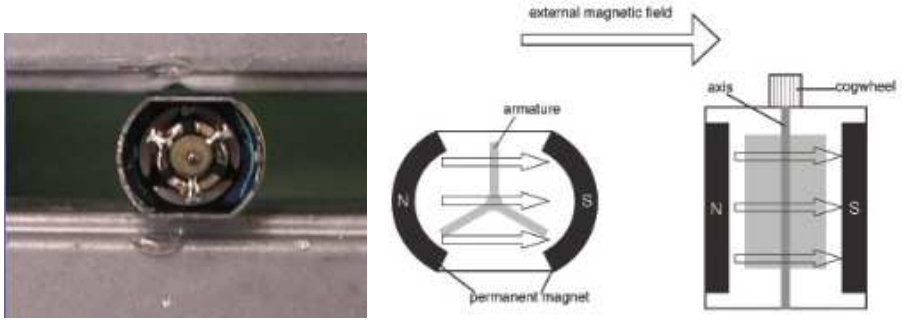

(a) Picture of the inside of a servo motor

(b) Sketch of the servo motor

Figure A.2: *General setup of the servo motor and the principle of movement induced by a magnetic coil and a bipolar permanent magnet*

stopper. As the potentiometer feeds back the information, that the correct position is still not reached, the motor keeps moving until the gear gets permanently damaged. The change of the polarity of the permanent magnet could be solved by switching also the applied current of the servo motor, which assigns again the correct voltage with the correct setting for the resistance of the potentiometer. In the second half of data taking the servo remained in the TPC and was exposed to high magnetic fields up to 4 Tesla. With the mentioned modification to the applied current the servo was operating also it was at that time placed for several days in the magnet facility.

Appendix B

Exceedance of the total FADC-range

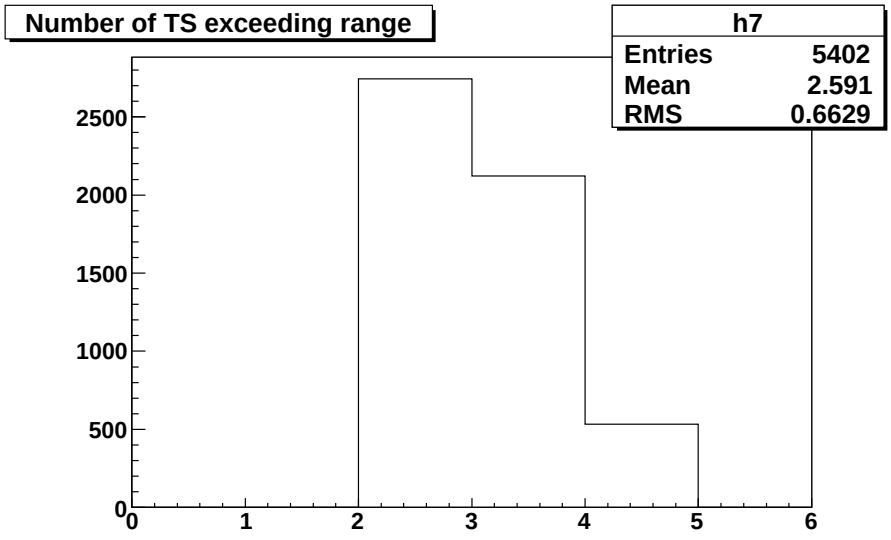

Figure B.1: *The figure shows the number of time slices for setting 1, which have been exceeding the total range of the preamplifier.*

In the Figures B.1, B.2, B.3 the number of time slices of the 3 T data sample are shown, which exceeds the total range of the preamplifier. The total range of a single channel is defined by the 8-bit Aleph preamplifiers minus the pedestal of this specific channel. If the total range of the preamplifier has been exceeded the position and charge reconstruction of this hit is seriously limited. Although

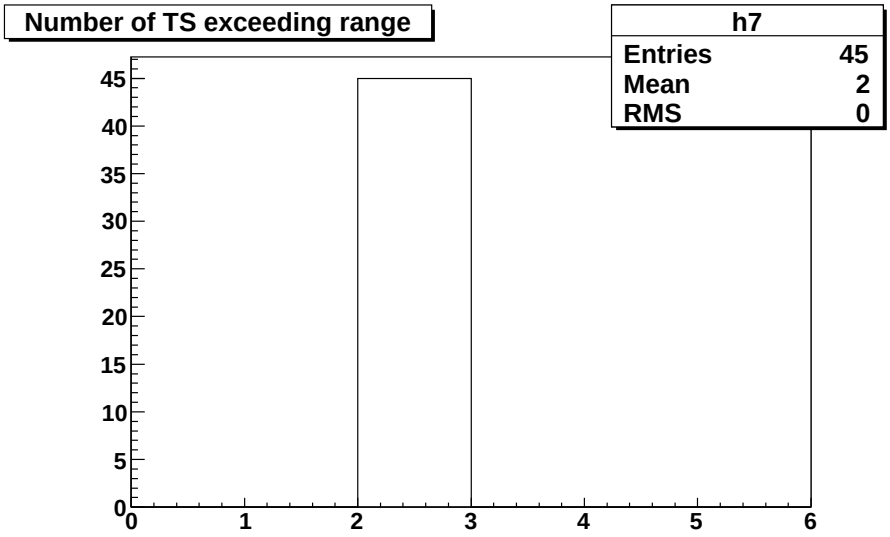

Figure B.2: *The figure shows the number of time slices for setting 2, which have been exceeding the total range of the preamplifier.*

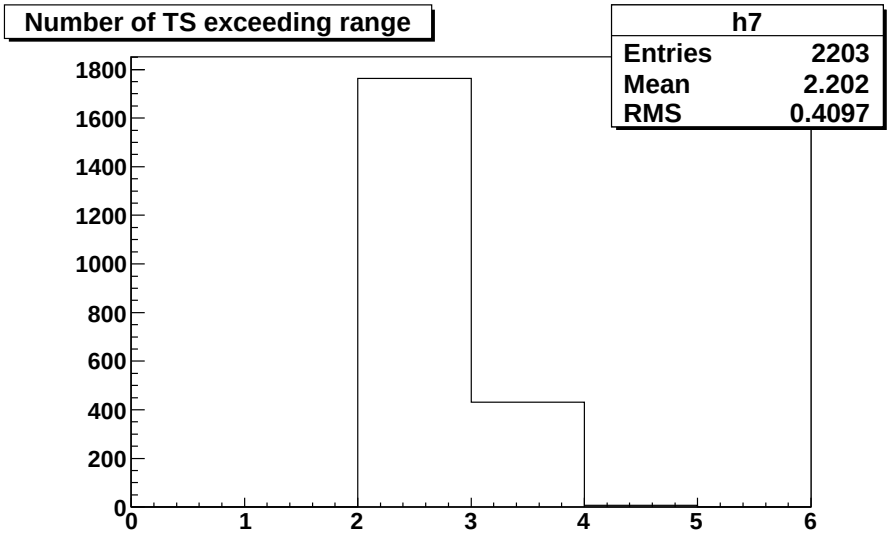

Figure B.3: *The figure shows the number of time slices for setting 1, which have been exceeding the total range of the preamplifier.*

such hits are marked in the Multifit reconstruction software as hits exceeding the limit, it seems evident, that these hits influence the point resolution. In setting 1 the highest amount of such hits occur. A combination of several effects can lead to this behavior of the preamplifier. One reason is the high laser intensity. If then the charge produced by the laser is accumulated on almost one pad the limit of the preamplifier is reached. The accumulation on one pad is of course depending on the strength of the magnetic field, which is responsible for the size of the transverse diffusion. As this effect only appears in the 3 T data files, it was not detected during the data taking, wherer an uniform amplification setting was chosen to make the results comparable for every magnetic field. As shown in Figure B.1 it has the biggest influence at setting 1, where the geometry of the tracks was such, that the charge of the higher intense beam was accumulated on mainly one pad.

Bibliography

[1] S. L. Glashow "Partial Symmetries of Weak Interactions"; Nuclear Physics **22** (1961) 579;
S. Weinberg, "A Model of Leptons"; Physical Review Letters **19** (1967) 1264
A. Salam, "Weak And Electromagnetic Interactions" in *Elementary Particle Theory* edited by N. Svartholm, page 367, Stockholm, 1969, Almqvist and Wiksell.

[2] H. Murayama, "Origin of Neutrino Mass"; presentation given on the summer school for Neutrinos in Cosmology, in Astro, Particle and Nuclear Physics, Erice, 17^{th} September, 2005

[3] Super-Kamiokande Collaboration, M. B. Smy et al., "Precise Measurement of the solar neutrino day/night and seasonal variation in Super-Kamiokande-I"; Phys. Rev. **D69** (2004) 011104, hep-ex/0309011

[4] K2K Collaboration; M. H. Ahn et al., "Indications of neutrino oscillation in a 250-km long baseline experiment"; Phys. Rev. Lett. **90** (2003) 041801, hep-ex/0212007

[5] SNO Collaboration; Q. R. Ahmad et al., " Measurement of the day and night neutrino energy spectra at SNO and constraints on neutrino mixing parameters"; Phys. Rev. Lett. **89** (2002) 011302, hep-ex/0204009

[6] KamLAND Collaboration; K. Eguchi et al., "First Results from KamLAND: Evidence for reactor anti-neutrino disappearance"; Phys. Rev. Lett. **90** (2003) 021802, hep-ex/0212021

[7] LHC Collaboration; "LHC Design Report Volume 1: The LHC Main Ring"; http://ab-div.web.cern.ch/ab-div/Publications/LHC-DesignReport.html

[8] ILC Collaboration; "International Linear Collider: Reference Design Report"; http://www.linearcollider.org/cms/

[9] G. Weiglein et al. [LHC/LC Study], "Physics interplay of the LHC and the ILC"; Phys. Rept. **426** (2006) 47, hep-ex/0410364

[10] ILCSC Parameters Document;

[11] ITRP Recommendation,

[12] P. W. Higgs, "Broken symmetries, massless particles and gauge fields"; *Phys. Lett.* **12** (1964) 132
P. W. Higgs, "Broken symmetries and the masses gauge bosons"; *Phys. Rev. Lett.* **13** (1964) 508
F. Englert and R. Brout, "Broken symmetry and the mass of gauge vector mesons"; *Phys. Rev. Lett.* **13** (1964) 321
G.S. Guralnik, C.R. Hagen, and T.W.B. Kibble, "Global conservation laws and massless particles", *Phys. Rev. Lett.* **13** (1964) 585

[13] M.W. Gruenewald, "Electroweak precision data: Global Higgs analysis"; (2003), hep-ex/0304023
S. Roth, "Standard Model Fits"; (2004), Recontres de Moriond, see http://moriond.in2p3.fr/QCD/2004/ThursdayAfternoon/Roth.pdf

[14] ALEPH Collaboration, R. Barate et al., "Search for the Standard Model Higgs boson at LEP"; *Phys. Lett.* **B565** (2003) 61, hep-ex/0306033.

[15] R. Haag, J. Lopuszanski, M. Sohnius, *Nucl. Phys.* **B88** (1975) 257

[16] J. Wess, B. Zumino, *Nucl. Phys.* **B70** (1974) 39
J. Wess, B. Zumino, *Nucl. Phys.* **49B** (1974) 52

[17] M. Battaglia, hep-ph/9910271.

[18] M.T. Dova, P. Garcia-Albia and W. Lohmann, hep-ph/0302113.

[19] ILC, Homepage: ILC, 2006, http://www.linearcollider.org

[20] J.A. Aguilar-Saavedra et al., Eur. Phys. J. C46, 43 (2006).

[21] H.U. Martyn, LC-PHSM-2003-07, hep-ph/0302024.

[22] LDC Collaboration; "Detector Outline Document For The Large Detector Concept"; 24^th August 2006, http://www.ilcldc.org/documents/dod/

[23] T. Barklow, Physics Impact of Detector Performance. http://www-conf.slac.stanford.edu/lcws05/program/talks/18mar2005.ppt, 2005, presented at 2005 International Linear Collider Workshop.

[24] H.J. Schreiber, "Branching Fraction Measurements of the SM Higgs with a Mass of 160 GeV at Future Linear Colliders"; LC-PHSM-2000-035.

[25] H.U. Martyn, "Detection of sleptons at a linear collider in models with small slepton neutralino mass diferences"; hep-ph/0408226, 2004

[26] A.R. Clark et al., PEP-4 Proposal (1976)

[27] C. Bowdery, Aleph Handbook 1995, Volume 1, Chapter V, ISBN 92-9083-072-7

[28] Delphi Collaboration; " Performance of the DELPHI detector"; *Nucl. Instr. and Meth.* **A 378** (1996) 57

[29] The STAR Collaboration; "The STAR Conceptual Design Report"; June 15, 1992, PUB-5347.

[30] ALICE TPC collaboration; "Technical Design Report of the Time Projection Chamber"; CERN/LHCC 2000-001, ALICE TDR 7, 7 January 2000

[31] T2K ND280 collaboration, "Conceptual Design Report"; September 6, 2005

[32] D. R. Nygren, "A Time Projection Chamber", Presented at the 1975 PEP Summer Study. **PEP 198** (1975)

[33] G. Charpak and F. Sauli, *Nucl. Instr. and Meth.* **113** (1973) 381

[34] H. Aihira et al., *Phys. Rev. Lett.* **61** (1988) 1263

[35] W.W.M. Allison and J.H. Cobb, *Annual Review of Nuclear Particle Science* **30** (1980) 253

[36] H.A. Bethe, "Handbuch der Physik 24/1"; Springer, Berlin, 1933, page 491

[37] M. Gruwe, "Studies of dE/dx capabilities of a TPC for the future Linear Collider TESLA"; *LC-Note* **Det** (2001) 043

[38] M. Hamann, "Studies for a Linear Collider Drift Chamber and Search for Heavy Stable Charged Particles in e^+e^- Collisions up to $\sqrt{s}$=209 GEV"; dissertation at Univerit"at of Hamburg 2003

[39] Michael Hauschild, "Progress in dE/dx techniques used for particle identification"; *Nucl. Instr. and Meth.* **A379** (1996) 436-441

[40] P. Langevin, C. R. Acad. Sci. Paris **145** (1908) 530

[41] M. Gruwe, "Gas studies for the TPC of a detector for the future Linear Collider TESLA"; *LC-Note* **Det** (1999) 003

[42] TESLA, Technical Design Report, Technical Report DESY 2001-11, DESY, Notkestraße 85, 22607 Hamburg, March 2001

[43] R.L. Gluckstern, "Uncertainties in track momentum and direction, due to multiple scattering and measurement errors "; *Nucl. Instr. and Meth.* **24** (381-389) 1963

[44] W. Blum, L. Rolandi, "Particle Detection with Drift Chambers", Springer (1993)

[45] H. Anderhub, M.J. Devereux, P.G. Seiler; *Nucl. Instr. and Meth.* **166** (1979) 581

[46] H.J. Hilke; *Nucl. Instr. and Meth.* **A252** (1986) 169

[47] M. Towrie, J.W. Cahill, K.W.D. Ledingham, et. al; *J. Physics B: At. Mol. Phys.* **19** (1986) 1989

[48] Melles Griot: "Transverse Modes and Mode Control"; Lilienthalstr. 30-32, 64625 Bensheim, Germany, http://www.mellesgriot.com/

[49] S. Kappler, "Development of a GEM-based TPC Readout for Future Collider Experiments"; PhD-thesis July 23^{th}, 2004

[50] F. Sauli, "GEM: A new concept for electron amplification in gas detector"; *Nucl. Instr. and Meth.* **A386** (1997) 531

[51] M. Hoch "Development of fast Tracking Detectors: Micro Strip Gas Chamber and GEM Gas Electron Multiplier", dissertation at Technisch Universität Wien, 1998

[52] Ansoft, "Maxwell", documentation online available: **http://www.ansoft.com/products/em/max3d/index.cfm**

[53] R. Veenhof, "GARFIELD, a drift chamber simulation program. Version 7.10", Jan. 2001, online available: **http://consult.cern.ch/writeup/garfield**

[54] S. Bachmann et al., "Charge amplification and transfer process in the gas electron multiplier"; *Nucl. Instr. and Meth.* **A438** (1999) 376

[55] G. Charpak et al.; *Nucl. Instr. and Meth.* **62** (1968) 235
G. Charpak et al.; *Nucl. Instr. and Meth.* **80** (1970) 13
G. Charpak et al.; *Annu. Rev. Nucl. Sci.* **20** (1970) 195

[56] P. Fonte et al., "Feedback and breakdown in parallel-plate chambers", *Nucl. Instr. and Meth.* **A305** (1991) 91

[57] H. Raether, "Electron Avalanches and Breakdown in Gases"; **Butterworth, London, 1964**

[58] S. Bachmann et al., "Performance of GEM detectors in high intenity particle beams"; *Nucl. Instr. and Meth.* **A470** (2001) 548

[59] G. Baum et al., "Proposal for a common muon and proton apparatus for structure and spectroscopy"; CERN/SPLSC 96-14 (1996)

[60] S. Bachmann et al., "Discharge studies and prevention in the gas electron multiplier(GEM)"; *Nucl. Instr. and Meth.* **A479** (2002) 294

[61] B. Boimska et al., "Robustness test of a system of MSGC+GEM detectors at the cyclotron facility of the Paul Scherrer institute"; *Nucl. Instr. and Meth.* **B61B** (1998) 498

[62] A. Bressan, "High rate behavior and discharge limits in micro-pattern detectors"; *Nucl. Instr. and Meth.* **A424** (1999) 321

[63] A. Kaukher, "A study of a readout electronics based on Time-to-Digital Converters for International Linear Collider TPC detector"; dissertation at Univerit"at of Rostock 2007

[64] T. Lux, "Studies for a Time Projection Chamber for the International Linear Collider and Measurement of Beauty Cross Sections in Deep Inelastic Scattering at HERA"; dissertation at Univerit"at of Hamburg 2005

[65] R. Diener; "Study of Reconstruction Methods for a Time Projection Chamber with GEM Gas Amplification System", graduate work at the University of Hamburg, May 2006

[66] FuG: "Power Supply", FuG Elektronik GmbH, Florianstr. 2, 83024 Rosenheim, Germany, http://www.fug-elektronik.de

[67] CAEN: "Technical Information Manual"; CAEN SpA - Corporate Headquarter, Via Vetraia , I-55049 Viareggio, Italy, http://www.caen.it/nuclear/product.php?mod=SY527

[68] O. Schäfer, "Ein Moniorsystem für gasbasierte Detektoren am Internationalen LInear Beschleuniger"; graduate work submitted at the Universität of Rostock, December 2005

[69] MBW: "Taupunktmessgeräte DP3-D-SH"; MBW Elektronik AG, Seminarstrasse 55, CH-5430 Wettingen, Swiss, - http://www.mbw.ch

[70] Teledyne Analytical Instruments, "Operating instructions for Model 3190 Series Trace Oxygen Analyzer" 16830 Chestnut Street, P.O. Box 1580, City f Industry, CA 91749-1580 USA, http://www.teledyneinstruments.com

[71] FAIRCHILD: "Instruction for the Installation, Operation and Maintenance of Fairchild Model 10 BP Back Pressure Regulator.", Fairchild Industrial Products Company, 3920 West Point BLVD, Winston-Salem, NC 27103-6708, http://www.fairchildproducts.com

[72] FAIRCHILD: "Pneumatic Precision Back Pressure Regulator Model 10 BP.", Fairchild Industrial Products Company, 3920 West Point BLVD, Winston-Salem, NC 27103-6708, http://www.fairchildproducts.com

[73] SETRA: "Model 280E/C280E Pressure Transducer for Corrosive Liquids or Gases Gauge, Compound and Absolute Pressures"; setra, 159 Swanson Road, Boxborough, MA 01719-1304, http://www.setra.com

[74] SETRA: "Installation Guide Model 267 and 267MR Differential Pressure Transducers "; setra, 159 Swanson Road, Boxborough, MA 01719-1304, http://www.setra.com

[75] M. Ball, N. Ghodbane et al. "A DAQ system for linear collider TPC prototypes based on the ALEPH TPC electronic"; *LC-Note* **Det** (2004) 120

[76] Big Sky Laser: "User's manual: ULTRA CFR Nd:YAG Laser System", Big Sky Laser Technologies, Inc. P.O. Box 8100 Bozeman, MT 59715-2001, USA, http://www.bigskylaser.com

[77] C. Czeranowsky, "Resonatorinterne Frequenzverdopplung von diodengepumpten Neodym-Lasern mit hohen Ausgangsleistungen im blauen Bereich", Phd-thesis, Hamburg 2002

[78] Bergmann Schaefer, "Lehrbuch der Experimentalphysik"; 8^{th} edition 1987, band III, page 159 ff.

[79] Field Master: "Power/Energy Analyzer User Manual", Coherent, branch Germany, Diestelstr. 5b, D-64807, http://www.coherent.de

[80] Computer Simulation Technology: "Handbook"; CST GmbH -Headquarters, Bad Nauheimer Str. 19, D-64289 Darmstadt, Germany, http://www.cst.com

[81] M.E. Janssen, "Auflösungsstudien an einer Zeit-Projektionskammer (TPC) mit GEM Gasverstärkungssystem"; December 2004, DESY-THESIS-2004-049

[82] Homepage: ROOT - Data Analysis Framework, CERN, CH, 2007, http://root.cern.ch/.

[83] Homepage: LCIO - data model for ILC detector studies, DESY, 2007, http://lcio.desy.de/.

[84] T. Lohse and W. Witzeling, "The Time Projection Chamber", Instrumentation in High Energy Physics (Advanced Series on Directions in High Energy Physics - Vol. 9)(June 1992)

[85] M.E. Janssen, "Performance Studies of a Time Projection Chamber at the ILC and Search for Lepton Flavor Violation at HERA II"; dissertation at Univerit"at of Hamburg May 2008

[86] R.K. Carnegie et al., "Resolution studies of cosmic ray tracks in a TPC with GEM readout", *Nucl. Instr. and Meth.* **A538** (2005) 372

[87] W.R. Leo, "Techniques for Nuclear and Particle Physics Experiments - A Howto Approach"; Springer-Verlag, New York Berlin Heidelberg, 1994 2nd Edition

[88] D. Karlen, P. Poffenberg, G. Rosenbaum, "TPC Performance in Magnetic fields with GEM and Pad Readout"; *Nucl. Instr. and Meth.* **A555** (2005) 80

[89] D. Karlen, Homepage: http://particle.phys.uvic.ca/ karlen/

[90] MAGBOLTZ Homepage; http://ref.web.cern.ch/ref/CERN/CNL/2000/001/magboltz

[91] R. Veenhof, "GARFIELD - A Drift Chamber Simulation Program", CERN Program Library W5050 (1984)

[92] F.W. Stöver, "Driftgeschwindigkeitsstudien an einer Zeit-Projektions-Kammer (TPC) bei unterschiedlichen Wassergehalten des Kammergases"; graduate work submitted at the Universit"at of Hamburg, März 2007

[93] K. Komar, "Studies on Two Track Resolution at a Time Projection Chamber"; Phd-thesis in preparation

[94] A. Münnich, "Simulation Studies for a High Resolution Time Projection Chamber at the International Linear Collider"; Phd-thesis published Mai 2007

[95] Jakob Hauschildt, "Optimierung eines Detektors an einem 500 GeV e^+e^- Beschleuniger", diploma thesis at the University of Hamburg, Juni 2000

[96] S. Lotze, "Ion Backdrift Minimisation in a GEM-Based TPC Readout"; Phd-thesis published April 2006

[97] M. Schumacher, "Pad readout geometries for a TPC with GEM readout for the TESLA linear collider"; LC-DET-2001-014

[98] Conrad Electronic: "Operating Instructions"; Conrad Electronic GmbH, Klaus-Conrad-Straße 1, D-92240 Hirschau, Germany, http://www.conrad.de

[99] Pontech: "SV 203 Servo Motor Controller Board / User's Manual"; Pontech 2700 E. Imperial Hwy., Suite N - Brea, CA 92821

[100] S. Grebe, "The problem of operating a servo in strong magnetic fields"; Summer Student Report, August, 2006

Persönlich Anmerkungen und Danksagung

Der Krieg ist der Vater aller Dinge

(Heraklit)

It's not what you are underneath, it's what you do that defines you.

(Rachel Daws in 'Batman Begins')

Der Forschung, der Lehre, der Bildung.

(Universität Hamburg, Hauptgebäude Edmund Siemers Allee)

Der 10. Januar 1995 war ein bedeutender Tag für mich. An diesem Tag kam ich nach Hamburg mit dem festen Vorsatz hier Physik zu studieren. Seitdem ist eine Menge Wasser die Elbe hinunter geflossen und mit der vorliegenden Doktorarbeit endet nun endgültig ein ganzer Lebensabschnitt und damit auch meine Zeit hier in Hamburg. Das Lernen jedoch geht weiter.

Sehr oft in diesen Jahren und speziell in den Jahren der Doktorarbeit kam mir der zitierte Satz von Heraklit in den Sinn. So wie ich ihn verstehe bedeutet er, dass nur der Kampf, die Auseinandersetzung mit einer Sache zu einem wirklichen Verstehen führt. Tatsächlich ist es wohl so, dass unser Gehirn bei einem erfolgreichen Lernprozess das gelernte um so stärker verankert, je grösser der vorangegangene Stress war. Heraklit hatte also recht und während der über fünf Jahre, die diese Doktorarbeit dauerte, kann ich seine Aussage aufgrund der von mir gemachen Erfahrungen nur bestätigen.

Nun also ist es geschafft und jeder kann die vorliegende Arbeit hinsichtlich ihrer wissenschaftlichen Qualität bewerten. Ich persönlich jedenfalls bin mit dem Ergebnis ganz zufrieden.

Das Aufkommen der modernen Naturwissenschaften in Europa im Zuge der Renaissance, veränderte eine wesentliche Sache im Hinblick auf die Generierung von Wissen. Jede Behauptung muss seither nicht nur theoretisch, sondern eben auch experimentell überprüfbar sein. Diese experimentelle Überprüfbarkeit führt wiederum dazu auch das technische Vermögen zu entwickeln, eine Behauptung zu beweisen. Während meiner Doktorarbeit hatte ich das grosse Glück einmal den gesamten Prozess der Verwirklichung von der Grundidee bis zur Auswertung zu durchlaufen und eigenverantwortlich zu gestalten. Eines lehrt es auf jeden Fall, sehr viel Geduld zu haben. Denn nicht immer stellt sich das, was in fünf Minuten als brilliante Idee auf einem Blatt Papier notiert wurde, hinterher als wirklich

realisierbar heraus.

Eine andere wichtige Erkenntnis ist die, dass sich keine dieser Ideen alleine verwirklichen lässt. Viele haben ganz entscheidend dazu beigetragen, dass ich diese Arbeit durchführen und tatsächlich auch abschliessen konnte. Einige Personen möchte ich ganz zu Anfang erwähnen, die sonst nicht so an exponierter Stelle stehen.

Zum einen ist da Jörn Schaffran, der vom mobilen Reinraum bis zum 8 mm Kupferleitung alles besorgen kann und gleichzeitig auch noch weiss wie man es sicher betreiben kann. Karin Troeger, die alle technischen Zeichnungen für mich anfertigte und damit mir und vor allem den Leuten vom Uni-workshop meine ganzen amateurhaften xfig Zeichnungen erspart hat. Der Gas-Gruppe unter Hr. von Schroeder möchte ich für ihre kompetente und völlig unbürokratische Hilfe danken, die leider auch nötig war, wenn mal wieder eine Gasflasche ausgelaufen war, ohne dass eine neue bestellt war. Das gleiche gilt für die Kryo-Gruppe unter Hr. Herzog, die wirklich einiges in Bewegung setzen konnten, als meine Gasleitungen mit 20000 ppm wahrhaftig unter Wasser stand. Dem schon erwähnten Uniworkshop verdanke ich die schnellst mögliche und unbürokratischst denkbare Fertigstellung wichtiger Teile meines Laser Positionierungssystems.

Eine ganz besonderen Dank gilt Ramona Matthes, ohne die fast obligatorische Tasse Kaffee am Morgen, die vielen netten Gespräche und guten Ratschläge wäre es wirklich schlimm um meinen Seelenfrieden bestellt gewesen.
Allen dafür vielen herzlichen Dank. DESY kann stolz sein solche tollen Mitarbeiter zu haben.

Dies trifft auch auf die TPC Gruppe, in der ich beinahe fünf Jahre arbeiten durfte. Es war mir eine Freude und Ehre mit euch allen zusammenarbeiten zu dürfen. Einer verdient sicher eine besondere Erwähnung: Matthias Janssen, der mit seinem enzyklopädischen Wissen, seiner Professionalität und vor allem seinem Teamgeist, die ganze Gruppe inspiriert hat.
Mein Dank gilt: Nabil Ghodbane, der mir mit unendlicher Geduld sehr viel in Punkto Elektronik beigebracht hat.
Peter Wienemann, der mir mit seinem Tatendrang und seiner effektiven Art der Programmierung einen grossen Schritt weiter geholfen hat.
Sascha Khaukher mit dem ich viel Zeit im Labor verbringen durfte danke ich für Rat und Tat, eine angenehmen Gesprächs- und Diskussionskultur und vielen kritischen Nachfragen, die mein Verständniss von Hardwarearbeit nachweislich gefördert hat.
Thorsten Lux, den man getrosst Mr. Medi-TPC nennen darf, danke ich für viele wichtige Tips beim Betreiben seiner TPC. Ich hoffe, ich habe das Banner weiter getragen.
Peter Schade (Peter der zweite) und Ralf Diener möchte ich für ihre Hilfe bei

den CST-Berechnungen zum Einfluss des Prisma Positionierungssystems auf die Feldhomogenität und den Vergleich zwischen single laser tracks Medi-TPC zu Big-TPC danken. Vor allem da diese Berechnunge unter erheblichem Zeitdruck in die Arbeit einfliessen mussten.

Der restlichen TPC Truppe, so wie ich sie in Erinnerung habe: Adrian Vogel, Lea Hallerman, Oliver Schäfer, Felix Stoever, Krisztof Komar und Klaus Dehmelt Danke ich von ganzem Herzen für die inspirierende gemeinsame Zeit. Ich kann nur hoffen, dass es euch genauso viel Spass gemacht hat wie mir.

Meinen drei Zimmergenossen Hendrik Maier, Ralf Diener und Matthias Janssen möchte ich noch mal besonders für die tolle Arbeitsatmosphäre im Altherrenzimmer danken. Getreu dem Wahlspruch: " Wer jemand unter 30 kennt, gehört nicht zum Establishment " hatten wir viele Diskussionen über Gott und die Welt und das Universum und den ganzen Rest (Einige der wenigen Dinge, die ich selbst im sonnigen Valencia vermisse).

Christoph Rosemann möchte ich für die vielen tollen Diskussionen über Budophilosophie und dem generellen Verständniss des Bushido danken.

Dr. Oleg Eyser, Dr. Steve Aplin, Dr. Philip Bechtle und Dr. Ties Behnke möchte ich für das Korrektur lesen und die vielen hervorragenden Verbesserungsvorschläge zu meiner Doktorarbeit danken.

Der ganzen FLC Gruppe danke ich für die tolle gemeinsame Zeit.

Meinen lieben Freunden während des Studiums danke ich für diese verrückten (fast) 13 Jahre. Wer hätte je gedacht, dass aus uns tatsächlich Physiker werden. Alles gute für euch: Lutz Tröger, Michael Flegel, Bodo Krause-Kyora, Oleg Eyser, Frauke Pascheke, Niklas Rega, Henning Lueders, Rene Eiselt und Gesa Netzeband.

Meinen beiden lieben Freunden Hajo Neumann und Cornelius Lockau möchte ich für den Lords-Table danken, meinem Lieblingskreis von Iaidokas nördlich und südlich der Elbe. Durch unser gemeinsames Taining und die anschliessenden italienischen Abende wäre ich sicher nicht so ein reicher Mensch.

Ganz besonders möchte ich mich bei meinen beiden Eltern Hans-Jörg und Ursula Ball bedanken, die mich massgeblich zu dem Menschen geprägt haben, der ich bin. Zudem wäre ohne ihre selbstlose finanzielle Unterstützung während des gesamten Studiums und speziell am Ende ich arbeitslos wurde, das ganze Projekt beinahe noch gescheitert.

Meiner lieben Freundin Christina möchte ich für ihre engelsgleiche Geduld, ihr

gütiges Wesen und ihr unglaubliches Verständnis mir gegenüber danken. Ohne dich Schatz hätte ich das alles nicht tun können.

Unendlich Dankbar bin ich für das große Geschenk unserer Tochter Sarah, die mir geholfen hat alle Dinge, wie auch diese Arbeit und die ganze Zeit am DESY und in der FLC Gruppe ins rechte Licht zu rücken.

Zu guter Letzt möchte ich noch Prof. Rolf-Dieter Heuer und Prof. Klaus Desch für das Gutachten dieser Arbeit danken.

Prof. Heuer und Dr. Ties Behnke möchte ich weiterhin für die Möglichkeit danken diese Arbeit in ihrer Gruppe durchzuführen.